Universität Hamburg

DER FORSCHUNG | DER LEHRE | DER BILDUNG

Novel ultrafast fiber laser sources utilizing fiber nonlinearities

Dissertation

zur Erlangung des Doktorgrades Doctor rerum naturalium
And der Fakultät für Mathematik, Informatik und Naturwissenschaften
Fachbereich Physik
der Universität Hamburg

vorgelegt von
Qian Cao
am
30.04.2020

Qian Cao

Matrikelnummer: 6543210

Notkestraße 85, 22607 Hamburg

"There is no happiness in the world,
but there is peace and freedom there."

– Alexander Pushkin

Abstract

Due to the lack of proper active gain media, mid-IR frequency combs in the molecular "fingerprint" region are normally implemented by difference frequency generation (DFG) process inside nonlinear crystals. In addition to granting an access to the long-wave ($>10~\mu$m) side of the mid-IR spectrum, DFG also offers a wide wavelength tunability, a high-repetition-rate (HRR) operation (>10 MHz), and a passive cancelation of the carrier-envelope phase offset, all of which enable a simplified experimental configuration for constructing mid-IR frequency combs.

Currently, DFG-based mid-IR frequency combs especially at wavelengths beyond 10 μm suffer from insufficient available power, mainly caused by un-optimized wavelength-shifting processes and an inefficient parametric interaction of the DFG process. Moreover, during conventional nonlinear fiber-optic wavelength-shifting methods, an excessive amount of relative timing jitter (RTJ) noise is introduced to the signal pulses, which later translates to the noise of the generated mid-IR idler pulses during the DFG process, and may significantly deteriorate the comb performance of the mid-IR frequency comb.

In this thesis, we numerically investigate several important issues that are related with constructing high-power, low-noise DFG-based mid-IR frequency combs. We first discuss two nonlinear fiber-optic methods, namely, soliton self-frequency shift (SSFS) and self-phase-modulation enabled spectral selection (SESS), by comparing their capability of generating wavelength-shifted signal pulses with a high pulse energy and a low RTJ noise. To elucidate an efficient approach for generating high-power mid-IR sources, we study the power scalability of DFG by investigating DFG processes under different launching conditions. Two sets of DFG with different pump wavelengths, 1.03 μm and 2 μm, are compared. Besides the power scalability, we also compare the noise transfer property of these two sets of DFG. We identify how the timing jitter noise of an offset-free frequency comb affects its comb characteristics through Monte-Carlo simulations. The comb line-width can be well estimated by using a geometrical β-separation line method. Finally, we demonstrate a 1-GHz passively offset-free laser source which is built based upon a Yb:fiber laser system and an alternative DFG schematic.

Enabled by novel nonlinear fiber-optic wavelength-shifting methods, the pulse energy of the wavelength-shifted signal pulses can be increased from sub-nJ level to tens-of-nJ or even hundreds-of-nJ level. Using such signal pulses to seed an optimized DFG system, a 50-MHz HRR mid-IR frequency comb with an average output power of >2.2-W is viable. We believe that such a source will open new avenues for novel scientific applications.

Zusammenfassung

Frequenzkämme im mittleren Infrarotbereich, dem Spektralbereich der molekularen Fingerabdrücke, können auf Grund fehlender direkter Verstärker-Medien, nur mit Hilfe von Differenzfrequenzbildung (DFG) in nichtlinearen Kristallen realisiert werden. Zusätzlich zum Zugang in den langwelligen Bereich (>10 μm) des mittleren Infrarotbereiches, ermöglicht DFG eine breite Wellenlängen Abstimmbarkeit, hohe Repetitionsraten (>10 MHz) und eine passive Stabilisierung der Träger-Einhüllenden-Phase. Alle diese Effekte können zur Konstruktion von Frequenzkämmen im mittleren Infrarotbereich benutzt werden.

Auf Grund von nicht optimierten Frequenzverschiebungsprozessen und eventuell uneffizienter parametrischer Wechselwirkungen der DFG selbst leiden DFG basierte mittelinfrarote Frequenzkämme, besonders jenseits von 10 μm, an unzureichender mittlerer Leistung. Außerdem führt herkömmliche Frequenzverschiebung in nichtlinearen Fasern zu zusätzlichem relativen Timing-Jitter (RTJ) auf dem Signalimpuls. Auch wird der relative Timing-Jitter infolge der Pulspropagation durch das System auf den später erzeugten Idlerimpuls während des DFG-Prozesses übertragen, was die Kohärenz des Frequenzkammes signifikant verschlechetert bzw. den Frequenzkamm sogar auslöschen kann.

In dieser Arbeit untersuchen wir numerisch einige wichtige Aspekte zur Erzeugung rauscharmer Frequenzkämme im mittleren Infrarotbreich mit hoher mittlerer Leistung basierend auf Differenzfrequenzbildung. Zuerst diskutieren wir zwei Techniken in der nichtlinearen Faser-Optik, namentlich die „Soliton-Selbst-Frequenzverschiebung" (SSFS) und die durch „Selbst-Phasenmodulation Ermöglichte Spektrale Selektion" (SESS) und vergleichen diese im Hinblick auf maximale Impulsenergie und minimalen RTJ. Dann untersuchen wir die Leistungsskalierbarkeit des DFG Prozesses für die Frequenzkammerzeugung im mittleren Infrarotbereich bei hoher Leistung. Zwei verschiedene DFG-Prozesse mit den Pumpwellenlängen 1.03 μm und 2 μm werden verglichen. Wir zeigen mittels Monte-Carlo Simulationen, wie der Timing-Jitter eines phasenschlupf-freien Frequenzkammes sich auf die Kammeigenschaften auswirkt. Die Kammbreite wird durch die geometrische Separations-Linien-Methode bestimmt. Zuletzt demonstrieren wir einen 1 GHz passiv phasenstabilisierten Laser, basierend auf einem Yb:Faserlasersystem und einer alternativen DFG-Methode.

Insgesamt wird in der Arbeit eine faseroptische nichtlineare Frequenzverschiebungsmethode demonstriert, welches die Impulsenergie des frequenzverschobenen Signalimpulses mit Pulsenergien im einstelligen Nanojoule-Bereich auf mehrere zehn Nanojoule verbessert. Die Nutzung dieser Signalimpulse als Eingangssignal für ein optimiertes DFG System ebnet den Weg hin zu 50-MHz- Frequenzkämmen im mittleren Infrarotbereich bei einer mittleren optischen Leistung > 2.2 W. In der Zukunft ermöglichen solche Lasersysteme vielzählige neue Anwendungen in Wissenschaft und Technik.

Contents

List of Figures

List of Tables

List of Abbreviations

AC	autocorrelation
AGS	$AgGaS_2$
AGSe	$AgGaSe_2$
AR	anti-reflection
ASE	amplified spontaneous emission
CEO	carrier-envelope offset
CEP	carrier-envelope phase
CSP	$CdSiP_2$
CW	continuous wave
DFG	difference frequency generation
EOM	electro-optic modulator
FWHM	full width at half maximum
GNLSE	generalized nonlinear Schrödinger equation
GDD	group delay dispersion
GVD	group velocity dispersion
GVM	group velocity mismatch
HNLF	highly nonlinear fiber
HRR	high repetition rate
HWP	half-wave plate
ITJ	integrated timing jitter
LMA	large mode area
M-C	Monte-Carlo
MFA	mode field area
MFD	mode field diameter
Mid-IR	mid-infrared
NIR	near-infrared
OFC	optical frequency comb
OPA	optical parametric amplifier
OPCPA	optical parametric chirped pulse amplifier

OPO	optical parametric oscillator
PBS	polarizing beam splitter
PCF	photonic crystal fiber
PPLN	periodically-poled lithium niobate
PSD	power spectral density
PZT	piezoelectric transducer
QCL	quantum cascade laser
QPM	quasi-phase matching
QWP	quarter-wave plate
RF	radio-frequency
RIN	relative intensity noise
RNG	random number generator
RS	Raman soliton
RTJ	relative timing jitter
SC	supercontinuum
SCG	supercontinuum generation
SESS	self-phase-modulation enabled spectral selection
SFG	sum frequency generation
SHG	second harmonic generation
SNR	signal to noise ratio
SPM	self-phase-modulation
SRS	stimulated Raman scattering
SSFS	soliton self-frequency shift
TOD	third order dispersion
TL	transform limited
WDM	wavelength-division multiplier
ZDW	zero dispersion wavelength

List of Publications

Peer-Reviewed Papers

[1] **Qian Cao**, Franz X. Kärtner, and Guoqing Chang, "Towards high power longwave mid-IR frequency combs: power scalability of high repetition-rate difference-frequency generation," Optics Express 28, 1369-1384 (2020).

[2] Manuscript in preparation on the topic "Effect of timing jitter on performance of DFG-based offset-free frequency combs".

[3] Yizhou Liu, Peter Krogen, Kyung-Han Hong, **Qian Cao**, Phillip Keathley, and Franz X. Kärtner, "Fiber-amplifier-pumped, 1-MHz, 1-μJ, 2.1-μm, femtosecond OPA with chirped-pulse DFG front-end," Optics Express 27, 9144-9154 (2019).

[4] Hsiang-Yu Chung, Wei Liu, **Qian Cao**, Rüdiger Greinert, Franz X. Kärtner, and Guoqing Chang, "Tunable, Ultrafast Fiber-Laser Between 1.15 and 1.35 μm for Harmonic Generation Microscopy in Human Skin," IEEE Journal of Selected Topics in Quantum Electronics 25, no. 1 (2018): 1-8.

[5] Hsiang-Yu Chung, Wei Liu, **Qian Cao**, Liwei Song, Franz X. Kärtner, and Guoqing Chang, "Megawatt peak power tunable femtosecond source based on self-phase modulation enabled spectral selection," Optics Express 26, 3684-3695 (2018).

[6] Gengji Zhou, **Qian Cao**, Franz X. Kärtner, and Guoqing Chang, "Energy scalable, offset-free ultrafast mid-infrared source harnessing self-phase-modulation-enabled spectral selection," Optics Letters 43, 2953-2956 (2018).

[7] Hsiang-Yu Chung, Wei Liu, **Qian Cao**, Franz X. Kärtner, and Guoqing Chang, "Er-fiber laser enabled, energy scalable femtosecond source tunable from 1.3 to 1.7 μm," Optics Express 25, 15760-15771 (2017).

[8] Han Li, Xin Huang, **Qian Cao**, Yun Zhao, Peiyun Li, Chenchen Wan, and Andy Chong, "Generation of three-dimensional versatile vortex linear light bullets (Invited Paper)," Chinese Optics Letters 15, 030009- (2017).

International Conferences

[9] **Qian Cao**, Franz X. Kärtner, and Guoqing Chang, "Towards high-power mid-IR frequency combs via 2-μm-pumped difference frequency generation," in Frontiers in Optics + Laser Science APS/DLS, OSA Technical Digest (Optical Society of America, 2019), paper JW4A.24.

[10] **Qian Cao**, Franz X. Kärtner, and Guoqing Chang, "Towards high power and low noise mid-infrared DFG ultrafast source," in Conference on Lasers and Electro-Optics, OSA Technical Digest (online) (Optical Society of America, 2017), paper STu3J.2.

[11] **Qian Cao**, Chen Li, Yizhou Liu, Xiang Gao, Zhigang Zhang, Franz X. Kärtner, and Guoqing Chang, "Passively offset-free Yb:fiber laser source with 1 GHz repetition Rate," in Conference on Lasers and Electro-Optics, OSA Technical Digest (online) (Optical Society of America, 2016), paper JTh2A.141.

[12] **Qian Cao**, Franz X. Kärtner, and Guoqing Chang, "Minimizing the timing jitter of Raman solitons and dispersive wave," in Ultrafast Optics X conference (Beijing, China, 2015).

[13] **Qian Cao**, Chenchen Wan, Xin Huang, and Andy Chong, "Three-Dimensional abruptly autofocusing optical wave packet," in CLEO: 2015, OSA Technical Digest (online) (Optical Society of America, 2015), paper FM1D.6.

[14] **Qian Cao**, Chenchen Wan, and Andy Chong, "Three-dimensional measurement of the Airy-Bessel wave packet propagation," in Frontiers in Optics 2014, OSA Technical Digest (online) (Optical Society of America, 2014), paper FTu5A.6.

[15] Yizhou Liu, Peter Krogen, K. Hong, **Qian Cao**, P. Keathley, and Franz X. Kärtner, "Compact 1-MHz, 1-μJ, few-cycle, passively CEP-stable 2-μm source," in Conference on Lasers and Electro-Optics, OSA Technical Digest (Optical Society of America, 2019), paper STh3E.5.

[16] Hsiang-Yu Chung, Liwei Song, Wei Liu, **Qian Cao**, Franz X. Kärtner, and Guoqing Chang, "Megawatt peak power femtosecond source at 1.3 μm based on self-phase modulation enabled spectral selection," in Conference on Lasers and Electro-Optics, OSA Technical Digest (online) (Optical Society of America, 2018), paper SM4K.4.

[17] Hsiang-Yu Chung, Wei Liu, **Qian Cao**, R. Greinert, Franz X. Kärtner, and Guoqing Chang, "Excitation wavelength optimization of harmonic generation microscopy in human skin enabled by fiber-based femtosecond source tunable in 1.15–1.35 μm," in Conference on Lasers and Electro-Optics, OSA Technical Digest (online) (Optical Society of America, 2018), paper AM1J.2.

[18] Hsiang-Yu Chung, Wei Liu, **Qian Cao**, and Guoqing Chang, "Er-fiber laser enabled femtosecond source tunable from 1.3 to 1.7 μm for nonlinear optical microscopy," in Conference on Lasers and Electro-Optics, OSA Technical Digest (online) (Optical Society of America, 2017), paper SM3L.2.

[19] Xin Huang, **Qian Cao**, Han Li, Peiyun Li, Chenchen Wan, and Andy Chong, "Generation of versatile vortex linear light bullet," in CLEO: 2015, OSA Technical Digest (online) (Optical Society of America, 2015), paper JTu5A.11.

XIII

Chapter 1

Introduction to the thesis

1.1 Introduction to mid-IR frequency combs

After two decades since its invention, optical frequency combs (OFCs) have revolutionized the field of precision spectroscopy and related areas [1–6]. Having the form of ultrafast, high-intense, phase-stable pulse trains in the time domain, OFCs can provide hundreds-of-thousands of comb lines in the spectral domain, offering a broadband spectral reference to the optical frequencies with high coherence, high precision, high stability, and high spectral intensity. Thanks to these features, OFCs have been facilitating applications such as absolute frequency measurement [7–9], measurement of fundamental physical constants [10], calibration of astronomical spectrographs [11], establishing links between radio frequency and optical frequency [12], development of an all-optical clock [13], distributing time standards [14], and molecular spectroscopy [15], to name a few.
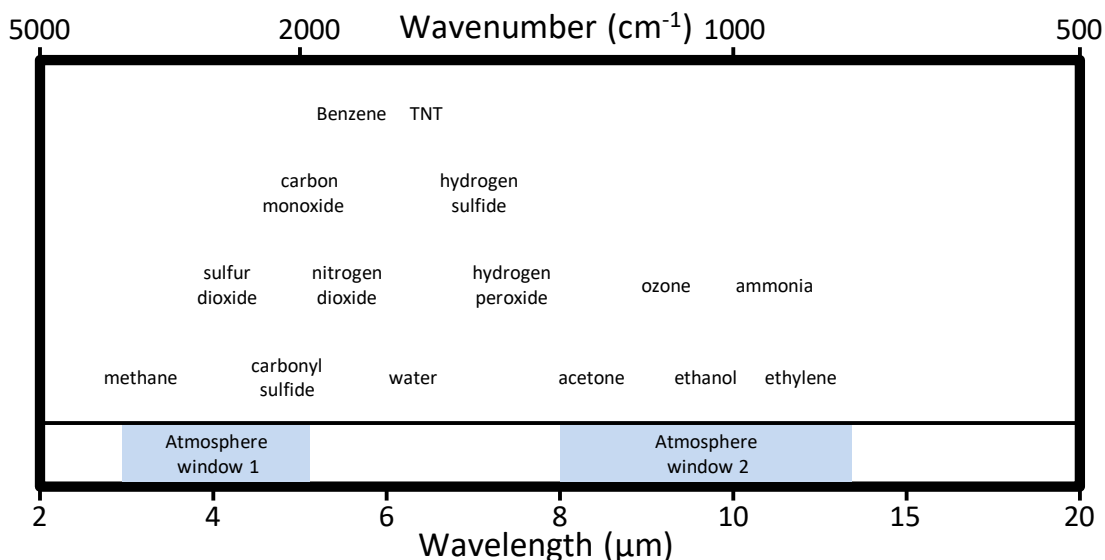
Figure 1.1: Molecular absorption and atmosphere window in the mid-IR range.
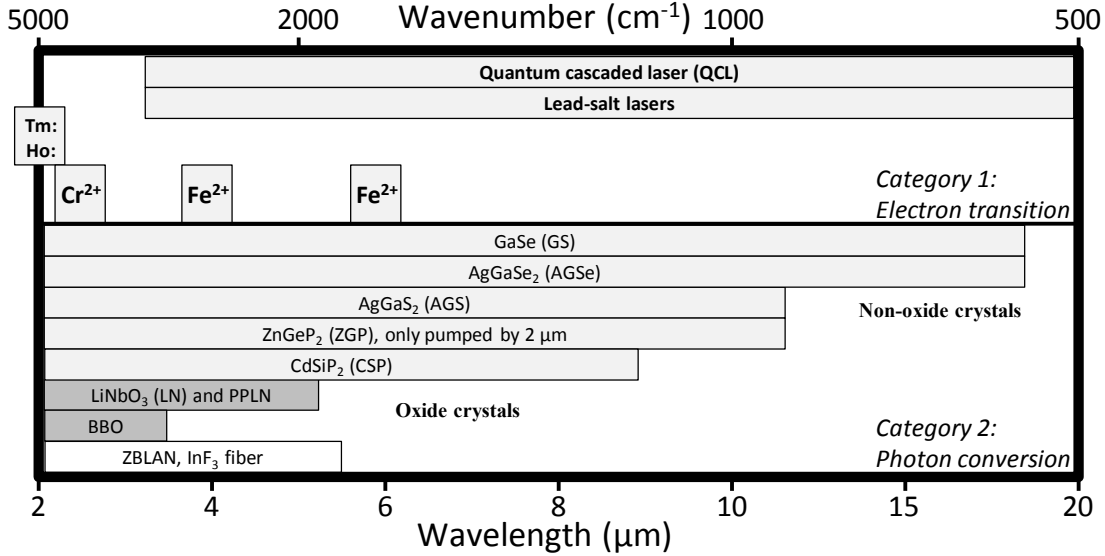
Figure 1.2: Access to mid-IR via electron transition and photon conversion.

Among OFCs with different operating wavelengths, frequency combs in the mid-infrared (mid-IR) range of 2–20 μm (500–5000 cm^{-1}) have attracted intense research interest due to their vast potential in molecular spectroscopic applications [16, 17]. As shown in Fig. 1.1, many molecules and molecular functional groups exhibit strong rotational/vibrational resonances in the mid-IR wavelength range*, which is, therefore, often termed as molecular "fingerprint" region. Using mid-IR sources in absorption spectroscopies or light detection and ranging applications, different molecules can be successfully sensed, distinguished and measured [18–20]. Such capabilities make mid-IR lasers an ideal candidate for monitoring industrial processes, environmental changes, and other security applications. If the phase of each comb line can be individually controlled, the resulting mid-IR frequency comb allows the coherent manipulation over molecular vibrational excitation [21]. Moreover, as shown in Fig. 1.1, the atmosphere has two relatively transparent windows in the range of 3–5 μm and 8–13 μm, making mid-IR sources promising in long-range transmission and detection through the atmosphere. The low Rayleigh scattering losses in mid-IR can facilitate tomography and imaging in turbid environments using mid-IR lasers. Ultrafast mid-IR sources also enable applications such as medical surgery [22], strong-field physics [23, 24], attosecond-sciences and high-harmonic generations [25].

To access mid-IR in the molecular "fingerprint" region, two categories of methods have been implemented. As listed in Fig. 1.2, they are (1) mid-IR generated via electronic transitions; (2) mid-IR generated via photon conversion. The first category of methods includes mid-IR quantum cascade lasers (QCL), lead-salt diodes, and other solid-state/fiber lasers utilizing direct gain media such as

---

*Data from Daylight Solutions.

rare-earth active ions (thulium and holmium) and transition metal chalcogenides (chromium and ferrum/iron). These mid-IR lasers normally feature low available average power, limited spectral bandwidth, limited wavelength tunability, limited access to long-wave mid-IR (>5-μm), poor beam quality, low spectral brightness, and complicated experimental configurations (for example, lead-salt diodes require a cryogenic cooling environment in order to emit mid-IR radiation) [17]. These limitations turn researchers to the second category of methods that generate mid-IR pulses via photon conversion, such as optical parametric processes utilizing $\chi^{(2)}$ nonlinearities inside nonlinear crystals and microresonator-based Kerr combs enabled by $\chi^{(3)}$ nonlinearities inside optical waveguides or filaments [17].

Among them, optical parametric processes are capable of converting mature near-infrared (NIR) sources into mid-IR sources [16, 17]. Compared with Kerr nonlinear combs, optical parametric processes have the potential of generating high-power, wavelength-tunable, long-wave (5–20 μm) mid-IR output with large spectral bandwidth, thus have become the most popular means for building mid-IR lasers. Optical parametric processes are used to construct mid-IR sources such as mid-IR optical parametric amplifiers (OPAs), mid-IR optical parametric oscillators (OPOs), and difference frequency generation (DFG) based mid-IR lasers.

The research interest on mid-IR OPAs is mainly geared towards applications that require high pulse energies. Since mid-IR pulses have a longer optical period than NIR pulses, intense mid-IR pulses are promising in high harmonic generation (HHG) [25] and other high field sciences [23, 24]. In a recent work, 4.2-μm, 12.4-fs, 0.88-cycle, carrier-envelope-offset phase (CEP) stable pulses have been "synthesized" from an OPA using a 2.1-μm optical parametric chirped-pulse amplifier (OPCPA) as the pump and CdSiP$_2$ (CSP) as the nonlinear crystal [26]. The resulting mid-IR pulses with 33-μJ pulse energy and 1.9-GW peak power have managed to generate isolated-HHG pulses up to the 19th order [27]. In a typical OPA setup, pump pulses with μJ level pulse energy are launched into the OPA system, and therefore, the repetition rate of OPA devices is set at the kHz or sub-kHz level so that thermal-related effects are prevented. In contrast, frequency combs are required to have high repetition rates (HRR) of at least >10-MHz, so that each comb line within the frequency comb can be clearly distinguished in the spectral domain. Therefore, OPA techniques, normally with a $<$MHz repetition rate, are not suitable for constructing mid-IR frequency combs.

When an OPA-device is resonantly pumped inside an external cavity, the device becomes an OPO. In the case of femtosecond pulses, the synchronization between the external cavity and the master laser system is crucial, which adds extra complexities in designing and operating OPO systems: (1) A stable synchronization needs to be established between the external cavity round-trip and the round-trip time of the pump laser cavity with high precision; (2) The net dispersion of the external cavity needs to be carefully managed to accommodate the dispersion caused by the nonlinear crystal; (3) The use of thin nonlinear crystals is preferred so that a broadband operation can be achieved for the OPO system, which limits the gain per cavity round-trip; (4) The optical components inside the cavity, in principle, should have low linear loss for all three interacting pulses. The coupling ratio for

the mid-IR output also needs to be kept low due to the limited gain per pass.

For all these reasons, designing and operating a mid-IR OPO is non-trivial. One crucial factor in designing a mid-IR OPO is the choice of nonlinear crystal. As shown in Fig. 1.2, to access mid-IR wavelengths shorter than 5 μm, periodically poled lithium niobate (PPLN) crystals have become the main workhorse for constructing mid-IR OPOs [28]. For example, using a degenerate OPO architecture [29] and 0.5-mm-thick PPLN crystals, NIR sources from erbium-fiber (Er:fiber) mode-locked lasers are converted into phase-coherent frequency combs [30]. The development of mid-IR OPOs towards longer wavelengths (5–20 μm) is still constrained by the limited choice of nonlinear crystals, as oxide crystals such as PPLN only transmits light up to 5 μm. Therefore, to access long-wave mid-IR, non-oxide crystals need to be employed. Non-oxide crystals are usually difficult to fabricate and have small band-gap, low thermal conductivity and low damage threshold. Only few nonlinear crystals have been used in constructing mid-IR OPOs. For example, a picosecond mid-IR source with an average power of 27.5-mW, centered at 6.45-μm, was demonstrated from an OPO system using a CSP crystal [31]. Recently, phase-stabilized 100-mW frequency combs near 10-μm have been demonstrated under an OPO architecture with a thulium-fiber (Tm:fiber) laser as the pump and AgGaSe$_2$ as the nonlinear crystal. Nevertheless, OPO-based mid-IR sources still suffer from an ineffective parametric interaction, a complex design of the resonant cavity, and a limited wavelength tunability in mid-IR.

Free of synchronizing the external cavity and capable of operating in HRR, DFG thus has become the most popular and the most straightforward means to obtain ultrafast mid-IR pulses and construct mid-IR frequency combs [32–36], especially in the long-wave side of the mid-IR spectrum (5–20 μm). In this thesis, we investigate several important issues that are related with constructing DFG-based mid-IR frequency combs.

1.2 DFG-based mid-IR frequency combs

In a typical DFG configuration, two synchronized pulse trains centered at different center wavelengths are frequency mixed in a nonlinear $\chi^{(2)}$ crystal. Here, we use the convention that the pulse train with a shorter center wavelength is called *pump* and the other one with a longer center wavelength is called *signal*. They generate *idler* pulses via the DFG process. Figure 1.3 illustrates the schematic of a typical DFG-based mid-IR frequency comb. Normally, a high-power, NIR laser system provides ultrafast NIR pulses with a pulse duration of hundreds of femtosecond and a repetition rate of >10 MHz. The pulse train enters a Mach-Zehnder interferometer. A portion of the light is split and wavelength-shifted towards a longer center wavelength via nonlinear optic methods, serving as the signal pulses for the DFG process. The signal pulses have an optical frequency of $\nu_n = n \cdot f_{\text{rep}} + f_{\text{ceo}}$. In the other arm of the interferometer, the pulses pass through an optical delay line and recombine with the signal pulses using a dichroic mirror, serving as the pump pulses for the DFG process. The pump pulses have
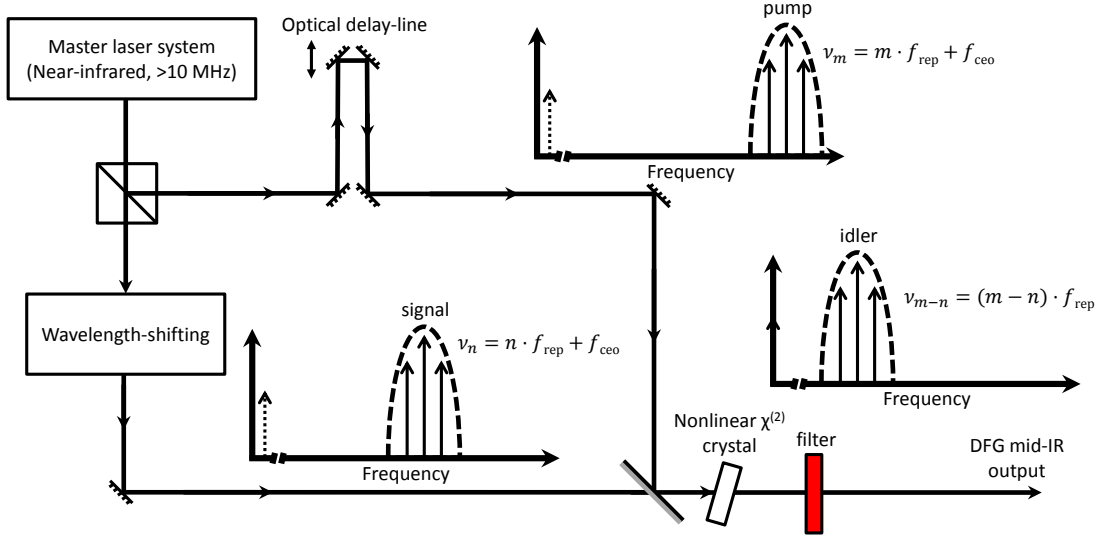
Figure 1.3: Schematic of DFG-based mid-IR frequency combs

an optical frequency of $\nu_m = m \cdot f_{\mathrm{rep}} + f_{\mathrm{ceo}}$. In this scenario, the pump pulses and the signal pulses can be tightly synchronized in the time domain [32–36]. Ideally, the signal pulses should be wavelength-tunable so that the generated mid-IR idler pulses can be tuned between 5–20 μm, covering the whole molecular "fingerprint" spectrum. If the signal pulses are derived in such a way that they share the same offset frequency f_{ceo} with the pump pulses, the frequency mixing between the pump pulses and the signal pulses generates mid-IR idler pulses with an optical frequency of

$$\nu_{m-n} = (m - n) \cdot f_{\mathrm{rep}} + (f_{\mathrm{ceo}} - f_{\mathrm{ceo}}), \tag{1.1}$$

$$\nu_{\tilde{n}} = \tilde{n} \cdot f_{\mathrm{rep}}. \tag{1.2}$$

Here $\nu_{\tilde{n}}$ stands for the optical frequency of the generated mid-IR idler pulses. Note here the new comb line with the index $\tilde{n}$ is generated by a coherent mixture between two sets of comb lines $\tilde{n} \equiv (m - n) = \mathrm{const.}$, but not a mixture of two individual comb lines. Equation 1.2 reveals that the idler has its offset frequency automatically fixed at zero [37], which leads to a significantly simplified experimental configuration for constructing mid-IR frequency combs [35]. After stabilizing the repetition rate f_{rep} of the master laser oscillator, the mid-IR pulse train forms a mid-IR frequency comb with well-defined optical frequencies.

In the laboratory, nonlinear fiber-optic methods such as soliton self-frequency shift (SSFS) have been widely used for deriving the signal pulses from pump pulses for seeding a DFG [33,35]. SSFS has a straightforward implementation and a wide wavelength tuning range for the wavelength-shifted signal pulses. However, due to the tight confinement of an optical pulse in a small fiber core, the excessive amount of nonlinear phase during the wavelength-shifting process prevents the generation of signal pulses with a high pulse energy. Normally, signal pulses gen-

erated via SSFS have a pulse energy at nanojoule level, two orders of magnitudes lower compared with the pump pulse which seeds the DFG process. This leads to an inefficient generation of the mid-IR idler during the DFG. The generated mid-IR idler has an available average power of a few mW. In [33], a 151-MHz, 2.2-W Yb:fiber laser system is used to drive a DFG-based mid-IR laser by using SSFS process for generating the signal pulses. The wavelength-shifted signal pulses, tunable between 1.15–1.65-μm, have a limited pulse energy of 40–150-pJ. Using a 0.5-mm-thick GaSe crystal to host the DFG process, the generated idler pulses, centered at 10-μm, have a pulse energy of 2-pJ, corresponding to an average power of 0.3-mW in the mid-IR. In a recent work utilizing an all-fiber setup [38], 1.55-μm pump pulses are mixed with 1.9-μm signal pulses in a 3-mm-thick orientation-patterned gallium phosphide (OP-GaP) crystal. The maximum achieved output power is 7.4-mW, centered at 7.5-μm. Moreover, during the wavelength-shifting process and DFG process, optical noise from the master laser system is translated to the mid-IR idler pulses due to the nonlinear nature of these processes. The resulting noises, especially the timing jitter noise, will significantly deteriorate the comb performance of the resulting mid-IR frequency combs [39].

The limited available average power in mid-IR, associated with excessive optical noises, harness the use of mid-IR frequency comb in spectroscopic applications, where a high signal-to-noise (SNR) ratio for detection and a precise reference to the optical frequency are required. In this thesis, we investigate several issues that are related with constructing high-power, low-noise DFG-based mid-IR frequency combs by answering the following questions: (1) Is it possible to use a nonlinear fiber-optic method to generate wavelength-tunable signal pulses with a high pulse energy ($>$10-nJ) and low noise? (2) How does the idler scale with respect to the pump/signal during the DFG process? (3) What is the most efficient way to generate a high-power mid-IR idler and what is the limitation for achieving a high-power mid-IR output? (4) How does the noise transfer during the wavelength-shifting process and the DFG process, and (5) How does the timing jitter noise of an offset-free frequency comb affect its comb characteristics? In the thesis, we answer these questions by performing numerical calculations and theoretical analysis, together with experimental results. Finally, we demonstrate a 1-GHz passively offset-free source with a center wavelength of 1030-nm, which is based upon a Yb:fiber laser system and an alternative DFG configuration.

1.3   Structure of the thesis

The thesis is structured as follows:

To construct DFG-based mid-IR frequency combs, the signal pulses for seeding the DFG process are normally derived from NIR pump pulses via nonlinear fiber-optic methods. In **Chapter 2**, we study two fiber-optic methods by solving the generalized nonlinear Schrödinger equation (GNLSE). These two methods are compared in their capabilities of (1) generating signal pulses with a high pulse energy; (2) generating signal pulses with low relative timing jitter (RTJ) noise;

and (3) achieving a high energy conversion efficiency.

To generate high-power mid-IR frequency combs via DFG, a thorough understanding in the energy scaling property of DFG is essential. In **Chapter 3**, we study the power scalability of DFG by solving the time-dependent coupled wave equations. We show that at a high repetition rate (HRR) of >10-MHz, the mid-IR idler scales linearly with respect to the power product of the pump and the signal, and, therefore, increasing the signal energy is as efficient as increasing the pump energy for idler energy scaling in HRR DFG. We compare 1-μm driven DFG with 2-μm driven DFG for their capability of generating mid-IR idlers. We find that the latter one is more promising in building high-power mid-IR frequency combs.

During the DFG process, the RTJ noise of the signal pulses is translated to the timing jitter noise of the idler pulses, which deteriorates the performance of the resulting mid-IR frequency comb with a broadened comb line-width and a reduced comb SNR. In **Chapter 4**, we perform numerical simulations to identify the noise transfer during the DFG process and the effect of the timing jitter noise on the comb characteristics. 2-μm driven DFG turns out to have less RTJ-RTJ noise transfer compared with 1-μm driven DFG. We also demonstrate that the line-width of an offset-free frequency comb can be well estimated by geometrically measuring its timing jitter noise spectrum and using the β-separation line method.

Apart from using DFG to generate mid-IR frequency combs, the scheme of DFG can be also applied in mixing two spectral components of a supercontinuum spectrum to generate offset-free idler pulses located in NIR. In **Chpater 5**, we demonstrate a 1-GHz passively offset-free laser source based upon such DFG schematic. The laser emitted by a 1-GHz Yb:fiber laser system, centered at 1030-nm, is spectrally broadened to generate a dispersive wave (DW) at 550-nm and a Raman soliton (RS) at 1170-nm. The frequency mixing between DW and RS inside a PPLN crystal generates an output idler centered at 1030-nm, which can be amplified by Yb:fiber amplifiers in the further.

Finally, **Chapter 6** concludes the thesis.

Chapter 2

Investigation of nonlinear fiber-optic wavelength-shifting

2.1 Introduction

The implementation of mid-infrared (mid-IR) frequency combs using difference frequency generation (DFG) requires the pump pulses and the wavelength-shifted signal pulses are frequency mixed with inside nonlinear $\chi^{(2)}$ crystals to generate the mid-IR idler pulses. In the laboratory, the pump pulses are normally provided by a high-power master laser system and its center wavelength is fixed in the near-infrared (NIR) range. The signal pulses are derived from the pump pulses via nonlinear optic methods. In this scenario, two pulse trains are tightly synchronized in the time domain. Ideally, the signal pulses are wavelength-tunable such that the center wavelength of the resulting mid-IR idler can be freely tuned in the long-wave mid-IR range (5–20 μm).

To wavelength shift the pump pulses, two categories of nonlinear optic methods have been implemented. The first category utilizes $\chi^{(2)}$ nonlinearity inside nonlinear crystals, such as optical parametric amplifier (OPA) and optical parametric oscillator (OPO). The second one utilizes $\chi^{(3)}$ nonlinearity inside optical fibers, such as supercontinuum generation (SCG) with re-amplification, soliton self-frequency shift (SSFS), and self-phase-modulation enabled spectral selection (SESS). Among these methods, SSFS and SESS do not rely upon the use of any active gain media, or nonlinear $\chi^{(2)}$ crystals, and, therefore, they have a straightforward experimental realization. Since both methods are not constrained by the finite gain bandwidth of any active media or the phase matching condition for the nonlinear crystals, SSFS and SESS can achieve a wide wavelength tuning range for the output signal pulses.

However, during the nonlinear fiber-optic wavelength shifting processes, additional optical noise will be introduced to the wavelength-shifted signal pulses. Due to the nonlinear nature of pulse propagation in optical fibers, the relative intensity noise (RIN) at the input will be translated into the relative timing jitter (RTJ) noise at the output. When the signal pulses are re-combined with the pump pulses

in a nonlinear crystal, such RTJ noise translates to the timing fluctuations and intensity fluctuations of the resulting mid-IR idler pulses. The noise on the mid-IR idler pulses can significantly deteriorate the performance of the resulting frequency combs with a reduced frequency precision and a degraded long-term stability.

In order to study SSFS/SESS's capability of generating wavelength-shifted signal pulses for seeding subsequent DFG experiments, we perform numerical simulations in this chapter. We first review the generalized nonlinear Schrödinger equation (GNLSE) in Section 2.2. GNLSE is the master equation that governs the spectral temporal evolution of an optical pulse for both SSFS and SESS process. In the study of SSFS processes (Section 2.3), we investigate SSFS inside several photonic crystal fibers (PCF): PCF-850, PCF-945, and PCF-975. We are particularly interested in the noise transfer characteristic of SSFS, for example, the RIN-RTJ noise transfer. By varying the launching conditions (input pulse energy, fiber length, and fiber type), we discover two strategies for minimizing the RIN-RTJ noise transfer of SSFS. In the study of SESS process (Section 2.4), we perform similar calculations for investigating the noise transfer of SESS in several large mode area (LMA) fibers: LMA-8, LMA-10, and LMA-15. We compare the noise transfer, the output pulse energy, and the energy conversion efficiency for SESS and SSFS. Finally, We summarize this chapter with a conclusion that SESS is a better candidate in comparison with SSFS, due to its capability of providing wavelength-shifted signal pulses with two orders of magnitude higher pulse energy and 20 times less RIN-RTJ noise transfer.

2.2 Generalized nonlinear Schrödinger equation (GNLSE)

The generalized nonlinear Schrödinger equation (GNLSE) is the master equation that governs the spectral temporal evolution for an ultrafast pulse propagating inside optical waveguides. To study fiber-optic nonlinear wavelength shifting methods such as soliton self-frequency shift (SSFS) and self-phase-modulation enabled spectral shift (SESS), GNLSE needs to be solved numerically. Derived from the classic Maxwell's equations [40], GNLSE models effects such as waveguide dispersions, Kerr nonlinearities and delayed nonlinear responses (for example, stimulated Raman scattering). GNLSE is written as

$$\frac{\partial A}{\partial z} + \frac{\alpha}{2}A + \beta_1 \frac{\partial A}{\partial t} + \frac{i}{2}\beta_2 \frac{\partial^2 A}{\partial t^2} - \frac{1}{6}\beta_3 \frac{\partial^3 A}{\partial t^3} + \dots$$
$$= i\gamma \left(1 + \frac{i}{\omega_0}\frac{\partial}{\partial t}\right) \left(A(z,t) \int\limits_0^\infty R(t')|A(z,t-t')|^2 dt'\right). \tag{2.1}$$

In the equation, $A(z,t)$ stands for the complex amplitude of the pulse envelope. It is normalized in a way so that $|A(z,t)|^2$ has the unit of the optical power (watt). z is the longitudinal coordinate in the direction of pulse propagation and t is the

laboratory time coordinate. In this notation, we assume the pulse is oscillating at the carrier frequency, i.e., $A(z,t)$ does not have the oscillation term $\exp(i \cdot \omega_c t)$.

The left-hand side of Eq. 2.1 includes all the linear effects that affect the pulse evolution during the pulse propagation, such as the linear gain/loss and the waveguide dispersion. "Linear" means these effects are independent of the pulse amplitude. α is the gain/loss coefficient. In the following context, as we consider passive pulse propagation and the waveguide is assumed to be loss-less, α is set as zero. β_n is the n-th order Taylor expansion coefficient of the propagation constant β expanded over the optical frequency ω. It is evaluated at the center frequency of the propagating pulse so that $\beta_n = \left.\dfrac{\partial^n \beta}{\partial \omega^n}\right|_{\omega=\omega_0}$. By definition, $v_\mathrm{g} = 1/\beta_1$ is the group velocity of the propagating pulse, β_2 the group velocity dispersion (GVD) coefficient, and β_3 the third order dispersion (TOD) coefficient. Dispersion effects at higher orders are not written here in Eq. 2.1, but they can be included.

The right-hand side of Eq. 2.1 models the nonlinear response of the optical waveguide, i.e., fused silica fiber. Since fused silica has a central symmetric structure, the nonlinear response only has odd order terms. The lowest order nonlinear response is the third order nonlinearity. In the equation, the nonlinear coefficient γ is

$$\gamma = \frac{n_2 \omega_0}{c A_\mathrm{eff}}. \tag{2.2}$$

In this expression, the nonlinear-index coefficient n_2 is 2.6×10^{-20} m^2/W for fused silica fibers. c the speed of light, and A_eff the effective mode field area (MFA) of the fiber. Normally, MFA is a function of the optical frequency, which adds another degree of dispersion to the equation. In this thesis, we neglect such frequency dependence.

In the equation, the temporal derivative $\dfrac{i}{\omega_0}\dfrac{\partial}{\partial t}$ stands for the self-steepening effect. It is responsible for the shock formation effect on the edge of a pulse. The strength of the nonlinear response is an integral over the time. To ensure the causality, it integrates from $t' = 0$ to $t' = \infty$. The response function $R(t)$ in the integral includes both the instantaneous (electrical) response and the delayed (vibrational, Raman) response. It is written as

$$R(t) = (1 - f_\mathrm{R}) \cdot \delta(t) + f_\mathrm{R} \cdot h_\mathrm{R}(t). \tag{2.3}$$

Here $\delta(t)$ is the mathematical delta function, which represents the self-phase modulation (SPM) effect. The factor f_R stands for the fractional contribution of the delayed Raman response. For fused silica fibers, f_R equals to 0.18. The Raman response function $h_\mathrm{R}(t)$ can be written by an empirical expression,

$$h_\mathrm{R}(t) = \frac{\tau_1^2 + \tau_2^2}{\tau_1 \tau_2^2} \cdot \exp\left(-\frac{t}{\tau_2}\right) \sin(\frac{t}{\tau_1}). \tag{2.4}$$

The parameters τ_1 and τ_2 are adjusted for fitting the actual Raman gain spectrum. Commonly, they are chosen to have the value $\tau_1 = 12.2$ fs and $\tau_2 = 32$ fs.

One common treatment for simplifying the equation is to introduce a moving time frame that is co-propagating with the optical pulse at the group velocity, $v_g = 1/\beta_1$. By having the following substitution,

$$T = t - z/v_g = t - \beta_1 z, \tag{2.5}$$

GNLSE (Eq. 2.1) is then written as

$$\frac{\partial A}{\partial z} + \frac{i}{2}\beta_2\frac{\partial^2 A}{\partial T^2} - \frac{1}{6}\beta_3\frac{\partial^3 A}{\partial T^3} + \cdots$$
$$= i\gamma\left(1 + \frac{i}{\omega_0}\frac{\partial}{\partial T}\right)\left(A(z,T)\int_0^\infty R(t')|A(z,T-t')|^2 dt'\right). \tag{2.6}$$

Such treatment reduces the temporal windows to a localized picosecond scale for the numerical calculations. In the following sections, we study the spectral temporal evolution of an optical pulse during SSFS process and SESS process by solving GNLSE.

2.3 Soliton self-frequency shift (SSFS)

When an optical pulse is propagating inside fused silica fibers, its spectral temporal evolution is under the influence of fiber dispersion and fiber nonlinearity. When the Kerr nonlinear phase balances with the anomalous dispersive phase, the pulse can propagate without changing its spectral temporal form. Such pulse is called an optical soliton [40]. In addition, the delay nonlinear response of the fiber can result in intra-pulse stimulated Raman scattering (SRS) effect, which continuously red-shifts the center wavelength of the soliton along pulse propagation [40–42]. Such soliton self-frequency shift (SSFS) can be understood as the blue-side spectral component of a soliton is amplifying the red-side spectral component via SRS effect along soliton propagation. In the implementation of DFG-based mid-IR frequency combs, SSFS technique has become a popular nonlinear fiber-optic method for generating wavelength-shifted signal pulses [33–35].

2.3.1 An example of SSFS in PCF-945

We first examine the SSFS process by calculating the spectral temporal evolution of an optical pulse when it propagates through a 50-cm-long PCF-945. During the pulse propagation, its spectral temporal evolution is dominated by soliton-related dynamics. We use it as an example for showing the unique features of SSFS process, such as the soliton fission, the formation of RS, and the intra-pulse SRS, all of which are important for understanding the SSFS process and its noise transfer property.

Figure 2.1 plots the dispersion map of PCF-945, together with two other PCFs that are used in the following simulations. Their specifications are listed in Appendix A. PCF-945 exhibits anomalous group velocity dispersion (GVD) ($\beta_2 < 0$)
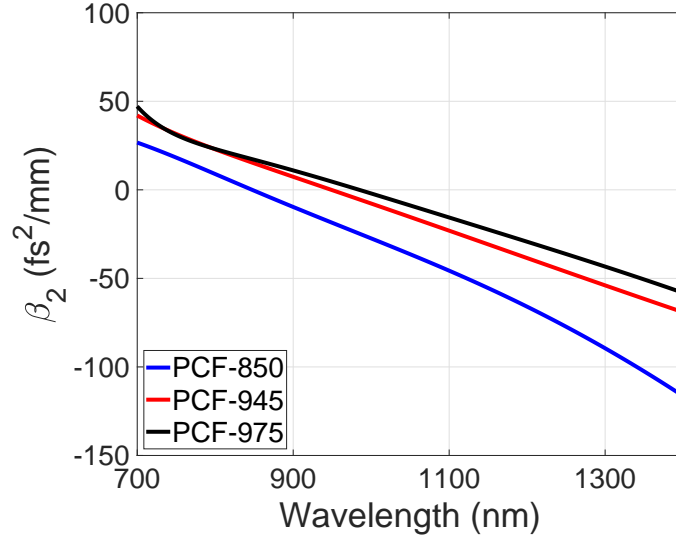
Figure 2.1: Dispersion map for PCF-850/945/975.

for wavelengths longer than 945-nm. Although it has been shown that anomalous dispersion is not a must for red-shifting an optical pulse [43], it is still essential for maintaining the temporal pulse profile when RS propagates a long distance inside the fiber. In the simulation, the input pulse has typical pulse parameters from a Yb:fiber laser system: a center wavelength of 1030-nm, a FWHM pulse duration of 250-fs, a hyperbolic secant square (sech^2) pulse profile, and a pulse energy of 1-nJ. The peak power for the input pulse is 3.53-kW. For PCF-945, γ_0 is 0.026 W^{-1}m^{-1}, β_2 is -12.3 fs^2/mm, and β_3 is 86.0 fs^3/mm at 1030-nm.

The pulse propagation inside the PCF is calculated by solving GNLSE using the standard split-step Fourier method [40]. Figure 2.2(a) and 2.2(b) plot the normalized spectral and temporal profile of the output pulse. The input pulse is plotted by black dashed lines in the same figure. At the output, three fundamental RS (plotted by black solid lines) have been formed with a well-isolated pulse profile in both spectral domain and time domain. RS are separated by picosecond in time. Compared with the input pulse, all RS pulses have a shorter pulse duration, which is a result of the soliton fission and the soliton area theorem [40].

Soliton area theorem defines the relationship between the pulse energy of the fundamental soliton and the soliton pulse duration. During the soliton propagation, Kerr nonlinearity balances the anomalous dispersive phase, maintaining the soliton pulse profile in the time domain. Soliton area theorem is written as

$$E_{\mathrm{p}} = \frac{2|\beta_2|}{|\gamma|\tau}. \tag{2.7}$$

Here E_{p} is the pulse energy of the soliton and τ is the soliton pulse duration (τ equals to the FWHM duration divided by 1.76). During the formation of these RS pulses (soliton fission), the pulse energy of each RS is determined by its soliton

(a) Spectrum of the input/output pulse (b) Temporal intensity profile
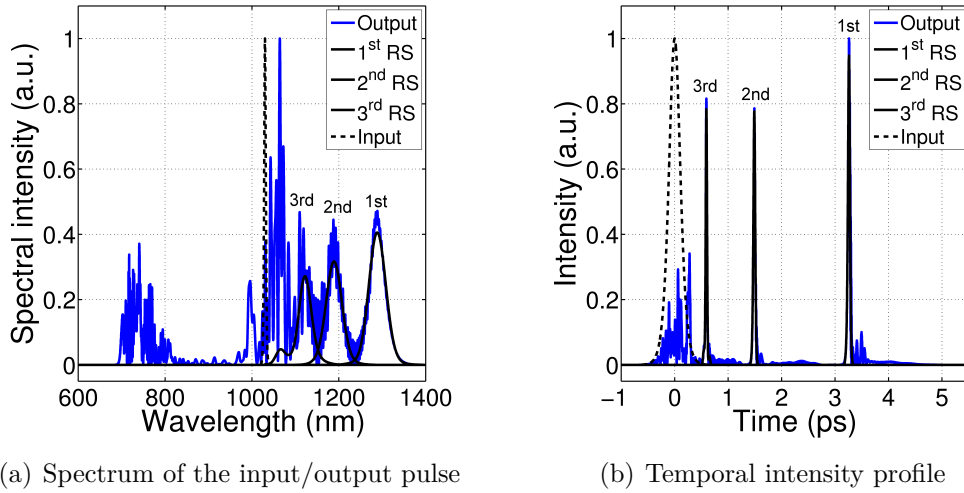
Figure 2.2: Propagation of 1 nJ, 250 fs pulse in a 50-cm-long PCF-945.

(a) Spectral intensity profile. Raman solitons (RS) are centered at 1290/1190/1120 nm, respectively. (b) Temporal intensity profile. At the output, the pulse develops three RS pulses. RS pulses are separated by few picoseconds in the time domain.

---

order [44]. Using the soliton theorem, the pulse energy of the RS can be estimated by the pulse duration of the RS, or vice versa. As shown in Fig. 2.2(b), RS pulse has a pulse duration of about 40 fs. According to the soliton area theorem, it limits the pulse energy of the RS pulse in a sub-nanojoule scale.

By plugging the expression of γ, we can translate Eq. 2.7 into

$$E_{\mathrm{p}} = \frac{2|\beta_2|cA_{\mathrm{eff}}}{n_2\omega_0\tau}. \tag{2.8}$$

Equation 2.8 indicates that it is possible to scale the RS pulse energy by increasing the effective mode field area (MFA) A_{eff} of the fiber. It has been demonstrated that higher-order mode (HOM) fibers can have a relatively large MFA of 44 μm^2 so that RS can be scaled to few nanojoules pulse energy [45,46]. HOM fibers are promising in further scaling the pulse energy of the RS pulse to tens of nanojoules [47]. Nevertheless, a transverse modal conversion is required for effectively coupling the pump pulses into HOM fibers, which compromises the simplicity of the laser system.

According to [44, 48], the soliton with different soliton order carries different pulse energy after the soliton fission. The pulse energy of the j-th order RS is

$$E_j = E_{\mathrm{p}} \cdot \frac{2N - 2j + 1}{N^2},$$
$$N^2 = \frac{L_{\mathrm{D}}}{L_{\mathrm{NL}}} = \frac{T_0^2}{|\beta_2|} \cdot \gamma \cdot P_0, \tag{2.9}$$

where P_0 is the peak power of the input pulse. Apparently, the 1st-order RS has the highest pulse energy. Since the pulse energy of the soliton determines the

rate of red-shifting [41, 42], each RS ends up with a different center wavelength at the output. As shown in Fig. 2.2(a), the center wavelength of these RS is 1290 nm, 1190 nm, and 1120 nm, respectively. Among them, the 1st order RS has the highest pulse energy of about 0.228 nJ. The 2nd order RS has a pulse energy of 0.168 nJ and the 3rd order RS has 0.133 nJ. Divided by the input pulse energy of 1 nJ, the energy conversion efficiency is 22.8%, 16.8%, and 13.3%, respectively. It is noteworthy that due to the intra-pulse SRS, the total pulse energy is not conserved during the process. The output pulse has a pulse energy of 0.937 nJ (The input pulse has 1 nJ). Since the 1st order RS has the strongest wavelength shift and it carries the most pulse energy, we limit our scope in studying the 1st order RS in the following sections.

To better understand and visualize the SSFS process, we plot the spectral temporal pulse profile along the propagation direction by 2D intensity graphs as shown in Fig. 2.3(a) and 2.3(b). The spectral temporal pulse profiles at several signature distances (0 cm, 5 cm, 8 cm, 10 cm, 20 cm, 30 cm, 40 cm, and 50 cm) are plotted in Fig. 2.3(c) and 2.3(d). In all figures, the intensity is normalized in a way such that the maximum intensity is unity at every distance. The pulse encounters three stages of evolution during the SSFS process:

(1) From 0 cm to 8 cm, the pulse evolution is dominated by self-phase-modulation (SPM) effect. After the pulse is launched into the fiber, its spectrum quickly broadens towards both directions in the spectral domain, which is a signature of SPM-enabled spectral broadening. The bandwidth of the pulse continuously increases, leading to a pulse compression in the time domain. At 8 cm, the pulse is significantly shorter compared with the input pulse.

(2) At 10 cm, the soliton fission takes places, abruptly changing the spectral temporal profile of the pulse. In the time domain, the pulse profile has a complex-structured intensity profile due to the constructive and destructive interference among large bandwidth spectral components. In the spectral domain, the pulse spectrum is broader than the spectrum at 8 cm. In fact, soliton fission is a result of a complex mixture of fiber nonlinearity, negative GVD and other higher order dispersion effects. As shown in Fig. 2.3(c), the 1st order RS is at around 1100 nm. It corresponds to an isolated pulse in the time domain. On the left-hand side of the spectrum, a distinct spectral lobe is generated at around 775 nm. This lobe is generated due to the parametric phase matching between the spectra on either side of the zero dispersion wavelength (ZDW) of the fiber (945 nm). In some literature, this spectrum is termed as "dispersive wave" (DW) [44]. Due to its mathematical analogy to the electromagnetic radiation emitted by a traveling charged particle, it is also called 'optical' Cherenkov radiation [49] [50].

(3) After 10 cm (soliton fission), the 1st order RS has intra-pulse SRS, which continuously red-shifts its spectrum. Its temporal pulse profile remains as a fundamental soliton during the pulse propagation. The center wavelength of the 1st order RS shifts to 1200 nm at 20 cm, 1230 nm at 30 cm, 1260 nm at 40 cm, and 1290 nm at 50 cm. Meanwhile, the 2nd order and 3rd order RS

(a) Spectral domain profile (2D)

(b) Time domain profile (2D)

(c) Spectral domain profile (sectioned)

(d) Time domain profile (sectioned)
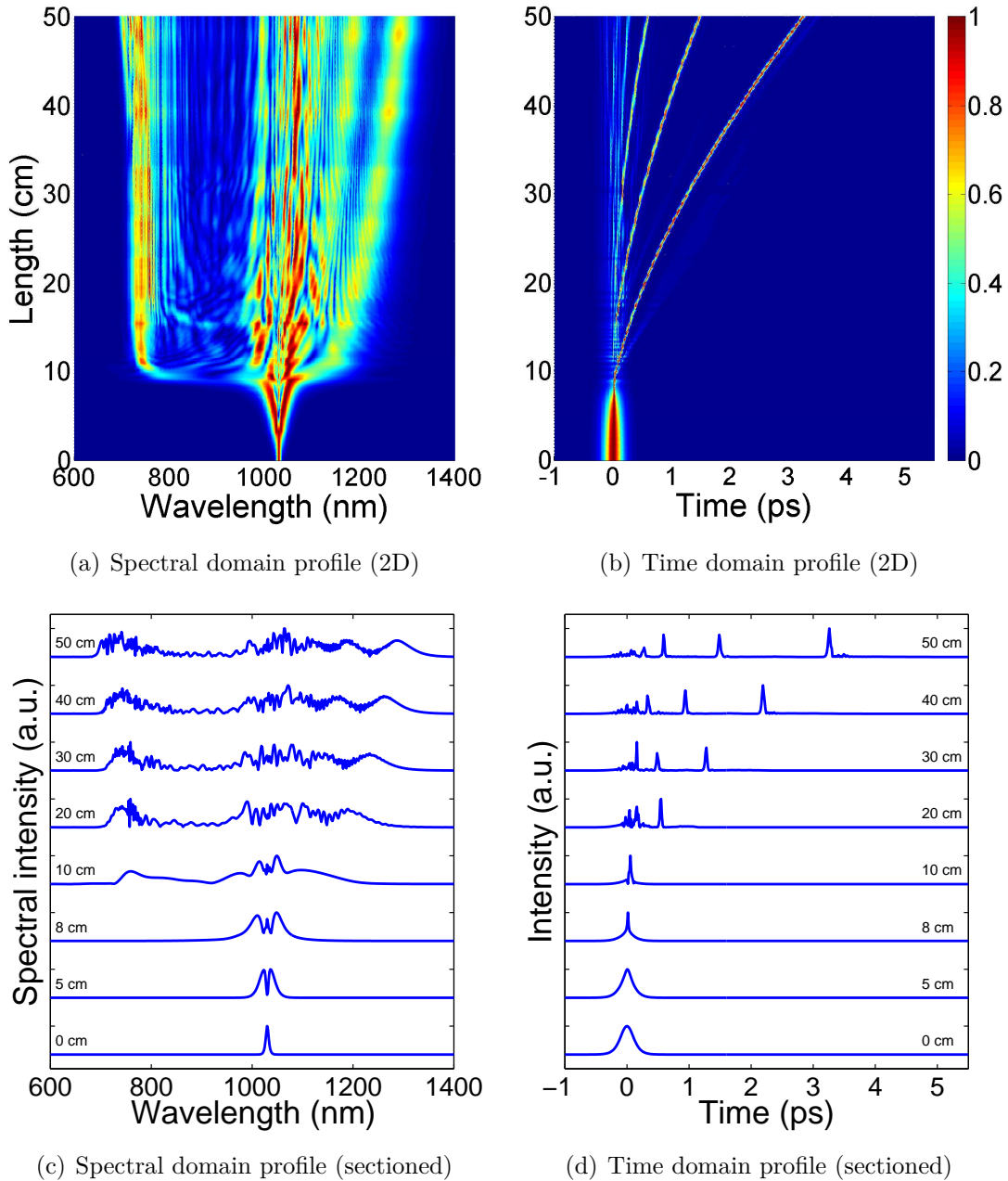
Figure 2.3: Spectral temporal evolution of 1 nJ, 250 fs pulse in a 50-cm-long PCF-945.

(a) Spectral domain pulse evolution along the fiber. (b) Time domain pulse evolution along the fiber. (c) Spectral domain pulse profile at signature distances. (d) Time domain pulse profile at signature distances.

are formed at around 18 cm and 25 cm. They also red-shift afterwards.

The 2D intensity graph of Fig. 2.3(b) shows three curved trajectories, representing the relative temporal shift of the RS pulses with respect to the input pulse. As RS pulse continuously red-shifts, its instantaneous group velocity is changing due to the fiber GVD. Therefore, RS propagates at a different group velocity during the pulse propagation. Since the rate of red-shifting is related with the input pulse energy [41, 42, 44], the relative intensity noise (RIN) at the input translates to a relative timing jitter (RTJ) noise at the output. The input RIN also causes additional center wavelength fluctuation and pulse energy fluctuation at the output. RTJ noise of the RS pulses later translates to the timing jitter noise of the mid-IR idler pulses during DFG. Since the timing jitter noise of a frequency comb laser determines its spectral stabilities [39], the RTJ noise of RS pulses needs to be minimized in order to construct a low-noise frequency comb.

2.3.2 Noise transfer of SSFS in PCF-945

During SSFS, the relative intensity noise (RIN) of the input pulses translates to the intensity fluctuation, relative timing jitter (RTJ) noise, and fluctuations of other pulse parameters for the Raman soliton (RS) pulses. These additional noises, especially the RTJ noise, harness the performance of the resulting mid-IR frequency combs by degrading the precision of the optical frequency. In a typical experimental setup, the wavelength-shifted RS pulses are filtered by a long-pass filter inserted at the output port of the PCF. RS pulses are then re-combined with femtosecond pump pulses inside a $\chi^{(2)}$ crystal in order to generate the mid-IR idler pulses. Effectively, the pump pulses act as an intensity gating in the time domain.

In the numerical simulation, we apply a similar hybrid spectral temporal filter. Taking the output pulse from Fig. 2.2 as an example, we use a 200-fs super-Gaussian temporal window and a 1200-nm long-pass filter. Figure 2.4 shows the use of such hybrid spectral temporal filtering. Figure 2.4(a) plots the time domain filtering and Figure 2.4(b) plots the spectral domain filtering.

The filtered RS pulse has a pulse duration of 40-fs and a spectral bandwidth of 45-nm. It is centered at 1290-nm and it carries 0.228-nJ pulse energy. Combined with pump pulses centered at 1030-nm, idler pulses at 5.1-μm can be generated. The time-bandwidth product of this filtered RS pulse is 0.324, very close to the minimum value of 0.315 for a hyperbolic secant square (sech^2) soliton pulse. The center-of-gravity position, or momentum [43], of the filtered RS pulse is 3258.6-fs.

To study the noise transfer of the SSFS process, we assume the change induced by the input intensity fluctuation is relatively minor so that it can be treated as a linear perturbation to the SSFS process. In other words, the additional noise is in proportion to the fluctuation of the input intensity. In the simulation, we introduce a $\pm 2\%$ change on the input pulse energy. We proceed the same numerical calculation to solve the pulse propagation and calculate the exiting time of the resulting RS pulse. The exiting time difference represents the additional RTJ noise induced by the input RIN. Similar treatment is taken to other pulse parameters,

(a) Time domain profile

(b) Spectral domain profile
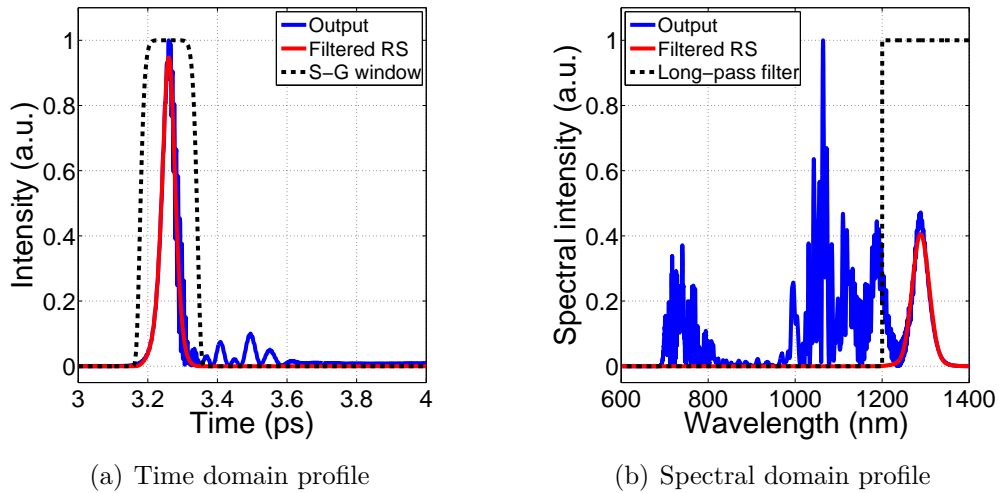
Figure 2.4: Numerical filtering for the 1st-order RS.

(a) Time domain profile. A 200-fs super-Gaussian window (black dash line) is applied to filter the RS pulse. (b) Spectral domain profile. A long-pass filter with a cut-off wavelength of 1200-nm is applied for numerically filtering the output spectrum.

---

such as the pulse duration, the center wavelength, and the pulse energy.

Figure 2.5(a) shows the temporal intensity profile of the filtered RS pulse when the input pulse energy is changed by ±2%. The exiting time of the RS pulses is 3180.3-fs, 3258.6-fs, and 3339.1-fs, respectively. In other words, 2% change on the input pulse energy leads to a timing error of ∼80-fs at the output. Consider the RS pulse has a pulse duration of 40-fs, such a timing error is significant. Meanwhile, the pulse duration of the RS pulse has a negligible change (<1-fs). In the following discussion, we discard the change of the pulse duration caused by the input RIN. The pulse energy of the filtered RS pulses is 0.226-nJ, 0.228-nJ, and 0.230-nJ. When the input changes ±2%, the resulting RS pulse energy changes ±1%. Figure 2.5(b) shows the spectra of the filtered RS pulses with a 2% input intensity change. The change of the center wavelength is <5-nm. The spectral bandwidth also has a negligible change. In the following sections, we only study the RIN-RTJ and RIN-RIN noise transfer during the SSFS process.

By adding more data points between ±2%, we calculate more data for showing the additional RTJ and RIN caused by the input RIN. Figure 2.6(a) shows the relative timing change of the RS versus the input RIN. The slope of the curve is about 40 fs/%. Figure 2.6(b) plots the relative intensity change of the RS pulse versus the input RIN. The slope is below unity, suggesting the output RS pulses have a lower RIN compared with the input pulses.

In the laboratory, high-power femtosecond laser systems can have an intensity drift of 1%. If the laser system is used for seeding SSFS processes, the resulting RS

(a) Intensity profile of filtered RS

(b) Spectrum of filtered RS
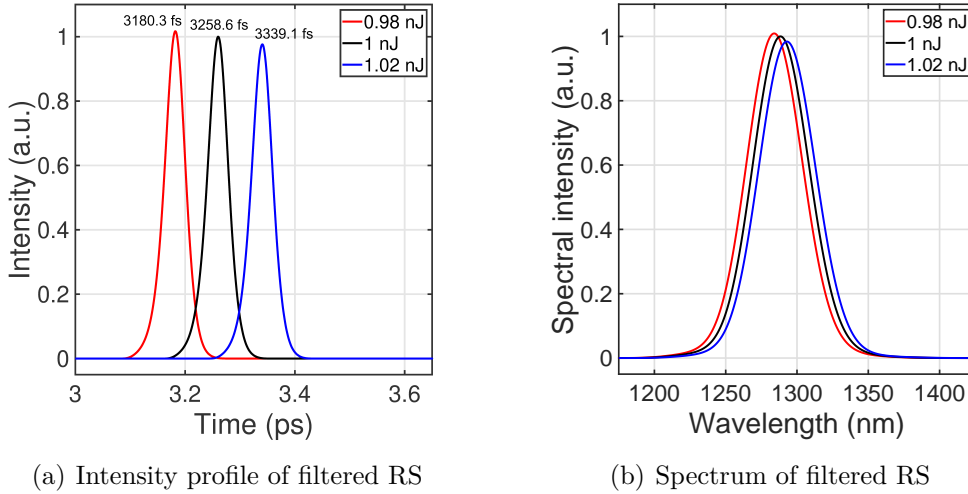
Figure 2.5: Influence of 2% input intensity change.

1-nJ, 250-fs pulse propagates a 50-cm-long PCF-945 with ±2% change at the input intensity. (a) Intensity profiles of the RS pulses. The exiting time of the RS pulses is 3180.3/3258.6/3339.1 fs, respectively. (b) Spectral intensity of the RS pulses. The center wavelength changes <5-nm.

(a) RS RTJ versus input RIN

(b) RS RIN versus input RIN
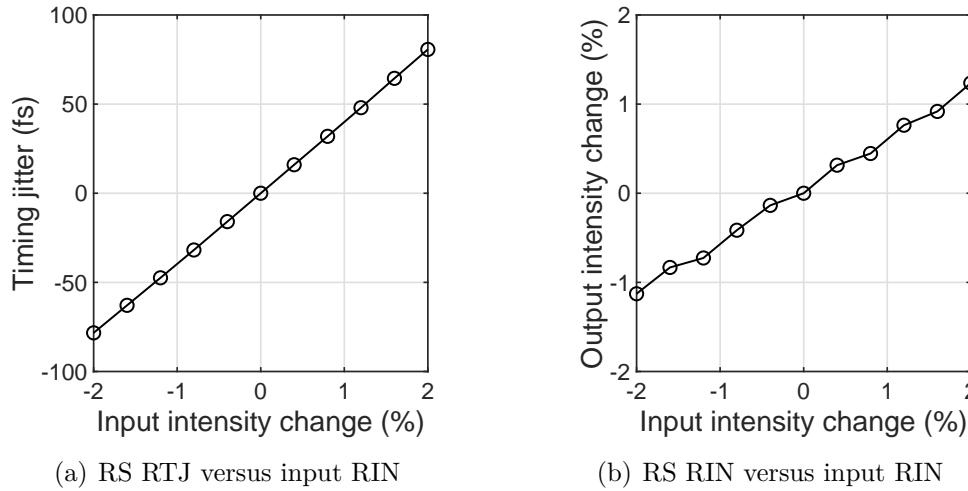
Figure 2.6: Additional RTJ and RIN caused by input RIN during SSFS.

1-nJ, 250-fs pulse propagates a 50-cm-long PCF-945 generates a wavelength-shifted RS pulse centered at 1290-nm. The change of the input pulse energy leads to the timing and the pulse energy change of the resulting RS pulse. (a) Relative timing jitter of the RS pulse versus the input intensity change. The slope is ∼40 fs/%. (b) Output intensity change versus the input intensity change.

PCF-945 (cm)	Input (nJ)	RS (nJ)	Conv. eff. (%)	RS Exiting time (fs)
15	1.26	0.295	23.4	398.4
25	0.91	0.230	25.4	768.3
50	0.56	0.170	31.1	1685.4
100	0.372	0.134	36.0	3642.2

Table 2.1: Soliton self-frequency shift under different launching conditions.

pulses have a RTJ of more than tens of femtoseconds. Such RS pulses with high timing jitter noise are unsuitable for seeding a DFG process to generate offset-free frequency combs. Since the additional RTJ noise is introduced external to the laser cavity, intra-cavity feeding-back systems are unable to suppress such RTJ noise. To effectively control the RTJ noise, the experimental parameters of the SSFS process needs to be optimized. In the next section, we show two strategies for minimizing the noise transfer of the SSFS process, especially the RIN-RTJ transfer.

2.3.3 Minimizing the noise transfer of SSFS

Noise transfer of SSFS at different fiber length

The rate of red-shifting during the SSFS process is related with the pulse energy of the corresponding RS pulse [41, 42], and, therefore, the center wavelength of the RS pulse can be continuously tuned by changing the input pulse energy. Meanwhile, the use of a longer PCF can also lead to a stronger wavelength shift for the RS pulses, and, therefore, a different combination of the PCF length and the input pulse energy can result in the same amount of wavelength shift. Therefore, the PCF length becomes a controlling variable for optimizing the noise transfer of the SSFS process.

For example, by setting the pulse energy of the input pulse at 1.26-nJ, 0.91-nJ, 0.56-nJ, and 0.372-nJ, PCF-945 with a fiber length of 15-cm, 25-cm, 50-cm and 100-cm can shift a 250-fs input pulse from 1030-nm to 1200-nm. Figure 2.7 shows the spectral temporal evolution of the input pulse inside PCF-945 with different fiber length. At the output, all 1st-order RS pulses have a center wavelength of 1200-nm. These RS pulses have a pulse energy of 0.295-nJ, 0.230-nJ, 0.174-nJ, and 0.134-nJ, respectively. The corresponding energy conversion efficiency is 23.4%, 25.4%, 31.1%, and 36.0%. The use of a longer PCF has the advantage of achieving a higher energy conversion efficiency. Meanwhile, as shown in the time-distance graph, for each process, RS pulse accumulates different amount of time delay during the SSFS process. The exiting time of these RS pulses is $T_{15cm} = 398.4$ fs, $T_{25cm} = 768.3$ fs, $T_{50cm} = 1685.4$ fs, and $T_{100cm} = 3642.2$ fs, respectively. The information for these SSFS processes is also summarized in Table 2.1.

Different combination of launching conditions (input pulse energy and PCF length) leads to the same amount of wavelength shift, and, the output RS pulse has
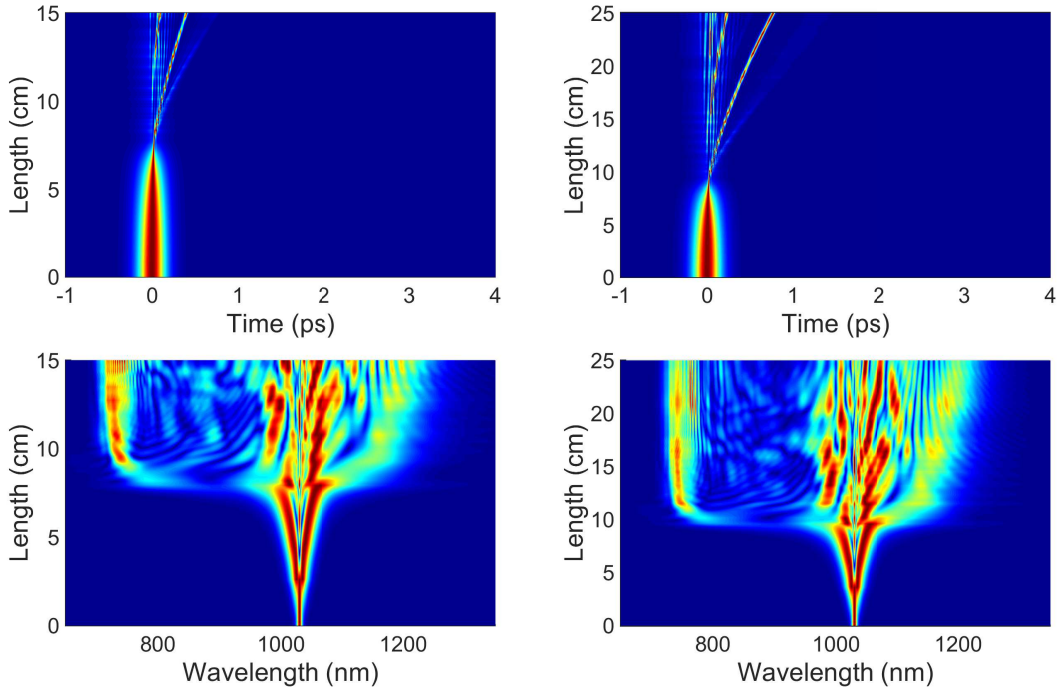
(a) 1.26-nJ input pulse energy, 15-cm PCF

(b) 0.91-nJ input pulse energy, 25-cm PCF
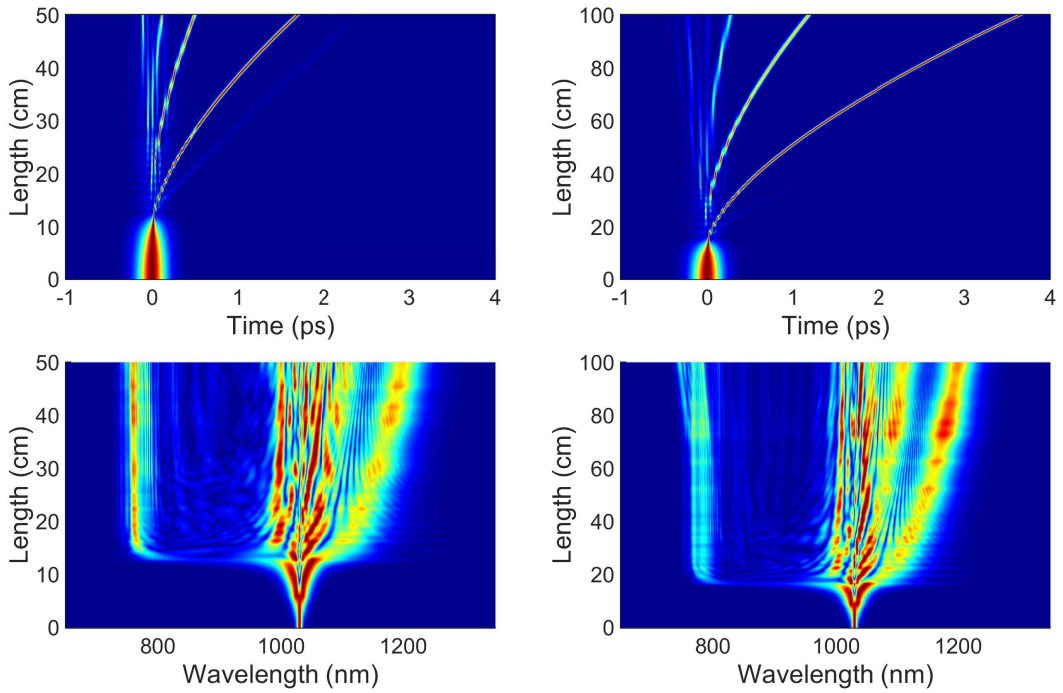
(c) 0.56-nJ input pulse energy, 50-cm PCF

(d) 0.372-nJ input pulse energy, 100-cm PCF

Figure 2.7: SSFS in PCF-945 under different launching conditions.

All SSFS processes shift the input pulses from 1030-nm to 1200-nm. The input pulse has a pulse duration of 250-fs and a center wavelength of 1030-nm.

λ_{RS} (nm)	L (cm)	RIN-RTJ (fs/%)	E_{in} (nJ)	E_{RS} (nJ)	Conv. eff. (%)
1150	25	6.88	0.610	0.192	31.5
	50	14.74	0.376	0.141	37.6
	100	29.33	0.240	0.108	44.8
1200	15	6.84	1.260	0.296	23.4
	25	10.93	0.910	0.231	25.4
	50	20.41	0.560	0.174	31.0
	100	44.07	0.370	0.133	36.0
1300	15	8.84	2.220	0.402	18.1
	25	24.96	1.470	0.319	21.7
	50	43.94	1.050	0.234	22.3
	100	64.16	0.720	0.180	25.0

Table 2.2: SSFS in PCF-945 with different fiber length

a different exiting time, which means the RIN-RTJ noise transfer of each process is also different. To study the RIN-RTJ noise transfer at different fiber length, we use the same numerical approach as we performed previously. We set the length of PCF-945 at 15-cm, 20-cm, 50-cm and 100-cm. Other pulse parameters remain unchanged. For a more systematic study, two more RS wavelengths (1150-nm and 1300-nm) are added into the comparison. If such RS pulses seed a difference frequency generation (DFG) with pump pulses centered at 1030-nm, they generate the output idler pulses at 9.87/7.27/4.95-μm, respectively.

We calculate the RIN-RTJ and RIN-RIN noise transfer for a 15/25/50/100-cm-long PCF-945 generating RS pulses at 1150/1200/1300-nm. The results are plotted in Fig. 2.8. The relative intensity of the input is varied between $\pm 2\%$ and all traces in the figures exhibit a linear trend, meaning the linear perturbation assumption is valid. For 15-cm PCF-945, it is not possible to produce a well-isolated RS pulse at 1150-nm and there is no data for it.

For all target RS wavelengths, the use of a shorter PCF introduces less RTJ to the output RS pulses. Meanwhile, different fiber length leads to a marginally different RIN at the output. For 1150-nm RS, the minimum noise transfer rate is 6.88 fs/% for 25-cm-long PCF-945; for 1200-nm RS, the minimum is 6.84 fs/% for 15-cm-long PCF-945; and for 1300-nm RS, the minimum is 8.84 fs/% for 15-cm-long PCF-945. Conversely, when 100-cm-long PCF-945 is in use, it introduces the largest amount of RTJ noise, which is about 7/5 times higher compared with 15/25-cm-long PCF.

Table 2.2 summarizes the RIN-RTJ transfer rate, together with the RS pulse energy and the energy conversion efficiency for the SSFS process at different fiber length. Apparently, the use of a shorter PCF achieves a substantial reduction on the RIN-RTJ noise transfer. Consider the total amount of wavelength shift is the

(a) RIN-RTJ transfer for 1150-nm RS

(b) RIN-RIN transfer for 1150-nm RS

(c) RIN-RTJ transfer for 1200-nm RS

(d) RIN-RIN transfer for 1200-nm RS

(e) RIN-RTJ transfer for 1300-nm RS

(f) RIN-RIN transfer for 1300-nm RS
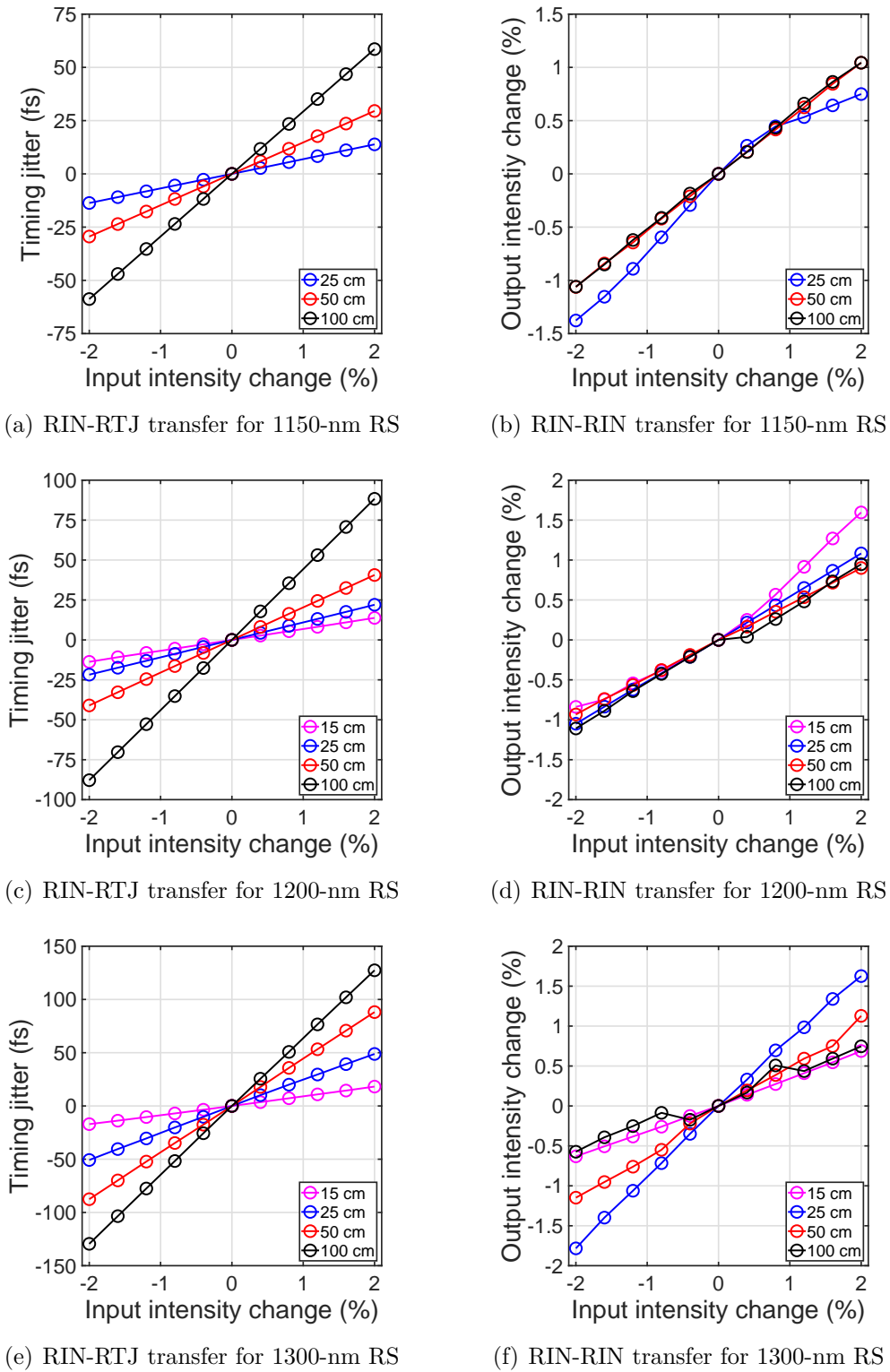
Figure 2.8: Noise transfer of SSFS in PCF-945 with different fiber length.

same for all SSFS processes, a "faster" red-shifting process produces a "quieter" output RS pulse with less RTJ noise. The use of a shorter fiber also produces more pulse energy in the RS pulses, which facilitates the generation of high-power, offset-free frequency combs. The use of a longer fiber can lead to a higher energy conversion efficiency, making it a good candidate when there is a limited output power from the master laser system.

Noise transfer of SSFS in different fiber

In the experiment, the noise transfer of the SSFS process can be also optimized by utilizing different PCF for hosting SSFS. Having a different design in the geometry (lattice pitch, air hole shape and diameter), refractive index, and type of lattice, different PCFs exhibit different dispersive characteristic, which is crucial for determining the noise transfer of the SSFS process. We choose to compare three PCFs: PCF-850, PCF-945 and PCF-975. The specifications of these PCFs are listed in Appendix A. The dispersion map for PCF-850 and PCF-975 can be found in Fig. 2.1. These PCFs have a zero dispersion wavelength (ZDW) at 850-nm, 945-nm, and 975-nm, respectively. Previous study has shown that the use of a shorter PCF can minimize the RIN-RTJ noise transfer. Thus we choose the length of fiber to be 15 cm and 25 cm. RS wavelength is still set at 1150-nm, 1200-nm, and 1300-nm. Other pulse parameters remain unchanged. Among these fibers, 15-cm-long PCF-975 is unable to produce a well-isolated RS pulse in the time domain. Thus we do not plot any trace for it.

Figure 2.9 plots the noise transfer of the SSFS process in 15-cm-long PCFs and Figure 2.10 plots the noise transfer of the SSFS process in 25-cm-long PCFs. Consider the input pulse has a center wavelength of 1030-nm, apparently PCF with a ZDW closer to the input pulse wavelength has less RIN-RTJ noise transfer. If same PCF is used, a shorter fiber (15-cm) introduces less RTJ noise. Table 2.3 summarizes the RIN-RTJ noise transfer for these PCFs. As shown, 15-cm-long PCF-945 can achieve a lowest RIN-RTJ noise transfer of 6.84 fs/% for 1200-nm RS, and 8.84 fs/% for 1300-nm RS. 25-cm-long PCF-975 achieves a lowest RIN-RTJ noise transfer of 4.0 fs/% for 1150-nm RS. Among these PCFs, PCF-975 has the largest mode-field diameter (MFD) of 3.3-μm, and, therefore, it requires the highest input pulse energy to achieve the same amount of wavelength shift. The energy conversion efficiency for PCF-975 is about 50% lower than the efficiency for PCF-850.

During SSFS processes, the instantaneous frequency of the RS pulse is continuously red-shifting, which grants a changing group velocity due to the fiber dispersion. Since the group velocity dispersion (GVD) coefficient β_2 is the second-order derivative of the propagation wave vector $\beta(\omega)$, a smaller β_2 leads to a reduced group velocity difference, assuming the frequency shift Ω_{RS} is the same during the SSFS process. Consequently, a smaller β_2 leads to less relative time delay between the input pulse and the RS pulse. The dispersion maps of PCFs (Fig. 2.1) show that PCF-975 has the lowest $|\beta_2|$ from 1030-nm to 1200-nm, and, therefore, the RS pulse accumulates the least amount of time delay T_{RS} during the SSFS process.
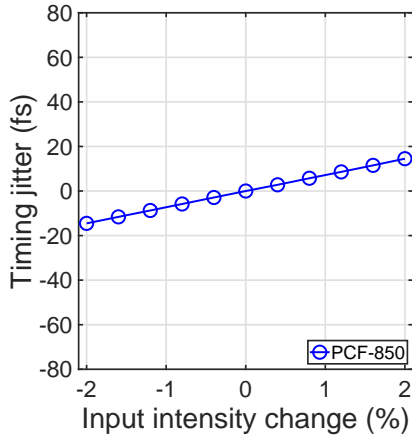
(a) RIN-RTJ transfer, 1150-nm RS
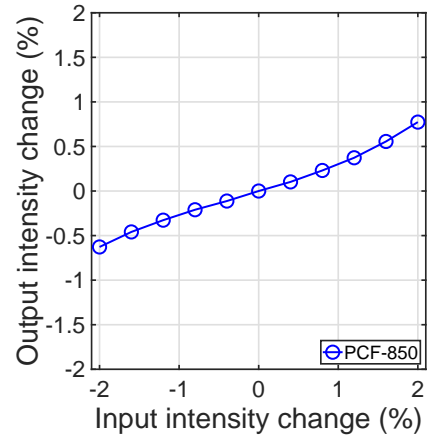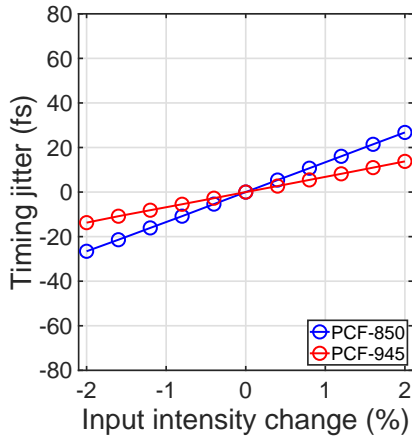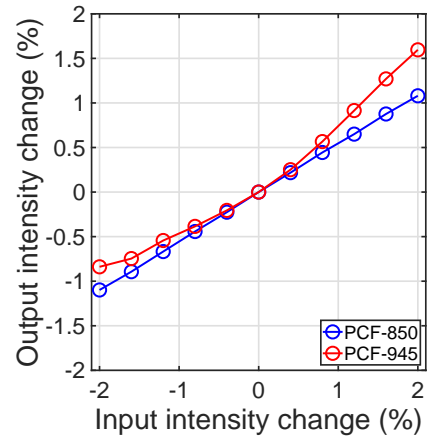
(b) RIN-RIN transfer, 1150-nm RS

(c) RIN-RTJ transfer, 1200-nm RS

(d) RIN-RIN transfer, 1200-nm RS
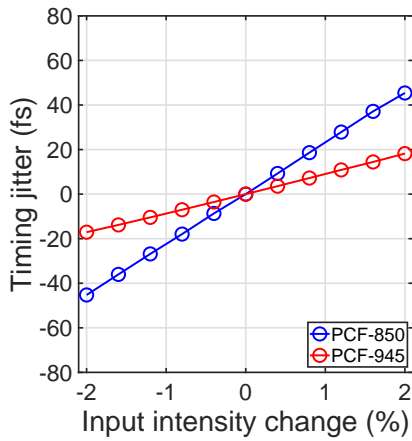
(e) RIN-RTJ transfer, 1300-nm RS
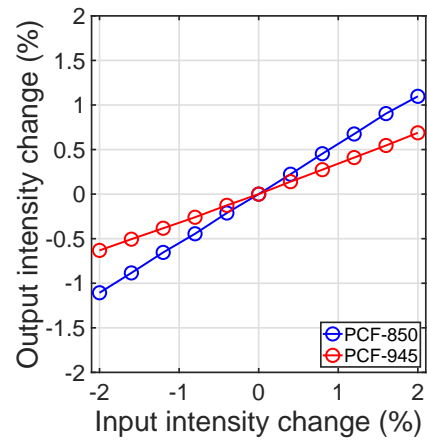
(f) RIN-RIN transfer, 1300-nm RS

Figure 2.9: Noise transfer of SSFS in 15-cm-long PCFs.
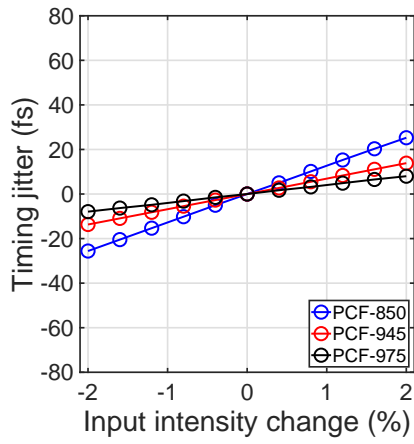
(a) RIN-RTJ transfer, 1150-nm RS
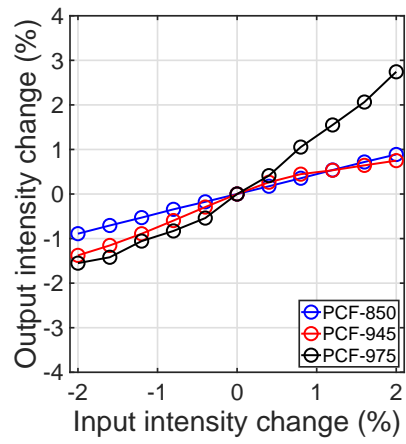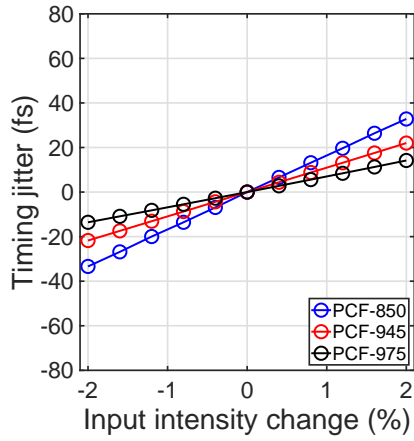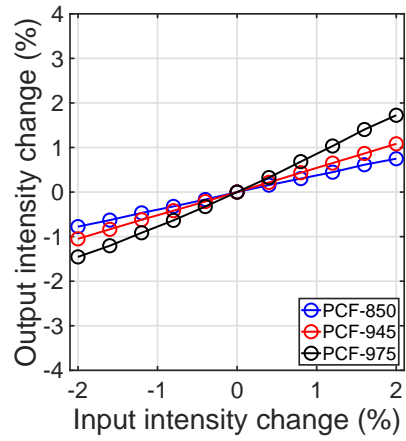
(b) RIN-RIN transfer, 1150-nm RS

(c) RIN-RTJ transfer, 1200-nm RS

(d) RIN-RIN transfer, 1200-nm RS
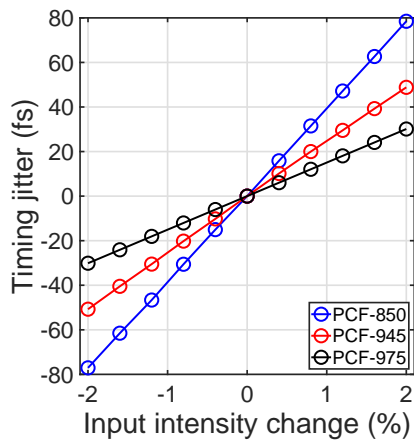
(e) RIN-RTJ transfer, 1300-nm RS
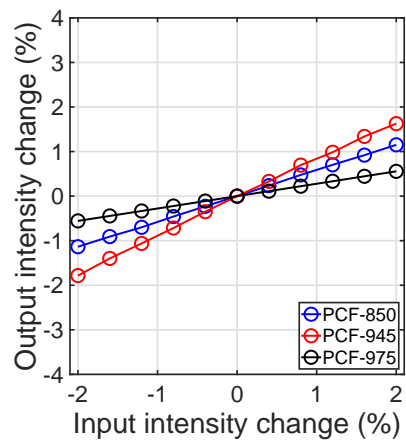
(f) RIN-RIN transfer, 1300-nm RS

Figure 2.10: Noise transfer of SSFS in 25-cm-long PCFs.

λ_{RS} (nm)	PCF type	RIN-RTJ (fs/%)	E_{in} (nJ)	E_{RS} (nJ)	Conv. eff. (%)
1150	PCF-850	7.23	0.527	0.170	32.2
	PCF-945	N/A	N/A	N/A	N/A
1200	PCF-850	13.4	0.745	0.200	26.8
	PCF-945	6.84	1.260	0.296	23.4
1300	PCF-850	22.8	1.180	0.259	22.0
	PCF-945	8.84	2.220	0.402	18.1

SSFS in PCF with a fiber length of 15-cm.

λ_{RS} (nm)	PCF type	RIN-RTJ (fs/%)	E_{in} (nJ)	E_{RS} (nJ)	Conv. eff. (%)
1150	PCF-850	12.7	0.326	0.133	40.7
	PCF-945	6.9	0.610	0.192	31.5
	PCF-975	4.0	0.930	0.223	23.5
1200	PCF-850	16.6	0.495	0.157	31.8
	PCF-945	10.9	0.910	0.230	25.4
	PCF-975	6.9	1.650	0.260	15.5
1300	PCF-850	38.8	0.880	0.208	23.6
	PCF-945	25.0	1.470	0.319	21.7
	PCF-975	15.1	4.000	0.385	9.4

SSFS in PCF with a fiber length of 25-cm.

Table 2.3: SSFS in different PCFs

T_{RS} is also the least sensitive with respect to the fluctuation of the input pulse energy, leading to a minimized RIN-RTJ noise transfer.

2.3.4 Summary of SSFS

In conclusion, SSFS is able to shift the center wavelength of the input pulse from 1030-nm to 1300-nm. The generated RS pulse can be freely tuned from 1150-nm to 1300-nm by varying the input pulse energy, which enables the generation of wavelength-tunable mid-IR frequency combs via DFG. RS pulse has a pulse duration of ~40-fs and a pulse energy of <1-nJ. Under the influence of the relative intensity noise (RIN) at the input, the resulting RS pulses have a large relative timing jitter (RTJ) with respect to the input pulses. Using non-optimal setups, a 1% input intensity fluctuation leads to a >60-fs timing error at the output. If the RS pulses are used for seeding a DFG, such large RTJ will harness the performance of the resulting frequency comb lasers by deteriorating the comb stability. Through

numerical investigations on the SSFS processes, we find that the experimental parameters can be optimized in two routes in order to minimize the RIN-RTJ noise transfer:

- Use a shorter PCF and a higher input pulse energy. A proper combination of the fiber length and the input pulse energy can achieve the same amount of wavelength shift. In a shorter fiber configuration, the RS pulse has a faster wavelength shifting and a reduced net group delay. Using 15-cm-long PCF-945, the RIN-RTJ noise transfer can be minimized to 9 fs/% (1% intensity fluctuation at the input leads to 9-fs RTJ at the output).

- Using PCF with a zero dispersion wavelength (ZDW) closer to the center wavelength of the input pulse. PCF-975 has a smaller $|\beta_2|$ compared with PCF-945 and PCF-850. In the SSFS process, a smaller $|\beta_2|$ results in less difference between the group velocities of the input pulse and the RS pulse so that RS accumulates less relative time delay during the SSFS process. The RIN-RTJ noise transfer can be thus minimized to a rate of 4 fs/%.

2.4 Self-phase-modulation enabled spectral selection (SESS)

Apart from using the delay nonlinear response of fused silica fibers (e.g., stimulated Raman scattering) to achieve wavelength shifting, the instantaneous response (e.g., Kerr nonlinearity) can also shift the center wavelength of the input pulse via self-phase-modulation (SPM) effect. In soliton self-frequency shift (SSFS), the nonlinear phase balances with the dispersive phase, and, therefore, the pulse energy of the RS pulse is normally capped under nano-joule level. On the other hand, SPM-enabled spectral selection (SESS) method does not require such phase balance and it has a much more straight-forward realization compared with SSFS [51]. Preferably, only a pure Kerr nonlinearity is needed in SESS. SPM can expand the bandwidth of the input pulse by few orders of magnitude. Due to its simple physical mechanism, the range of experimental parameters (pulse energy, pulse duration and the choice of fiber) for SESS is also larger compared with SSFS. Moreover, it is possible to scale the pulse energy of the wavelength-shifted pulse by reducing the length of the fiber for SESS.

The key component for SESS is the large mode area (LMA) fiber, which enables single mode pulse propagation with a reduced fiber nonlinearity and a higher damage threshold [52] [53]. Compared with conventional single mode fibers whose mode field area (MFA) is at the order of tens of μm^2, LMA fibers have a MFA of hundreds or more than thousands of μm^2. It leads to applications such as amplifying an intense laser or amplifying single frequency signal, where the elimination of fiber nonlinearity is always welcomed. On the other hand, by proper controlling the fiber nonlinearity, LMA fibers can be also used for building wavelength-tunable ultrafast sources. Using LMA fibers, SESS has been used to construct wavelength-shifted sources for biological studies, for example, deep tissue imaging [54] [55].

(a) Pulse energy fixed at 50-nJ   (b) LMA-8 fixed at 10-cm-long
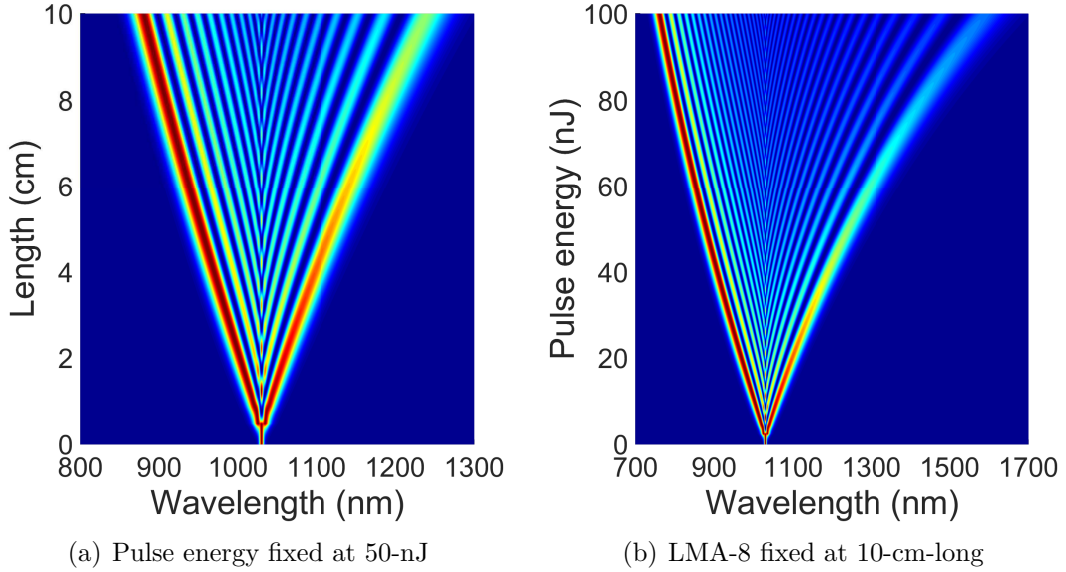
Figure 2.11: Spectral evolution with SPM effect only.

1030-nm, 250-fs pulse propagates inside a LMA-8 fiber with only SPM effect. (a) Spectral evolution when the pulse energy is fixed at 50 nJ. (b) Spectral evolution when LMA-8 is fixed at 10-cm. The input pulse energy varies from 0 to 100-nJ.

Benefitted by the high peak power and the high pulse energy at the output, SESS is also a good candidate for providing wavelength-shifted signal pulses for seeding difference frequency generation (DFG) lasers [36].

To study SESS process in LMA fibers, we first re-visit the generalized nonlinear Schrödinger equation (GNLSE) that governs the spectral temporal evolution for femtosecond pulse propagation. In GNLSE (Eq. 2.1), the left-hand side terms model all linear effects such as fiber dispersion and linear gain/loss. Since these effects only change the pulse profile in the time domain, the dispersive pulse propagation does not lead to any spectrum broadening. The right-hand side terms in GNLSE model the nonlinear responses from the fiber, such as SPM, self-steepening and stimulated Raman scattering (SRS). If we discard all the dispersive terms and only consider the SPM effect, GNLSE reduces to

$$\frac{\partial A}{\partial z} = i\gamma \left|A\right|^2 A. \tag{2.10}$$

Equation 2.10 has an analytical solution of $A(z, T) = A(0, T) \cdot \exp(i \cdot \gamma \left|A\right|^2 z)$, which gives the spectral evolution of an optical pulse with pure SPM effect.

We first consider the case when a 1030-nm, 250-fs sech^2 pulse with a fixed pulse energy of 50-nJ propagates through a 10-cm-long LMA-8 fiber. The specification of LMA-8 fiber can be found in Table A.2. Figure 2.11(a) plots the spectral evolution of the pulse along the fiber. The pulse accumulates nonlinear phase along the pulse propagation, translating to a spectral broadening from a single lobe to multiple,

29

well-isolated spectral lobes. This is a signature sign of SPM effect. The spectrum is continuously broadening in both directions in the spectral domain. At the distance of 10 cm, the right-most lobe of the spectrum has a center wavelength of 1250 nm. The left-most lobe of the spectrum is centered at 875 nm. Both lobes carry about 11 nJ pulse energy, 22% of the input pulse energy.

We then calculate the case where the LMA-8 fiber is fixed at 10-cm-long. The input pulse energy varies from 0 to 100-nJ. Figure 2.11(b) plots the spectral evolution against the increasing pulse energy. Since the nonlinear phase increases in proportion to the input pulse energy, the resulting right/left-most lobe has more red/blue-shift. In other words, the center wavelength of the right/left-most lobe can be continuously tuned by changing the input pulse energy.

This example shows the spectral broadening when only SPM effect is taken into consideration. By inserting a long-pass/short-pass filter at the output, the filtered right-most/left-most lobe forms a source whose center wavelength is red-shifted/blue-shifted with respect to the input pulses. Since a DFG laser requires signal pulses at a longer center wavelength, we only consider the right-most lobe in the following study of SESS.

During the SESS process, if we do not consider any dispersion effect, the net nonlinear phase can be written as

$$\Phi_{\mathrm{NL}} = \gamma \cdot P_0 \cdot L = \frac{n_2 \omega_0}{c A_{\mathrm{eff}}} \cdot P_0 \cdot L, \tag{2.11}$$

where P_0 stands for the peak power of the input pulse and L the length of the SESS fiber. Equation 2.11 shows that, in addition to scale the pulse energy of the SESS pulse by increasing A_{eff}, a reduction of the fiber length can also scale the pulse energy. As long as the product $P_0 \cdot L$ is the same, the net nonlinear phase is the same and the resulting right-most spectra lobe has the same amount of wavelength shift. Consequently, the pulse energy of the SESS pulse can be scaled by shortening the SESS fiber length [51].

2.4.1 An example of SESS in LMA-8

After adding the corresponding dispersive terms and the non-instantaneous nonlinear response terms to GNLSE, we calculate a practical SESS process inside a 10-cm-long LMA-8 fiber. The dispersion map for LMA-8 is plotted in Fig. 2.12. The input pulse is a 1030-nm, 78-nJ, 250-fs sech^2 pulse. We solve GNLSE using the standard split-step Fourier method and we plot the spectral temporal profiles of the input/output pulses in Fig. 2.13(a) and 2.13(b). During the SESS process, the pulse undergoes a SPM-dominated pulse evolution and the output spectrum develops 20 lobes. The right-most lobe centered at 1200-nm can be filtered by inserting a long-pass filter of 1170-nm at the output. The filtered spectrum and the corresponding temporal pulse profile are plotted by red solid lines in the figures. The filtered spectrum centered at 1200-nm has a 3-dB spectral bandwidth of ~36-nm and the filtered pulse has a pulse duration of 65-fs, a pulse energy of 10.4-nJ, and a peak power of 140.7-kW. The energy conversion efficiency for this
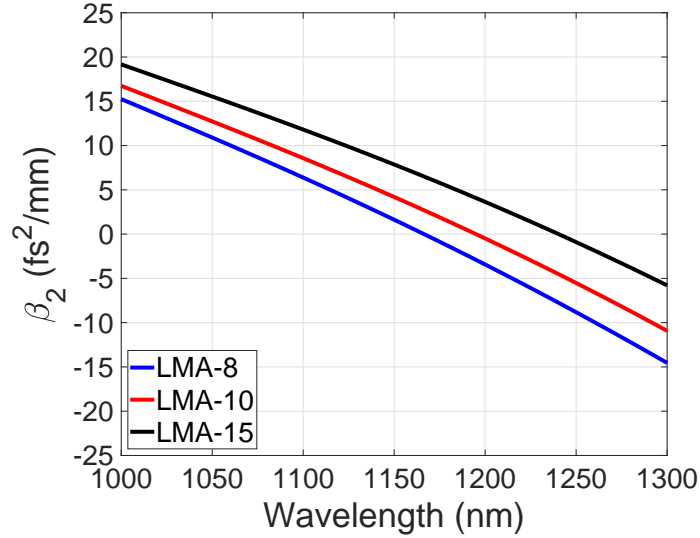
Figure 2.12: Dispersion map for LMA-8/10/15.

process is 13.3%. Consider the input pulse has a bandwidth of 5-nm, SESS process can shift the center wavelength of the input pulse from 1030-nm to 1200-nm, and broaden the optical spectrum by a factor of 7 at the same time. Figure 2.13(c) plots the filtered pulse profile, together with its TL-form and compressed form. Due to the use of a short fiber, the filtered SESS pulse is quasi-transform limited (TL) with a pulse duration of 50-fs, reaching 90% peak intensity of the TL pulse.

To further demonstrate the pulse evolution during the SESS process, we plot the spectral temporal pulse evolution along the fiber in Fig. 2.14(a) and 2.14(b). The length of LMA-8 fiber further extends to 15-cm. The spectral temporal pulse profiles at several signature distances (0 cm, 3 cm, 6 cm, 9 cm, 12 cm, and 15 cm) are plotted in Fig. 2.14(c) and 2.14(d). As plotted in Fig. 2.11(b), When the input pulse energy is 78-nJ, a 10-cm-long LMA-8 fiber with no dispersion and SRS is able to shift the right-most spectral lobe from 1030-nm to 1400-nm. With the inclusion of the fiber dispersion and SRS effect, the right-most lobe only shifts to 1200-nm. As shown in Fig. 2.14(c), the optical spectrum has a bandwidth of >300-nm at 9 cm. In the time domain, the dispersive phase caused by such large bandwidth leads to a distorted pulse profile, which is termed as optical wave breaking [40]. Further extending the length of the fiber to 15-cm only results a marginally broader spectrum.

LMA-8 fiber has a zero dispersion wavelength (ZDW) at around 1175-nm. It exhibits normal dispersion at <1175-nm and anomalous dispersion at >1175-nm. When the SPM-dominated spectrum broadening has shifted the right-most lobe over the ZDW, the pulse enters the "soliton" regime where soliton-related dynamics dominates the pulse evolution and soliton self-frequency shift (SSFS) takes place. It is noteworthy that when the spectral components are at both side of ZDW, they can exchange pulse energy via dispersive wave (DW) generation, which introduces

(a) Spectral profile of the output pulse

(b) Temporal intensity profile

(c) SESS pulse compression
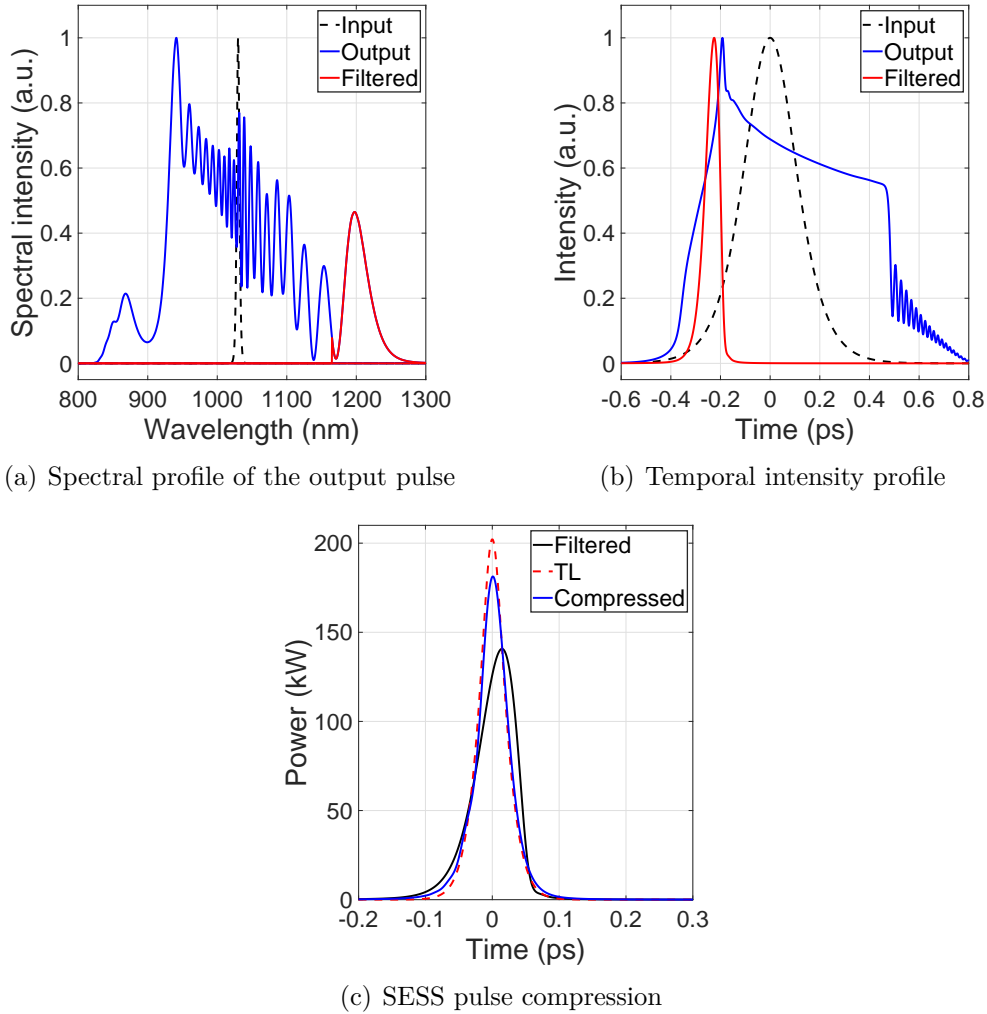
Figure 2.13: Output of 78 nJ, 250 fs pulse in a 10-cm-long LMA-8.

(a) Spectral intensity profile. The right-most lobe has a center wavelength of 1200-nm. (b) Temporal intensity profile. The filtered pulse is quasi-transform-limited (TL). (c) The compression of the SESS pulse.

excessive phase noise and degrade the coherence of the spectrum [44].

When the SPM effect is dominating the spectral evolution, the spectrum broadening is in proportion to the nonlinear SPM phase (Eq. 2.11). The spectrum broadening caused by SPM can be also understood as a photon-photon interaction where $2 \cdot \omega_2 = \omega_1 + \omega_3$ ($\omega_1 < \omega_2 < \omega_3$). The cross section of this transformation is in proportion to the pulse energy. However, when the soliton-related dynamics is dominating the pulse evolution, the intra-pulse SRS is a photon-phonon interaction where a pump photon translates to a Stoke photon during the process, $\omega_p = \omega_s + \Omega_{\text{vib}}$. The rate of the SSFS wavelength shifting is thus in proportion to the cross section of SRS, much lower compared with SPM. Consequently, the

(a) Spectral domain profile (2D)

(b) Time domain profile (2D)

(c) Spectral domain profile (sectioned)

(d) Time domain profile (sectioned)
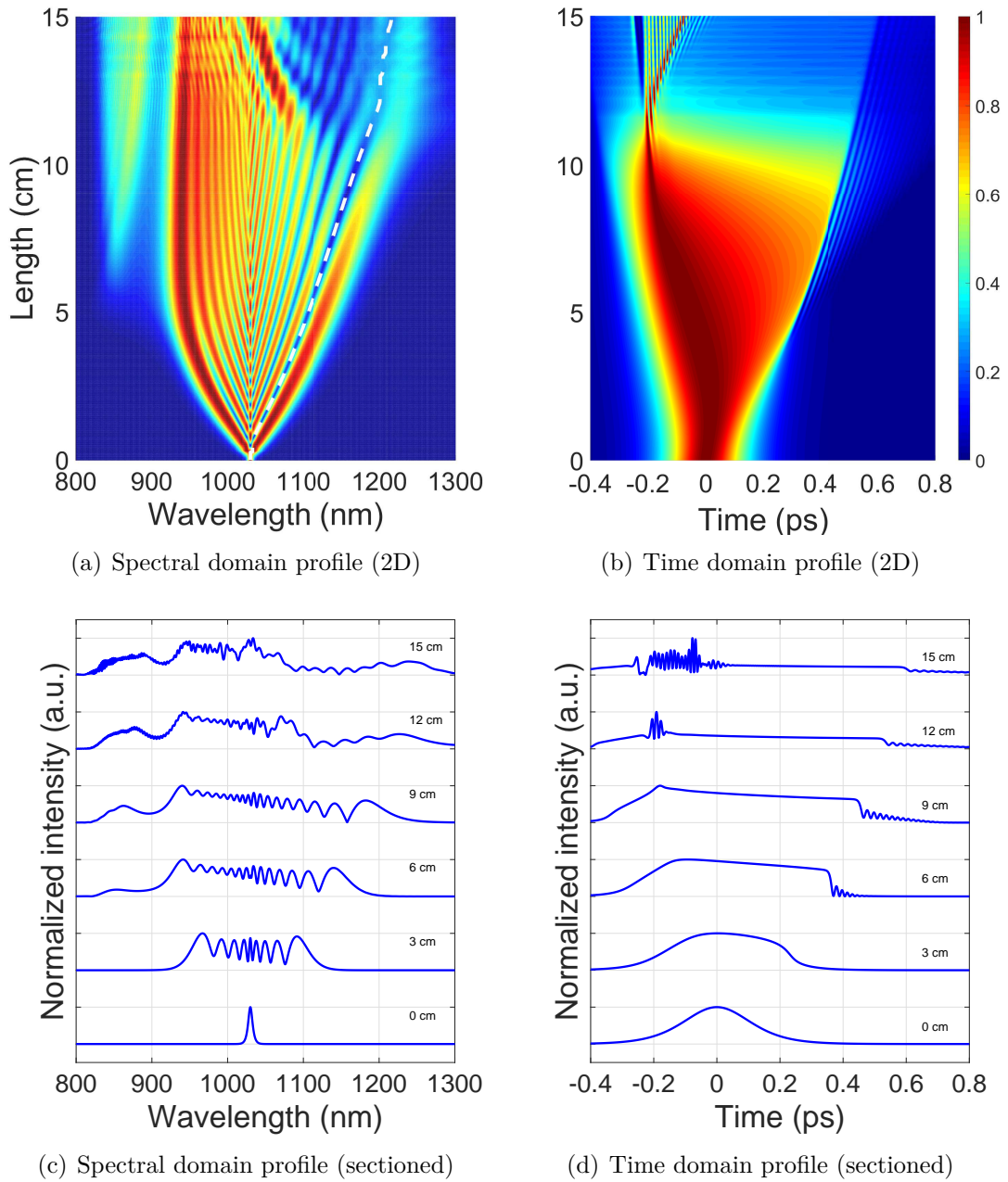
Figure 2.14: Evolution of 78 nJ, 250 fs pulse in a 15-cm-long LMA-8.

(a) Spectral domain pulse evolution along the fiber. The white dashed line shows the cut-off wavelength of the long-pass filter. (b) Time domain pulse evolution along the fiber. (c) Spectral domain pulse profile at signature distances. (d) Time domain pulse profile at signature distances.

(a) Spectral profile of the output pulse

(b) Temporal intensity profile

(c) SESS pulse compression
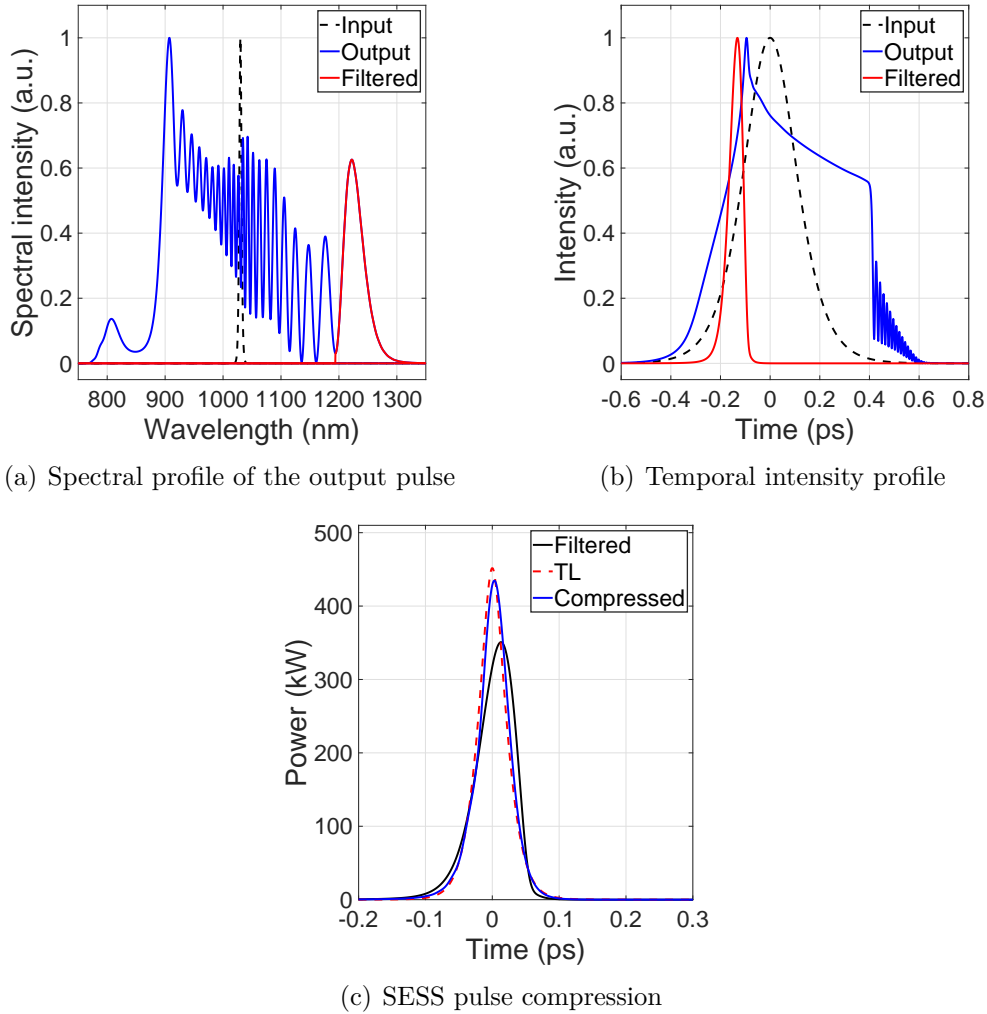
Figure 2.15: Output of 156 nJ, 250 fs pulse in a 5-cm-long LMA-8.

(a) Spectral intensity profile. The right-most lobe has a center wavelength at 1230-nm. (b) Temporal intensity profile. The filtered pulse is quasi-transform-limited (TL). (c) The compression of SESS pulse.

right-most spectral lobe has a much slower wavelength shifting when the spectrum crosses the ZDW and enters the "soliton" regime. Optimally, LMA-fiber length should be cropped to ensure that SPM is dominating the spectral evolution. This also limits an effective wavelength shift of the SESS pulses after they enter the "soliton" regime.

To demonstrate the energy scalability of SESS, we change the launching condition into an input pulse energy of 156-nJ and a LMA-8 fiber length of 5-cm. According to Eq. 2.11, the net nonlinear phase for SESS remains the same as long as the product between the input pulse energy and the fiber length is unchanged. Figure 2.15 plots the spectral temporal profiles of the input/output pulse and the

(a) Spectral domain profiles   (b) Time domain profiles
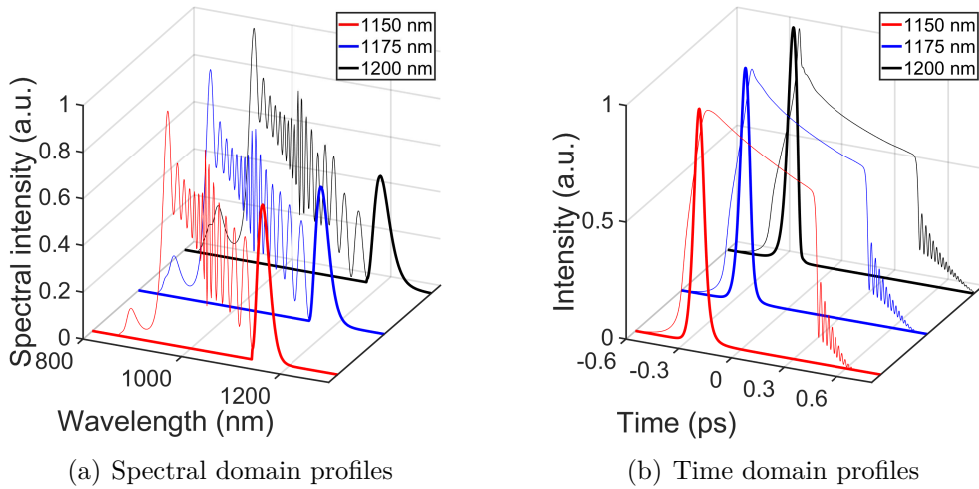
Figure 2.16: SESS process in a 10-cm-long LMA-8.

SESS process in a 10-cm-long LMA-8 fiber generates a wavelength-shifted pulse centered at 1150/1175/1200-nm. (a) Spectral domain pulse profiles. (b) Time domain pulse profiles.

corresponding SESS pulse compression. Due to a reduction of fiber length, SESS process has less dispersion effect. As a result, the right-most lobe centers at 1230-nm (1200-nm in 10-cm-long LMA-8). By inserting a long-pass filter at 1194-nm, the filtered SESS spectrum has a 3-dB bandwidth of ∼40-nm. The filtered pulse carries 24.6-nJ pulse energy (10.4-nJ in10-cm-long LMA-8), corresponding to an energy conversion efficiency of 15.8% (13.3% in 10-cm-long LMA-8). After the pulse compression, the compressed SESS pulse can have a peak power of >400-kW (175-kW in 10-cm-long LMA-8). Compared with SSFS, SESS can achieve an energy scaling by cutting down the fiber length. The generated SESS pulses can have tens of nanojoules in pulse energy and hundreds of kilowatts in peak power.

2.4.2   Noise transfer and energy scaling of SESS

In this section, we investigate SESS processes in different LMA fibers with different fiber length, with a particular emphasis on the noise transfer and the energy scalability of SESS. We compare SESS and SSFS in their capability of generating wavelength-shifted signal pulses for seeding DFG processes.

SESS in a 10-cm-long LMA-8

Using a 10-cm-long LMA-8 fiber, the center wavelength of the right-most spectral lobe can be tuned by changing the pulse energy of the input pulse. When the input pulse energy is 55/67/78-nJ, the generated wavelength-shifted SESS pulse centers at 1150/1175/1200-nm. Figure 2.16 plots the spectral temporal profiles of

(a) RIN-RTJ noise transfer

(b) RIN-RIN noise transfer

(c) SESS wavelength versus input E

(d) SESS timing versus input E

Figure 2.17: Noise transfer of SESS in a 10-cm-long LMA-8.

Noise transfer in a 10-cm-long LMA-8 fiber. (a) RIN-RTJ noise transfer. (b) RIN-RIN noise transfer. (c) SESS center wavelength versus input pulse energy. (d) SESS pulse timing versus input pulse energy.

the output pulse and the filtered SESS pulse. All SESS pulses have a quasi-TL form. The SESS pulses have a pulse energy of 8.9/9.6/10.3-nJ, corresponding to an energy conversion efficiency of 14.4%/14.4%/13.2%, respectively. If the SESS pulses are frequency mixed with pump pulses centered at 1030-nm, the generated mid-IR idler pulses center at 9.87/8.35/7.27-μm.

When the intensity of the input pulse is fluctuating, the resulting SESS pulse has a temporal position fluctuation and an intensity fluctuation. To study the noise transfer of SESS processes inside a 10-cm-long LMA-8 fiber, we perform similar calculations as in the study of SSFS. The results are plotted in Fig. 2.17. Figure 2.17(a) shows that when the input intensity is fluctuating by $\pm 2\%$, the

resulting SESS pulse has a relative timing jitter of <1-fs, 80 time lower compared with the SSFS process inside a 100-cm-long PCF-945 (Fig. 2.8). Figure 2.17(b) shows that $\pm 2\%$ input intensity fluctuation leads to about $\pm 1\%$ output intensity fluctuation, indicating SESS has a similar RIN-RIN noise transfer compared with SSFS.

In SSFS, RS pulses are propagating in the anomalous dispersion regime for the entire process. Since a higher input pulse energy can increase the amount of red-shift, the resulting RS accumulates more group delay because of the negative GVD β_2. Therefore, RIN-RTJ curves for SSFS process have a positive slope. For SESS process, when the pulse is propagating in the normal dispersion regime, a higher input pulse energy can increase the net nonlinear phase, further red-shift the SESS pulse and result in less group delay due to the positive β_2. If the center wavelength of the SESS pulse is in the normal dispersion regime, for example, 1150-nm, the RIN-RTJ noise transfer has a negative slope (-0.5 fs/% for 1150-nm). If the center wavelength of the SESS pulse is in the anomalous dispersion regime, the RIN-RTJ noise transfer has a positive slope (+0.5 fs/% for 1200-nm). If the SESS pulse has a center wavelength close to the ZDW of the LMA fiber, SESS process features a minimized RIN-RTJ noise transfer with a slope close to zero.

Figure 2.17(c) plots the center wavelength of the SESS pulse when the input pulse energy varies from 50-nJ to 80-nJ. The SESS wavelength scales linearly with respect to the input pulse energy in the range from 1140-nm to 1210-nm. Figure 2.17(d) plots the corresponding timing position of the SESS pulse versus SESS wavelength. The first-order derivative of this curve is in proportion to the RIN-RTJ noise transfer rate. Apparently, SESS process features a minimized RIN-RTJ noise transfer when the center wavelength of the SESS pulse is 1185-nm.

SESS in LMA-8 with different fiber length

Similar with SSFS, we expect the RIN-RTJ noise transfer of SESS process can be minimized by using a shorter fiber. We perform calculations by setting the length of LMA-8 at 5-cm and SESS wavelength at 1150/1175/1200-nm. The corresponding input pulse energy for the SESS process is 95/117/135-nJ, respectively. Figure 2.18 plots the noise transfer of SESS inside a 5-cm-long LMA-8. The RIN-RTJ noise transfer is reduced by using a shorter LMA fiber. The RIN-RIN noise transfer is marginally larger. Table 2.4 summarizes the RIN-RTJ noise transfer rate for LMA-8 fiber at 5-cm and 10-cm, together with the pulse energy of the SESS pulse and the corresponding energy conversion efficiency. Using a 5-cm-long LMA-8 fiber, the RIN-RTJ noise transfer is optimized to 0.32 fs/% for generating 1200-nm SESS pulses, meaning 1% intensity fluctuation at the input leads to <0.32-fs timing fluctuation of the SESS pulse, 20 times lower compared with SSFS in a 15-cm-long PCF-945 (results shown in Table 2.2).

Moreover, since the SESS pulse is not limited by the soliton area theorem, its pulse energy can exceed tens of nanojoules, two orders of magnitude higher compared with the RS pulse from SSFS (22.8 nJ versus 0.296 nJ). The pulse energy of the SESS pulse can be scaled by cropping LMA fiber length and increasing the
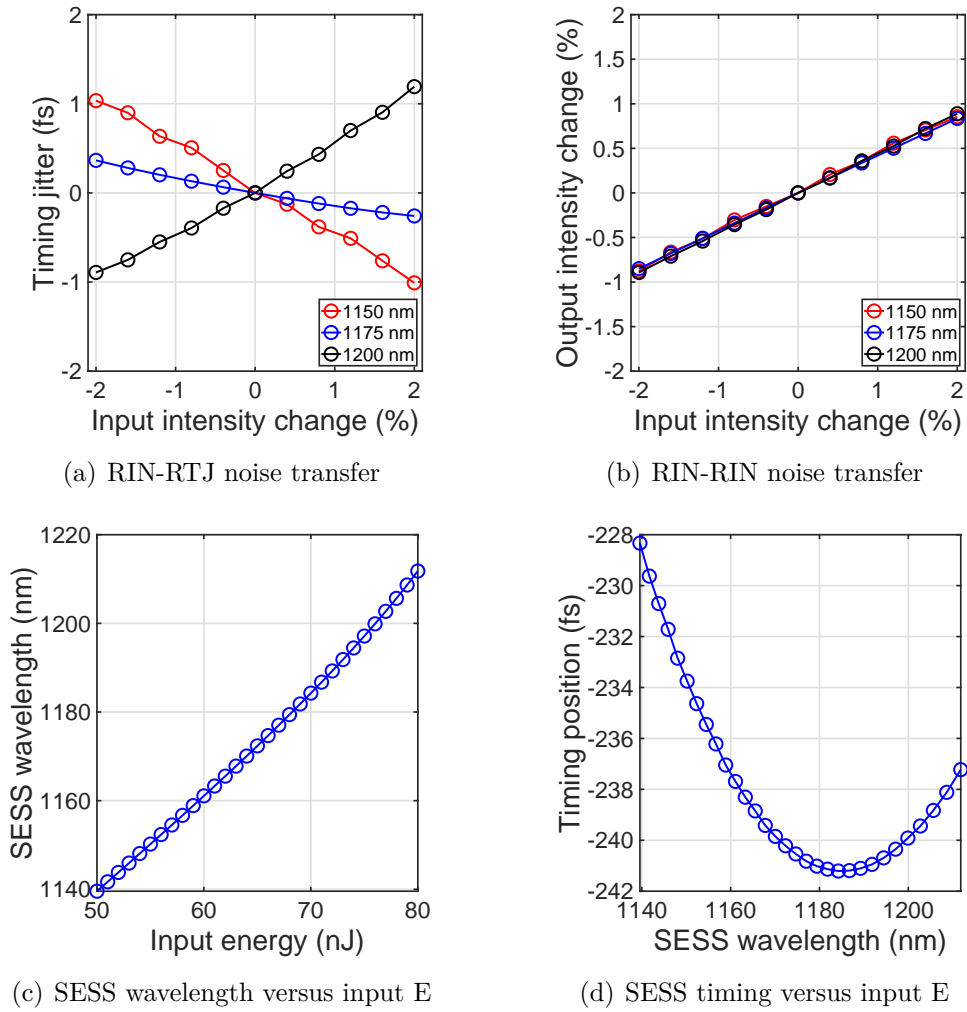
(a) RIN-RTJ noise transfer

(b) RIN-RIN noise transfer
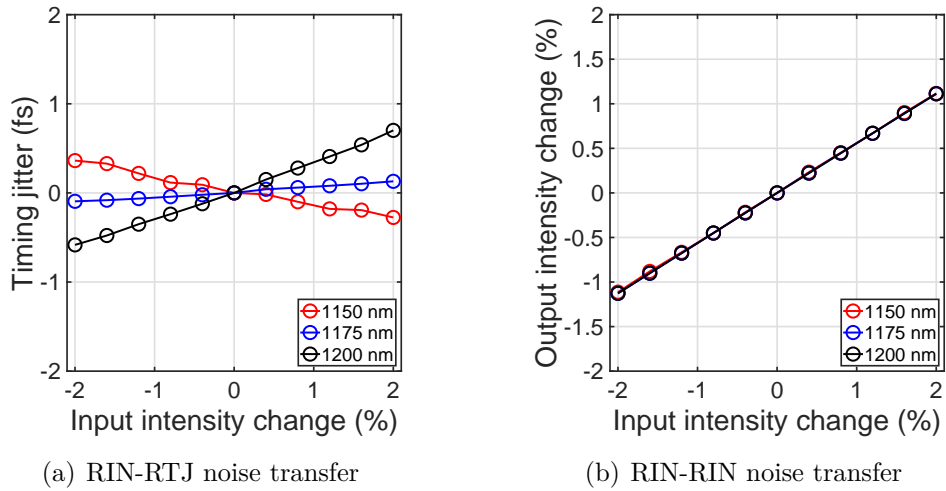
Figure 2.18: Noise transfer of SESS in a 5-cm-long LMA-8.

Noise transfer in a 5-cm-long LMA-8 fiber. (a) RIN-RTJ noise transfer. (b) RIN-RIN noise transfer.

λ_{SESS} (nm)	L (cm)	RIN-RTJ (fs/%)	E_{in} (nJ)	E_{SESS} (nJ)	Conv. eff. (%)
1150	5	-0.16	95.0	18.7	19.7
	10	-0.51	55.0	8.9	16.1
1175	5	0.06	117.0	21.0	18.0
	10	-0.16	67.0	9.6	14.4
1200	5	0.32	135.0	22.8	16.9
	10	0.52	78.0	10.3	13.2

Table 2.4: SESS in LMA-8 with different fiber length

input pulse energy. A reduction of the LMA fiber length also results in less net dispersion effect, leading to a higher energy conversion efficiency. Conversely, SSFS process has a higher energy conversion when SSFS is configured with a longer fiber and a lower input pulse energy.

SESS in different LMA fibers

The pulse energy of the SESS pulse can be further scaled by utilizing LMA fibers with a larger mode field area (MFA). We choose two more LMA fibers into the comparison: LMA-10 and LMA-15. The specifications and dispersion map for these two fibers can be found in Table A.2 and Fig. 2.12. We calculate SESS processes with the LMA fiber length fixed at 5-cm. SESS process generates an

(a) 5-cm-long LMA-10
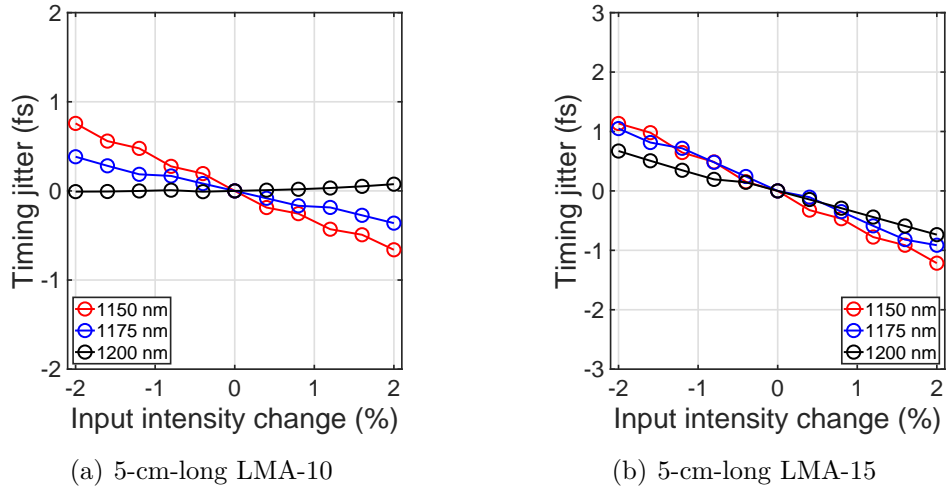
(b) 5-cm-long LMA-15

Figure 2.19: Noise transfer of SESS in LMA-10 and LMA-15.

RIN-RTJ noise transfer in LMA-10 and LMA-15 is calculated. (a) 5-cm-long LMA-10 fiber. (b) 5-cm-long LMA-15 fiber.

λ_{SESS} (nm)	LMA type	RIN-RTJ (fs/%)	E_{in} (nJ)	E_{SESS} (nJ)	Conv. eff. (%)
	LMA-8	-0.16	95.0	18.7	19.7
1150	LMA-10	-0.35	132.0	25.2	19.1
	LMA-15	-0.59	302.0	55.3	18.0
	LMA-8	0.06	117.0	21.0	18.0
1175	LMA-10	-0.18	162.0	28.2	17.1
	LMA-15	-0.51	374.0	62.1	16.3
	LMA-8	0.32	135.0	22.8	16.9
1200	LMA-10	0.02	191.0	30.9	16.2
	LMA-15	-0.34	446.0	68.5	15.0

Table 2.5: SESS in LMA-8, LMA-10 and LMA-15

output pulse centered at 1150/1175/1200-nm.

Figure 2.19 plots the RIN-RTJ noise transfer for these two fibers. Due to a different dispersion map, LMA-10 and LMA-15 exhibits different RIN-RTJ noise transfer compared with LMA-8. LMA-10 has a ZDW of 1195-nm and LMA-15 has a ZDW of 1240-nm. The RIN-RTJ noise transfer curve has a negative slope when the center wavelength of the SESS pulse is at 1150/1175/1200-nm. The absolute value of the slope (RIN-RTJ noise transfer rate) decreases when the SESS wavelength increases from 1150-nm to 1200-nm.

Table 2.5 summarizes the RIN-RTJ noise transfer rate for 5-cm-long LMA-8/LMA-10/LMA-15 fibers, together with the pulse energy of the SESS pulse and the corresponding energy conversion efficiency. Using a 5-cm-long LMA-15 fiber, 1150-nm SESS pulse has >55-nJ in pulse energy with an energy conversion efficiency of 18.0%. Later we show in Chapter 3 that, if such signal pulses mix with 1030-nm, 200-nJ pump pulses inside a 2-mm-long GaSe, the generated idler pulses have >1.3-nJ pulse energy centered at 10-μm, corresponding to an average output power of 40-mW at 30-MHz. When the repetition rate of the laser system is stabilized, such long-wave, high-power, low-noise frequency comb is promising in many spectroscopic applications.

2.4.3 Comparison between SESS and SSFS

To compare SESS processes and SSFS processes, we calculate the generation of wavelength-shifted signal pulses spanning from 1164-nm to 1208-nm. If such signal pulses are frequency mixed with pump pulses centered at 1030-nm in a DFG setup, the generated mid-IR idler pulses have a center wavelength from 7-μm to 11-μm. For SESS process, we choose 5-cm-long LMA-8/LMA-10/LMA-15 fibers. For SSFS process, we choose a 25-cm-long PCF-975. Such choice is able to minimize the RIN-RTJ noise transfer according to previous investigations. The corresponding RIN-RTJ noise transfer, signal pulse energy, and the energy conversion efficiency are calculated and the results are plotted in Fig. 2.20.

The results shows that both processes can generate the wavelength-shifted signal pulse for seeding a DFG. Compared SSFS, SESS has the following features:

- SESS has a significantly reduced RIN-RTJ noise transfer compared with SSFS. When the input pulse has 1% intensity fluctuation, an optimized SSFS process still introduces ∼5-fs relative timing jitter to the output RS pulse. Meanwhile, SESS process introduces an additional timing jitter of <0.5-fs, 20 times less compared with SSFS. This result is also consistent with experimental measurements [56,57]. Wavelength-shifted signal pulses with low timing jitter noise is favorable for generating low-noise mid-IR frequency comb via DFG.

- Not limited by the soliton area theorem, SESS process is able to generate signal pulses with a pulse energy of >50-nJ. For SSFS process, the generated signal pulses have a pulse energy of <0.3-nJ. We show later in Chapter 3 that, the key for realizing high-power mid-IR frequency comb is to increase the pulse energy of the signal pulses to the same level of pump pulses. In this respect, SESS is a better candidate for generating signal pulses with >50-nJ pulse energy.

- Both SESS and SSFS process has an energy conversion efficiency of ∼15%. When the signal pulse has less wavelength shift, the conversion efficiency is marginally higher.

(a) RIN-RTJ transfer of SESS

(b) RIN-RTJ transfer of SSFS

(c) SESS pulse energy

(d) RS pulse energy

(e) Conversion efficiency of SESS

(f) Conversion efficiency of SSFS
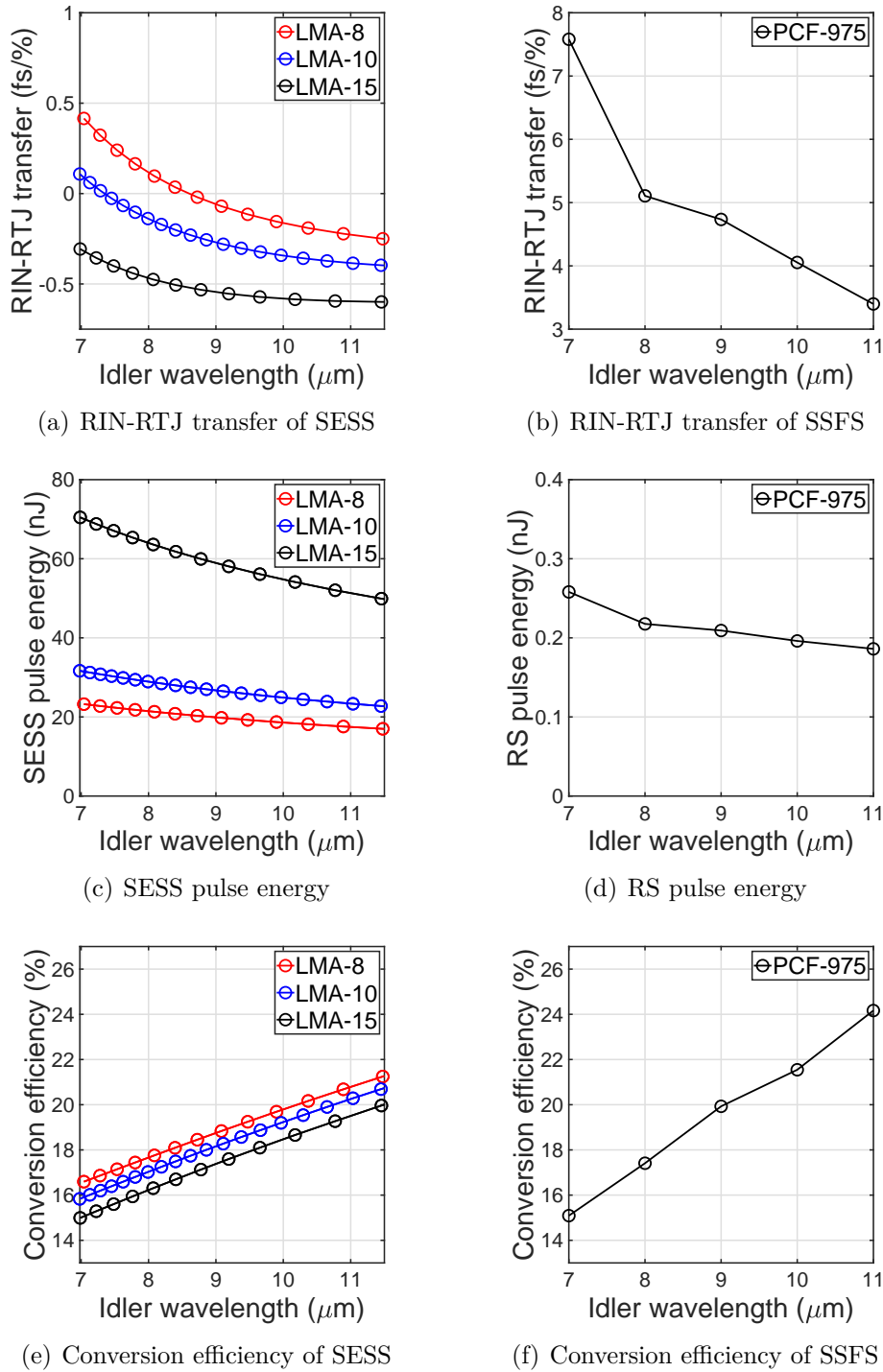
Figure 2.20: Comparison between SESS and SSFS.

SESS in 5-cm-long LMA-8/LMA-10/LMA-15 fibers is compared with SSFS in a 25-cm-long PCF-975. (a) RIN-RTJ noise transfer for SESS. (b) RIN-RTJ noise transfer for SSFS. (c) SESS pulse energy. (d) RS pulse energy. (e) SESS energy conversion efficiency. (f) SSFS energy conversion efficiency.

2.5   Summary of the chapter

In this chapter, we investigated two nonlinear fiber-optic wavelength shifting methods, soliton self-frequency shift (SSFS) and self-phase-modulation enabled spectral selection (SESS), with a particular emphasis on the noise transfer characteristics for both processes. For SSFS process, the generated wavelength-shifted signal pulses feature a relative low pulse energy of <1-nJ. During the SSFS process, an excessive amount of relative timing jitter is introduced to the signal pulses due to the large net group delay during the process. By using a shorter fiber and a PCF with a zero-dispersion-wavelength (ZDW) closer to the center wavelength of the input pulse, the noise transfer from the relative intensity noise (RIN) at the input to the relative timing jitter (RTJ) noise at the output can be minimized from a rate of >50 fs/% to <5 fs/%.

Compared with SSFS, SESS is a better candidate for generating wavelength-shifted signal pulses with a >50-nJ pulse energy and a ∼20 times less RIN-RTJ noise transfer. By shortening down the fiber length or increasing the fiber mode field area (MFA), the pulse energy of the wavelength-shifted SESS pulse can be further scaled up to hundreds-of-nanojoules. The wavelength-shifted SESS pulses with a high pulse energy and a low relative timing jitter noise can facilitate the generation of high-power, low-noise mid-IR frequency combs by using a difference frequency generation (DFG) setup. In the next chapter, we study the power scalability of DFG-based mid-IR frequency combs.

Chapter 3

Power scalability of DFG-based mid-IR frequency combs

3.1   Introduction

Due to the lack of active gain media, the implementation of long-wavelength "fingerprint" mid-infrared (mid-IR) frequency combs relies heavily upon the use of parametric frequency down-conversion from mature near-infrared (NIR) sources [16, 17] via difference frequency generation (DFG). Currently, mid-IR frequency combs in the "fingerprint" region (especially for wavelengths beyond 10 μm) still suffer from low available average power, which leads to a reduced signal-to-noise ratio (SNR) for detection and, therefore, severely limits their use in practical spectroscopic applications. Many research efforts are geared towards finding an efficient power scaling method to achieve high-power mid-IR frequency combs [58]. For a DFG process, the nonlinear crystal should be transparent, or at least relatively transparent, for all three interacting waves. Among nonlinear crystals (shown in Fig. 1.2), only non-oxide crystals can access the long-wave side of the mid-IR spectrum (5–20 μm). These non-oxide crystals exhibit a lower damage threshold compared with oxide crystals that work in near-infrared (NIR). At high pump intensity, multiphoton absorption (MPA) together with poor thermal conductivity causes the temperature rising inside the crystals. If the pulse repetition rate is too high to allow enough time for heat dissipation, the crystal temperature continues to rise, which eventually causes damage. Our experimental results showed that at 30-MHz repetition rate, around 200-nJ, 200-fs pulses at 1.03-μm can damage a GaSe crystal even for a loosely focused beam radius of 200-μm [36]. It corresponds a maximum input average power of 6-W. This damage threshold thus sets the upper limit of the allowed pulse energy for the input pump/signal pulses, leading to a low pulse energy (and low average power) for the output mid-IR pulses.

Above analysis naturally leads to the following questions for constructing high-power mid-IR frequency combs: (1) For HRR DFG, how does the idler power scale with respect to input pump/signal power? (2) For our current experimental condition, how far are we from the OPA regime? (3) In general, how to achieve

powerful HRR mid-IR pulses?

In this chapter we answer these questions by analyzing DFG processes inside GaSe crystals. We firstly study DFG seeded with continuous waves (CWs) by solving the coupled wave equations in Section 3.2. It allows us to identify a linear operation regime for DFG, in which the idler scales linearly with both the pump and the signal. Therefore increasing the signal energy can be as efficient as increasing the pump energy for idler energy scaling. We then introduce the time-dependent coupled wave equations in Section 3.3 and numerically investigate the DFG seeded with femtosecond pulses in Section 3.4 and Section 3.5. We show that group-velocity mismatch (GVM) plays an essential role in determining the idler energy scalability. Two possible DFG options are compared for generating mid-IR pulses centered at 9.87 μm: (1) pump/signal at 1.03/1.15 μm and (2) pump/signal at 2.0/2.508 μm. We refer to them as 1-μm driven and 2-μm driven DFG, respectively. The GVM in the 2-μm driven DFG is much less than the 1-μm driven case, and thus exhibits superior energy scalability for the idler pulses. For example, our simulation indicates that 44.2-nJ pulses at 9.87 μm can be achieved by mixing 500-nJ, 2.0-μm pump pulses and 100-nJ, 2.508-μm signal pulses in a 2-mm-thick GaSe crystal. At 50-MHz repetition rate, this corresponds to more than 2 watts average power at the output. We show in Section 3.6 that using a recently invented fiber-optic method, the implementation of a high-power mid-IR frequency combs is practically feasible. Section 3.7 summarize this chapter.

3.2 DFG with continuous waves

3.2.1 Coupled wave equations

To understand the energy scaling property of DFG process that generates mid-infrared (mid-IR) idler pulses, we first re-visit the classic theory of continuous waves (CW) DFG so that physical insights can be gained.

CW DFG is precisely modeled by the coupled wave equation [59, 60]. The exact solution to the equations can be used to study the general behavior of DFG processes under different launching conditions, such as the growth of the idler with an increasing pump or signal, the saturation of the parametric gain due to excessive amount of input pump/signal, and the power scaling of the idler with respect to the pump/signal. In the study of CW DFG, effects such as broadband phase matching, higher order dispersion, and time-dependent electric field are not considered, all of which play a substantial role in determining the energy scaling property of pulsed DFG. Nevertheless study on CW DFG still offers a picture of general DFG process. Later we apply the knowledge gained from the CW DFG to the pulsed DFG.

Coupled wave equations are developed from the classic Maxwell's equations for describing the situation when three optical waves are co-propagating inside a nonlinear $\chi^{(2)}$ medium [60, 61]. During propagation, three waves change energy with each other through nonlinear dipole oscillations. Using the coupled wave equations,

optical parametric processes such as OPA, OPO, DFG, sum frequency generation
(SFG) and second harmonic generation (SHG) can be precisely modeled.

In the equations, all three waves for nonlinear interaction are assumed to be
monochromatic, planar waves. The nonlinear $\chi^{(2)}$ medium is also assumed to be
an optical medium so that material absorption is not taken into consideration.
In reality, material absorption plays an important role in determining whether
the nonlinear crystal is suitable for hosting DFG processes that generate mid-
IR. The crystal has to be transparent or relatively transparent for all interact-
ing waves in order to ensure an effective generation of the idler. For example,
mid-IR wavelengths longer than 5 μm can be only accessed by non-oxide crys-
tals such as GaSe [33, 35, 62–67], GaAs [34], AgGaS$_2$ (AGS) [68] and AgGaSe$_2$
(AGSe) [62, 69–71], to name a few. For wavelengths shorter than 5 μm, oxide
crystals such as periodically-poled lithium niobate (PPLN) can be used [33]. With
these assumptions, the coupled wave equations are written as

$$
\frac{\mathrm{d}A_1(z)}{\mathrm{d}z} = i\frac{\omega_1}{n_1 c}d_\mathrm{eff}A_3(z)A_2^*(z)\mathrm{e}^{-i\Delta kz},
$$
$$
\frac{\mathrm{d}A_2(z)}{\mathrm{d}z} = i\frac{\omega_2}{n_2 c}d_\mathrm{eff}A_3(z)A_1^*(z)\mathrm{e}^{-i\Delta kz}, \qquad (3.1)
$$
$$
\frac{\mathrm{d}A_3(z)}{\mathrm{d}z} = i\frac{\omega_3}{n_3 c}d_\mathrm{eff}A_1(z)A_2(z)\mathrm{e}^{+i\Delta kz}.
$$

In the equations, the complex amplitude of the optical field is expressed by $A_i(z)$,
in the longitudinal coordinate z of the nonlinear $\chi^{(2)}$ medium. The amplitude of
$A_i(z)$ equals to $|A_i| = \sqrt{\dfrac{2I_i}{\varepsilon_0 n_i c}}$, where I_i is the optical irradiance (intensity), ϵ_0 is
the vacuum permittivity, c is the speed of light, and n_i is the refractive index of the
medium. ω_i is the angular frequency of the optical wave, d_eff is the effective non-
linear coefficient, and $\Delta k = k_3 - k_2 - k_1$ is the difference between the propagation
wave vectors of the optical waves. In this section, we assume perfect phase match
so that $\Delta k = 0$. Later in this chapter, we will show the spectral bandwidth of the
generated idler is largely dependent on the phase matching condition, especially
when a thick nonlinear crystal is used to host DFG process.

In the equations, we use the notation $\omega_3 \geq \omega_2 \geq \omega_1$. For DFG process, $\omega_1 =
\omega_3 - \omega_2$ is generated. We also use the convention that the wave with highest center
frequency ω_3 is called pump, ω_2 is called signal and ω_1 is called idler.

The exact solution to the coupled wave equations has the mathematical form
of Jacobi elliptic functions. Jacobi elliptic functions are periodic functions over
the propagation distance z. Detailed derivation to the exact solution can be found
in these references [59, 61]. Here we only give the solution. For DFG process,
normally the idler has zero input, $A_1(0) = 0$. At the output, the intensity of each

wave can be written as,

$$I_1(z) = \frac{\omega_1}{\omega_3} \cdot I_{30} \cdot (1 - \text{sn}^2(\varsigma + \varsigma_0, \gamma)),$$

$$I_2(z) = I_{20} + \frac{\omega_2}{\omega_3} \cdot I_{30} \cdot (1 - \text{sn}^2(\varsigma + \varsigma_0, \gamma)),$$

$$I_3(z) = I_{30} \cdot \text{sn}^2(\varsigma + \varsigma_0, \gamma).$$

(3.2)

In the solution, sn is the elliptic sine function. The modified nonlinear interaction strength is expressed by $\varsigma = z \cdot d_{\text{eff}} \cdot \sqrt{\frac{2\omega_1\omega_2\omega_3}{\varepsilon_0 c^3 n_1 n_2 n_3}} \cdot \sqrt{(\frac{I_{20}}{\omega_2} + \frac{I_{30}}{\omega_3})}$, with an offset $\varsigma_0 = \int_0^1 \frac{dx}{\sqrt{1-x^2} \cdot \sqrt{1 - \gamma \cdot x^2}}$. In the integral, the parameter $\gamma = \frac{I_{30}/\omega_3}{I_{20}/\omega_2 + I_{30}/\omega_3}$ describes the ratio between the input pump flux and the total input flux. I_{i0} stands for the input intensity and $I_{\text{in}} = I_{10} + I_{20} + I_{30}$ is the total input intensity.

The exact solution has a mathematical form (Jacobi elliptic function) that cannot be further simplified. In order to write the solution in a more analytical fashion, DFG process is assumed to have a strong input pump so that the pump wave can be consider constant during the process, i.e., $A_3(z) = A_3(0)$. Coupled wave equations are then reduced to two equations which describe the evolutions of the signal wave and the idler wave. At the output, the signal and the idler can be written using hyperbolic trigonometric functions. The output idler has a sinh square expression [60,61], where $\sinh(x) = \frac{(e^x - e^{-x})}{2}$,

$$I_1(z) = \frac{\omega_3}{\omega_2} I_{20} \cdot \sinh^2(\Gamma z),$$

$$\Gamma^2 = \frac{2\omega_2\omega_1 d_{eff}^2}{n_1 n_2 n_3 \varepsilon_0 c^3} \cdot I_{30}.$$

(3.3)

The sinh sqaure express is used as a comparison with the exact solution to the equations. In the following sections, we show this expression can be further simplified under certain conditions.

3.2.2 CW DFG inside a 0.2-mm-thick GaSe

To show the power scaling property of DFG process, we first study CW DFG process inside a 0.2-mm-thick GaSe crystal. GaSe is a non-oxide crystal whose transparent window covers the entire "fingerprint" wavelengths (5–20 μm). GaSe also has a birefringence that enables broadband phase matching conditions (e.g., $n_o = 2.800$ and $n_e = 2.468$ at 1030 nm). To generate mid-IR idler, the pump can be set at 1030 nm [33,36], 1550 nm [62], 2 μm [63–65] and beyond [66,67]. In this example, we choose the pump centered at 1030 nm and the signal centered at 1150 nm. Such combination generates an idler centered at 9.87 μm. To phase match all three waves, type-I DFG scheme is employed, which means the pump is e-polarized and the signal/idler are o-polarized (ooe scheme). Phase matching is achieved by setting an internal crystal angle of 14.4°. It corresponds to an external crystal
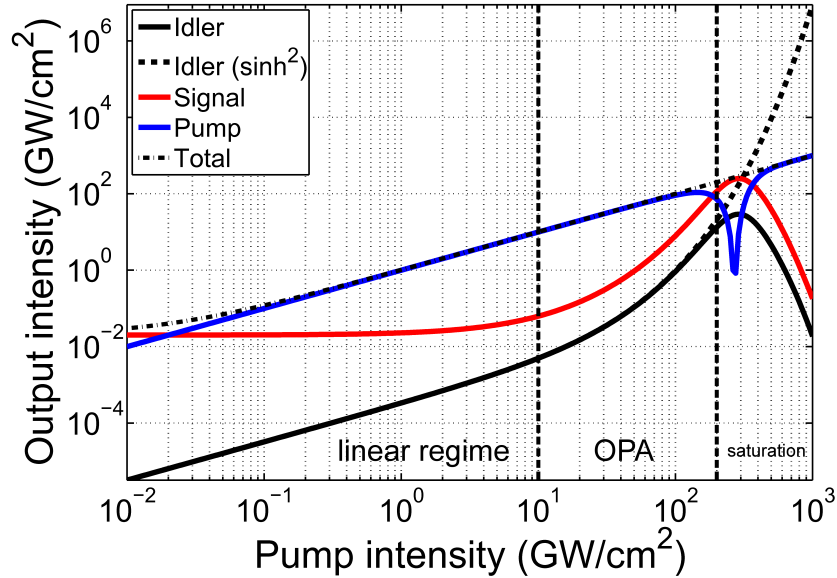
Figure 3.1: CW DFG outputs from a 0.2-mm-thick GaSe crystal.

The outputs from a DFG process inside a 0.2-mm-thick GaSe crystal. The signal has a fixed intensity at 20 MW/cm² and the pump has an intensity varying from 10 MW/cm² to 10^3 GW/cm². The output intensities are calculated by using the exact solution to the coupled wave equations. The output idler is also expressed by the sinh square expression (black dashed line). The total intensity of the inputs is plotted as a dash-dotted line as a reference to the output intensity. The vertical dashed lines indicate three different operation regimes for the DFG process.

angle of $\sim 43°$. In this scenario, the process has an effective nonlinear coefficient d_{eff} of 59.2 pm/V.

We first study the case when the input signal has a fixed intensity at 20 MW/cm² while the input pump intensity varies from 10 MW/cm² to 10^3 GW/cm². The pump, signal, and idler at the output are calculated using the exact solution to the coupled wave equations (Eq. 3.2). The sinh square expression (Eq. 3.3) is also used for calculating the idler, as a comparison. Figure 3.1 plots the output intensity of the three waves as a function of input pump intensity. The total intensity of the inputs is also plotted in a dash-dotted line as a reference.

Figure 3.1 shows that the idler experiences three different stages as the pump is increasing. (1) When the pump is below 10 GW/cm², the idler grows linearly with respect to the pump. We refer to this DFG operation regime as the linear regime; (2) When the pump is between 10-200 GW/cm², the idler has a more abrupt, exponential growth. The signal also grows exponentially in this region, which is a signature characteristic that defines a practical OPA system. We refer to this operation regime as the OPA regime for the DFG process; (3) When the pump intensity exceeds 200 GW/cm², the idler growth starts to saturate and reaches a
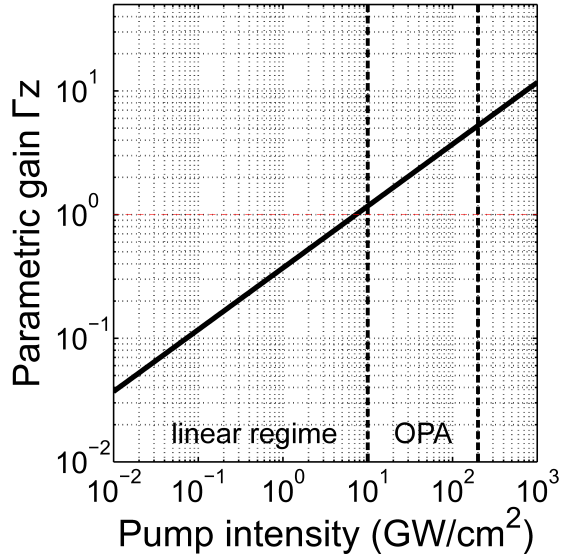
Figure 3.2: Parametric gain Γz for CW DFG.

Parametric gain Γz versus the input pump intensity. For the linear regime, $\Gamma z \ll 1$. For the OPA regime, $\Gamma z \gg 1$. When the pump exceeds 200 GW/cm^2, the output idler cannot be expressed by the sinh square expression.

maximum when the pump intensity is at about 300 GW/cm^2. At the maximum, DFG process converts all the pump photons into the signal/idler photons and the pump is completely depleted. After that, back conversion process occurs and the signal/idler photons are back-converting to the pump photons.

Within the linear regime and the OPA regime, the idler calculated by the exact solution (black solid line) and the sinh square expression (black dashed line) are nearly identical. Thus we can use the latter expression to write the idler in a more analytical fashion. In Equation 3.3, the unitless parameter Γz represents the strength of the parametric interaction, describing how efficient three waves change energy with each other. It also determines the operation regime for the DFG process. We plot in Fig. 3.2 the corresponding parametric gain Γz versus the input pump intensity. As Figure 3.2 shows, when $\Gamma z \ll 1$, the parametric interaction is weak and DFG process operates in the linear regime. When $\Gamma z \gg 1$, the parametric interaction is strong and DFG process operates in the OPA regime. It is noteworthy that when the pump exceeds 200 GW/cm^2, the output idler calculated by the sinh square expression does not agree with the exact solution because the parametric gain is so strong that the input pump starts to deplete. The strong pump assumption also becomes invalid and therefore the intensity of the output waves needs to be calculated by the exact solution.

In the linear regime where $\Gamma z \ll 1$, we can substitute $\sinh^2(\Gamma z)$ in Eq. 3.3 using

its first order Taylor expansion, which leads to

$$I_{\text{idler}} = \frac{2\omega_1\omega_3 d_{\text{eff}}^2}{n_1 n_2 n_3 \varepsilon_0 c^3} \cdot I_{20} \cdot I_{30} \cdot L^2. \tag{3.4}$$

Here L is the crystal thickness. This expression clearly shows that when DFG operates in the linear regime, the idler intensity is proportional to the product between the pump intensity and the signal intensity. Thus increasing the signal can have the same effect as increasing the pump for scaling up the idler. In contrast, when DFG operates in the OPA regime, $\Gamma z \gg 1$ so that $e^{\Gamma z} \gg e^{-\Gamma z}$. Then, the sinh function can be approximated by the exponential function ($\sinh(x) = \dfrac{e^x - e^{-x}}{2}$), and the idler can be written as

$$
\begin{aligned}
I_{\text{idler}} &= \frac{1}{4} \cdot \frac{\omega_3}{\omega_2} \cdot I_{20} \cdot e^{2\Gamma z}, \\
\Gamma &= \sqrt{\frac{2\omega_2\omega_1 d_{\text{eff}}^2}{n_1 n_2 n_3 \varepsilon_0 c^3} I_{30}}.
\end{aligned}
\tag{3.5}
$$

Equation 3.5 indicates that the idler scales exponentially with respect to the square root of the input pump intensity and linearly to the input signal intensity. Therefore in the OPA regime, increasing the pump is more efficient for scaling up the idler compared with increasing the signal.

The pump threshold intensity I_{th}, which separates the linear regime and the OPA regime for DFG, can be defined by setting Γz unity. I_{th} is written as

$$I_{\text{th}} = \frac{n_1 n_2 n_3 \varepsilon_0 c^3}{2\omega_1\omega_2 d_{\text{eff}}^2} \cdot \left(\frac{1}{L}\right)^2. \tag{3.6}$$

For our DFG calculation (0.2-mm-thick GaSe, type-I DFG process with inputs centered at 1030/1150 nm), the pump threshold intensity is 7.3 GW/cm² according to this expression, which is close to the results shown in Fig. 3.1. When the input pump is below this threshold intensity, DFG process operates in the linear regime.

To show specifically how the idler scales in different operation regimes, we set the input signal at 2 MW/cm², 20 MW/cm², and 200 MW/cm², respectively, and then calculate the idler as a function of the pump using the exact solution. The results in Fig. 3.3(a) show that, for all three DFG processes, the idler grows linearly until the input pump reaches a threshold intensity of about 10 GW/cm². It is consistent with the theoretical prediction from Eq. 3.3, as the parametric gain Γz is independent on the level of the signal intensity. Therefore the threshold pump intensity I_{th} does not change with respect to the signal. After the linear regimes, the idler experiences exponential growth as the DFG process starts to enter the OPA regime. Finally, the idler growth saturates. It is noteworthy that DFG with different input signal saturates at different pump intensities and it can be only evident when the exact solution is used in the calculation. The sinh square expression is only valid when the pump is not depleted. After the idler reaches the maximum, DFG back-converts the signal/idler photons to the pump photons.

(a) DFG with a fixed signal   (b) DFG with a fixed pump
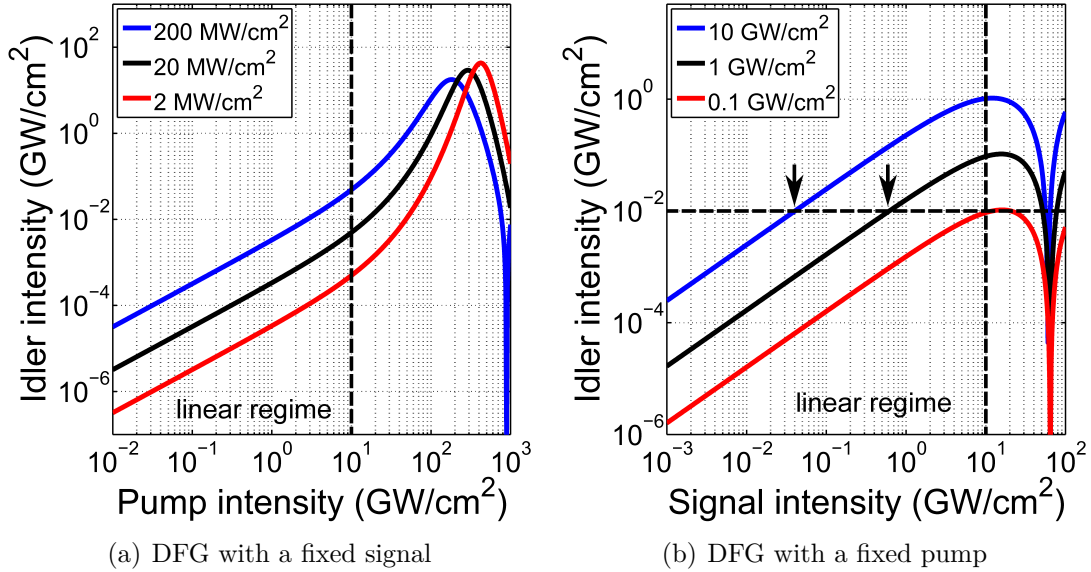
Figure 3.3: Idler under different launching conditions for CW DFG.

A type-I DFG process inside a 0.2-mm-long GaSe is used to examine the growth of the idler under different launching conditions. (a) The input signal is fixed at 2 MW/cm^2, 20 MW/cm^2, and 200 MW/cm^2. The input pump increases from 10 MW/cm^2 to 10^3 GW/cm^2. (b) The input pump is fixed at 0.1 GW/cm^2, 1 GW/cm^2, and 10 GW/cm^2. The input signal increases from 1 MW/cm^2 to 100 GW/cm^2.

Above analysis of the linear regime of the DFG process is based upon the strong pump assumption. We are also interested in the situations when such assumption turns invalid, i.e., when the signal is much stronger than the pump. Therefore, we calculate DFG processes with the input pump fixed at 0.1 GW/cm^2, 1 GW/cm^2, and 10 GW/cm^2 while the input signal increases from 1 MW/cm^2 to 100 GW/cm^2 in order to inspect how the idler scales with respect to the signal. The idler is again calculated using the exact solution and the results are plotted in Fig. 3.3(b). For all three traces, the idler grows linearly with respect to the signal when the signal is below 10 GW/cm^2, regardless of the input pump intensity. When the signal exceeds 10 GW/cm^2, the growth of the idler quickly saturates and reaches a maximum. After the maximum, the idler drops as it is back-converted to pump and then rises again.

The signal threshold intensity that triggers the saturation of the DFG process is close to the pump threshold intensity I_{th} in the previous plots, which can be explained by the exact solution to the coupled wave equations (Eq. 3.2). In the exact solution, the modified nonlinear interaction strength ς has a dependence on $\sqrt{(\frac{I_{20}}{\omega_2} + \frac{I_{30}}{\omega_3})}$. Therefore, if the total input photon flux is below certain threshold

value, the parametric interaction is weak and DFG process stays in the linear regime. When the total input photon flux continues to increase and exceeds the threshold value, the strength of the parametric interaction is strong and the idler no longer scales linearly. In this case, the DFG process operates in the OPA regime, if the input pump is much stronger than the signal, or the DFG process operates in a saturated state where the pump is depleted, if the input signal is much strong than the pump.

Figure 3.3(b) also suggests the advantage of increasing the input signal for scaling up the idler. Comparing two arrow-marked points in Fig. 3.3(b) where same amount of output idler is generated, DFG process on the black trace has a total input intensity of around 1.6 GW/cm^2, while the other one on the red trace has a total input intensity of around 10 GW/cm^2. Indeed Eq. 3.4 clearly indicates that for producing the same amount of idler, setting the input signal intensity equal to the input pump intensity can minimize the total optical intensity incident onto the crystal. It corresponds to a DFG process with higher photon conversion efficiency and less thermal load to the crystal. Moreover, the nonlinear crystal experiences less multiple photon absorption effect from the inputs as the signal photon possesses less photon energy compared with the pump photon.

The pump threshold intensity (here, it is 7.3 GW/cm^2) can be further translated for estimating the pump threshold pulse energy when the DFG process is seeded with femtosecond pulses. If we assume a loosely focused beam size $2w_0$ of 250 μm and a pulse duration of 200 fs, the pump threshold pulse energy is 717 nJ. To operate the DFG process in the OPA regime, the input pump pulse energy has to be more than 717 nJ.

However, in reality, the maximum input pulse energy that can be launched onto the crystal is constrained. GaSe has a band-gap of around 2.1 eV and thus it exhibits strong two-photon absorption if the input pulses have a center wavelength shorter than 1180 nm. GaSe also has low damage threshold and poor thermal conductivity compared with other nonlinear crystals. MPA effect causes temperature rising inside the crystals. At HRR, if the time between two pulses is too short for heat disspation, the crystal temperature can continue to rise, eventually leading to crystal damage. Our experimental results showed that at 30 MHz repetition rate, around 200 nJ, 200 fs pulses at 1.03 μm can damage a GaSe crystal even for a loosely focused beam radius of 200 μm [36]. It corresponds a maximum input average power of 6 W. This damage threshold thus sets the upper limit of the allowed pulse energy for the input pump/signal pulses, leading to a low average power for the output mid-IR pulses. As a result, DFG process can only operate in the linear regime for HRR systems, and the idler is proportional to the product of the pump and the signal [36].

In the following section of this chapter, we introduce the time-dependent coupled wave equations for analyzing DFG process with femtosecond pulses. The linear regime theory in the CW DFG will be tested for pulsed DFG. We study two cases (1) Pulsed DFG seeded with an input pump centered at 1030 nm; (2) Pulsed DFG seeded with an input pump centered at 2 μm. They are referred as 1-μm driven DFG and 2-μm driven DFG, respectively.

3.3   Time-dependent coupled wave equations

Implementation of mid-IR frequency combs via DFG involves mixing of femtosecond pulses. Nevertheless, above analysis of the CW case provides physics insight on the energy scaling property of DFG process seeded by pulses. The essential difference between the CW DFG and the pulsed DFG is that the field amplitude in the pulsed case now becomes time dependent to describe a pulse envelope. Because the pump/signal/idler pulses are centered at different wavelengths, the material dispersion of the nonlinear crystal also renders them propagating at different group velocities. The resulting group-velocity mismatch (GVM) leads to the temporal walk-off among the three pulses, which in turn decreases the nonlinear interaction strength and leads to a less efficient pump-to-idler conversion. Moreover, the group-velocity dispersion (GVD) effect also needs to be taken into account in the pulsed case because a combination of GVD and GVM may introduce complicated chirp to the idler pulse.

To characterize the temporal evolution of optical pulses during the DFG process, a localized time coordinate τ is introduced to the coupled wave equations (Eq. 3.1). Dispersive terms such as GVM and GVD are added to the equations. Slow-varying-envelop assumption (SVEA) is also used as we do not consider the case when the interacting pulse has sub-cycle or few-cycle pulse duration. The resulting time-dependent coupled wave equations are written as

$$\frac{\partial A_1(z,\tau)}{\partial z} + \left(\frac{1}{v_{g,1}} - \frac{1}{v_{g,3}}\right)\frac{\partial A_1(z,\tau)}{\partial \tau} + \frac{i\beta_{2,1}}{2}\frac{\partial^2 A_1(z,\tau)}{\partial \tau^2} = i\frac{\omega_1 d_{\text{eff}}}{n_1 c}A_3 A_2^* e^{-i\Delta kz},$$

$$\frac{\partial A_2(z,\tau)}{\partial z} + \left(\frac{1}{v_{g,2}} - \frac{1}{v_{g,3}}\right)\frac{\partial A_2(z,\tau)}{\partial \tau} + \frac{i\beta_{2,2}}{2}\frac{\partial^2 A_2(z,\tau)}{\partial \tau^2} = i\frac{\omega_2 d_{\text{eff}}}{n_2 c}A_3 A_1^* e^{-i\Delta kz}, \quad (3.7)$$

$$\frac{\partial A_3(z,\tau)}{\partial z} + \frac{i\beta_{2,3}}{2}\frac{\partial^2 A_3(z,\tau)}{\partial \tau^2} = i\frac{\omega_3 d_{\text{eff}}}{n_3 c}A_1 A_2 e^{+i\Delta kz}.$$

In the equations, the relative time coordinate τ is introduced by setting a time frame that is co-propagating with the pump pulse, $\tau = t - \dfrac{z}{v_{g,3}}$. $v_{g,i} = \partial \omega_i/\partial k_i$ stands for the group velocity of the optical pulse. $\beta_{2,i}$ stands for the GVD coefficient for each pulse. For GaSe crystals, β_2 at 1030 nm is 1037 fs^2/mm. If an unchirped 150 fs Gaussian pulse propagates through a 2-mm-thick GaSe crystal, the pulse duration is broadened to 155 fs at the output. The change on pulse duration is minimal. Thus in the equations we only consider the dispersion effect up to its second order (GVD). If a shorter pulse duration is employed, the change will be more significant and higher order dispersion terms should be added.

In the previous calculation of CW DFG in Section 3.2.2, we choose GaSe to have a thickness of 0.2 mm. In a practical pulsed DFG, the crystal thickness can be set longer. The use of a thicker crystal can increase the parametric interaction between pump and signal, generating more idler. However, such scaling only takes place to a certain extent, because GVM effect between the pump pulse and the signal pulse reduces their temporal overlap. Therefore the effective length for parametric interaction is shorter than the physical length of the crystal. After propagating

certain distance inside the crystal, it is possible that the pump pulse no longer overlaps with the signal pulse, which eliminates the generation of a mid-IR idler. For example, for a type-I DFG process mixing 1030-nm pump and 1150-nm signal, the GVM between pump and signal is 97 fs per mm for a GaSe crystal. In other words, if both inputs are shorter than 100 fs, after propagating 1-mm distance inside the crystal, the parametric interaction is significantly weakened due to an insufficient temporal overlap between pulses.

If the pump pulse and the signal pulse has a Gaussian pulse profile and a FWHM pulse duration of τ_2 (for signal) and τ_3 (for pump), according to Equation 3.7, the growth of the idler pulse is in proportion to the product between the pump electric field and the signal electric field. In other words, $\dfrac{\partial A_1}{\partial z} \propto |A_3| \cdot |A_2| \propto \exp(-\dfrac{2.77}{2} \cdot (\dfrac{\tau^2}{\tau_2^2} + \dfrac{\tau^2}{\tau_3^2}))$. Due to a GVM effect, the pump pulse and the signal pulse travel in different group velocity. After propagating a distance of L inside the crystal, they have a temporal offset of $\dfrac{L}{v_{\mathrm{g},2}} - \dfrac{L}{v_{\mathrm{g},3}}$ and the growth of the idler is reduced accordingly. We thus define a maximum nonlinear crystal thickness $2L_{\mathrm{max}}$ by setting the growth of the idler drops to $1/e^2$ of its maximum.

$$L_{\mathrm{crystal}} = 2 \cdot L_{\mathrm{max}} = 2 \cdot \sqrt{\frac{4 \cdot \tau_2^2 \tau_3^2}{2.77 \cdot (\tau_2^2 + \tau_3^2)}} \cdot \left(\left|\frac{1}{v_{\mathrm{g},2}} - \frac{1}{v_{\mathrm{g},3}}\right|\right)^{-1}. \tag{3.8}$$

If we assume the signal pulse has a FWHM duration of 130 fs, the pump pulse has a FWHM duration of 170 fs, and the GVM between them is 96.5 fs/mm ($v_{\mathrm{g},2} = c/2.912$ and $v_{\mathrm{g},3} = c/2.941$), the maximum nonlinear crystal thickness is 2.5 mm according to Eq. 3.8. It means that for crystal longer than 2.5 mm, the growth of the idler starts to saturate due to the lack of temporal overlap between the pump pulses and the signal pulses.

In the spatial domain, the pump and the signal have orthogonal polarization states due to type-I phase matching scheme. The pump is e-polarized and the signal is o-polarized. Because of the birefringence of the nonlinear crystal, the Poynting vectors (energy flux) of the pump and the signal also travel in different direction. For type-I DFG mixing 1030-nm pump and 1150-nm signal inside GaSe crystals, the input beams have a spatial walk-off of 68 mrad, which is about 3.9°. When the pump beam travels 1-mm distance inside the crystal, it has a spatial walk-off of 68 μm with respect to the signal beam. Such spatial walk-off will also affect the strength of the parametric interaction if the input beams are tightly focused.

3.4 1-μm driven DFG

DFG using GaSe crystal as the hosting medium can be pumped at several wavelengths. In this section, we study HRR DFG process seeded with pump pulses with a center wavelength of 1030 nm. We refer to it as 1-μm driven DFG. We first

give an example of 1-μm driven DFG in Section 3.4.1 to demonstrate the temporal behavior of pulsed DFG. In Section 3.4.2, the energy scaling of 1-μm driven DFG is studied by varying the launching conditions of 1-μm DFG processes. Section 3.4.3 shows the change of the output idler pulse when GaSe crystals with different crystal thickness is employed. Finally, in Section 3.4.4, we summarize the energy scaling property of 1-μm driven DFG.

3.4.1   An example of 1-μm driven DFG

We first calculate type-I DFG process inside a 2-mm-thick GaSe crystal as an example to show the characteristics of DFG process in terms of pulse energy, duration, chirp and spectral bandwidth of the output idler. The input pump is a 170-fs, 100-nJ sech^2 pulse centered at 1030 nm and the input signal is a 130-fs, 1-nJ sech^2 pulse centered at 1150 nm. They generate an output idler pulse centered at 9.87 μm.

In the spatial domain, both the pump beam and the signal beam are focused into a 200-μm radius Gaussian beam inside the crystal. They are fully overlapped in the center of the crystal. We assume the generated idler beam has the same beam size as the inputs. The spatial walk-off effect is introduced to the equations by changing the nonlinear coefficient d_{eff} according to the overlapping area of two beams.

In the time domain, propagation through a 2-mm-long GaSe generates 193-fs pump/signal walk-off. At the input, we place the pump pulse ahead of the signal pulse by 96.5 fs, one half of the total walk-off. Because the signal pulse travels faster than the pump pulse ($v_{g,2} = c/2.912$ versus $v_{g,3} = c/2.941$), the signal pulse passes through the pump pulse and stays 96.5 fs ahead of the pump at the crystal output. In this scenario, the pump-signal temporal overlap is nearly maximized, which guarantees an efficient generation of the idler pulse.

We use the standard split-step Fourier method to solve the time-dependent coupled wave equations (Eq. 3.7). The normalized intensity profiles of the output pulses are plotted in Fig. 3.4(a). The signal pulse at the input (red dashed line) is also plotted for illustrating the temporal walk-off effect. In the figure, the idler pulse is magnified by 5,000 and the signal pulses by 50 for better visibility. The idler pulse travels fastest inside GaSe crystals with a group velocity of $v_{g,1} = c/2.761$. Consequently, the newly generated idler quickly moves out of the pump-signal overlapping region and therefore the idler pulse at the output has a FWHM duration of 800 fs, much longer than the pump/signal pulses.

Figure 3.4(b) plots the growth of the idler pulse energy against the GaSe crystal thickness. At the end of the crystal, the idler has a pulse energy of 21.9 pJ, which corresponds to a quantum efficiency (pump photon to idler photon) of 0.24%. Since the photon conversion efficiency is low, the pump pulse does not have noticeable change in its temporal intensity profile, as shown in Fig. 3.4(a). When the idler pulse travels out of the crystal, Fresnel transmission at the crystal-air interface introduces 31% loss. After the crystal, the idler has a pulse energy of 15.1 pJ, corresponding to an average output power of 0.45 mW for a 30-MHz repetition
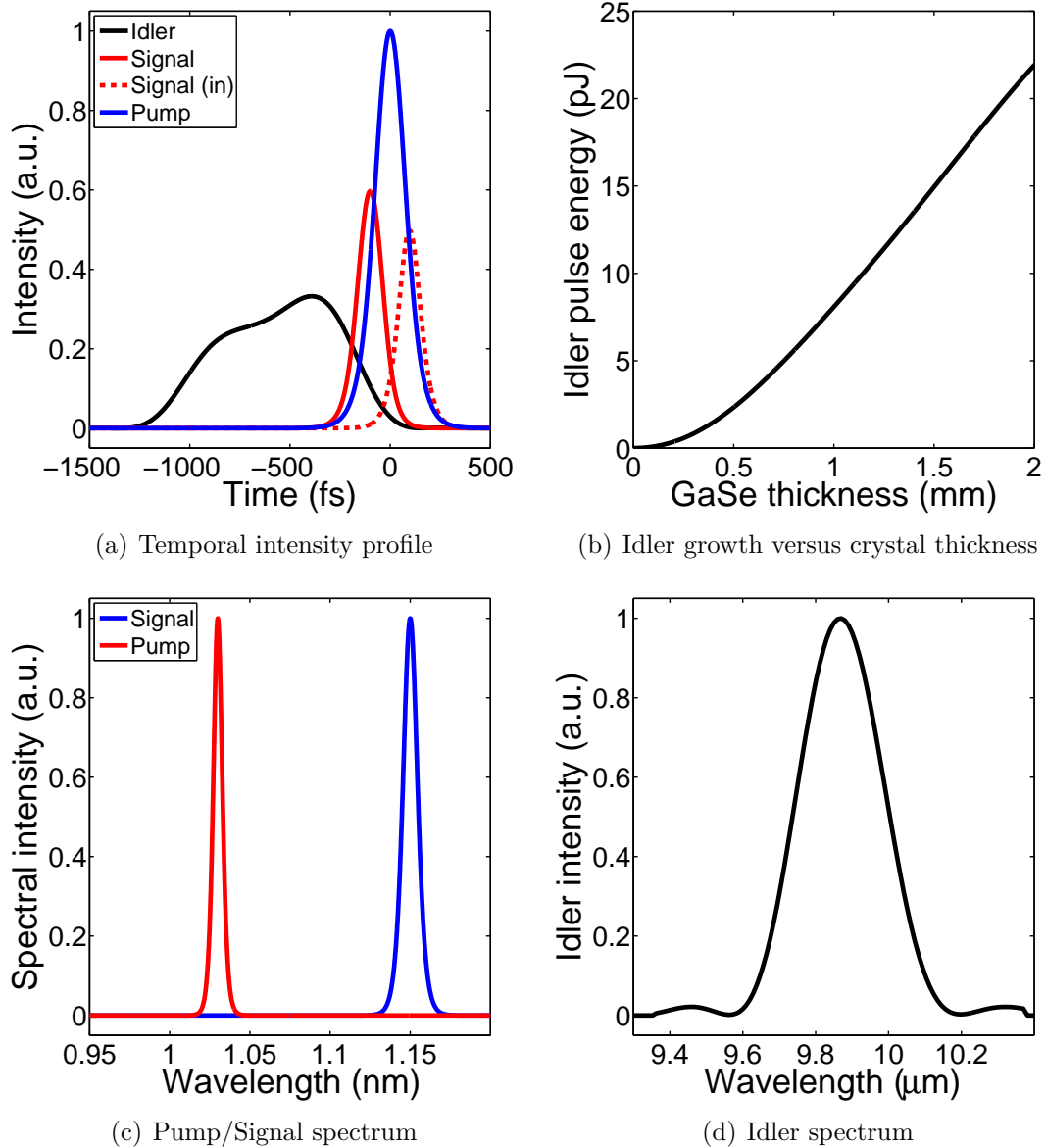
(a) Temporal intensity profile

(b) Idler growth versus crystal thickness

(c) Pump/Signal spectrum

(d) Idler spectrum

Figure 3.4: 1-µm driven DFG inside a 2-mm-thick GaSe crystal.

Type-I DFG process inside a 2-mm-thick GaSe crystal. The DFG process is pumped with a 1030-nm, 170-fs, 100-nJ pulse and seeded with a 1150-nm, 130-fs, 1-nJ signal pulse. (a) Normalized intensity profiles of the output pulses. The input signal is also plotted in a red dashed line in order to demonstrate the temporal walk-off effect. The signal profile is magnified by 50 and the idler is magnified by 5,000. (b) Idler pulse energy versus GaSe thickness. (c) Input pump/signal spectrum. (d) Output idler spectrum.

(a) Idler pulse and its TL form

(b) Compressing GDD

(c) Compressed idler pulse at -43,000 fs^2

(d) Compressed idler pulse at +41,500 fs^2
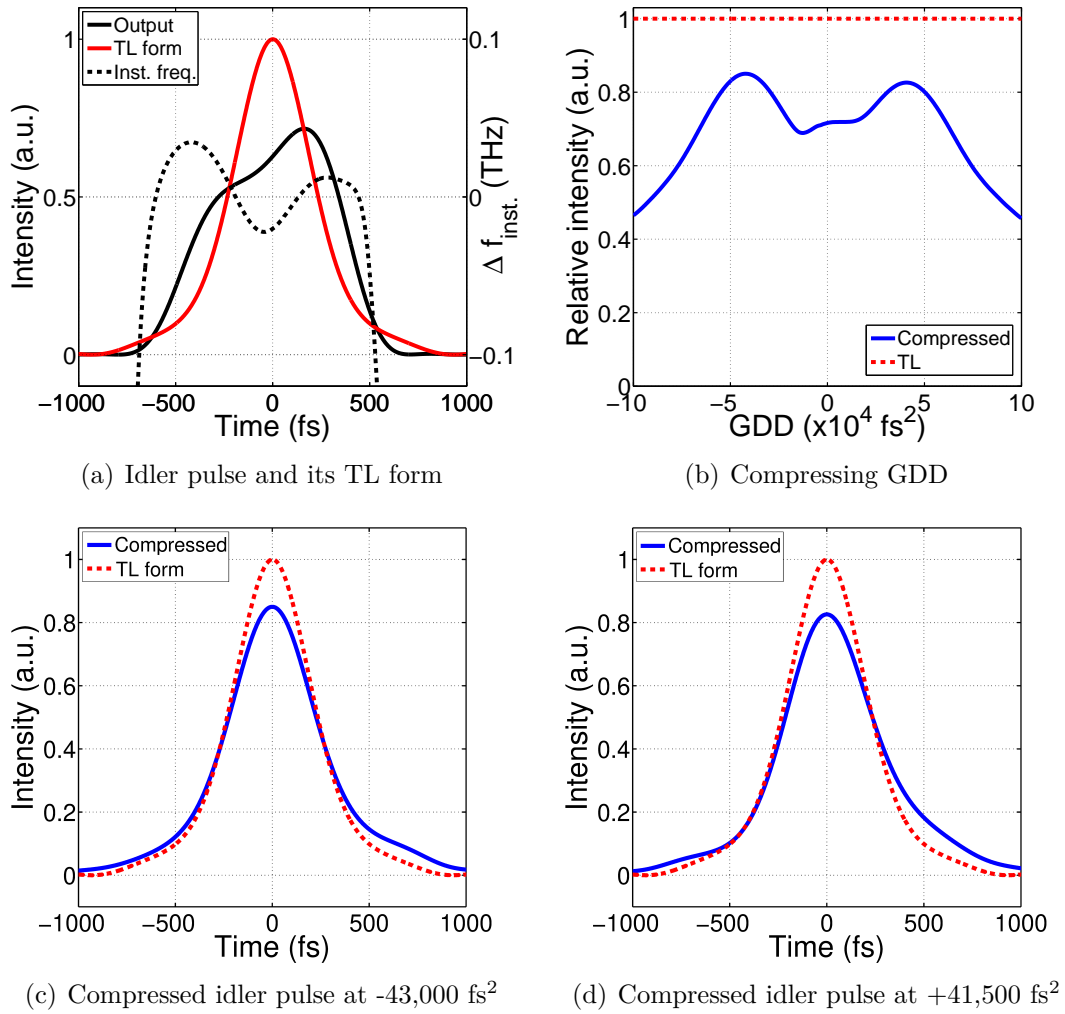
Figure 3.5: Compression of the idler pulse

(a) Intensity profile of the output idler pulse and the TL pulse (to the left axis). The instantaneous frequency is also plotted in a black dashed line (to the right axis). (b) Peak intensity of the compressed idler pulse against dechirping GDD. (c) Compressed idler pulse at -43,000 fs^2 GDD. (d) Compressed idler pulse at +41,500 fs^2 GDD.

rate system.

In the spectral domain, the input pump/signal spectra are plotted in Fig. 3.4(c) and the output idler spectrum is plotted in Fig. 3.4(d). At the output, the idler has a spectral bandwidth of 260 nm, which supports a 420-fs transform-limited (TL) pulse. To show the chirping and compression of the idler pulse, we plot in Figure 3.5(a) the intensity profile of the output idler pulse and the idler pulse in its TL form. The idler pulse has ∼71% peak intensity of its TL form. The instantaneous frequency of the idler pulse is also plotted in a black dashed line (to

the right axis).

The uncompressed idler is negatively chirped in the leading part and positively chirped in the trailing part. Such chirping profile is due to the complex interplay between the GVD and GVM. Since the idler pulse travels the fastest inside the crystal ($v_{g,1} = c/2.761$ versus $v_{g,2} = c/2.912$ and $v_{g,3} = c/2.941$), its leading lobe, generated in the beginning part of the DFG process, encounters significant temporal walk-off with respect to the pump/signal pulse. After the leading lobe walks out of the overlapping part of the pump/signal pulse, it turns negatively chirped due to the material dispersion (negative GVD). On the other hand, the trailing lobe of the idler has less temporal walk-off and it always stays within the envelope of the pump pulse. It also possesses less material dispersion as it is generated in the ending part of the crystal. The temporal phase of the newly generated idler equals to the phase difference between the pump and the signal. Combined together, the trailing part is positively chirped. Overall, the chirp on the output idler pulse is more prone to the GVM effect as GVM force the idler pulse traveling out of the pump/signal pulse. If a thin layer of nonlinear crystal is used for hosting DFG process, the output idler will be close to its TL form.

The output idler pulse can be compressed by adding either positive group delay dispersion (GDD) or negative GDD. We screen the dechirping GDD from -10^5 fs^2 to $+10^5$ fs^2 and calculate the corresponding peak intensity of the compressed pulse. The results are shown in Fig. 3.5(b). Adding a GDD of -43,000 fs^2 or +41,500 fs^2 can effectively dechirp the output idler pulse. At -43,000 fs^2, the compressed pulse reaches 85% peak intensity of the TL pulse and has a FWHM pulse duration of 521 fs (420 fs for TL pulse). At +41,500 fs^2, the compressed pulse reaches 82% peak intensity of the TL pulse and has a FWHM pulse duration of 537 fs. The intensity profile of the compressed idler pulse, together with the TL pulse, is plotted in Fig. 3.5(c) and 3.5(d).

3.4.2 Energy scaling of 1-µm driven DFG

To investigate the energy scaling property of 1-µm driven DFG, we alter the launching conditions of the DFG process and calculate the resulting pulse energy of the output idler. Previous study on CW DFG has shown three operating regimes for DFG process: the linear regime, OPA regime and the saturation regime. Increasing the pump over a threshold can lead to OPA-like exponential scaling of the idler. When the pump is below the threshold, the idler scales linearly. Written in Eq. 3.6, the threshold pump intensity has an L^{-2} dependence on the parametric interaction length L. In the case of pulsed DFG, several factors such as GVD, GVM, spatial walk-off, pulse shape and beam shape reduce the effective length of the parametric interaction, making DFG less efficient. The threshold pump pulse energy needs to be found by numerical calculations.

We first calculate DFG processes with the signal energy fixed at 0.1 nJ, 1 nJ and 10 nJ. For each signal energy the pump energy increases from 0.1 nJ to 4 µJ. Other technical parameters remain unchanged. Figure 3.6(a) shows the pulse energy of the output idler as a function of input pump pulse energy. As we expect

(a) DFG process with signal fixed   (b) DFG process with pump fixed
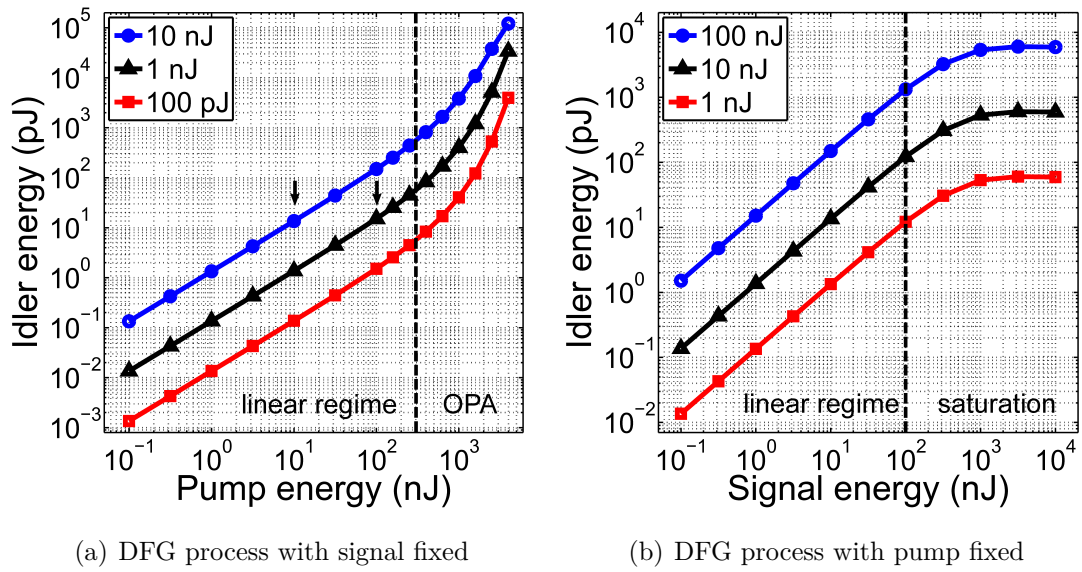
Figure 3.6: Idler energy scaling of 1-μm driven DFG.

Type-I DFG process inside a 2-mm-thick GaSe crystal is examined under different launching conditions. (a) The signal energy is fixed at 0.1 nJ, 1 nJ and 10 nJ. The pump increases from 0.1 nJ to 4 μJ. (b) The pump energy is fixed at 1 nJ, 10 nJ and 100 nJ. The signal increases from 0.1 nJ to 10 μJ.

from the CW case, DFG in the pulsed case can operate in the linear regime or the OPA regime as well. For the pump energy below 300 nJ, DFG process operates in the linear regime. The idler scales linearly with respect to the input pump energy even as the input signal energy varies from 0.1 nJ to 10 nJ. When the pump exceeds 300 nJ, the DFG process transits into the OPA regime in which the output idler grows exponentially as a function of the input pump energy. The threshold pump pulse energy in this case is 300 nJ.

At low repetition rates ($\leq$0.1 MHz), input pump pulses with μJ–mJ pulse energy are allowed [72] for seeding the DFG process, making DFG operated in the OPA regime. For HRR (e.g., $\geq$10 MHz) DFG systems, crystal damage limits the allowed input pulse energy at the hundreds of nJ level, making DFG operate in the linear regime. It is noteworthy that when plotting the simulation results for the pulsed case, we use the pulse energy rather than the optical intensity to better quantify the three pulses. We can also translate pulse energy into corresponding peak intensity to compare with the CW case. For example, the pump threshold of 300 nJ with 200-μm beam waist and 170-fs pulse duration corresponds to a peak intensity of 1.4 GW/cm^2. For the CW case to have a pump threshold intensity at 1.4 GW/cm^2, the required GaSe thickness needs to be 0.46 mm according to Eq. 3.6, which is much shorter than 2 mm—the actual GaSe thickness used for the pulsed case. This is apparently anticipated because the GVM-caused walk-
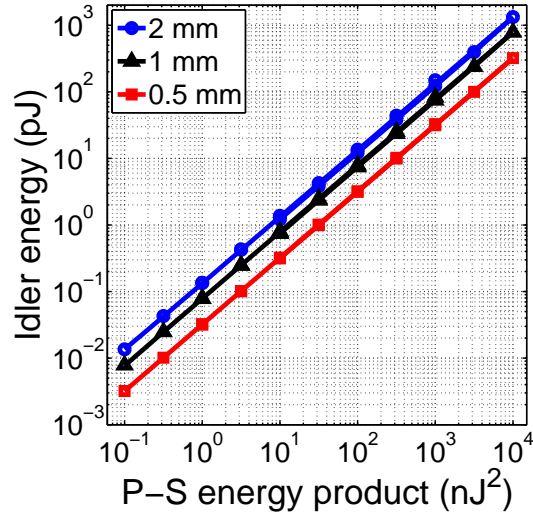
Figure 3.7: Idler versus pump-signal energy product for 1-µm driven DFG.

Idler pulse energy scales linearly with respect to the pump-signal pulse energy product. DFG process with GaSe crystal thickness at 0.5 mm (red square), 1 mm (black triangle) and 2 mm (blue circle) is examined.

off weakens the interaction between the pulses, leading to an effective interaction length shorter than the actual thickness of the crystal.

The three curves in Fig. 3.6(a) also suggest that different combinations of pump-signal energy can generate idler with the same pulse energy. For example, DFG between 10-nJ pump and 10-nJ signal results in 15-pJ idler pulses (the arrow-marked blue circle); the same idler pulse energy can also be achieved using 100-nJ pump and 1-nJ signal (the arrow-marked black triangle). Given that a higher pulse energy may damage the crystal, the former scheme (i.e., 10-nJ pump and 10-nJ signal) is preferred. Furthermore, this scheme has an improved efficiency of converting near-IR photons to mid-IR photons (0.25% versus 0.025% in pump-to-idler quantum efficiency).

To show how the idler pulse energy scales with the signal pulse energy, we calculate the DFG processes with the pump energy fixed at 1 nJ, 10 nJ and 100 nJ and the signal energy increased from 0.1 nJ to 10 µJ. As the results in Fig. 3.6(b) show, the idler pulse energy grows linearly until the input signal reaches about 100 nJ, and then the idler growth starts to saturate. Different from the curves in the CW DFG case (Fig. 3.3(b)) where the idler drops after reaching the maximum, the large temporal walk-off of the idler pulse from the pump/signal pulses prevents the back conversion process such that the idler pulse energy eventually saturates to a constant value.

The results in Fig. 3.6(a) and 3.6(b) indicate that the idler pulse energy scales linearly with the pulse-energy product between the pump pulse and the signal pulse when the DFG process operates in the linear regime. Therefore, increasing

GaSe (mm)	k	b
0.5	0.03206	-0.00001
1	0.0786	-0.0003
2	0.1327	0.0030

Table 3.1: Linear scaling of the idler in 1-μm driven DFG.
$$y = k \cdot x + b.$$
y: idler pulse energy in [pJ], x: pump-signal pulse energy product in [nJ·nJ].

Linear regression coefficients for 1-μm driven DFG process that operates in the linear regime. This table can be served as a look-up-table for estimating the pulse energy of the output idler.

---

the pump energy or the signal energy leads to the same scaling of the idler energy.

Figure 3.7 shows the linear relationship between the idler pulse energy with the product of pump/signal pulse energy at three GaSe thicknesses: 0.5 mm, 1 mm and 2 mm. In the simulation, we keep both the pump/signal pulse energy below 100 nJ to ensure that DFG operates in the linear regime. Due to the GVM-caused walk-off effect, increasing the GaSe thickness is inefficient for energy scaling the idler. The results in Fig. 3.7 show that increasing the crystal thickness form 0.5 mm to 1 mm improves the idler energy by a factor of 2.4; however, further increasing the thickness from 1 mm to 2 mm only results in 1.7 times improvement. Nevertheless DFG between 100-nJ pump and 100-nJ signal in a 2-mm-thick GaSe generates idler pulse of 1.33-nJ energy, corresponding to 40-mW average power for a 30-MHz laser system. At 30-MHz repetition rate, the pulse energy at the input is still below the crystal damage threshold according to our previous experimental results [36].

We apply linear regression for the data shown in Fig. 3.7. Table 3.1 summarizes the regression coefficients for DFG process that operates in the linear regime. The linear relationship can be applied as long as both the pump and signal pulse energy is under 100 nJ, which covers a wide range of experimental parameters. The table provides a rough estimation for output idler pulse energy.

3.4.3   1-μm driven DFG at different GaSe thickness

Figure 3.7 shows that increasing the GaSe crystal thickness can scale up the pulse energy of the idler. It is not shown that the use of a thicker GaSe crystal changes the characteristic of the output idler, such as pulse duration, spectral bandwidth, and chirp. Here we study 1-μm driven DFG with a GaSe thickness varying from 0.5 mm to 4 mm. The inputs are 100-nJ pump and 100-nJ signal. Other parameters remain the same as previous, except for the initial time delay between the pump pulse and the signal pulse. To compensate different amount of temporal walk-off from GaSe crystals with different crystal thickness, the initial time delay is set individually in each case so that the generated idler has the maximum pulse

(a) Intensity profile of the output idler

(b) Pulse energy and quantum efficiency
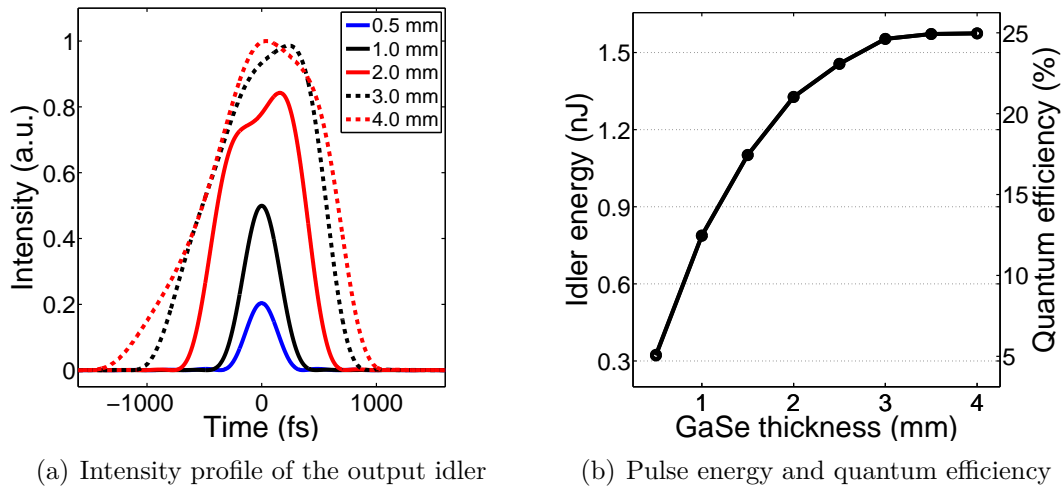
Figure 3.8: Idler profile and pulse energy of 1-μm driven DFG at different GaSe thickness.

1-μm driven DFG is studied with GaSe thickness varying from 0.5 mm to 4 mm. Both inputs have 100-nJ pulse energy. (a) Normalized intensity profile of the idler pulse. (b) Pulse energy of the idler and the quantum efficiency for pump-to-idler photon conversion.

energy.

We simulate each DFG process and plot in Figure 3.8(a) the normalized intensity profile of the output idler pulse with the crystal thickness at 0.5 mm, 1 mm, 2 mm, 3 mm, and 4 mm, respectively. The use of thicker crystal results in an idler with longer pulse duration, which is mainly caused by the excessive amount of GVM between the idler pulse and the pump/signal pulse. GVM between idler (9.87 μm) and pump (1030 nm) is about 600 fs per mm. The idler generated in the early stage of the process accumulates larger relative temporal shift with respect to the idler generated in the latter stage. At the output, the generated idler thus has longer pulse duration compared with the input pump/signal pulse.

The use of thicker nonlinear crystal can generate an idler with more pulse energy. Figure 3.8(b) plots the pulse energy of the output idler versus GaSe crystal thickness (to the left axis). Here we already consider the Fresnel loss on the back facet of the crystal. The growth of the idler saturates when the GaSe crystal is thicker than 3 mm. As indicated in Eq. 3.8, the maximum nonlinear crystal thickness is estimated to be 2.5 mm, which agrees well with the curve shown in the figure.

Using a 3-mm-thick GaSe, idler with 1.55-nJ pulse energy can be generated. The saturation of the idler growth is due to the GVM between the pump pulse and the signal pulse. In the same figure, the corresponding pump-to-idler quantum efficiency is also plotted (to the right axis). The quantum efficiency reaches ∼25%

(a) Spectral bandwidth and pulse duration
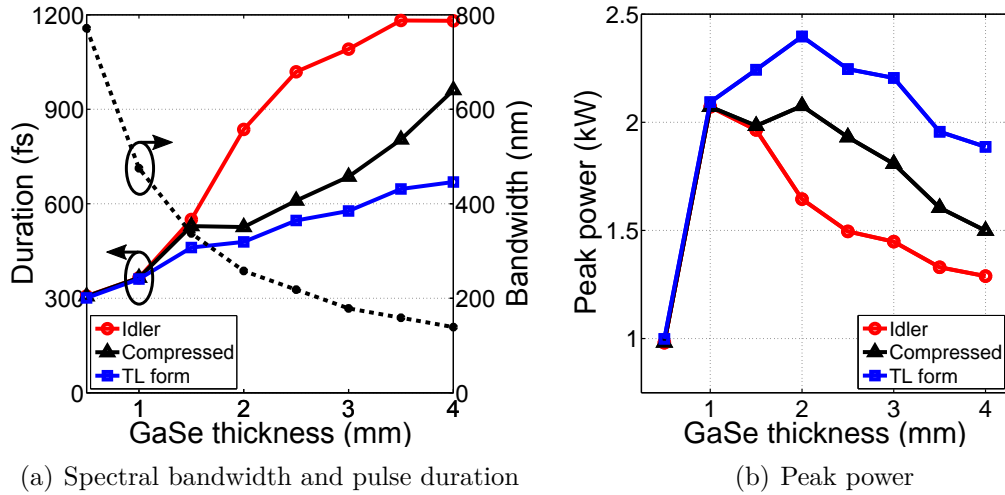
(b) Peak power

Figure 3.9: Idler bandwidth, pulse duration and peak power of 1-μm driven DFG at different GaSe thickness.

1-μm driven DFG is studied with GaSe thickness varying from 0.5 mm to 4 mm. (a) Spectral bandwidth of the output idler (to the right axis) and pulse duration of the output idler pulse, the compressed idler pulse, and TL idler pulse (to the left axis). (b) Peak power of the output idler pulse, the compressed idler pulse, and TL idler pulse.

when the GaSe crystal is 3-mm-thick. Large GVM between pump and signal in 1-μm driven DFG leads to an ineffective parametric interaction for generating the idler. The maximum quantum efficiency for 1-μm driven DFG is 25%, given 1030-nm, 170-fs pump pulse and 1150-nm, 130-fs signal pulse. In terms of an energy conversion efficiency, a total input pulse energy of 200-nJ generates a ∼1.5-nJ idler, which corresponds to an energy conversion efficiency of merely 0.75%.

Other than idler pulse energy, crystal thickness also affects the spectral bandwidth of the idler due to the phase matching condition for broadband inputs. Figure 3.9(a) plots the spectral bandwidth of the idler versus crystal thickness (to the right axis). The idler bandwidth decreases from 770 nm to 140 nm as the GaSe thickness increases from 0.5 mm to 4 mm. The reduced spectral bandwidth translates to a TL pulse with longer pulse duration. We plot in the same figure the FWHM pulse duration of the output idler pulse (circle), the compressed pulse (triangle) and the TL idler pulse (square). The uncompressed idler pulse has a duration varying from 300 fs to 1180 fs. For a thin GaSe crystal (≤1.5 mm), the idler pulse is nearly transform-limited; for a thicker GaSe crystal, the temporal walk-off renders a complicated chirp to the idler pulse and degrades the quality of the compressed pulses. By adding a quadratic spectral phase, the idler can be partially compressed. The compressed idler has ∼70% peak power of its TL pulse.

For certain nonlinear applications in the mid-IR wavelength range (e.g., su-

(a) 2.5-mm-thick GaSe

(b) 3.0-mm-thick GaSe
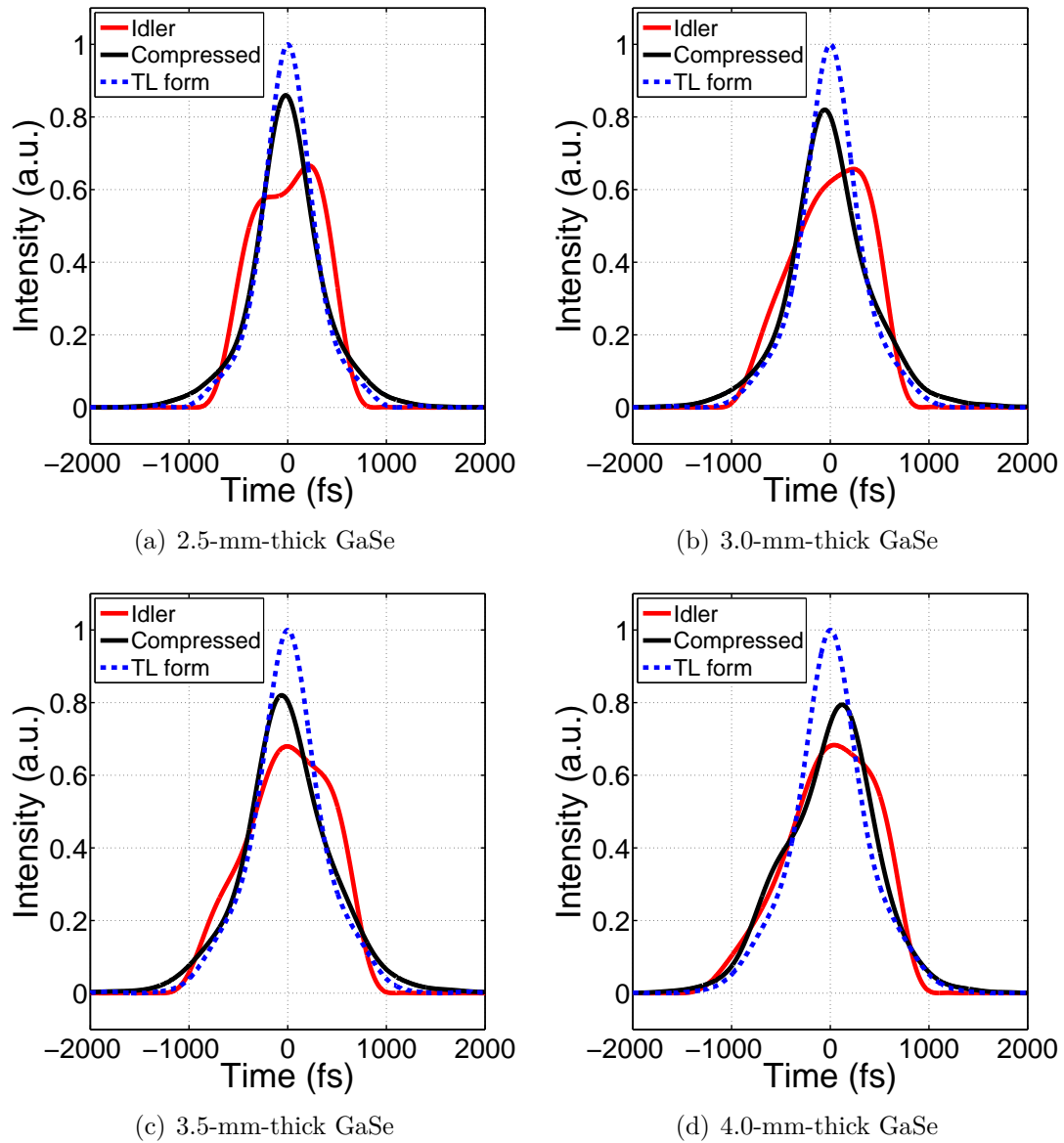
(c) 3.5-mm-thick GaSe

(d) 4.0-mm-thick GaSe

Figure 3.10: Normalized intensity profiles of the idler at different GaSe thickness.

1-µm driven DFG is studied with the GaSe thickness varying from 0.5 mm to 4 mm. The normalized intensity profiles of the uncompressed output idler pulse (red line), the compressed idler pulse (red line), and TL-form idler pulse (blue dashed line) are plotted.

percontinuum generation and high harmonic generation), pulse peak power is of particular importance. Figure 3.9(b) shows the peak power as a function of GaSe thickness for the output idler pulse (circle), the compressed pulse (triangle), and the TL pulse (square). The intensity profiles of the output, compressed, and TL idler pulses for GaSe thickness being at 2.5 mm, 3.0 mm, 3.5 mm, and 4.0 mm are plotted in Fig. 3.10.

Figure 3.9(b) shows the peak power of the idler starts to decrease when the GaSe crystal is thicker than 2 mm. The use of a thicker GaSe crystal renders a narrower idler spectral bandwidth, a larger temporal walk-off and a lower peak power for the generated idler. If higher peak power rather than higher pulse energy is preferred by the applications, the results in Fig. 3.9(b) suggests that a GaSe crystal of 1 mm thick is best suited; the resulting idler pulse requires no post compression and has a peak power of 2.1 kW.

3.4.4 Summary of 1-μm driven DFG

Above analysis has shown the energy scaling capability of 1-μm driven DFG process. The characteristics of the generated mid-IR idler pulses are also discussed in terms of spectral bandwidth, pulse duration, pulse compression and peak power. The results indicates several drawbacks of 1-μm driven DFG inside GaSe crystals:

- For HRR DFG, the total input pulse energy to be launched into GaSe crystals is limited to hundreds of nano-joule level, which is mainly caused by multiple photon absorption (MPA) effect and poor thermal conductivity of GaSe crystals. When the pump/signal pulses are centered at 1.03/1.15 μm, at a repetition rate of 30 MHz, their total pulse energy is capped under 200 nJ to prevent catastrophic crystal damage. Such limitation directly leads to a limited pulse energy of the idler pulses at nano-joule level (1.5 nJ as shown in Fig. 3.8(b). It also eliminates the possibility of OPA regime operation for the DFG process, which requires an input pump pulse with more than 300-nJ pulse energy.

- GVM between the pump pulses and the signal pulses results an inefficient generation of the mid-IR idler. GVM between pump and signal is 96.5 fs per mm for type-I DFG process inside GaSe crystals. When the pulses are propagating inside the crystal, GVM between pump and signal significantly reduces their overall temporal overlap. Shown in Fig. 3.8(b), the growth of the output idler saturates when the GaSe thickness exceeds 3 mm. Further increasing the crystal thickness is inefficient for scaling the idler. A maximum pump-to-idler quantum efficiency of 25% is achieved when 4-mm-thick GaSe crystal is used to host the DFG process.

- GVM between idler pulses and pump/signal pulses broadens the idler pulse during the DFG process. When the GaSe crystal is more than 2-mm-thick, the generated idler pulse has a temporal chirp that cannot be fully compensated. After adding a proper GDD, the compressed idler pulse can reach ∼80% peak intensity of its TL pulse. The compressed idler pulse can have a peak power of 2-kW.

To overcome all these drawbacks, one strategy is to shift the center wavelength of the pump/signal pulses to longer wavelengths, where GaSe crystals can exhibit less MPA so that more pulse energy can be launched to the crystal. For example, if 2.0-µm pump pulses and 2.5-µm signal pulses are mixed inside GaSe crystals to generate idler pulses centered at 9.87-µm, two-photon absorption and even three-photon absorption can be mitigated. Shifting the pump/signal wavelengths also changes the phase matching condition, which may increase the spectral bandwidth of the output idler. At 2-µm range, the pump/signal wavelength is closer to the mid-IR wavelength. Therefore, pump/signal pulses are propagating at a group velocity that is closer to the group velocity of the mid-IR idler pulse. Therefore, GVM of 2-µm driven DFD is lower compared with 1-µm driven DFG, making it possible for further scaling the idler. In the next section of this chapter, we study DFG processes with the input pump pulses centered at 2 µm.

3.5   2-µm driven DFG

In this section, we study DFG process that generates mid-IR idler pulses with the pump pulses centered at 2 µm. We firstly compare several important parameters for 1-µm and 2-µm driven DFG such as group velocity mismatching coefficients, phase matching angle, phase matching bandwidth and Fresnel transmittance in Section 3.5.1. Then two examples of 2-µm driven DFG are given in Section 3.5.2 to demonstrate the superiority of 2-µm driven DFG in boosting the parametric interaction strength. Section 3.5.3 shows the energy scaling capability of 2-µm driven DFG. The possibility of OPA regime operation for 2-µm driven DFG is shown. In Section 3.5.4, the influence of GaSe thickness on the output idler is studied. Finally, we conclude in Section 3.5.5.

3.5.1   Comparison between 1-µm and 2-µm driven DFG

Previous studies on the energy scaling capability of 1-µm DFG have shown that GVM plays a crucial role in determining how effectively three waves in DFG process can exchange energy. A straightforward speculation is that smaller pump-signal GVM allows the use of a thicker GaSe crystal and may significantly increase the yield of mid-IR pulses. Smaller pump-idler GVM also facilitates the generation of few-cycle, ultrashort idler pulses with high peak power at the output. To compare 2-µm driven DFG with 1-µm driven DFG, we calculate the corresponding GVM coefficients of the DFG processes where the input pump is centered at 1.03 µm, 2 µm and the output idler is chosen to have a center wavelength from 5 µm to 15 µm.

The GVM coefficients are plotted in Fig. 3.11. For 1-µm driven DFG, to generate an idler center at 10 µm, pump pulses and signal pulses (blue line in Fig. 3.11(a)) have a GVM of about 100 fs/mm. If the input pump/signal pulse has a pulse duration of 170/130 fs, the maximum crystal thickness is 3 mm by a rough estimation. This agrees with the results shown in previous secitons (Fig. 3.8(b)).
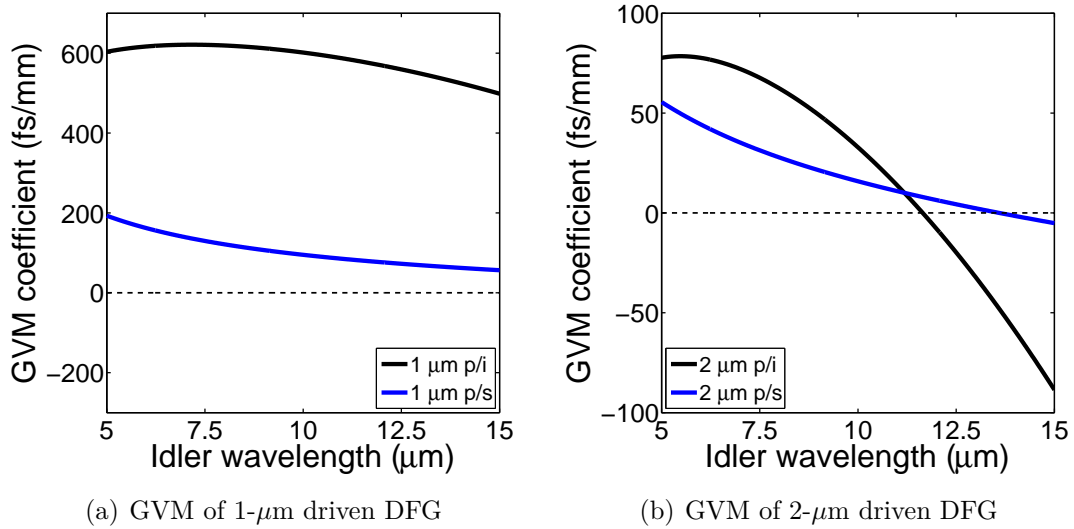
(a) GVM of 1-μm driven DFG   (b) GVM of 2-μm driven DFG

Figure 3.11: GVM coefficients of 1-μm and 2-μm driven DFG.

1-μm driven DFG and 2-μm driven DFG are compared in terms of group velocity mismatch coefficients. DFG process with the pump centered at 1.03/2 μm is set to generate an idler with a center wavelength from 5 to 15 μm. (a) GVM coefficients for 1-μm driven DFG. (b) GVM coefficients for 2-μm driven DFG.

For 2-μm driven DFG, GVM between the pump pulses and signal pulses is about 20 fs/mm for generating 10-μm idler pulses, which is 5 times less compared with the case of 1-μm pump. Therefore, GaSe crystal with $\sim$5 times more thickness can be used to host the DFG process. Using GaSe crystal with the same thickness, 2-μm driven DFG has the advantage of generating more idler due to a reduced GVM and an increased temporal overlap between pump pulses and signal pulses.

Meanwhile, GVM between pump pulses and idlers pulses is also significantly smaller for 2-μm driven DFG (32 fs/mm versus 600 fs/mm for genearting 10-μm idler). A reduced pump-idler GVM enables the generation of few-cycle idler pulses with high peak power at the output.

If we recall the formula that defines the pump threshold intensity (Eq. 3.6),

$$I_{\text{th}} = \frac{n_1 n_2 n_3 \varepsilon_0 c^3}{2\omega_1 \omega_2 d_{\text{eff}}^2} \cdot (\frac{1}{L})^2.$$

Assume the generated idler has the same center wavelength (ω_1 is unchanged), the pump threshold intensity for 2-μm DFG increases by roughly a factor of 2 due to a lower value of signal center frequency ω_2. Meanwhile, the reduced GVM allows the use of a thicker GaSe crystal, which scales the nonlinear interaction length L by a factor of 5. If the nonlinear crystal has the same thickness, a reduced GVM also results in a longer effective nonlinear interaction length. Since the threshold pump intensity has a L^{-2} dependence, the pump threshold intensity for 2-μm DFG may be reduced by one order of magnitude. Translated into pulse energy, the pump

(a) Phase matching angle   (b) Spatial walk-off angle
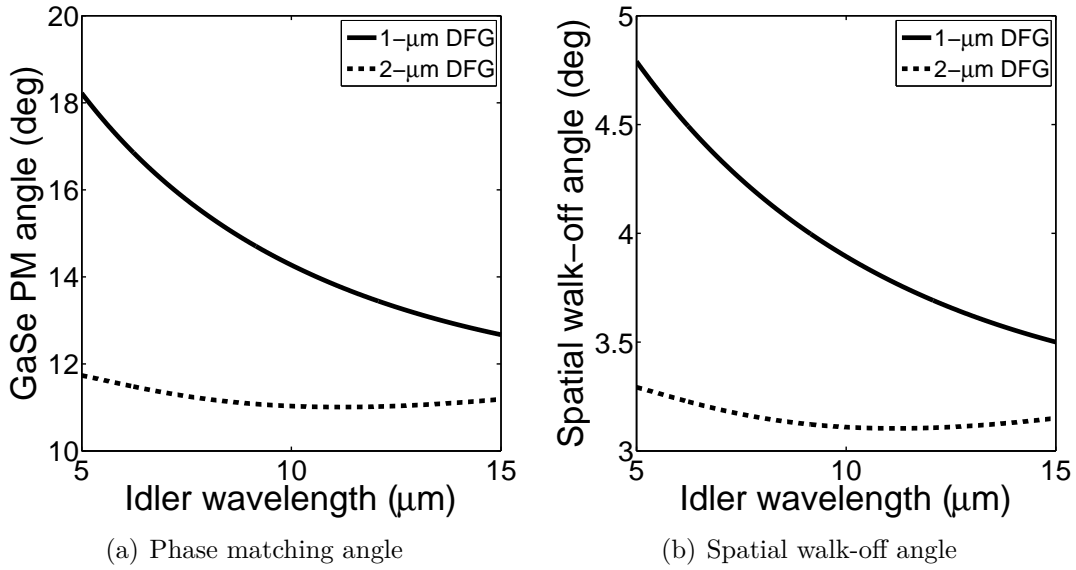
Figure 3.12: Phase matching and spatial walk-off of 1-µm and 2-µm driven DFG.

1-µm driven DFG and 2-µm driven DFG are compared in terms of (a) Phase matching angle and (b) Spatial walk-off angle.

threshold pulse-energy can be down to 100-nJ or even sub-100-nJ level, assuming other parameters such as beam size, pulse shape and pulse duration are the same.

Besides GVM, shifting the pump wavelength from 1.03 µm to 2 µm also changes the phase matching condition of the DFG process. Figure 3.12(a) plots the phase matching angle of GaSe crystals for type-I DFG process with the pump centered at 1.03 µm and 2 µm respectively. When the idler wavelength changes from 5 to 15 µm, the corresponding phase matching angle varies ∼5 degrees for the 1-µm driven DFG (solid line in Fig. 3.12(a)); for 2-µm driven DFG (dashed line in Fig. 3.12(a)), it changes less than 1 degree. Phase matching with less dispersion renders a DFG process that is able to generate a broadband idler, which enables the generation of extremely short pulses in mid-IR [73].

The change of phase matching angle also alters the spatial walk-off of the input beams. GaSe is an extremely soft crystal (0 on its Mohs hardness scale). Its crystalline structure forbids any cutting angle except for being cut perpendicularly with respect to the optical axis [17]. Therefore, phase matching angle determines the incident angle of the input beams. Since the pump beam is e-polarized and the signal beam is o-polarized, the input beams accumulate spatial walk-off as they propagate inside the crystal. We plot in Fig. 3.12(b) the spatial walk-off angle between the pump beam and the signal beam for type-I DFG process inside the GaSe crystal. It shows 2-µm DFG has less spatial walk-off compared with 1-µm DFG. For example, for generating an idler at 10 µm, 2-µm DFG has a spatial walk-off angle of 3.1 degree while 1-µm DFG has 3.9 degree. A spatial walk-off angle

67

(a) PM bandwidth of 1-μm DFG   (b) PM bandwidth of 2-μm DFG
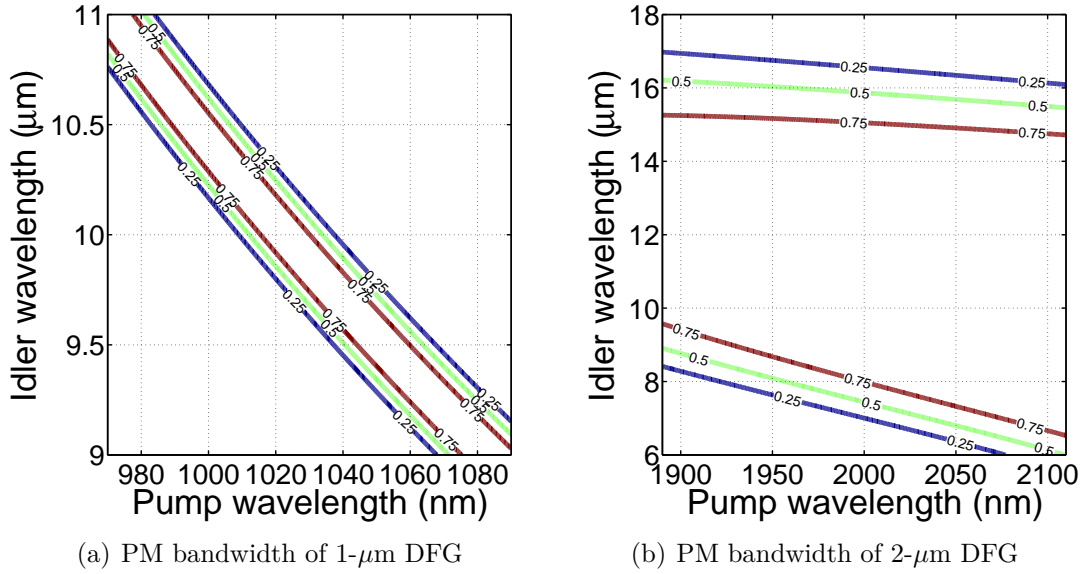
Figure 3.13: Phase matching bandwidth of 1-μm and 2-μm driven DFG.

1-μm driven DFG and 2-μm driven DFG are compared in terms of phase matching bandwidth. The contour of $|\text{sinc}(\Delta k \cdot L)|$ is plotted to illustrate the phase matching conditions. The GaSe crystal is 1-mm-thick. (a) Phase matching bandwidth of 1-μm DFG. (b) Phase matching bandwidth of 2-μm DFG.

---

of 3.1 degree equals to 54 mrad. When the pump and signal propagate 1-mm-long distance inside the crystal, they have a transverse walk-off of 54 μm. If both beams have a loosely focused beam size (e.g., more than 200 μm), the spatial walk-off does not have significant impact on the strength of the parametric interaction. A reduced spatial walk-off thus allows the experimental scheme of tight focusing, which can effectively boost the intensity of the input beams so that more idler can be generated.

Setting the crystal angle at the phase matching angle, we can calculate the phase matching bandwidth of the DFG process. Parameter $|\text{sinc}(\Delta k \cdot L)|$ can be used to characterize the phase matching bandwidth of the DFG process [60]. We plot in Figure 3.13 the contour of $|\text{sinc}(\Delta k \cdot L)|$ versus pump/idler wavelength. In this plot, the GaSe crystal is chosen to have a thickness of 1 mm. The figure shows that 2-μm DFG has broader phase matching bandwidth compared with 1-μm DFG. When the pump wavelength is fixed at 2 μm, the contour plot shows the idler can have a FWHM phase matching bandwidth spanning from 8 μm up to 16 μm. For 1-μm DFG, the idler has a phase matching bandwidth of less than 500 nm.

Finally we compare the Fresnel reflection loss at the surfaces of GaSe crystal. Since GaSe crystals cannot be coated with any anti-reflection (AR) coating, Fresnel reflection causes a large portion of energy loss for the inputs. At the back facet

(a) Fresnel transmission of 1-µm DFG
(b) Fresnel transmission of 2-µm DFG
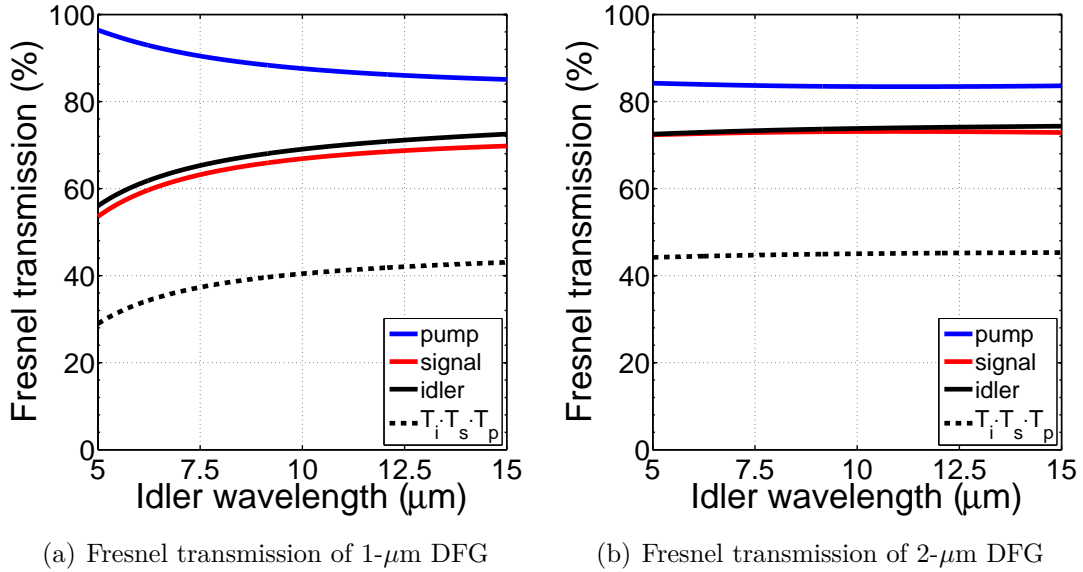
Figure 3.14: Fresnel transmission of 1-µm and 2-µm driven DFG.

1-µm driven DFG and 2-µm driven DFG are compared in terms of Fresnel transmission. For pump and signal, Fresnel transmission occurs at the front facet of the crystal. For idler, it occurs at the back facet. (a) Fresnel transmission of 1-µm DFG. (b) Fresnel transmission of 2-µm DFG.

of GaSe crystal, Fresnel reflection also attenuates the pulse energy of the output idler. We calculate the Fresnel transmission (in terms of power transmittance) for all three waves involved in the DFG process. For the pump wave and the signal wave, Fresnel transmission occurs at the front facet of the crystal. While for the idler wave, Fresnel transmission occurs at the back facet. The results are shown in Fig. 3.14. The product of all three Fresnel transmittances is plotted in a black dashed line. For generating an idler at 10 µm, 2-µm DFG has about 10% less overall energy loss compared with 1-µm DFG.

3.5.2 Two examples of 2-µm driven DFG

Above comparison has shown the potential of 2-µm driven DFG in scaling the pulse energy of the output idler. To study 2-µm DFG, we first give two examples of 2-µm driven DFG inside a 2-mm-thick GaSe. To generate an idler centered at 9.87 µm, the signal is set to be centered at 2.51-µm. In the first example, the pump is 100 nJ and the signal is 1 nJ. In the second one, the pump is 100 nJ and the signal is 100 nJ. Other technical parameters such as pulse duration, pulse shape and beam size remain unchanged. The initial temporal delay between the pump pulses and the signal pulses is adjusted to accommodate the GVM-caused temporal walk-off, so that DFG process is optimized to generate the most pulse energy in the idler.
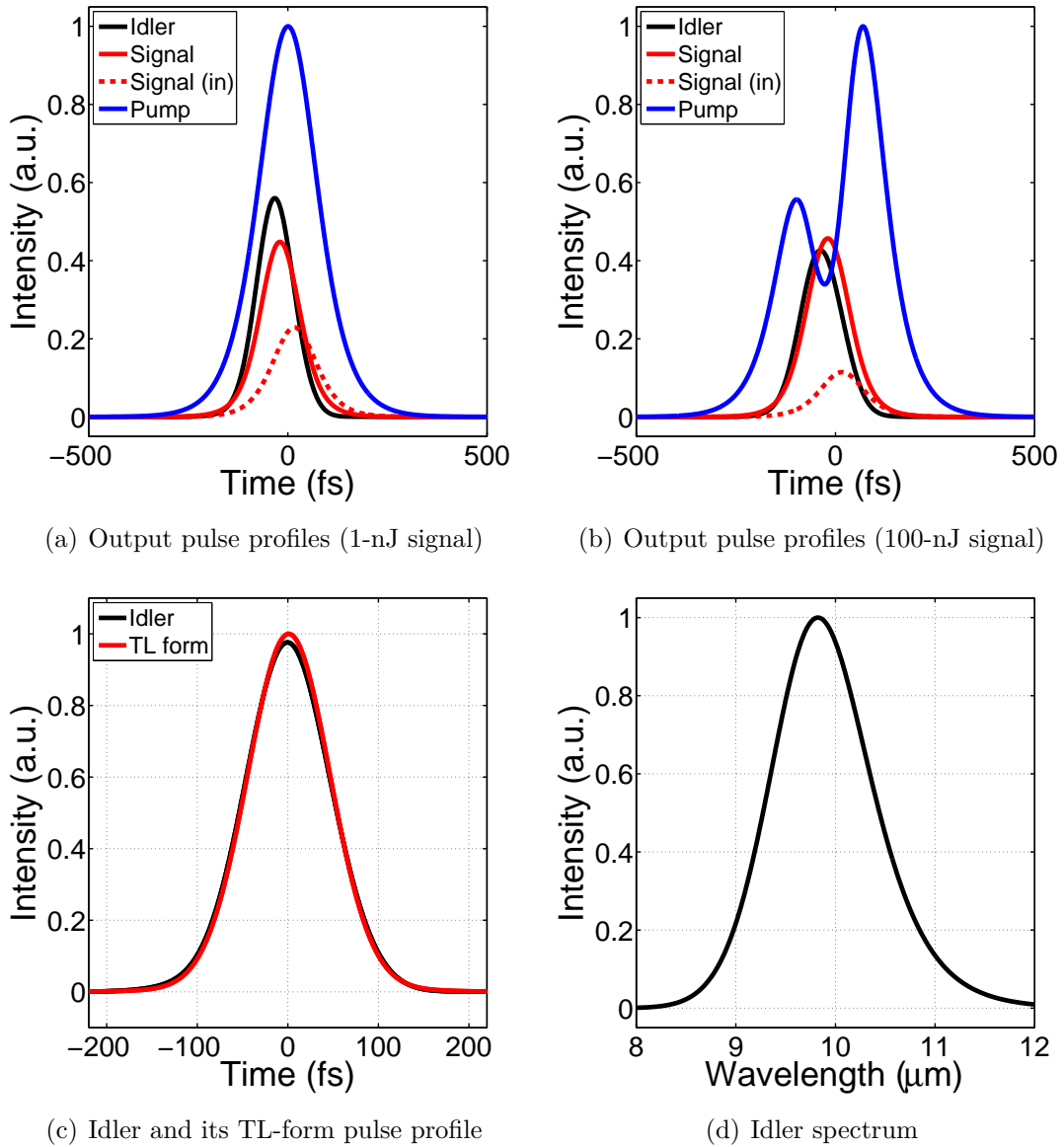
(a) Output pulse profiles (1-nJ signal)

(b) Output pulse profiles (100-nJ signal)

(c) Idler and its TL-form pulse profile

(d) Idler spectrum

Figure 3.15: 2-μm driven DFG inside a 2-mm-thick GaSe crystal.

Type-I DFG process inside a 2-mm-thick GaSe. DFG process is seeded with a 2-μm, 170-fs, 100-nJ pump and a 2.51-μm, 130-fs signal. In (a), signal is 1 nJ and in (b) signal is 100-nJ. (a) Normalized intensity profile of the output pulses. The signal profile is magnified by 20 and the idler is magnified by 200. (b) Normalized intensity profile. The signal is de-magnified by 10 and the idler is plotted as it is. (c) The output idler pulse and its TL-form. (d) Idler spectrum.

By solving the time-dependent coupled wave equations, the normalized intensity profiles of the output pulses are calculated and the results are plotted in Fig. 3.15(a) and 3.15(b). The signal pulse at the input is also plotted in red dashed lines to illustrate the temporal walk-off effect. In Fig. 3.15(a), the signal is magnified by 20 and the idler is magnified by 200. In Fig. 3.15(b), the signal is de-magnified by 20 and the idler is plotted as it is.

For 1-nJ signal, DFG process generates 0.1-nJ pulse energy at the output idler. The output pump pulse does not have noticeable change in its intensity profile. For 100-nJ signal, the idler has 6.9-nJ pulse energy at the output. In Fig. 3.15(b), there is a noticeable intensity dip on the output pump pulse, indicating the pump is partially depleted during the process. Therefore, increasing the signal from 1 nJ to 100 nJ does not result in 100 times scaling of the idler pulse energy. When the input pump has 100-nJ pulse energy, DFG process no longer operates in the linear regime. In contrast, in the case of 1-µm driven DFG, 100-nJ pump with 100-nJ signal generates ∼1.33-nJ pulse energy in idler and the DFG process is in the linear regime.

At the output, idler pulses from 1-nJ signal DFG and 100-nJ signal DFG has similar temporal pulse profile. For both cases, the output idler is quasi-transform limited (TL). Figure 3.15(c) plots the normalized intensity profile of the output idler pulse together with its TL-form. The idler has ∼110-fs FWHM pulse duration and it corresponds to ∼3.3 optical cycles. They have a peak power of 0.9-kW and 52.6-kW, respectively. In the spectrum domain, the idler in both cases has ∼1150-nm FWHM spectral bandwidth. The output spectrum of the idler is plotted in Fig. 3.15(d).

3.5.3 Energy scaling of 2-µm driven DFG

2-µm driven DFG is able to generate an idler with quasi-TL pulse profile even when a 2-mm-thick GaSe is in use. When the input pump/signal has 100-nJ pulse energy, DFG process starts to deplete the pump indicating that 2-µm driven DFG is more efficient than 1-µm driven DFG. To study the energy scaling, we simulate the 2-µm driven DFG by setting the input signal energy at 0.1 nJ, 1 nJ and 10 nJ, and for each signal energy the input pump energy varies from 0.1 nJ to 3 µJ. The GaSe thickness is still set at 2 mm. The pulse energy of the output idler is calculated and the results are plotted in Fig. 3.16(a).

The three curves in Fig. 3.16(a) exhibit similar dependence on input pump pulse energy as those curves in Fig. 3.6(a). As we have expected, the threshold pump pulse energy now decreases to 100 nJ, which is indicated by a vertical dashed line in Fig. 3.16(a). When the pump is lower than 100 nJ, the idler scales linearly. When the pump pulse energy exceeds 100 nJ, DFG process transits into the OPA regime and the idler has an exponential gain with respect to the input pump. Compared with 1-µm DFG, the threshold pump pulse energy is reduced by a factor of 3. Due to less pump-signal GVM, 2-µm DFG generates more idler than 1-µm DFG. For example, at the same input condition of 100-nJ pump and 10-nJ signal (circled point in Fig. 3.16(a), the 1-µm driven DFG generates idler of 0.15

(a) DFG process with signal fixed

(b) DFG process with pump fixed
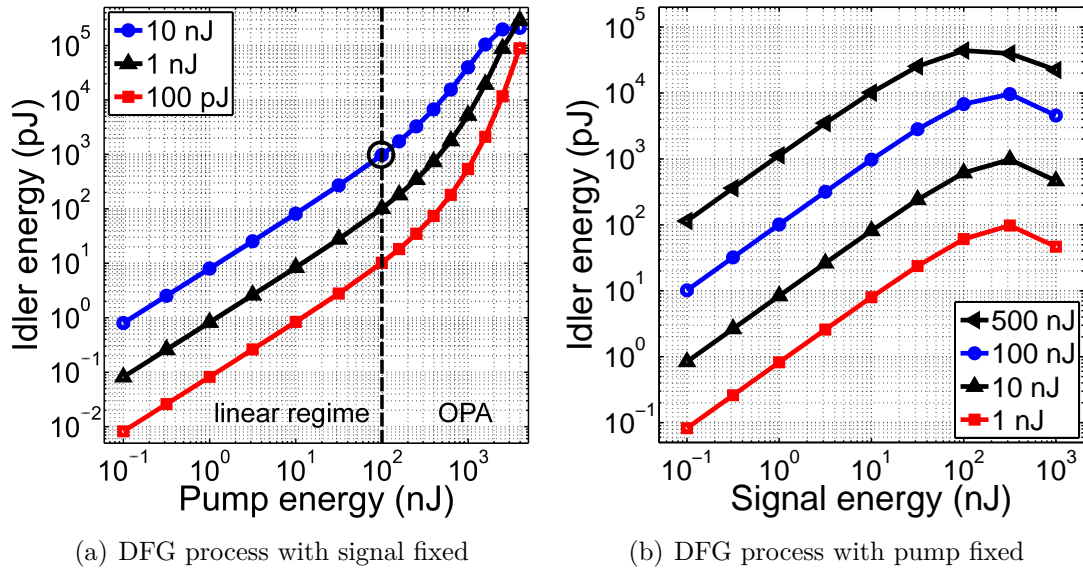
Figure 3.16: Idler energy scaling of 2-μm driven DFG.

Type-I DFG process inside a 2-mm-thick GaSe is examined under different launching conditions. (a) The signal energy is fixed at 0.1 nJ, 1 nJ, and 10 nJ. The pump increases from 0.1 nJ to 4 μJ. (b) The pump energy is fixed at 1 nJ, 10 nJ and 100 nJ. The signal increases from 0.1 nJ to 10 μJ.

nJ while the 2-μm one generates 0.98 nJ idler, representing nearly one order of magnitude improvement.

To show how the idler pulse energy scales with the signal pulse energy, we calculate the DFG processes with the pump energy fixed at 1 nJ, 10 nJ and 100 nJ and the signal energy increased from 0.1 nJ to 1 μJ; the results are shown as red square curve, black upward-pointing triangle curve and blue circle curve in Fig. 3.16(b). Similar as the results in Fig. 3.6(b), the idler pulse energy in the 2-μm driven DFG grows linearly and then starts to saturate as the input signal pulse increases. However, a distinct difference appears for the signal energy increased beyond ∼300 nJ: the idler energy saturates to a constant value in the 1-μm driven DFG while it drops to a lower value in the 2-μm case. This is also due to less GVM in the 2-μm DFG, which leads to a more efficient interaction of the three waves such that power back conversion from signal/idler to pump takes place when the signal energy exceeds 300 nJ. The transition between the linear regime and the saturation regime of 2-μm driven DFG is indicated by a vertical dashed line in Fig. 3.16(b).

In [65], 30-W, 32-fs pulses generated by a Tm:fiber laser at 2-μm with 50-MHz repetition rate are incident onto a GaSe crystal for intra-pulse DFG. The results indicate that 600-nJ pulse energy at 2-μm remains below the crystal damage threshold given that the peak intensity at the focus reaches 75 GW/cm^2 [65]. As

the results in Fig. 3.16(a) show, the HRR DFG starts to enter OPA regime as the pump pulse energy exceeds 100 nJ. To show how the idler pulse energy scales with the input signal energy when the DFG operates in the OPA regime, we plot in Fig. 3.16(b) black left-pointing triangle curve corresponding to 500-nJ pump energy. In the OPA regime, the idler starts to saturate at a lower input signal pulse energy of 100 nJ. Nevertheless, our simulation results indicate that DFG between a 500-nJ pump pulse and 100-nJ signal pulse in a 2-mm-thick GaSe crystal generates an idler pulse with 44.2-nJ energy and 135-fs duration, corresponding to 317-kW peak power. In this case, a total input pulse energy of 600 nJ can generate 44.2-nJ pulse energy at the output idler. It corresponds to an energy conversion efficiency of 7.4%, which is one order of magnitude higher than the one in 1-µm driven DFG (0.75%). At 50-MHz repetition rate, the idler pulse energy translates to an output average power of 2.2 watts.

As shown in Fig. 3.16(a), the pump threshold pulse-energy is 100-nJ when the GaSe crystal is 2-mm-thick. According to Eq. 3.6, this threshold level can be further reduced by increasing the crystal thickness. To verify this trend, we simulate DFG processes with GaSe thickness being 2-mm, 4-mm, 8-mm, and 10-mm. In order to prevent pump depletion, a "small" signal with 1-pJ pulse energy is used to seed the DFG process. The pump increases from 0.1-nJ to 1-μJ. The pulse energy of the output idler is calculated and the results are plotted in Fig. 3.17. In each figure, we plot the linear fit of the idler under the linear regime operation using a black dashed line, so that the distinction between the linear regime and the OPA regime is more evident.

As shown, the threshold pump pulse energy at different GaSe thickness is 100-nJ, 30-nJ, 20-nJ and 20-nJ. It scales with L^{-2} until GaSe thickness exceeds 4-mm. When the GaSe crystal is thicker than 4-mm, temporal walk-off between pump pulses and signal pulses starts to saturate the strength of the parametric interaction. When the GaSe crystal is 8-mm-thick, the threshold pump pulse energy reaches a minimum level of around 20-nJ. Further increasing the crystal thickness does not constitute an efficiency approach for scaling the idler. Using 100-nJ pump and 1-pJ signal, idler pulses with pulse energy of 0.4 pJ, 1.1 pJ, and 1.2 pJ are generated by GaSe crystal with a crystal thickness of 4 mm, 8 mm, and 10 mm, respectively.

3.5.4   2-µm driven DFG at different GaSe thickness

Finally, we investigate the effect of crystal thickness on 2-µm driven DFG and compare it with the 1-µm driven DFG. 2-µm DFG process with the GaSe thickness varying from 0.5 mm to 4 mm is simulated with the input pump/signal pulse energy set at 100-nJ. The normalized intensity profiles of the output idler pulses are plotted in Fig. 3.18(a). Due to less pump/idler GVM, the output idler pulses have a more symmetric pulse profile compared with their 1-µm counterparts as shown in Fig. 3.8(a). Figure 3.18(b) plots the pulse energy as a function of GaSe thickness (to the left axis), showing that the idler energy starts to saturate as the crystal thickness exceeds 3.5 mm; It is noteworthy that, unlike the case of

73

(a) 2-mm-thick GaSe

(b) 4-mm-thick GaSe

(c) 8-mm-thick GaSe

(d) 10-mm-thick GaSe
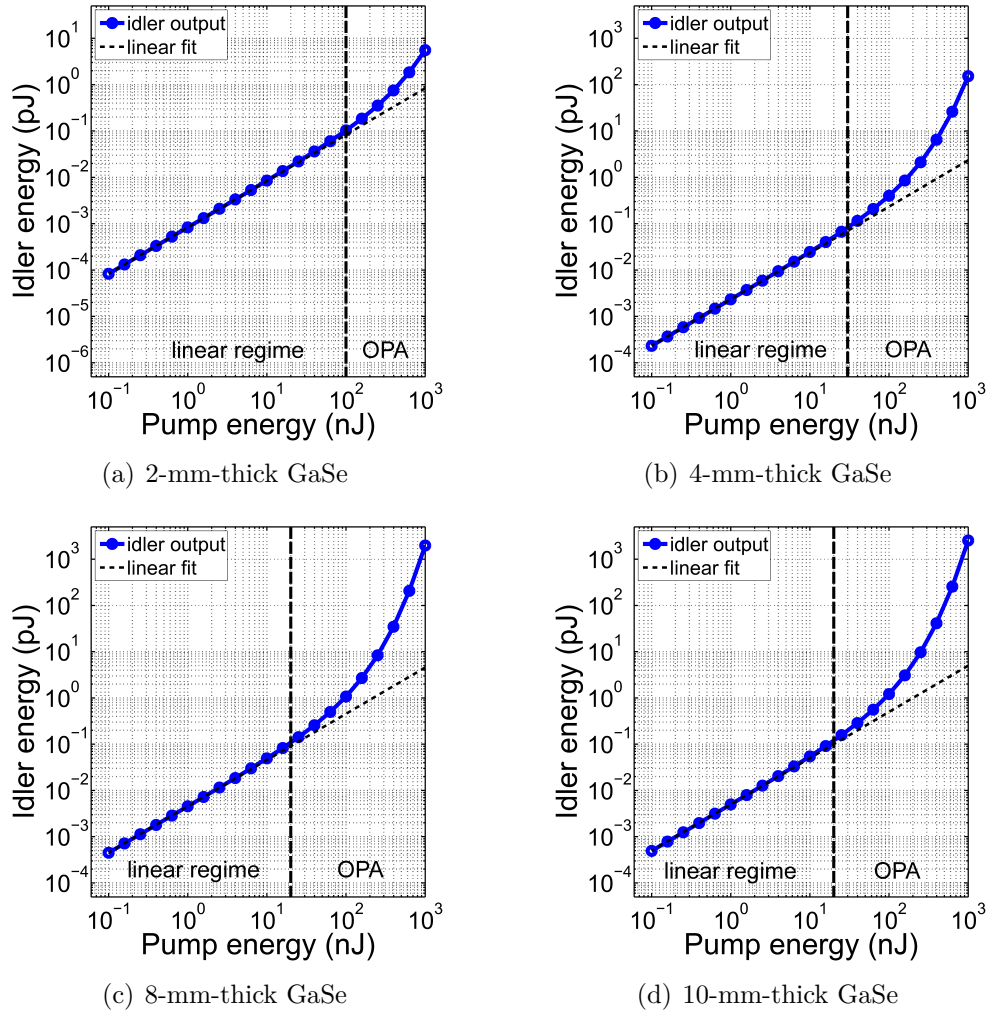
Figure 3.17: Threshold pump pulse energy of 2-μm driven DFG.

Type-I DFG process is examined to show the change of threshold pump pulse energy with different GaSe thickness. GaSe thickness of 2-mm, 4-mm, 8-mm and 10-mm is selected. For each plot, the signal has 1-pJ pulse energy.

1-μm DFG, the saturation of the idler growth is not caused by the saturated pump-signal temporal overlap, but caused by pump depletion. The pump-to-idler quantum efficiency versus GaSe crystal thickness, plotted in Fig. 3.18(b), shows that more than 75% pump photons have been converted into idler photons when a 3-mm-thick GaSe crystal is hosting the DFG process. Using a 3-mm-thick GaSe, 9.58-nJ idler pulses can be generated, representing 6 times improvement compared with the 1-μm driven DFG (1.55 nJ idler pulse energy). For a repetition rate of 30 MHz, such pulse energy leads to $\sim$300-mW average power. For 2-μm driven DFG, the photon conversion ratio can exceed 76%, which is 3 times higher than the case of 1-μm driven DFG (24.5%).

(a) Intensity profile of the output idler

(b) Pulse energy and quantum efficiency

Figure 3.18: Idler profile and pulse energy of 2-μm driven DFG at different GaSe thickness.

2-μm driven DFG is studied with GaSe thickness varying from 0.5 mm to 4 mm. Both inputs have 100-nJ pulse energy. (a) Normalized intensity profile of the idler pulse. (b) Pulse energy of the idler and the quantum efficiency for pump-to-idler photon conversion.
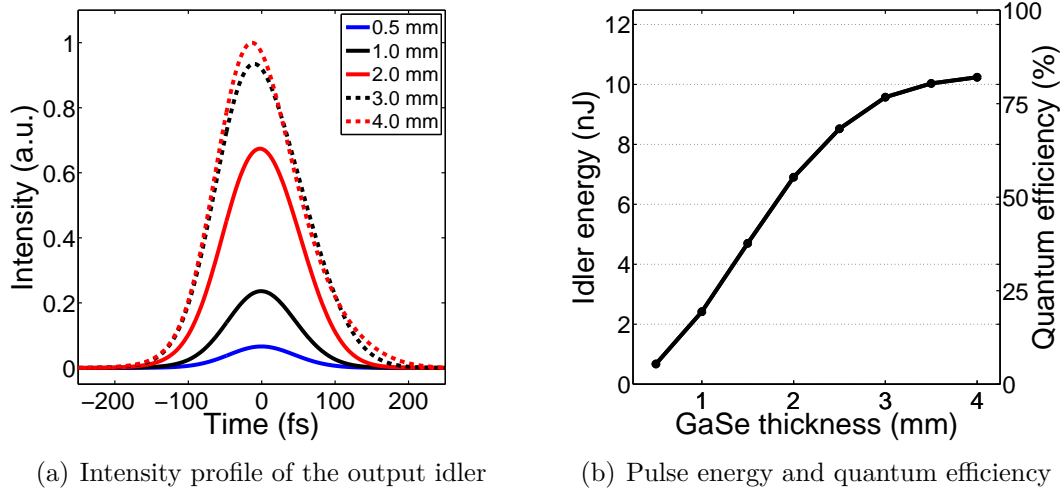
Figure 3.19(a) plots the spectral bandwidth versus the crystal thickness (black dashed line, to the right axis). The idler bandwidth decreases from 1150 nm to 964 nm as the crystal thickness increased from 0.5 mm to 4 mm. Clearly the idler resulted from 2-μm driven DFG has a much larger spectral bandwidth than can be achieved from the 1-μm driven DFG. Consequently the idler pulse generated from 2-μm driven DFG is much shorter with the duration varying between 105 fs and 135 fs (circle marked line in Fig. 3.19(a)). Given that the corresponding TL pulse duration varies between 105 fs and 120 fs (square marked line in Fig. 3.19(a)), the idler pulse is close (within 85%) to be transform-limited. By simply adding proper GDD, the idler pulse can be dechirped to be nearly transform-limited (triangle marked line in Fig. 3.19(a)).

Figure 3.19(b) shows the peak power as a function of GaSe thickness for the output idler pulse (circle), the compressed pulse (triangle), and the TL pulse (square). Different from the 1-μm driven DFG, all the peak powers in the 2-μm case increase with an increased GaSe crystal thickness. Thanks to the short pulse duration and higher pulse energy, the idler peak power can reach as high as 72 kW when a 4-mm-thick GaSe crystal is used for hosting 2-μm driven DFG, nearly two orders of magnitude improvement from the 1-μm case (1.3 kW). Such a high peak power is crucial for important nonlinear mid-IR applications.
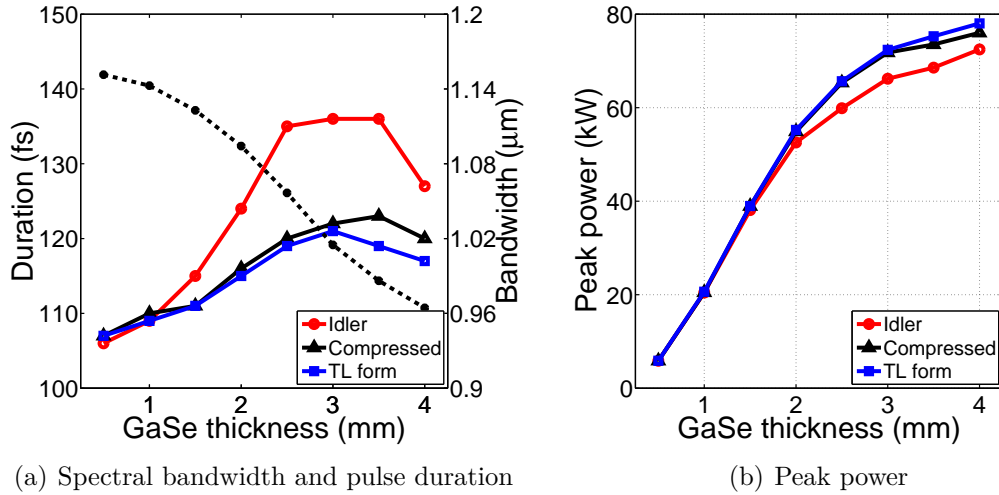
(a) Spectral bandwidth and pulse duration

(b) Peak power

Figure 3.19: Idler bandwidth, pulse duration and peak power of 2-μm driven DFG at different GaSe thickness.

2-μm driven DFG is studied with GaSe thickness varying from 0.5 mm to 4 mm. (a) Spectral bandwidth of the output idler (to the right axis) and pulse duration of the output idler pulse, the compressed idler pulse and TL idler pulse (to the left axis). (b) Peak power of the output idler pulse, the compressed idler pulse and TL idler pulse.

3.5.5 Summary of 2-μm driven DFG

To conclude, thanks to a reduced pump-signal GVM, 2-μm driven DFG has superior energy scalability in generating high-power mid-IR idler pulses compared with 1-μm driven DFG. The pump/idler GVM for 2-μm driven DFG is also much lower compared with 1-μm driven DFG, enabling the generation of mid-IR idler pulses that are close to transform-limited. Moreover, the input pulses in 2-μm driven DFG have intrinsically less photon energy compared with the inputs of 1-μm driven DFG, and, therefore, we anticipate a higher damage threshold for the nonlinear crystal in 2-μm driven DFG. Our previous results showed that GaSe crystal suffers crystal breakdown if the input pulses, centered around 1-μm, have a total input power of 6-W [36]. In [65], it was shown that GaSe crystals can be launched with a total input power of 30-W, if the inputs are centered at 2-μm with a repetition rate of 50-MHz. It translates to a total input pulse energy of 600-nJ. In our calculations, we simulate the situation where a 2-mm-thick GaSe is seeded with 100-nJ signal pulses and 500-nJ pump pulses in a 2-μm driven DFG scheme. The generated mid-IR idler pulses, centered around 9.87-μm, can have a pulse energy of >44-nJ and a peak power of 320-kW. At a repetition rate of 50-MHz, mid-IR sources with a total optical power of >2.2-W will open up avenues for many applications.

3.6   Possible experimental implementation

In DFG, the signal pulses are usually derived from the pump pulses using second-order nonlinear susceptibility offered by nonlinear optical crystals (OPA or OPO) or third-order nonlinearity in an optical fiber. The latter method is more attractive as the derived signal pulses share the same f_{ceo} as the pump pulses and the resulting mid-IR pulses have set f_{ceo} automatically to zero. To convert the resulting mid-IR sources into mid-IR frequency combs, only the repetition rate f_{rep} needs to be stabilized, which significantly simplifies the overall experimental setup. Fiber-based wavelength-shifting method is also straightforward to be implemented and offers a broad wavelength tuning range, both of which are preferred in constructing mid-IR frequency combs.

In general, however, optical fibers exhibit poor energy scalability due to the massive amount of nonlinearity caused by the tight confinement of the femtosecond pulses in a small mode area. As a result, the signal pulses that are derived using fiber-optic methods are normally much weaker than the pump pulses. For example, a widely used fiber-optic method to obtain the signal pulses is to employ Raman soliton self-frequency shift in an optical fiber [33]. Raman soliton pulses normally have nanojoule or even sub-nanojoule level pulse energy, especially for the case where the pump pulses are centered at 1.03 μm, an operating wavelength range for mature high-power Yb-doped fiber laser systems. For example, Axel Ruehl *et al.* used a 2.2-W, 151-MHz Yb:fiber laser source to derive the signal pulses by generating Raman solitons in 25-cm-long highly nonlinear suspended-core fiber [33]. The resulting signal pulses are tunable between 1.15 to 1.65 μm with pulse energies varying from 0.04–0.15 nJ. After mixing the signal and the pump in a 0.5-mm-thick GaSe crystal, the DFG process produces 0.3-mW average output power at 10 μm, which corresponding to 2-pJ pulse energy in the mid-IR range. For 2-μm driven inter-pulse DFG, C. R. Phillips *et al.* used a 72-MHz Tm:fiber laser system that produces 150-fs, 2.0-μm pulses with watt-level average power [34]. The signal pulses obtained via Raman soliton generation in fluoride fiber centers at 2.5-μm with 30-mW average power, corresponding to a pulse energy of 0.42-nJ. Using a quasi-phase-matching DFG scheme in 2-mm-thick orientation-patterned GaAs, they generated 6.7–12.7-μm idler pulses with 1.3-mW average power.

The simulation results presented in Section 3.4 and 3.5 clearly point towards a more efficient way for power scaling of HRR DFG: increase the signal pulse energy to a level comparable with the pump pulse. In other words, generation of high-energy, wavelength-tunable signal pulses constitutes the solution to achieve high power mid-IR frequency combs. Recently we demonstrated an energy-scalable fiber-optic technique in order to derive wavelength-tunable signal pulses. We employ self-phase-modulation (SPM) to broaden a narrow input optical spectrum to generate well-isolated spectral lobes and then spectrally filter the left-most/right-most spectral lobes to produce nearly transform-limited femtosecond pulses [51]. Based on a 30-MHz Yb:fiber laser system, such SPM-enabled spectral selection (SESS) approach is able to generate 100 fs pulses with up to 20 nJ pulse energy,
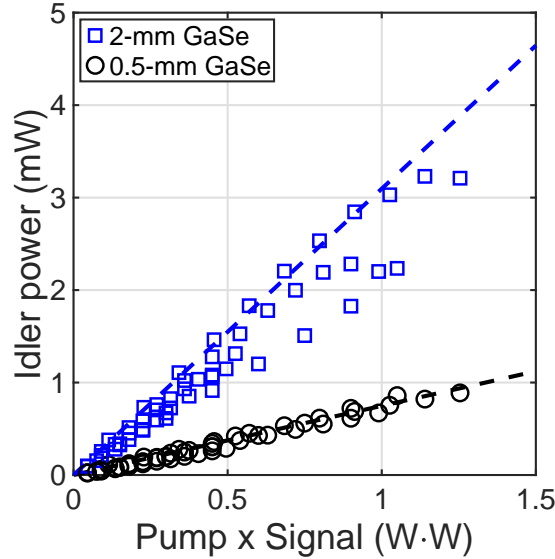
Figure 3.20: Idler versus pump-signal product.

Comparison between experimental data (circles and squares) and simulation results. Here we assume 30% linear loss for the mid-IR idler when it propagates from the nonlinear crystal to the detector.

tunable in the range of 1100-1200 nm [51]. Using these SESS pulses as the signal and the other portion of the Yb:fiber laser output as the pump, DFG process inside a 2-mm-thick GaSe crystal can generate mid-IR output in the wavelength region of 7-18 μm [36]. Among them, the mid-IR output at 9.5 μm has 5.4-mW average power, corresponding to 180-pJ pulse energy [36].

Using wavelength-shifted SESS pulses as the signal pulses for seeding DFG, we measure the power of the mid-IR idler versus the product between pump power and signal power. The experiment utilizes a 30-MHz, 15-W, high-power Yb:fiber laser system as the master laser source [36]. In DFG, the pump has a center wavelength of 1030-nm, the signal 1150-nm, and the idler 9.87-μm. The pump pulse and the signal pulse has similar pulse parameters as our numerical calculations on 1-μm driven DFG. In the experiment, the mid-IR idler is generated in a 2-mm/0.5-mm-thick GaSe crystal. The results are plotted in Fig. 3.20 by blue squares (2-mm GaSe) and black circles (0.5-mm GaSe). Apparently, for 1-μm driven DFG, the idler has a linear growing trend with respect to the product between pump and signal. We plot in the same figure the idler power predicted by numerical simulations (i.e., linear fit from Table 3.1) using blue/black dashed lines. Here we assume the mid-IR idler has a linear loss of 30% when it propagates from the crystal to the detector. The power discrepancy for 2-mm GaSe results may be due to the absence of multi-photon absorption in our modeling.

SESS exhibits excellent energy scalability and can be adapted to other laser wavelengths as well. For example, employing an ultrafast Er:fiber laser centered

at 1.55 μm, we implemented a SESS source tunable from 1.3 μm to 1.7 μm with up to 16-nJ pulse energy [74]. We further showed that such increasing the input pulse energy to $\sim$1-μJ (offered by an OPA source) produced >100-nJ femtosecond pulses at 1.3 μm and 1.7 μm with a pulse peak power reaching the MW level.

SESS can be also applied on a high power 2-μm laser system, for example, a Tm:fiber laser at tens of MHz repetition rate and provides 2-μm femtosecond pulses with $\sim \mu J$ level pulse energy. Using proper fiber to implement SESS, signal pulses tunable in 2.2–2.9 μm with >100-nJ energy are possible and should enable generation of $\sim$40 nJ mid-IR pulses tunable in 6–20 μm.

3.7 Summary of the chapter

In conclusion, we numerically investigated HRR DFG processes that generate mid-IR idler, in which the crystal damage threshold limits the allowed pulse energy. We show that, different from OPAs based on low repetition-rate DFG, HRR DFG may operate in the linear regime, in which the idler pulse energy scales almost linearly with respect to the pump/signal pulse energy. Consequently increasing the signal energy is as efficient as increasing the pump energy for idler energy scaling in HRR DFG. We compare 1-μm driven DFG and 2-μm driven DFG, and demonstrate that 2-μm driven DFG has the following advantages:

(1) The idler energy scalability benefits from smaller GVM, and therefore 2-μm driven DFG associated with a reduced GVM compared with the 1-μm driven case exhibits superior energy scalability for the idler pulses. More important, higher crystal damage threshold is expected due to the lower photon energy, and therefore more energetic pump pulses are allowed in the 2-μm driven DFG, which results in operation of inter-pulse DFG in the OPA regime.

(2) The 2-μm driven DFG experiences a smaller dispersion and a larger phase matching bandwidth, which in conjunction with the reduced GVM results in much shorter idler pulses with close to be transform-limited pulse duration. Under the same launching conditions, the peak power of idler pulses generated in the 2-μm driven DFG is nearly two orders of magnitude higher than can be achieved from the 1-μm driven DFG (e.g., 72 kW versus 1.3 kW).

The key for achieving high power, HRR DFG is to obtain high energy ($\geq$100 nJ) signal pulses. We show that SESS is a feasible approach to produce these required signal pulses. Ongoing work is to implement such HRR DFG experimentally and demonstrate its energy scalability. We anticipate that long-wave mid-IR frequency combs with >2-W average power can be achieved by 2-μm driven inter-pulse DFG, which will open up avenues for many applications.

Chapter 4

Noise of DFG-based mid-IR frequency combs

4.1 Introduction

Ultrafast mid-infrared (mid-IR) lasers with a center wavelength spanning from 5 to 20 μm (molecular "fingerprint" region) have attracted strong research attention due to their capability of coherently exciting the rotational and vibrational resonances of various biological/chemical molecules [17]. After locking the repetition rate f_{rep} and the carrier-envelope offset frequency f_{ceo} of a mode-locked mid-IR laser to low-noise, stable references, for example, low-noise radio-frequency (rf) sources [75] and ultrahigh-Q stable optical references [76], the resulting mid-IR frequency comb provides hundreds-of-thousands of comb lines with well-defined optical frequencies [16]. Equipped with rapidly developing technologies such as dual-comb detection [18, 77–79], enhancement cavities [80, 81] and electro-optic sampling [82], mid-IR frequency combs in the molecular "fingerprint" region have become an enabling tool for powerful spectroscopic applications.

In the time domain, phase-stable optical pulses are emitted from the comb laser in a time interval of t_{rt}. The time interval t_{rt} corresponding to the round-trip time of the master laser cavity is defined by the time separation between the pulse envelopes of two consecutive pulses. Due to the cavity dispersion, the intra-cavity phase velocity v_{p} differs from the intra-cavity group velocity v_{g}. In each round-trip, there is a pulse-to-pulse phase slippage between the carrier and the envelope. Such phase slippage is termed as the carrier-envelope phase offset ϕ_{ce} (CEP).

Figure 4.1(a) depicts the time domain picture of two consecutive pulses for illustrating t_{rt} and ϕ_{ceo}. In the plot, blue dashed lines represent the pulse envelope and black solid lines the electric field (carrier). As Fig. 4.1(a) shows, the envelopes of two pulses are separated by t_{rt} in the time domain, which is normally at the scale of tens of nanosecond. For a 30-MHz laser system, t_{rt} is 33.3-ns. For the right pulse plotted in Fig. 4.1(a), the peak of the electric field is aligned with the peak of the pulse envelope so that its carrier is in phase with its envelope. For the left pulse plotted in Fig. 4.1(a), there is a phase slippage of ϕ_{ce} between the carrier

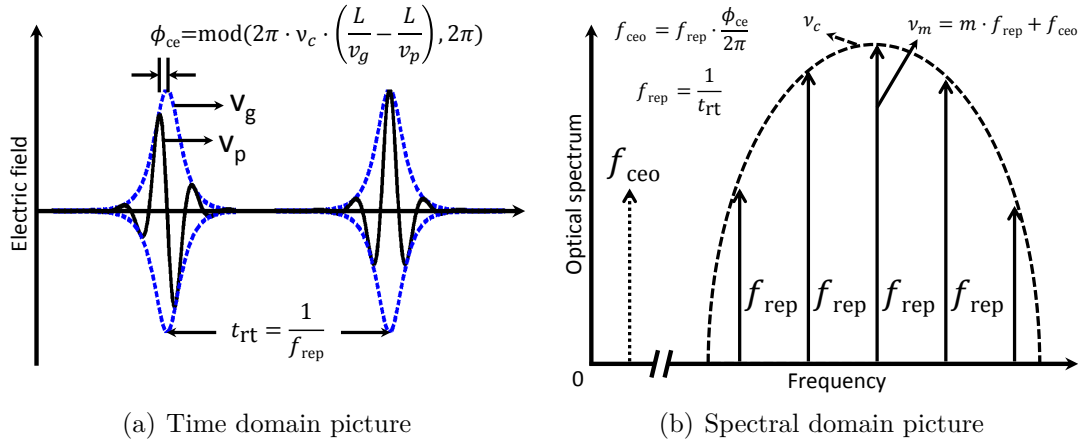(a) Time domain picture (b) Spectral domain picture

Figure 4.1: Output from a frequency comb laser.

(a) Time domain picture of two consecutive pulses from a frequency comb laser. Blue dashed lines represent the pulse envelope and black solid lines represent the electric field. (b) Spectral domain picture of a frequency comb output. Black dashed line plots the envelope of the optical spectrum. Extending the equally spaced longitudinal modes towards the frequency origin, there exists an "imaginary" mode f_{ceo} between 0 and f_{rep}.

and the pulse envelope. Theoretically, the carrier-envelope phase offset is defined by

$$\phi_{\text{ce}} = 2\pi \cdot \nu_c \cdot (\frac{L}{v_{\text{g}}} - \frac{L}{v_{\text{p}}}), \tag{4.1}$$

where ν_c stands for the optical carrier frequency and L is the net cavity length. Normally, under such definition, the offset phase is at the order of $10^5 \cdot \pi$ [75,83]. However, as the electric field is oscillating at the carrier frequency, this "theoretical" offset phase can be downshifted to 0–2π by adding appropriate multiples of 2π.

When the electric field of a pulse train containing multiple pulses is Fourier-transformed, the resulting spectrum consists of equally spaced lines in the spectral domain. Figure 4.1(b) plots the spectral domain picture of a frequency comb output. It is noteworthy that the Fourier-transform of single optical pulse is a continuum centered around ν_c (shown as black dashed line in Fig. 4.1(b)). It is the constructive and destructive interference among multiple phase-stable pulses that leads to the formation of comb-like structure. As shown in Fig. 4.1(b), the spacing between the comb lines f_{rep} is the inverse of the pulse-to-pulse separation in the time domain

$$f_{\text{rep}} = \frac{1}{t_{\text{rt}}}. \tag{4.2}$$

Extending the comb lines towards the origin results in an "imaginary" comb line that falls between 0 and f_{rep}. Using Fourier transform's identities, the offset fre-

82

quency f_{ceo} is expressed by

$$f_{\text{ceo}} = \frac{\phi_{\text{ce}}}{2\pi} \cdot f_{\text{rep}}. \tag{4.3}$$

Apparently, the optical frequency of the mth comb line can be then written as

$$\nu_m = m \cdot f_{\text{rep}} + f_{\text{ceo}}, \tag{4.4}$$

where m is an integer. As long as both f_{rep} and f_{ceo} are stabilized, the resulting frequency comb provides hundreds-of-thousands of comb lines and each comb line has a well-defined optical frequency.

To construct a frequency comb, both the repetition rate f_{rep} and the offset frequency f_{ceo} need to be precisely measured and referenced. The repetition rate, f_{rep}, can be easily measured by imposing the optical pulse train into a fast photodiode and analyzing the rf spectrum of the photodiode signal [84]. To stabilize f_{rep}, the most straightforward and commonly used approach is to tune the cavity length via intra-cavity piezoelectric transducer (PZT) devices [85–88]. Normally PZT device only has a servo bandwidth of tens of kHz. A properly design PZT mount can achieve >100 kHz bandwidth [89, 90]. To achieve faster feedback control, intra-cavity electro-optic modulator (EOM) devices are also employed, which offer a controlling bandwidth from several hundred kHz to a few MHz [91–94].

Meanwhile, the detection of f_{ceo} is achieved by heterodyne beat measurement such as $1f$-$2f$ interferometer [6, 95]. In a typical $1f$-$2f$ interferometer, the source of interest needs to be spectrally broadened to an octave-spanning spectrum. This is usually achieved by launching the optical pulse into a short piece of highly nonlinear fiber (HNLF) for super-continuum generation (SCG) process. The octave-spanning spectrum contains the optical frequencies $\nu_{2m} = 2m \cdot f_{\text{rep}} + f_{\text{ceo}}$ and $\nu_m = m \cdot f_{\text{rep}} + f_{\text{ceo}}$ sharing same f_{ceo}. The latter one is then frequency-doubled to generate a second-harmonic signal with a center frequency of $2\nu_m = 2m \cdot f_{\text{rep}} + 2 \cdot f_{\text{ceo}}$. The heterodyne beat between ν_{2m} and $2\nu_m$, therefore, generates the f_{ceo} signal in the radio-frequency range which can be detected using a fast photodiode. The f_{ceo} signal is then compared with a stable rf source to generate the error signal for controlling f_{ceo}.

To control the offset frequency f_{ceo}, the error signal can be applied in a feedback or a feed-forward scheme. The feedback control of f_{ceo} can be achieved by changing the net cavity phase. The pump power is usually selected as the control variable, because modulating the pump power allows changing the intra-cavity pulse intensity, which in turn controls the accumulated nonlinear phase inside the cavity. Therefore, f_{ceo} can be controlled by modulating the pump diode current [85–88, 90, 96], or controlling the pump power using an EOM device [97]. The net cavity phase can be also directly modulated using an intra-cavity graphene-based modulator [94, 98], or an intra-cavity saturable-absorber mirror as opto-optical modulator [99]. Feed-forward control of the offset frequency f_{ceo} is to change the pulse-to-pulse phase difference outside the laser cavity. As a cavity-external approach, it does not influence the intra-cavity mode-locking process, which is inherently more robust. The feed-forward control can be achieved by us-

ing an acousto-optic frequency shifter [100–102] to modulate the optical frequency of all comb lines.

The stabilization of the offset frequency f_{ceo} is highly dependent on the signal-to-noise ratio (SNR) of the detected f_{ceo} signal, which is fundamentally limited by shot noise in detection. In the SCG process that generates the octave spanning spectrum, HNLF with anomalous dispersion is usually employed. During SCG, excess amplitude fluctuations and additional phase noises are introduced due to modulation instability and other noise transfer mechanisms, leading to a degraded SNR of f_{ceo} detection. The stabilization of f_{ceo} is also limited by the bandwidth of the feedback (feed-forward) system, normally <1 MHz. Moreover, the stabilization of f_{ceo} via modulating the pump diode current may result in complicated intra-cavity dynamics, as the change of intra-cavity pulse intensity changes the net cavity phase and the round-trip time simultaneously [75]. Therefore, the feedback loop for controlling f_{ceo} can "fight" against the feedback loop for controlling f_{rep}, which significantly deteriorates the stability of the resulting frequency comb.

Apart from using a tedious experimental setup for detecting and referencing f_{ceo}, passive CEP cancelation has been proposed and implemented [37]. By launching two pulse trains with different center frequency but same f_{ceo} to difference-frequency generation (DFG) process, the output idler pulse train can have f_{ceo} automatically set at zero [37]. Such passive f_{ceo} stabilization scheme has been successfully applied to construct DFG-based mid-IR frequency combs [33, 35, 68].

In the time domain, DFG process involves nonlinear interaction between optical pulses. To fully characterize a pulse train, a complex numerical array can be used to describe the complex field of each individual pulse. The length of the array equals to the sampled time span divided by the time resolution, which easily exceeds 1,000 if we assume the sampled time span is 5 times longer than the pulse duration. Therefore, a pulse train containing thousands-to-millions of pulses is represented by millions-to-billions of complex numbers, resulting an unrealistically large size of data for computation. Alternatively, as has been used in most theoretical studies [83, 103–106], if we treat the optical pulse as an entity and sample the pulse train by its repetition rate f_{rep}, the parameters for characterizing a single pulse reduce to the pulse energy E_p, pulse width τ_p, center frequency ν_c, chirp C, peak power P_{p} and the optical phase ϕ. For a pulse train, each consecutive pulse is separated by an interval of t_{rt} and a phase slippage of ϕ_{ce}. It is noteworthy that some parameters for describing the pulse are redundant. For example, by assuming certain pulse shape, the peak power can be calculated from the pulse energy, pulse width, and chirp.

If all these parameters have no temporal fluctuations, the pulse train becomes a "perfect" frequency comb and each comb line within the comb spectrum has a line-width that is inversely proportional to the observation time. If the observation time is infinitely long, the comb line becomes a mathematical δ-function. However, all these parameters for describing the pulse have temporal fluctuations, imposing uncertainties to the resulting frequency comb lines. These noises, especially the timing jitter noise and the optical phase noise, deteriorate the comb performance by broadening the comb line-width and elevating the comb background level [39]. The

noise causes direct impact on applications(e.g., frequency metrology, spectroscopic applications and optical atomic clocks) where a precise reference to the optical frequency and high detection SNR are required.

The noises originate from several sources: (1) noise of the master laser system; (2) noise introduced during the wavelength shifting process; and (3) noise introduced during the DFG process. In this chapter, we investigate the effect of timing jitter noise of DFG-based offset-free mid-IR frequency combs. We first give a brief introduction to the master fiber laser noise in Section 4.2. Then we calculate the noise transfer of DFG process in Section 4.3. During DFG, the relative timing jitter between pump pulses and signal pulses translate to the timing and intensity fluctuation of the generated idler pulses. Two DFG are compared in this section: DFG with a pump at 1.03-μm and DFG with a pump at 2-μm. The noise transfer during 2-μm driven DFG is $\sim$5 times less than 1-μm driven DFG. Finally, we study the relationship between the timing jitter noise and the comb characteristic in Section 4.4. We investigate how timing jitter noise with different noise spectrum can affect the comb line-width and the comb signal-to-noise ratio (SNR). We show that by using β-separation line method, the comb line-width can be well estimated by geometrically measuring the noise spectrum of timing jitter noise. An reduction of low-frequency $1/f^2$ noise can narrow the comb line-width from 40-kHz to 2-kHz and increase the comb SNR by 15-dB.

4.2   Noise of mode-locked fiber lasers

In this section, we discuss the noise of mode-locked fiber laser with a particular emphasis on the intensity noise and timing jitter. The theoretical study on the noise performance of mode-locked lasers begins with the soliton perturbation theory proposed by Haus [103, 107]. The relationship between intra-cavity noise sources and perturbations of laser parameters is identified by solving the master equation with an inclusion of perturbation terms. Later, Paschotta points out that the theory can be safely applied to other non-solitonic mode-locked lasers [104, 105]. He determines the performance of a mode-locked laser under the influence of quantum-limited noise. The noise of a mode-locked laser turns out to be highly dependent on the cavity parameters, such as net intra-cavity dispersion [108–110], net cavity gain [111], intra-cavity filtering [112–114], and mode-locking regime [115]. Since a full comprehensive explanation on mode-locked laser noise is too lengthy to fit into this section, here we give a brief introduction to this topic.

Figure 4.2 illustrates the schematic of a typical mode-locked fiber laser system. Normally, it consists of a fiber-based mode-locked oscillator (shown in the dashed line box), a fiber amplifier, and a pulse compressor. After the compressor, the laser system can emit $\sim$100-fs, >100-nJ pulse trains at >10-MHz to the subsequent DFG system. In the sketch, the noise sources at different sections of the laser system are indicated by red text. The intra-cavity feedback system for controlling f_{rep} and f_{ceo} is indicated by gray text.

If the cavity is properly adjusted, only one pulse is circulating inside the oscilla-
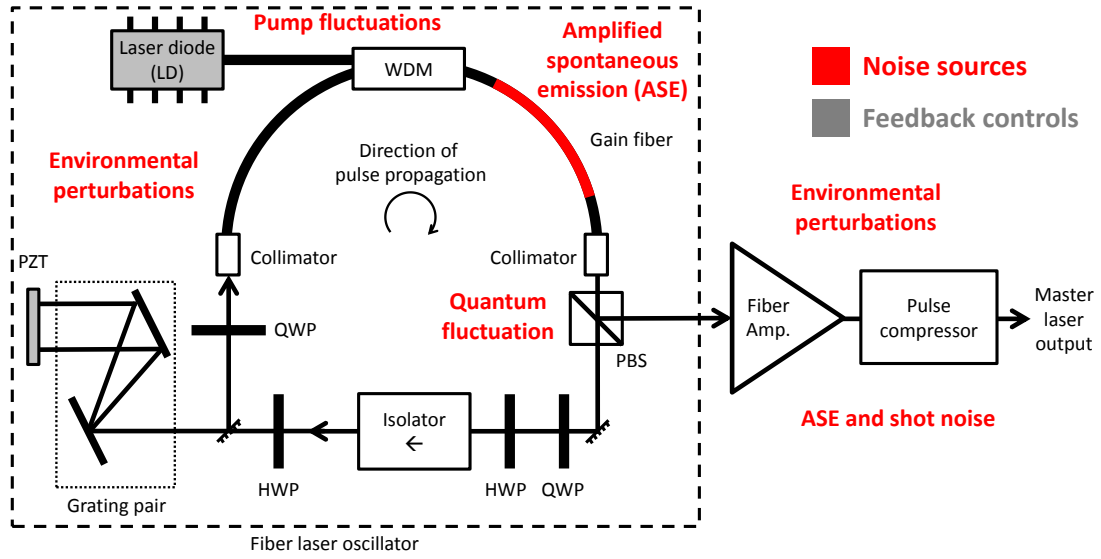
Figure 4.2: Schematic of a mode-locked fiber laser system

A typical mode-locked fiber laser system consists of a fiber laser oscillator, a fiber amplifier, and a pulse compressor. Inside the cavity, the circulating pulse is prone to pump fluctuations, ASE, and environmental perturbations (technical noises). When the pulse is coupled out, zero-point fluctuations of the vacuum field also influences. External to the cavity, the pulse has additional environmental perturbations, ASE, and shot noise when passing through the fiber amplifier and pulse compressor. (WDM, wavelength-division multiplier; QWP, quarter wave plate; HWP, half wave plate; PBS, polarizing beam splitter; PZT, piezoelectric transducer.)

---

tor at any time. For each round-trip, the pulse passes through gain fiber, standard single-mode fiber, polarization controls, dispersion controls, an isolator, and an output coupler. The pump source for the laser cavity is usually a cw-laser diode and it is coupled into the cavity via fiber-based WDM. In this example, mode-locked operation can be achieved by a "virtual" saturable absorber enabled by nonlinear polarization evolution (NPE) [116]. Once mode-locked, the cavity emits phase stable pulse train at the output. The output pulse is characterized by its pulse energy E_p, pulse width τ_p, center frequency ν_c, chirp C, and spectral bandwidth $\Delta\Omega$. Each consecutive pulse is separated by a time interval of $t_{\rm rt} = 1/f_{\rm rep}$ and a phase slippage of $\phi_{\rm ce}$. Among these parameters, we are particularly interested in the pulse energy fluctuation ΔE_p and the timing jitter $\Delta\tau$. The timing jitter $\Delta\tau$ is defined by the temporal position shift between a noise-perturbed pulse and a hypothetical noise-less pulse.

When the pulse is circulating inside the cavity and propagating outside the cavity, the pulse "picks" up noises during propagation, amplification, and compression. Intra-cavity noise sources include: (1) quantum noise, such as ampli-

fied spontaneous emission (ASE) noise; (2) environmental perturbation (technical noise), such as temperature fluctuations and mechanical vibrations; and (3) pump-induced noise. Extra-cavity noise sources include: (1) ASE noise that is introduced during pulse amplification; and (2) environmental perturbation such as vibration and path-length fluctuation.

For both intra-cavity and extra-cavity circumstances, the physical mechanisms that transfer the noise from noise sources to pulses are similar. When the pulse is circulating inside the cavity, it accumulates noise during each round-trip. Since only portion of the pulse is output coupled and the rest is still circulating inside the cavity, the circulating pulse still possess the noise from last round-trip. In other words, the noise of the intra-cavity pulse is correlated over certain time span. As a result, the intra-cavity noise is more pronounced compared with the extra-cavity noise because it is related with the noise during a longer time span. The autocorrelation function of the pulse fluctuation (i.e., energy fluctuation ΔE_p, timing error $\Delta \tau$) can be translated into the noise power spectral density (PSD) function via Wiener-Khinchin theorem. Conversely, the extra-cavity noise normally has much less correlation over the time. The same perturbation causes white *phase* noise outside the cavity, while it causes white *frequency* noise inside the cavity [106]. For example: the path length fluctuation ΔL_{in} inside the laser cavity is equivalent to the repetition rate fluctuation δf_{rep} and it results in a *frequency* shift of all comb modes; Meanwhile, the path length fluctuation ΔL_{ex} outside the cavity leads to a *phase* shift.

Inside the cavity, different noise sources act differently, depending on the type of the noise source, the pulse parameter, noise transfer mechanism, and other laser dynamics that couple different types of noise. Firstly, the fundamental limit of any mode-locked laser is the quantum noise. Quantum noise arises from ASE noise inside gain media and additional shot noise due to cavity losses. It influences the pulse energy E, center frequency ν_c, pulse duration τ_p and the timing position of the intra-cavity pulse [104, 105]. It is noteworthy that quantum noise can be coupled into timing jitter noise in two routes: (1) quantum noise directly changes the temporal position of the intra-cavity pulse; (2) quantum noise alters the center frequency of the intra-cavity pulse and changes the net delay of the pulse due to Gordon-Haus jitter [41]. When the intra-cavity pulse is coupled out, it is also influenced by zero-point fluctuation of the vacuum field reflected at the output coupling mirror. Therefore, the noise PSD of intensity noise and timing jitter noise is dominated by quantum-limited white noise at high Fourier frequencies, where other types of noise (technical noise and pump-induced noise) decays.

Secondly, the mode-locked laser is influenced by environmental perturbations (technical noise) such as vibration, acoustic noise, and temperature fluctuation. These technical noises cause the laser fluctuations in various manners. For example, temperature fluctuation can change both the net cavity length and the net group velocity of the propagating pulse. Vibration of the intra-cavity mirror can change not only cavity length but also cavity loss. The complex interplay between technical noise and laser fluctuation can be well explained by the elastic tape model [117], where the equal-spaced longitudinal modes across the spectrum

87

are considered to have a fixed, characteristic point, ν_{fix}, depending on the circumstances. Nevertheless, technical noise sources mainly change the laser parameters in a relatively slow and long-term scale, meaning the laser noises are influenced by technical noises mainly at lower frequencies, normally up to few kHz.

Thirdly, the laser cavity is prone to pump fluctuations induced by pump-current instability and other environmental perturbations. The translation from pump noise to laser noise is non-instantaneous, which is a result of the delayed response of the gain medium. In other words, the gain medium acts as a low-pass filter in translating the pump noise into the laser noise. The "cut-off" frequency is near the relaxation oscillation frequency of the gain medium, which is normally at several hundreds of kilohertz. The laser response to the pump noise quickly rolls off beyond the relaxation oscillation frequency. In [106], it is pointed out that laser noise is dominated by pump-induced noise at low-middle range of frequencies.

Finally, intra-cavity elements mix the noise of different laser parameters. These elements include saturable absorber, dispersion, Kerr nonlinearity, Kramers-Kronig-related phase changes, self-steepening effect, Raman effect [104, 105] and other mechanisms that couple physical parameters of the pulse. The noise translation can be either linear or nonlinear to the pulse intensity. For example, a passive pulse propagation introduces additional timing jitter due to the center frequency fluctuation of the pulse. During pulse propagations, the intensity noise results in additional phase noise via the fiber nonlinearity.

When the pulse with noise is propagating outside the cavity, it is not only prone to extra-cavity noise sources, but also influenced by the noise transfer during pulse propagation. When the pulse has high pulse energy, it leads to large nonlinearity even when the pulse propagates a small distance inside an optical fiber. In this instance, depending on the circumstances, additional intensity, timing, and center frequency fluctuations are introduced due to the intensity noise of the input pulse.

For a free-running mode-locked laser, the timing jitter noise and the optical phase noise are divergent at low frequency. For a free-running laser, there lacks a "time" standard to regulate the timing position of the circulating pulse and therefore the timing position undergoes a "random-walk". As a result, the variance of the timing error $\sigma_{\Delta\tau}^2$ grows over the observation time and timing jitter noise is dominated by $1/f^2$ noise at low frequencies. At high frequencies, timing jitter noise is quantum-noise limited and it has a white, flat noise spectrum. On the other hand, intensity noise and center frequency noise are bounded as there exists a restoring force to regulate these fluctuations once the cavity is mode-locked. The restoring force can be gain saturation or a finite gain bandwidth.

In the experiment, high-power master laser output is used to generate the signal pulses via fiber-optic nonlinear wavelength shifting, for example, soliton self-frequency shift (SSFS). The resulting signal pulses have large RTJ with respect to the pump pulses. In a recent research [56], PSD of RTJ noise for wavelength-shifted Raman soliton is measured by a balance optical cross-correlator (BOC) setup [118]. It reveals that during SSFS, a large portion of RTJ is caused by RIN of the pumping pulses due to the dispersive pulse propagation inside nonlinear optical fibers. If SSFS is not optimized, the resulting signal pulses have a RTJ with

a standard deviation $\sigma_{\Delta\tau}$ or integrated timing jitter (ITJ) of 63.9 fs. Using optimized configuration, RTJ can be reduced to about 6.7 fs. In the subsequent DFG experiment, which generates the offset-free mid-IR frequency comb, RTJ between pump pulses and signal pulses causes timing jitter and pulse energy fluctuation of the output idler pulses. In the next section, we study such noise transfer during DFG. We study the noise transfer by simulating two sets of DFG processes: (1) DFG with an input pump centered at 1.03-μm (1-μm driven DFG); and (2) DFG with an input pump centered at 2-μm (2-μm driven DFG).

4.3   Noise transfer during DFG

DFG process is seeded with pump pulses and signal pulses to generate mid-IR idler pulses. Normally, the signal pulses are derived from the replica of the pump pulses via $\chi^{(2)}$ nonlinearity from parametric processes or $\chi^{(3)}$ nonlinearity from optical fibers. Using this scheme, the signal pulses are well synchronized with the pump pulses in the time domain. However, due to the nonlinear nature of the wavelength shifting methods, the signal pulses have additional timing fluctuation with respect to the pump pulses. During DFG, such relative timing jitter (RTJ) is translated to the timing and intensity fluctuation of the output idler pulses. Since the idler pulses form the mid-IR frequency comb, the generation of low-noise idler is of particular importance. If the idler pulses have excessive timing jitter noise and relative intensity noise (RIN), the resulting frequency comb has large comb line-width (>10 kHz), high intensity fluctuations, and low SNR in detection, all of which can significantly degrade the performance of the frequency comb, especially in applications that require a precise optical reference and a high SNR.

In this section, we numerically study the noise transfer during DFG with a focus on the additional noise originated by RTJ between input pump pulses and signal pulses. When the timing position of the signal pulses is fluctuating with respect to the pump pulses, the generated idler pulses have different timing $\Delta\tau$ with respect to the pump pulses as well. The idler pulses also have pulse energy fluctuation ΔE_p due to the change of the parametric interaction. The change on the center frequency of the pulse ν_c, chirp C and pulse duration τ_p is relatively minor. Normally, these parameters have minimal effect in determining the spectral performance of the resulting frequency comb [39]. We study and quantify the noise transfer for both 1-μm and 2-μm driven DFG operating in different regimes.

4.3.1   Noise transfer in 1-μm driven DFG

To demonstrate the changes initiated by RTJ between the pump pulses and the signal pulses, we give an example of 1-μm driven DFG process seeded with 170-fs, 1030-nm, 100-nJ pump pulses and 130-fs, 1150-nm, 100-nJ signal pulses inside a 2-mm-thick GaSe. The generated idler centers at 9.87 μm. As we have studied in Section 3.4.2, such launching conditions set the DFG process operating in the linear regime. At the input, we vary the initial temporal delay between pump pulses and

(a) Input pump/signal pulse with RTJ   (b) Output idler pulse
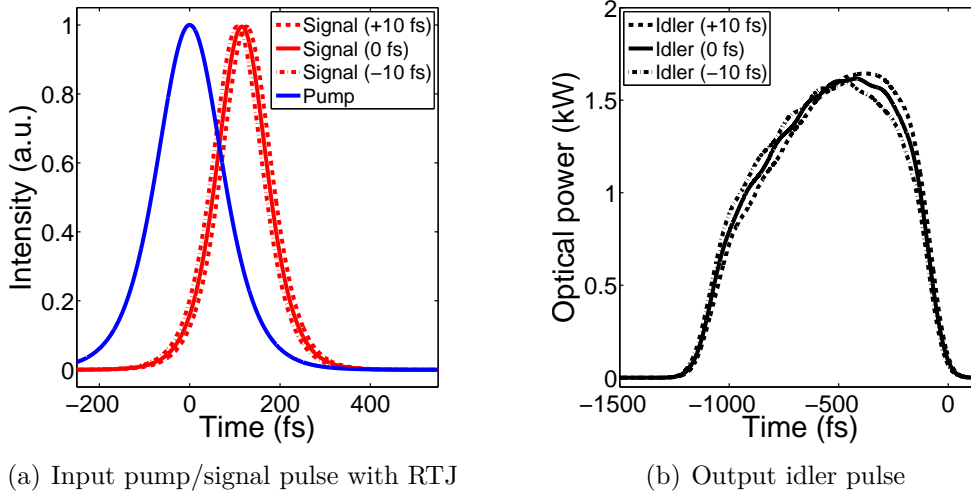
Figure 4.3: Example of noise transfer in 1-μm driven DFG.

1-μm driven DFG inside a 2-mm-thick GaSe is examined under the presence of RTJ between pump pulses and signal pulses. Both input pulses have 100-nJ pulse energy. The initial time delay between the pump/signal pulse is set at the optimal value (0 fs), and optimal value with $\pm$10 fs offset. (a) Normalized intensity profiles for the input pulses. (b) Output idler pulse profile in the unit of optical power.

signal pulses to emulate the presence of RTJ. Since an optimal temporal delay exists to maximize the generated idler's pulse energy, we set the initial temporal delay at the optimal value, and optimal value with $\pm$10 fs offset. We refer to them as "0 fs" and "$\pm$10 fs". The normalized intensity profiles of the input pump/signal pulses are plotted in Fig. 4.3(a). By solving the time-dependent coupled wave equations (Eq. 3.7), the idler pulses at the output are calculated and plotted in Fig. 4.3(b). The idler profile corresponds to its optical power after exiting the crystal.

The results in Fig. 4.3(b) shows that the manually imposed RTJ leads to the timing fluctuation on the output idler. The center-of-gravity temporal position of the idler pulses is -564.0 fs (-10 fs), -545.1 fs (0 fs), and -526.4 fs (+10 fs), respectively. During DFG, 10-fs RTJ between pump and signal is "amplified" to about 18.8-fs RTJ between pump and idler. This is a result caused by the nonlinear parametric interaction and the subsequent linear pulse propagation. For example, when the input RTJ is set at -10 fs, the idler is generated earlier compared with the case of 0-fs RTJ and +10-fs RTJ. After the idler is generated, it undergoes passive pulse propagation and accumulates relative temporal delay due to the pump-idler group velocity mismatch (GVM). Consequently, the idler pulses in DFG with -10-fs RTJ come fastest among the three cases as it propagates the most distances inside the crystal and accumulates the most group delay.

It is noteworthy that the temporal position of the idler pulse is calculated in a

90

time frame that is co-propagating with the pump pulses, and, therefore, it stands for the "relative" timing difference between the pump pulses and the idler pulses. To calculate the temporal position of the idler pulses in the lab frame, the timing of the pump pulses also needs to be included. The timing jitter noise of the pump pulses is related with the repetition rate f_{rep} noise of the master laser system, and it can be controlled by adding a feedback loop to the master laser cavity for stabilizing f_{rep}. However, the RTJ of the idler pulses shown in Fig. 4.3 is introduced during DFG process, which is external to the cavity. This additional RTJ on the idler pulses cannot be compensated by the intra-cavity feedback systems and it needs to be minimized by reducing the noise transfer during DFG and optimizing the wavelength shifting process so that less RTJ is introduced to the signal pulses.

The idler pulses shown in Fig. 4.3(b) have different pulse energy, which represents the additional relative intensity noise induced from input RTJ. The pulse energy is 1.326 nJ (-10 fs), 1.331 nJ (0 fs), and 1.327 nJ (+10 fs), respectively. Apparently, when the signal pulses have the "optimal" timing position, the parametric interaction is optimized so that the generated idler pulses have highest pulse energy. When the signal pulses have a timing position that is off "optimal", the generated idler has less pulse energy. The relative change on the idler pulse energy is about 0.4% for an input RTJ of 10 fs.

In Figure 4.3(b), the intensity profiles of output idler pulses are also slightly different. However, in most theoretical analysis of optical frequency combs [83, 103–106], the optical pulse in a pulse train is characterized by its pulse energy E_p, timing jitter $\Delta\tau$, pulse duration τ_p, center frequency ν_c, chirp C, and carrier-envelop offset phase ϕ_{ce}. The performance of the frequency comb, such as comb line-width, precision of the optical frequency, and comb SNR is determined by the noise spectrum of theses parameters, particularly ΔE_p and $\Delta\tau$ (RIN and RTJ noise) [39]. Since the optical pulse of interest is sampled in a time interval that is inverse to the repetition rate f_{rep}, normally at tens of nanosecond, the change of the envelope function, which is at femtosecond scale, can be discarded. The change of the pulse envelope also has minor impact on the performance of the frequency comb. In the following section, we do not consider the change of the output idler pulse's envelope caused by input RTJ.

The change on the pulse duration of the output idler pulse τ_p is also minimal with the introduction of RTJ. The idler pulses shown in Fig. 4.3(b) have a root-mean-square (rms) pulse duration of 550.8 fs (-10 fs), 548.7 fs (0 fs), and 546.2 fs (+10 fs), respectively. The relative change is about 0.4% for 10-fs input RTJ. The center frequency of the output idler ν_c and its chirp C has negligible change. In the following part of this section, we do not consider the change of the pulse duration τ_p, the center optical frequency ν_c, and the chirp C that are caused by input RTJ during DFG.

By varying the RTJ of the input pump/signal pulses between ± 20 fs around the optimal value, we calculate the corresponding timing fluctuation and relative intensity fluctuation of the output idler pulses. The input pump/signal pulses have 100-nJ pulse energy, ensuring that DFG operates in the linear regime. GaSe is set at 0.1 mm, 1 mm, 2 mm, and 4 mm so that noise transfer for 1-μm driven
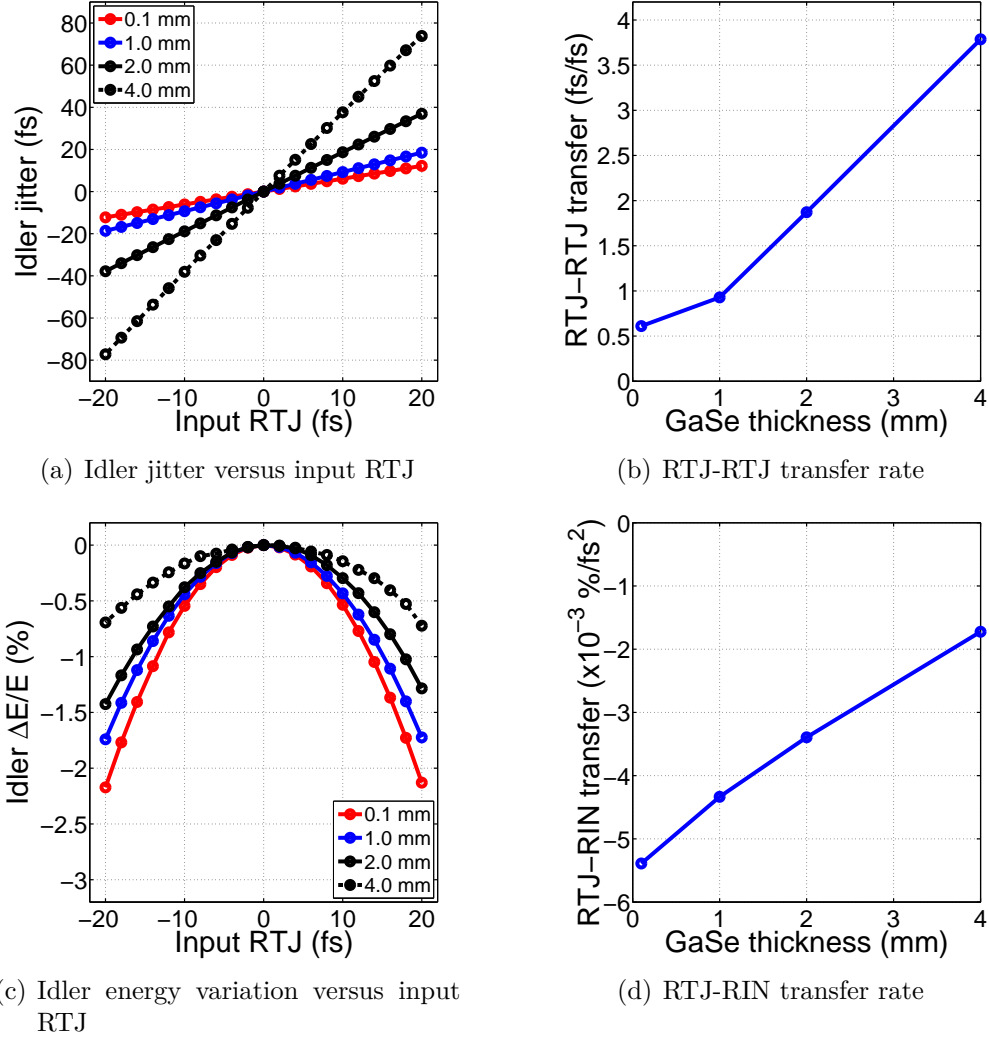
(a) Idler jitter versus input RTJ

(b) RTJ-RTJ transfer rate

(c) Idler energy variation versus input RTJ

(d) RTJ-RIN transfer rate

Figure 4.4: Noise transfer in 1-μm driven DFG (linear regime).

1-μm driven DFG is examined under the presence of RTJ. Pump is 100-nJ and signal is 100-nJ. DFG operates in the linear regime. (a) Idler timing jitter versus input RTJ. (b) RTJ-RTJ transfer rate versus GaSe crystal thickness. (c) Relative energy (intensity) fluctuation of the idler versus input RTJ. (d) RTJ-RIN transfer rate versus GaSe crystal thickness.

DFG at different crystal thickness can be examined. The optimal temporal delay between the pump pulses and signal pulses at the input is changed accordingly to accommodate different crystal thickness.

Figure 4.4(a) plots the timing fluctuation of the output idler pulses against the input RTJ. RTJ of the output idler pulses has a linear relationship to RTJ of the input signal pulses. When the GaSe crystal is thicker, the curve is steeper. The slope of the curves, which stands for the RTJ-RTJ transfer rate, is 0.61 fs/fs (0.1 mm), 0.93 fs/fs (1.0 mm), 1.87 fs/fs (2.0 mm), and 3.79 fs/fs (4.0 mm), respectively. Figure 4.4(b) plots the RTJ-RTJ transfer rate versus GaSe thickness. DFG process in a 0.1-mm-thick GaSe crystal has the lowest RTJ-RTJ noise transfer rate of <1, which is a result of minimized GVM-related effect. When a 0.1-mm-thick GaSe is used, RTJ noise is "suppressed" during DFG. In this situation, the pump pulses act as an intensity gating for regulating the temporal position of the output idler pulses, and therefore, the resulting idler RTJ is smaller than the signal RTJ. When the GaSe crystal becomes thicker, more RTJ is introduced to the output idler pulses. As plotted in Fig. 4.4(b), the RTJ-RTJ transfer rate increases in proportion to the crystal thickness, indicating that the timing fluctuation of the idler pulses is correlated with GVM effect.

Meanwhile, input RTJ also causes the intensity (pulse energy) fluctuation of the output idler pulses. Figure 4.4(c) plots the relative intensity fluctuation ($\Delta E_p/E_p$) of the output idler versus input RTJ. All the curves resemble a parabola but with different radius of curvature. The radius of curvature, which stands for the RTJ-RIN transfer rate, increases as the GaSe crystal becomes thicker, indicating the RTJ-RIN transfer is reduced with increased crystal thickness. Figure 4.4(d) shows the second-order polynomial coefficient of the parabola versus GaSe thickness. As we can see, DFG in a 0.1-mm-thick GaSe crystal has the highest RTJ-RIN transfer of about -5.4×10^{-3} %/fs^2. If the input RTJ is 10 fs, the pulse energy of the output idler fluctuates at a rate of 0.54%. For a 4-mm-thick GaSe crystal, the RTJ-RIN transfer rate reduces to -1.8×10^{-3} %/fs^2. For type-I DFG process between 1030 nm pump and 1150 nm signal, the pump-signal GVM is 97 fs/mm and a 0.1-mm-thick GaSe crystal causes 9.7-fs temporal walk-off. An input RTJ of 10 fs can significantly change the temporal overlapping condition. Conversely, if a 4-mm-thick GaSe is hosting DFG, the total pump-signal temporal walk-off is 390 fs. Consequently, an input RTJ of 10 fs has less change to the temporal overlap, resulting in less RTJ-RIN transfer.

Above analysis shows the noise transfer characteristic for 1-μm driven DFG that operates in the linear regime. When DFG operates in OPA regime, both the signal and the idler have an exponential gain from the parametric process, and we expect the overall gain for the signal/idler is more sensitive to the initial timing position of the signal pulse. To study DFG operating in OPA regime, we set the input signal at 1-nJ and the input pump at 500-nJ. According to the results shown in Section 3.4.2, DFG operates in OPA regime under such launching conditions. Similar to previous calculations, we manually add an input RTJ of ±20 fs and calculate the corresponding timing and pulse energy fluctuation of the output idler pulses RTJ-RTJ and RTJ-RIN noise transfer is calculated based on
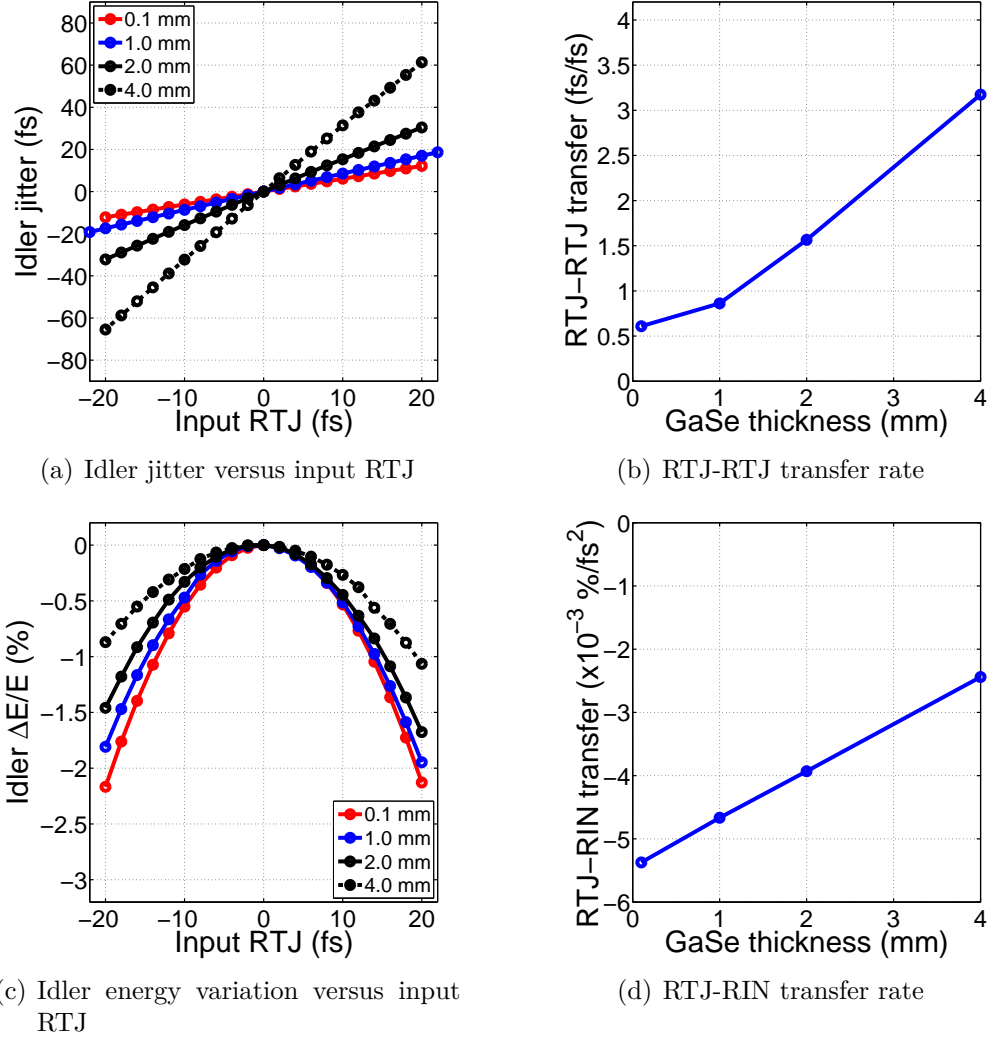
(a) Idler jitter versus input RTJ

(b) RTJ-RTJ transfer rate

(c) Idler energy variation versus input RTJ

(d) RTJ-RIN transfer rate

Figure 4.5: Noise transfer in 1-μm driven DFG (OPA regime).

1-μm driven DFG is examined under the presence of RTJ. Pump is 500-nJ and signal is 1-nJ. DFG operates in OPA regime. (a) Idler timing jitter versus input RTJ. (b) RTJ-RTJ transfer rate versus GaSe crystal thickness. (c) Relative energy (intensity) fluctuation of the idler versus input RTJ. (d) RTJ-RIN transfer rate versus GaSe crystal thickness.

(a) RTJ-RTJ transfer rate versus pump

(b) RTJ-RIN transfer rate versus pump
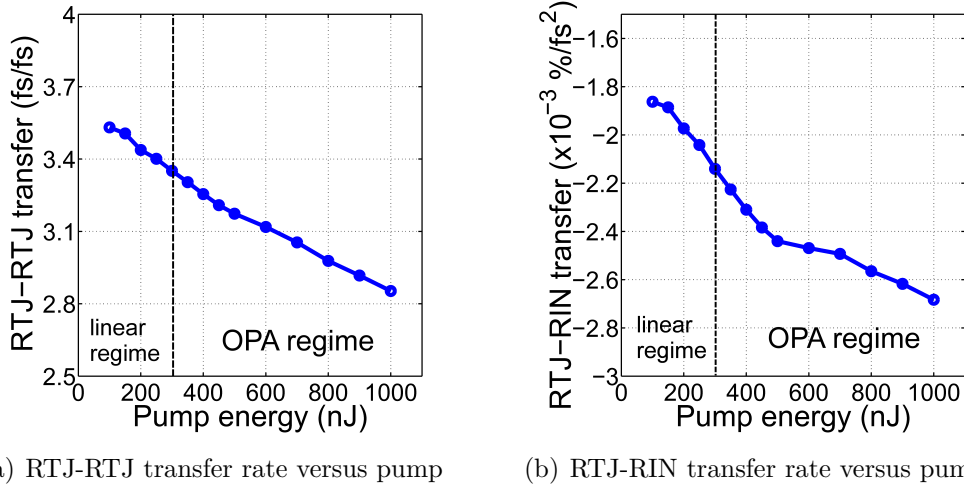
Figure 4.6: Noise transfer in 1-μm driven DFG with signal fixed.

1-μm driven DFG is examined under the presence of RTJ. Signal is fixed at 1-nJ and pump is increasing from 100-nJ to 1-μJ. GaSe is 4-mm-thick. (a) RTJ-RTJ transfer rate versus pump energy. (b) RTJ-RIN transfer rate versus pump energy.

the results. GaSe is set at 0.1 mm, 1 mm, 2 mm, and 4 mm.

Figure 4.5(a) shows RTJ of the output idler versus RTJ of the input signal. The RTJ-RTJ transfer rate is 0.61 fs/fs (0.1 mm), 0.86 fs/fs (1 mm), 1.57 fs/fs (2 mm), and 3.17 fs/fs (4 mm), respectively. Figure 4.5(b) plots the RTJ-RTJ transfer rate versus GaSe thickness. Compared with DFG in the linear regime, DFG in OPA regime has a marginally reduced RTJ-RTJ transfer. In OPA regime, DFG offers more gain. When three pulses (pump, signal, and idler) are propagating in the first-half of the crystal, the signal pulses have more gain compared with the case of linear DFG. During the second-half, the idler pulses have a faster growth since the signal pulses have been amplified during the first-half. The idler generated during the second-half of DFG forms the majority of the final output idler pulse. As a result, the timing position of the output idler pulses is largely determined by the timing of the idler generated in the second-half of the crystal, which has less GVM effect due to less propagation distances. Therefore, RTJ-RTJ transfer for DFG in OPA regime is lower compared with DFG in the linear regime.

Figure 4.5(c) plots the relative pulse energy change versus input RTJ. The RTJ-RIN transfer rate versus GaSe thickness is plotted in Fig. 4.5(d). Similar with DFG in the linear regime, DFG in OPA regime also has a lower RTJ-RIN transfer for thicker crystals. However, the rate of RTJ-RIN transfer is higher compared with DFG in the linear regime. For example, using 4-mm-thick GaSe, DFG in OPA regime has a RTJ-RIN transfer of -2.4×10^{-3} %/fs^2, whereas DFG in the linear regime has -1.7×10^{-3} %/fs^2.

To systematically compare DFG operating in the linear regime and OPA regime,

we carry out noise transfer calculation by fixing the input signal at 1-nJ and increasing the input pump from 100-nJ to 1-μJ. GaSe is chosen to be 4-mm-thick. As shown in Section 3.4.2, DFG transits into OPA regime when the pump pulse energy exceeds 300-nJ. The corresponding noise transfer rates are calculated and the results are shown in Fig. 4.6. Figure 4.6(a) plots RTJ-RTJ transfer versus pump energy and Figure 4.6(b) plots RTJ-RIN transfer versus pump energy.

The curve in Fig. 4.6(a) shows that the RTJ-RTJ transfer decreases with increased pump. Apparently, increasing the pump can effectively increase the parametric interaction. When the input pump is increasing, more idler is generated, especially during the second-half of DFG process where the signal has been amplified during the first-half. As a result, the output idler accumulates less net GVM for an increased pump, resulting less RTJ-RTJ transfer. When DFG operates in the OPA regime, the gain is offered to the signal (and the idler) in an exponential fashion. Therefore, the pulse energy of the output signal/idler pulses is more sensitive to the change of parametric interaction, which is related to the timing position of the input signal pulses. As a result, increased pump leads to larger RTJ-RIN transfer and therefore DFG in OPA regime has a higher RTJ-RIN transfer rate (Fig. 4.6(b)) compared with DFG in the linear regime.

To study DFG in the saturation regime, we set the input signal at 300-nJ and the input pump at 100-nJ. According to the results shown in Section 3.4.2, DFG operates in the saturation regime under these launching conditions. We perform similar simulations to calculate the RTJ-RTJ and RTJ-RIN noise transfer.

Figure 4.7(a) plots the induced RTJ versus input RTJ at different GaSe thickness and Figure. 4.7(b) plots the RTJ-RTJ transfer rate versus GaSe thickness. The RTJ-RTJ transfer rate is 0.61 fs/fs (0.1 mm), 0.97 fs/fs (1.0 mm), 2.08 fs/fs (2.0 mm), and 4.14 fs/fs (4.0 mm), respectively. Compared with DFG in the linear regime and OPA regime, DFG in the saturation regime has the highest RTJ-RTJ transfer. For DFG in the saturation regime, pump pulses are partly depleted during the second-half of DFG. Since a large portion of the final output idler pulses is generated during the first-half, the idler pulses undergo more propagation distances and accumulate more temporal delay. As a result, DFG in the saturation regime has the highest RTJ-RTJ noise transfer.

On the other hand, as plotted in Fig. 4.7(c) and Fig. 4.7(d), DFG in the saturation regime has the lowest RTJ-RIN noise transfer. This is also a result of pump depletion. For example, for 4-mm-thick GaSe, the input pump (100 nJ) has 38.1-nJ pulse energy after DFG. Inside the crystal, 5-nJ idler pulses are generated. The corresponding pump-to-idler quantum efficiency is 54.7% (saturation regime), 24.7% (linear regime), and 0.5% (OPA regime), respectively. For DFG with a quantum efficiency of 54.7%, the pump has a strong "gating" effect on the pulse energy of the idler and DFG has less dependence on the timing position of the input signal pulses. For DFG in the saturation regime, the RTJ-RIN transfer is minimal, compared with DFG in the linear regime and OPA regime.

To sum up, we plot in Figure 4.8 the RTJ-RTJ and RTJ-RIN noise transfer rate for 1-μm driven DFG in different operation regimes. Figure 4.8(a) plots the RTJ-RTJ transfer rate, showing that DFG in the OPA regime has the least RTJ-RTJ
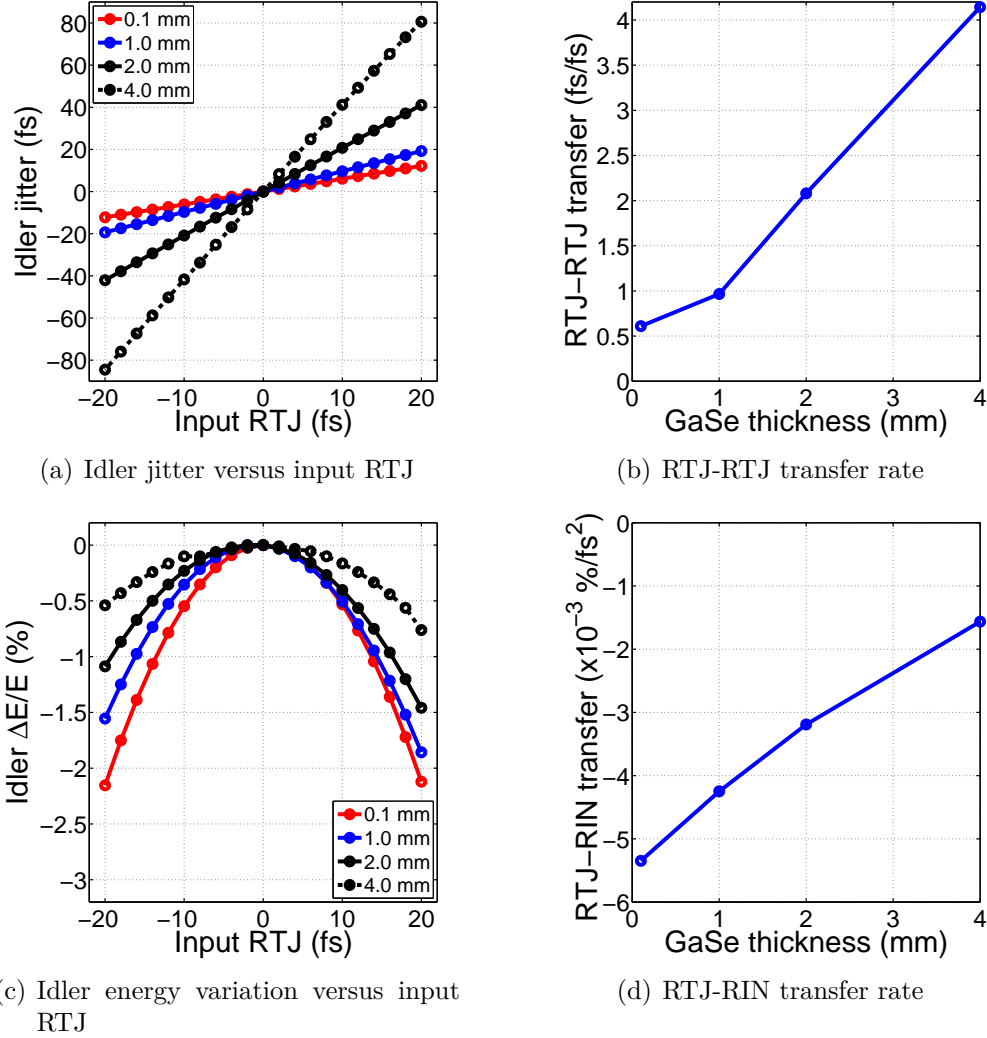
(a) Idler jitter versus input RTJ

(b) RTJ-RTJ transfer rate

(c) Idler energy variation versus input RTJ

(d) RTJ-RIN transfer rate

Figure 4.7: Noise transfer in 1-μm driven DFG (saturation regime).

1-μm driven DFG is examined under the presence of RTJ. Pump is 100-nJ and signal is 300-nJ. DFG operates in the saturation regime. (a) Idler timing jitter versus input RTJ. (b) RTJ-RTJ transfer rate versus GaSe thickness. (c) Relative energy (intensity) fluctuation of the idler versus input RTJ. (d) RTJ-RIN transfer rate versus GaSe thickness.

(a) RTJ-RTJ transfer rate   (b) RTJ-RIN transfer rate
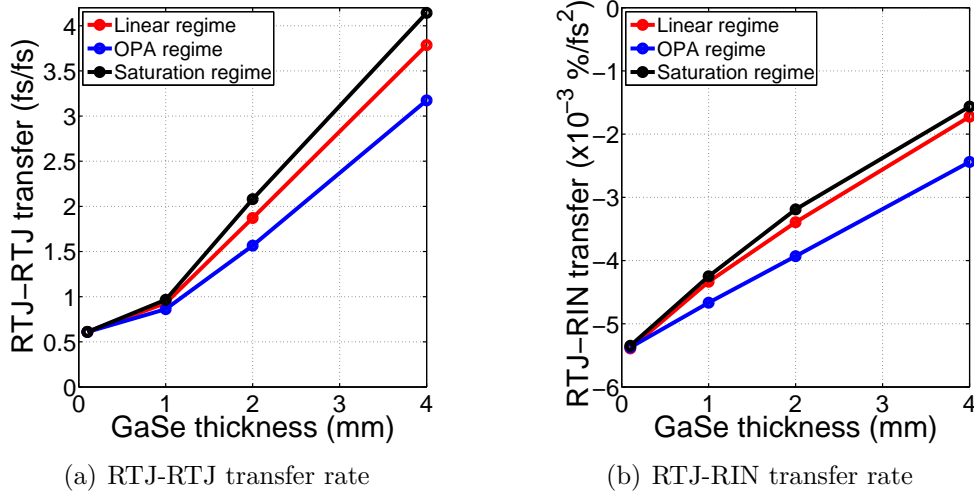
Figure 4.8: Noise transfer rate in 1-μm driven DFG.

The RTJ-RTJ and RTJ-RIN noise transfer is studied for 1-μm driven DFG in the linear regime (red lines), OPA regime (blue lines), and the saturation regime (black lines). (a) RTJ-RTJ transfer rate versus the GaSe crystal thickness. (b) RTJ-RIN transfer rate versus the GaSe crystal thickness.

transfer. The results in Fig. 4.8(b) indicates that DFG in the saturation regime has the least RTJ-RIN transfer.

For offset-free frequency combs, timing jitter noise, or the repetition rate noise, strongly affects the spectral characteristic of the comb lines. The timing jitter noise translates to the optical frequency noise in a quadratic scaling fashion [119]. In other words, $S_{\delta\nu}(f) = \dfrac{\nu^2}{f_{\text{rep}}^2} \cdot S_{\delta f_{\text{rep}}}(f)$. To reduce the RTJ noise of the output idler pulses, one effective approach is to use a thinner GaSe crystal. For example, the RTJ-RTJ noise transfer is reduced by roughly a factor of 4 if the crystal thickness is reduced from 4-mm to 1-mm. However, a reduced crystal thickness leads to insufficient parametric interaction for DFG, which prevents the generation of high-power output idler. In Section 3.5, we show that DFG process with the input pump centered at 2-μm has advantages over 1-μm driven DFG for more effectively scaling the pulse energy of the idler pulses. In 2-μm driven DFG, the center wavelength of the pump/signal/idler is closer to each other and GVM effect is significantly lower compared with 1-μm driven DFG. Since the RTJ-RTJ noise transfer is affected by GVM, we anticipate a different noise transfer.

4.3.2 Noise transfer in 2-μm driven DFG

For 2-μm driven DFG, pump-signal GVM is about 20 fs/mm for generating an output idler centered at 10-μm, while it is about 100 fs/mm for 1-μm driven DFG. The pump-idler GVM for 2-μm driven DFG is also much smaller compared with

(a) Idler jitter versus input RTJ

(b) RTJ-RTJ transfer rate

(c) Idler energy variation versus input RTJ

(d) RTJ-RIN transfer rate
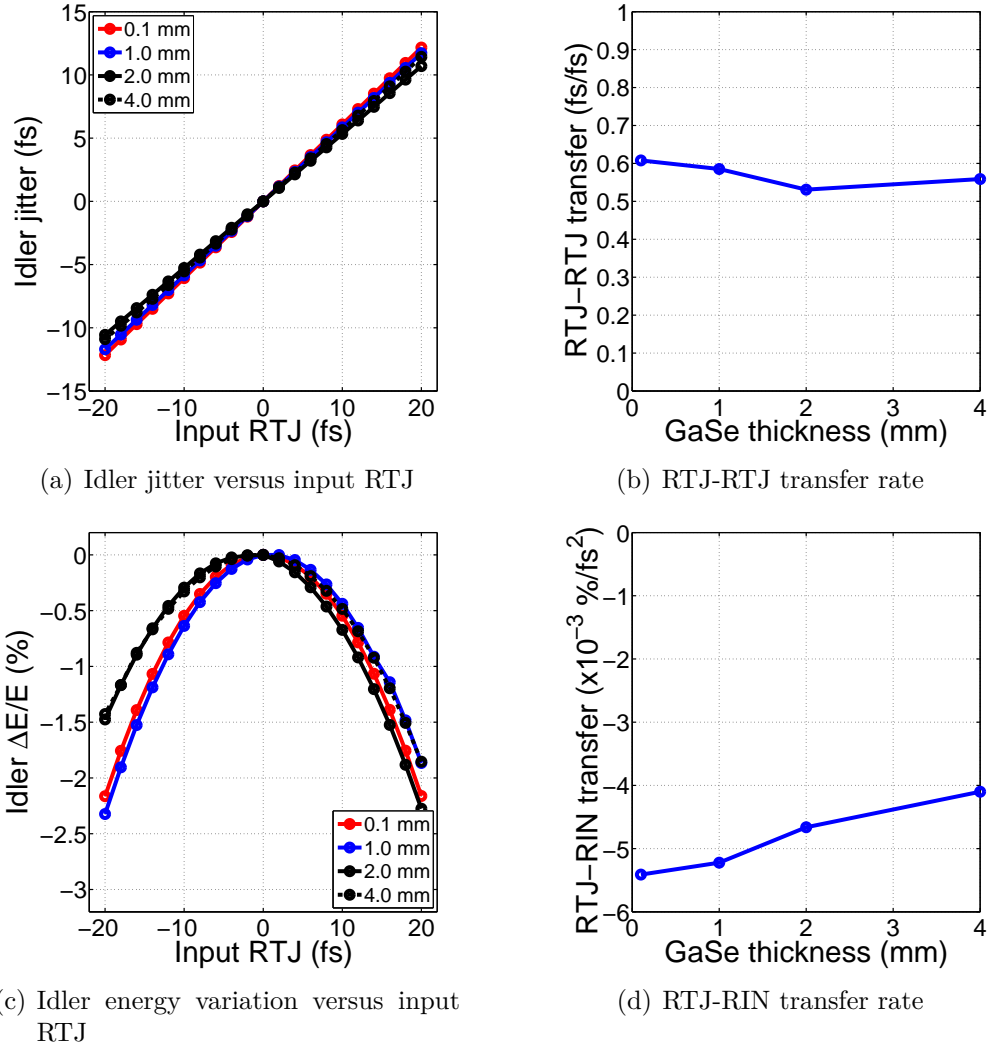
Figure 4.9: Noise transfer in 2-μm driven DFG.

2-μm driven DFG is examined under the presence of RTJ between 100-nJ pump pulses and 100-nJ signal pulses. (a) Idler timing jitter versus the input RTJ. (b) RTJ-RTJ transfer rate versus the GaSe crystal thickness. (c) Idler energy (intensity) variation versus the input RTJ. (d) RTJ-RIN transfer rate versus the GaSe crystal thickness.

1-μm driven DFG (32 fs/mm versus 600 fs/mm). A reduced GVM has several advantages: (1) the pump-signal temporal overlap is significantly increased, which facilitates the generation of high-power output idler; (2) less pump-idler GVM benefits the generation of ultra-short idler pulses; and (3) the idler pulses have less temporal walk-off with respect to the pump pulses, leading to less RTJ-RTJ noise transfer.

To study the noise transfer, we simulate 2-μm driven DFG seeded with 170-

99

fs, 2-μm pump pulses and 130-fs, 2.15-μm signal pulses. The generated idler centers at 9.87-μm. GaSe thickness is set at 0.1 mm, 1 mm, 2 mm, and 4 mm. After calculating a wide range of experimental parameters (different combination of pump pulse energy and signal pulse energy), we discover that the noise transfer in 2-μm driven DFG has minimal difference for DFG operating in different regime due to low pump-signal GVM. Here we select one situation where both the pump and the signal have 100-nJ pulse energy at the input. According to Section 3.5.3, such launching conditions set DFG operate in the linear regime.

The noise transfer is calculated and the results are plotted in Fig. 4.9. Figure 4.9(a) shows RTJ of the output idler versus RTJ of the input signal. Due to a reduced GVM, the RTJ-RTJ transfer in 2-μm driven DFG has less dependence on the thickness of GaSe crystals. As Figure 4.9(b) shows, the RTJ-RTJ noise transfer rate is about 0.55 fs/fs for GaSe crystal being from 0.1-mm to 4-mm, much lower compared with 1-μm driven DFG. For example, when the GaSe crystal is 4-mm-thick, 1-μm driven DFG has a RTJ-RTJ noise transfer of 3.5 fs/fs, while 2-μm driven DFG has a RTJ-RTJ noise transfer of 0.5 fs/fs, which is 7 times lower.

Figure 4.9(c) plots the intensity fluctuation caused by the input RTJ. The radius of curvature for all curves is similar, indicating the RTJ-RIN transfer rate is at the same level for different crystal thickness. Figure 4.9(d) plots the RTJ-RIN transfer rate versus the GaSe thickness. The RTJ-RIN transfer is slightly reduced for a thicker GaSe crystal. The transfer rate averages at about -4.8×10^{-3} %/fs^2, which is higher than the RTJ-RIN noise transfer rate in 1-μm driven DFG ($\sim$ -3.5×10^{-3} %/fs^2 for a 2-mm-thick GaSe). For 2-μm driven DFG, the GVM between pump and signal is about 20 fs/mm, which provides an increased temporal overlap between pump pulses and signal pulses, leading to a more efficient generation of the idler. Meanwhile, an input RTJ of 10-fs can, therefore, have more change in the temporal overlapping condition, resulting higher RTJ-RIN noise transfer rate. Compared with 1-μm driven DFG, 2-μm driven DFG has about 2 times more RTJ-RIN transfer when the GaSe crystal is 4-mm-thick.

To conclude, 2-μm driven DFG exhibits 7 times lower RTJ-RTJ noise transfer compared with 1-μm driven DFG due to its low pump-signal and pump-idler GVM in GaSe crystals. Meanwhile, since 2-μm driven DFG offers larger parametric gain to the idler, the RTJ-RIN noise transfer is marginally higher compared with 1-μm driven DFG.

4.4 Relationship between timing jitter noise and comb spectrum

DFG-based mid-IR frequency combs are generated via frequency mixing two pulse trains with different center wavelengths. Given the pump/signal pulses share the same f_{ceo}, the generated mid-IR idler pulses have the offset phase ϕ_{ce} automatically canceled. As has been studied in Section 4.3, these offset-free idler pulses have additional RTJ noise and relative intensity noise (RIN) after DFG. Adding together

(a) Timing jitter of mode-locked pulse   (b) Timing jitter of offset-free pulse
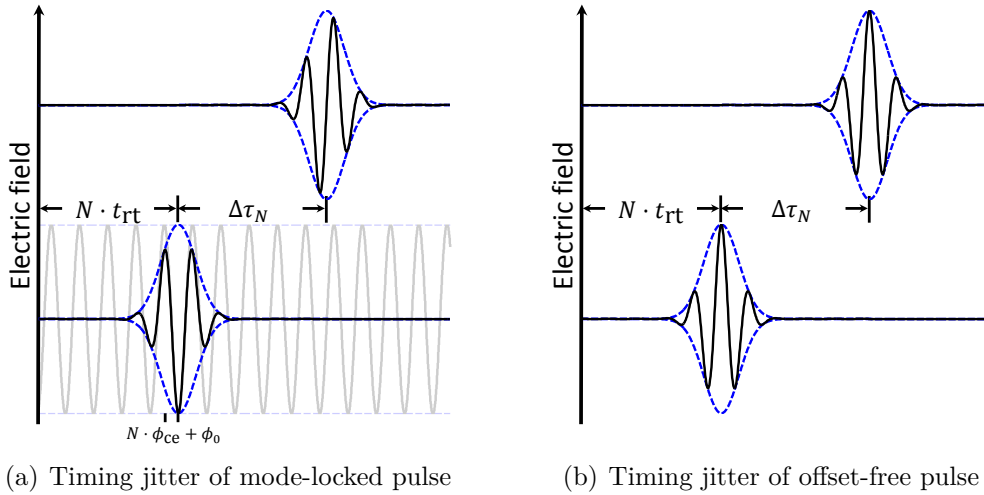
Figure 4.10: Timing jitter of mode-locked pulses and offset-free pulses.

The presence of timing jitter on pulses from a mode-locked laser system and offset-free pulses are different. (a) For mode-locked pulses, timing jitter does not change the phaser of the electric field. (b) For offset-free pulse, since its electric field is always in phase with its envelope, timing jitter causes the temporal shifting of the electric field as well.

with the timing jitter noise and RIN of the pump pulses, these noises of the offset-free pulses render the mid-IR frequency combs with broadened comb line-width and reduced comb SNR.

Unlike optical pulses from mode-locked laser systems whose optical phase is determined by the mode-locked oscillators and subsequent amplification systems, the optical phase of offset-free pulses is constantly locked with the pulse envelope. We illustrate the difference between pulses from mode-locked lasers and offset-free pulses generated via DFG in Fig. 4.10. The envelope and the electric field of the Nth pulse from a pulse train are plotted. Figure 4.10(a) plots the pulse from a mode-locked laser system with the presence and absence of timing jitter. In the plot without the timing jitter (lower graph in Fig. 4.10(a)), the phasor of the electric field is also plotted in a gray sinusoid trace to illustrate the optical carrier.

When timing jitter noise is absent, the envelope of the Nth optical pulse is centered at $N \cdot t_{\mathrm{rt}}$ in the time domain. Its electric field has a phase slippage of $(N \cdot \phi_{\mathrm{ce}} + \phi_0)$ with respect to its envelope. ϕ_{ce} the intra-cavity carrier envelope offset phase and ϕ_0 stands for the additional optical phase the pulse accumulates external to the cavity. Here, ϕ_0 is considered constant with respect to N, i.e., we assume all the pulses from a pulse train experience same phase external to the cavity. When timing jitter is present, the pulse envelope is shifted by an amount of $\Delta\tau_N$ in the time domain. For each pulse, $\Delta\tau_N$ is intrinsically different. The correlation function of the timing jitter $\Delta\tau_N$ can be translated to the power spectral density

(PSD) $S_{\Delta\tau}(f)$ of the timing jitter noise by the Wiener-Khinchin theorem. When $\Delta\tau_N$ is completely uncorrelated, $S_{\Delta\tau}(f)$ has a white noise spectrum.

If we consider the phase jitter $\Delta\phi_N$ is uncorrelated with the timing jitter, the phasor of its electric field does not change with respect to the timing jitter $\Delta\tau_N$. In this scenario, the optical field (which is proportional to the electric field) of a pulse train can be written as (similar to Equation (65) in [120])

$$
\begin{aligned}
A(t) = \sum_{N=-\infty}^{+\infty} & a(t - N \cdot t_{\text{rt}} - \Delta\tau_N) \\
& \cdot \exp[-i \cdot 2\pi\nu_c(t - N \cdot t_{\text{rt}})] \exp[-i \cdot (N \cdot \phi_{\text{ce}} + \phi_0 + \Delta\phi_N)].
\end{aligned}
\tag{4.5}
$$

Here $a(t)$ is the noise-less amplitude of the optical field. $\Delta\tau_N$ and $\Delta\phi_N$ stands for the timing jitter and phase jitter of the Nth pulse of a pulse train.

Meanwhile, as plotted in Figure 4.10(b), the offset-free pulse is generated via DFG and its electric field is always in phase with respect to its envelope. In other words, $\phi_{\text{ce}} \equiv 0$. When the pulse has a timing jitter of $\Delta\tau_N$, its phasor also shifts by an amount of $2\pi\nu_c \cdot \Delta\tau_N$. The optical field of the offset-free pulse train shifts together with its envelope in the time domain, which writes the optical field of a pulses train as

$$
A(t) = \sum_{N=-\infty}^{+\infty} a(t - N \cdot t_{\text{rt}} - \Delta\tau_N) \cdot \exp[-i \cdot 2\pi\nu_c(t - N \cdot t_{\text{rt}} - \Delta\tau_N)].
\tag{4.6}
$$

Here $\Delta\tau_N$ is the timing jitter of the Nth pulse of a pulse train, with a PSD of $S_{\Delta\tau}(f)$. Since a temporal shift of $(N \cdot t_{\text{rt}} + \Delta\tau_N)$ corresponds to a phasor multiplier of $\exp[i \cdot 2\pi\nu \cdot (N \cdot t_{\text{rt}} + \Delta\tau_N)]$ in the Fourier (spectral) domain, the spectral field of an offset-free pulse train with timing jitter noise is then written as

$$
\tilde{A}(\nu) = \sum_N \tilde{a}(\nu) \cdot \exp[i \cdot 2\pi\nu \cdot (N \cdot t_{\text{rt}} + \Delta\tau_N)],
\tag{4.7}
$$

where $\tilde{a}(\nu)$ stands for the frequency component (Fourier transform) of the optical field. The modulus square of $\tilde{A}(\nu)$ gives the optical spectrum of the pulse train.

$$
I(\nu_c) = \left|\tilde{A}(\nu_c)\right|^2.
\tag{4.8}
$$

In this section, we use Monte-Carlo (M-C) method to calculate the optical spectrum of the offset-free frequency comb under different types of timing jitter noises. Three types of timing jitter noises are discussed: (1) white timing jitter noise where $S_{\Delta\tau}(f) = S_0$; (2) $1/f^2$ timing jitter noise where $S_{\Delta\tau}(f) \propto 1/f^2$; and (3) hybrid timing jitter noise. For hybrid timing jitter noise, $S_{\Delta\tau}(f)$ is dominated by $1/f^2$ noise at low Fourier frequencies, and by white noise at high frequency. We determine the relationship between the comb line with the timing jitter noise. We show that the comb line-width is more related with the low-frequency noise while the signal-to-noise ratio (SNR) of the comb is related with the white noise at high frequencies. By suppressing the timing jitter noise at low frequencies, the comb can have narrower line-width and increased SNR.

In the following simulation, we assume a pulse train with a repetition rate $f_{\rm rep}$ of 30 MHz and a center wavelength of 10 μm. The center frequency of the pulse ν_c is 30 THz. Around the optical frequency $\nu = \nu_c$, there exists a comb line with a mode index of 1,000,000. In the calculation, the spectrum of this comb line is calculated by assigning a series of random numbers to $\Delta\tau$. The random numbers are based upon random-noise-generator (RNG) from computer CPU. The random number $\Delta\tau_N$ has a mean value $\langle\Delta\tau\rangle = 0$ and a standard deviation of $\sigma_{\Delta\tau}$ [83, 104, 105].
$\sigma_{\Delta\tau}$ can be calculated by its definition $\sigma_{\Delta\tau}^2 = \dfrac{1}{N}\cdot\sum\limits_N (\Delta\tau_N)^2$ or calculated from its noise PSD (In the following, we always use a single-sided PSD),

$$\sigma_{\Delta\tau}^2 = \int_{1/t_{\rm ob}}^{f_{\rm rep}/2} S_{\Delta\tau}(f)\cdot df. \tag{4.9}$$

Here the upper limit of the integral is the Nyquist frequency, which is 15-MHz. The lower limit of the integral is inverse to the observation time, ensuring that the timing jitter is always convergent.

In the calculation, we set an observation time of 1-ms so that in each realization (observation) 30,000 pulses are "observed". In other words, 30,000 random numbers need to be generated and assigned to $\Delta\tau_N$. The random numbers from computer CPU via MatLAB random function can be considered as white noise source, as each number in the series is uncorrelated with each other. To convert the white noise into "$1/f^2$" and "hybrid" noise, we use the computational algorithm as suggested in [121]. For "$1/f^2$" timing jitter noise, the knee frequency $f_{\rm knee}$ [121] is set at the Nyquist frequency, 15-MHz. For hybrid timing jitter noise, $f_{\rm knee}$ is varied.

4.4.1 White timing jitter noise

For white timing jitter noise, $S_{\Delta\tau}(f)$ is independent on the Fourier frequency. The integrated timing jitter (ITJ) of white timing jitter noise increases with increased observation time and it is always convergent. We calculate the optical spectrum at the frequency $\nu = \nu_c$ by setting the timing jitter variance $\sigma_{\Delta\tau}^2$ at $(2\text{ fs})^2$, $(5\text{ fs})^2$, $(10\text{ fs})^2$, and $(15\text{ fs})^2$. It is noteworthy that the pulse train has a center wavelength of 10 μm and its optical period is 33.3 fs. This stands as a reference in determining how "noisy" the timing jitter is with respect to the carrier period.

We perform M-C simulation and plot in Fig. 4.11(a) the spectra of the comb with white timing jitter noise. The comb without any timing jitter noise is also plotted in a blue dashed line as a comparison. In the graph, the spectra are normalized in log scale with a peak of 30 dB. Due to the noise nature of computational method, the comb is too "noisy" to offer meaningful knowledge. Therefore, we carry out 100 independent realizations and take the averaged optical spectrum as the result so that the effect from RNG is minimized. The averaged comb line from 100 realizations is plotted in Fig. 4.11(b). Meanwhile, the timing jitter series in each realization is recorded, Fourier transformed, and taken modulus square for calculating timing jitter PSD. The averaged PSD of 100 realizations is plotted in Figure 4.11(c) (to the left axis). Calculated from PSD, the corresponding ITJ is

(a) Comb spectra (single realization)

(b) Comb spectra (100 realizations)

(c) PSD and ITJ of white timing jitter noise

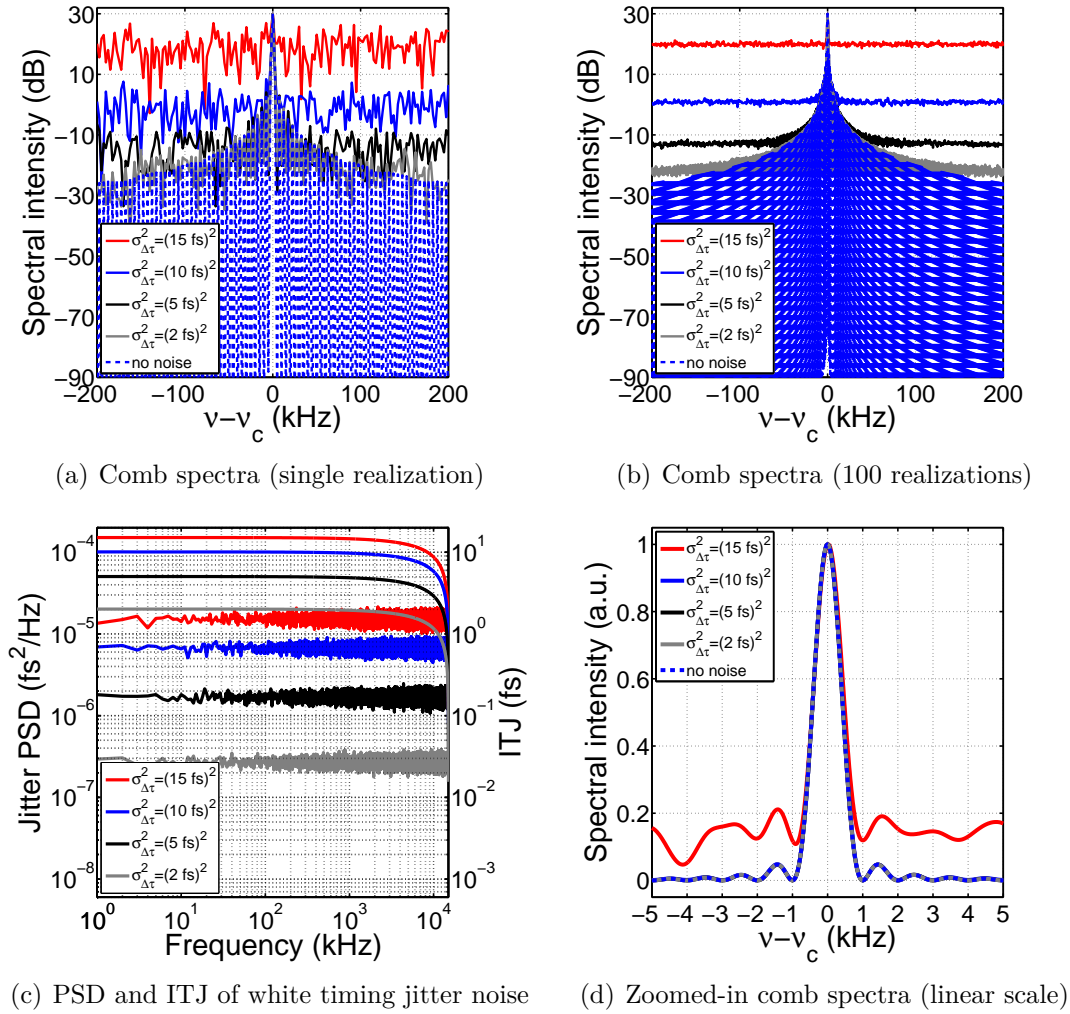(d) Zoomed-in comb spectra (linear scale)

Figure 4.11: Frequency comb with white timing jitter noise.

The optical spectrum at $\nu = \nu_c$ is calculated with white timing jitter noise. (a) Comb spectra of single realization. (b) Comb spectra of 100 realizations. (c) Power spectral density (PSD) and integrated timing jitter (ITJ) (d) Zoomed-in comb spectra in linear scale. Note here the blue/black/gray curve overlaps with the dashed blue line (no noise).

plotted in the same graph (to the right axis). By zooming-in the curves shown in Fig. 4.11(b), we plot in Fig. 4.11(d) the normalized comb spectra in linear scale. Note here the comb line with $\sigma_{\Delta\tau}^2$ of $(2\,\text{fs})^2$, $(5\,\text{fs})^2$, and $(10\,\text{fs})^2$ are nearly identical to the comb line without timing jitter noise.

The results show that frequency comb with white timing jitter noise has different background level away from the comb center. The zoomed-in spectra shows the comb has the same FWHM line-width near comb center. White timing jitter noise contributes to the background of the frequency comb and therefore reduces

the visibility or the SNR of the comb. For example, for white timing jitter noise at $(2 \text{ fs})^2$, the background is at -23 dB. Consider the comb has a peak of 30 dB. The comb line has a SNR of 53-dB. For $\sigma_{\Delta\tau}^2$ being $(5 \text{ fs})^2$, $(10 \text{ fs})^2$, and $(15 \text{ fs})^2$, SNR is 43-dB, 29-dB, and 10-dB, respectively. By inspecting the ITJ plot shown in Fig. 4.11(c), we notice that a large portion of the timing jitter noise is contributed by PSD at high frequency ($>10^3$ kHz). Those high-frequency noises have minimal changes to the spectrum that is close to the comb center $\nu = \nu_c$, As suggested in [122], the modulation caused by high-frequency noises is too fast to exert a significant effect on the comb line-width. Instead, these high-frequency noises have more contribution and result in the spectral background of the frequency comb.

If we re-visit Equation 4.7, the spectral field at $\nu = \nu_c$ can be written as

$$
\begin{aligned}
\tilde{A}(\nu_c) &= \sum_N \tilde{a}(\nu_c) \cdot \exp[i \cdot 2\pi\nu_c \cdot (N \cdot t_{\text{rt}} + \Delta\tau_N)] \\
&= \tilde{a}(\nu_c) \sum_N \exp(i \cdot 2\pi \frac{\nu_c}{f_{\text{rep}}} N) \cdot \exp(i \cdot 2\pi\nu_c \cdot \Delta\tau_N) \\
&= \tilde{a}(\nu_c) \sum_N 1 \cdot \exp(i \cdot 2\pi\nu_c \cdot \Delta\tau_N).
\end{aligned}
\tag{4.10}
$$

If $\nu_c \cdot \Delta\tau_N \ll 1$, the exponential function can be approximated by its first-order Taylor expansion. $\tilde{A}(\nu_c)$ is then written as

$$
\begin{aligned}
\tilde{A}(\nu_c) &= \tilde{a}(\nu_c) \sum_N (1 + i \cdot 2\pi\nu_c \cdot \Delta\tau_N) \\
&= \tilde{a}(\nu_c) \cdot N + i \cdot 2\pi\nu_c \cdot \tilde{a}(\nu_c) \cdot \sum_N \Delta\tau_N.
\end{aligned}
\tag{4.11}
$$

Consider $\Delta\tau_N$ is white noise (uncorrelated), the following identity can be used.

$$
\langle \Delta\tau_i \cdot \Delta\tau_j \rangle = \delta_{ij} \cdot \langle \Delta\tau_i^2 \rangle = \delta_{ij} \cdot \sigma_{\Delta\tau}^2
\tag{4.12}
$$

The spectral intensity at $\nu = \nu_c$ is then written as

$$
I(\nu_c) = \left| \tilde{A}(\nu_c) \right|^2 = N^2 \cdot |\tilde{a}(\nu_c)|^2 + N \cdot |\tilde{a}(\nu_c)|^2 \cdot 4\pi^2\nu_c^2 \cdot \sigma_{\Delta\tau}^2.
\tag{4.13}
$$

Similarly, the spectral field at the frequency $\nu = \nu_c + \frac{1}{2}f_{\text{rep}}$ is

$$
\begin{aligned}
\tilde{A}(\nu_c + \frac{1}{2}f_{\text{rep}}) &= \sum_N \tilde{a}(\nu_c + \frac{1}{2}f_{\text{rep}}) \cdot \exp[i \cdot 2\pi(\nu_c + \frac{1}{2}f_{\text{rep}}) \cdot (N \cdot t_{\text{rt}} + \Delta\tau_N)] \\
&= \tilde{a}(\nu_c + \frac{1}{2}f_{\text{rep}}) \cdot \sum_N \exp(i\pi N) \cdot \exp[i \cdot 2\pi(\nu_c + \frac{1}{2}f_{\text{rep}}) \cdot \Delta\tau_N] \\
&= \tilde{a}(\nu_c + \frac{1}{2}f_{\text{rep}}) \cdot \sum_N (-1)^N (1 + i \cdot 2\pi(\nu_c + \frac{1}{2}f_{\text{rep}}) \cdot \Delta\tau_N) \\
&= \tilde{a}(\nu_c + \frac{1}{2}f_{\text{rep}}) \cdot i \cdot 2\pi(\nu_c + \frac{1}{2}f_{\text{rep}}) \cdot \sum_N (-1)^N \Delta\tau_N.
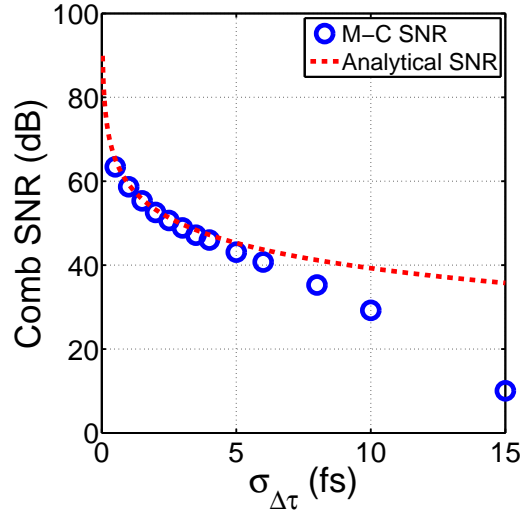\end{aligned}
\tag{4.14}
$$

Figure 4.12: SNR of frequency comb with white timing jitter noise.

SNR calculated by analytical expression (Eq. 4.16) has good agreement with the M-C simulations when the timing jitter noise is below 5-fs.

Consider the spectral amplitude has minimal change with an offset of $\frac{1}{2}f_{\text{rep}}$ and the optical carrier is significantly larger than the repetition rate, we can apply $\tilde{a}(\nu_c + \frac{1}{2}f_{\text{rep}}) \approx \tilde{a}(\nu_c)$ and $\nu_c \gg f_{\text{rep}}$, the spectral intensity at $\nu = \nu_c + \frac{1}{2}f_{\text{rep}}$ is

$$I(\nu_c + \frac{1}{2}f_{\text{rep}}) = \left| \tilde{A}(\nu_c + \frac{1}{2}f_{\text{rep}}) \right|^2 = N \cdot |\tilde{a}(\nu_c)|^2 \cdot 4\pi^2 \nu_c^2 \cdot \sigma_{\Delta\tau}^2. \tag{4.15}$$

The SNR of the frequency comb at $\nu = \nu_c$ can be thus calculated by

$$\text{SNR}(\nu_c) = \frac{N^2 \cdot |\tilde{a}(\nu_c)|^2 + N \cdot |\tilde{a}(\nu_c)|^2 \cdot 4\pi^2 \nu_c^2 \cdot \sigma_{\Delta\tau}^2}{N \cdot |\tilde{a}(\nu_c)|^2 \cdot 4\pi^2 \nu_c^2 \cdot \sigma_{\Delta\tau}^2} \approx \frac{N}{4\pi^2 \nu_c^2 \cdot \sigma_{\Delta\tau}^2}. \tag{4.16}$$

The expression shows that in the presence of white timing jitter noise, higher timing jitter variance leads to lower SNR. When the observation time is longer (more pulse is observed), the resulting frequency comb spectrum has higher SNR. SNR is proportional to the observation time. As the timing jitter noise translates to a phasor multiplier of $\exp(i \cdot 2\pi\nu_c \cdot \Delta\tau_N)$ in the spectral domain, a higher ν_c results in larger phase variation. When the optical frequency of the comb line is higher, the resulting comb line has lower SNR.

We use this formula to calculate SNR with $N = 30,000$ and $\nu_c = 30$ THz and compare the analytical SNR with results from Monte-Carlo simulations. Figure 4.12 plots the analytical SNR in a red dashed line together with Monte-Carlo SNR in blue circles. When the white timing jitter noise is below 5-fs, two methods lead to similar SNR. When the timing jitter exceeds 5-fs, the phasor of the optical field has large fluctuation and the first-order approximation for re-writing the phasor (Eq. 4.11) is no longer valid.

(a) Comb spectra (single realization)

(b) Comb spectra (multiple realizations)

(c) PSD and ITJ of white timing jitter noise

(d) Zoomed-in comb spectra (linear scale)
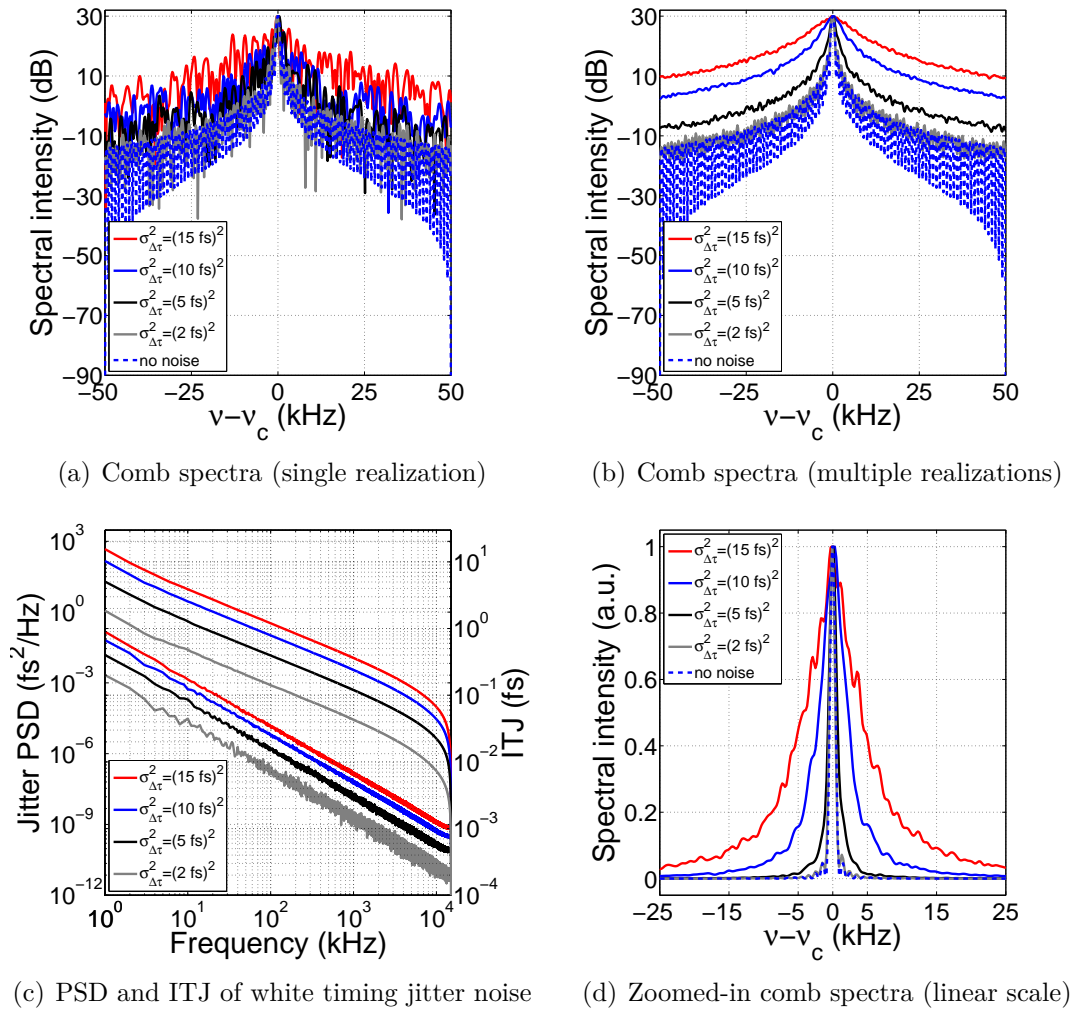
Figure 4.13: Frequency comb with $1/f^2$ timing jitter noise.

The optical spectrum at $\nu = \nu_c$ is calculated with $1/f^2$ timing jitter noise. (a) Comb spectra of single realization. (b) Comb spectra of multiple realizations. (c) Power spectral density (PSD) and integrated timing jitter (ITJ). (d) Zoomed-in comb spectra in linear scale.

4.4.2 $1/f^2$ timing jitter noise

For $1/f^2$ timing jitter, $S_{\Delta\tau}(f)$ is inversely proportional to frequency square, i.e., $S_{\Delta\tau}(f) \propto 1/f^2$. Note here the frequency f is the Fouerier frequency of the timing jitter PSD, but not the optical frequency ν. Since the pulse train is sampled at the repetition rate (30-MHz), noise PSD has an upper limit of 15-MHz (Nyquist frequency). $1/f^2$ noise is also called random-walk noise due to the fact that the timing jitter variance increases with increased observation time. In M-C simulation, we use an observation time of 1-ms so that the timing jitter is always bounded.

We choose the $1/f^2$ timing jitter noise to have a timing jitter variance $\sigma^2_{\Delta\tau}$ of $(2 \text{ fs})^2$, $(5 \text{ fs})^2$, $(10 \text{ fs})^2$, and $(15 \text{ fs})^2$ in the M-C simulations. The resulting comb at $\nu = \nu_c$ using a single realization is calculated and then plotted in Fig. 4.13(a). Similar with the spectra shown in Fig. 4.11(a), the comb line calculated by single realization has large spectral intensity fluctuation and the comb line-width cannot be determined. Therefore, we perform 200 realizations to calculate the averaged comb spectra and jitter PSD. The resulting comb spectra are shown in Fig. 4.13(b). The corresponding PSD and ITJ are plotted in Fig. 4.13(c).

The spectra of the frequency comb under $1/f^2$ timing jitter noise are completely different from those with white timing jitter noise: white timing jitter noise contributes to the raised background level without changing the line-width of the comb; in contrast, $1/f^2$ timing jitter noise changes both the comb line-width and the comb SNR. Figure 4.13(d) plots the comb line in a linear scale in order to show the comb structure. The comb line has a Lorentzian-like line shape with a FWHM of 1.0 kHz $((2 \text{ fs})^2)$, 1.3 kHz $((5 \text{ fs})^2)$, 4.2 kHz $((10 \text{ fs})^2)$, and 8.6 kHz $((15 \text{ fs})^2)$, respectively. Because we choose an observation time of 1 ms, the noise-less comb has a 1-kHz line-width. In other words, the FWHM of the comb with 2 fs timing jitter noise is mainly caused by the limited observation time rather than the timing jitter noise.

We know single-frequency lasers with a white frequency noise exhibits the well-known Lorentzian line shape with Schawlow-Townes-Henry line-width [123, 124]. If the white frequency noise is $S_{\delta\nu}(f) = h_0$, the comb has a comb line-width of πh_0 [125]. In the case of optical frequency combs, the comb-like structure is a result of constructive and destructive interference pattern among multiple pulses. If we assume the pulse train is offset-free, the optical frequency noise can be derived from the timing jitter noise $S_{\Delta\tau}(f)$ via repetition rate noise $S_{\delta f_{\text{rep}}}(f)$ and the elastic-tape model (ETM) [104, 126].

Given the round-trip time of the master laser cavity is inversely proportional to the repetition rate, $t_{\text{rt}} = \dfrac{1}{f_{\text{rep}}}$, the round-trip time fluctuation can be written as

$$\delta t_{\text{rt}} = -\frac{1}{f_{\text{rep}}^2} \cdot \delta f_{\text{rep}}. \tag{4.17}$$

Note δt_{rt} stands for the fluctuation of the round-trip time inside the cavity, which is a continuous function over time. The timing jitter of the output pulses can be calculated by integrating $\delta t_{\text{rt}}/t_{\text{rt}}$, which is written as

$$\Delta\tau = \int \frac{\delta t_{\text{rt}}}{t_{\text{rt}}} \cdot dt = -\frac{1}{f_{\text{rep}}} \cdot \int \delta f_{\text{rep}} \cdot dt. \tag{4.18}$$

Alternatively,

$$\frac{\partial}{\partial t}\Delta\tau = -\frac{1}{f_{\text{rep}}} \cdot \delta f_{\text{rep}}. \tag{4.19}$$

Applying the differentiation identity of Fourier-transform relates the timing jitter

noise $S_{\delta\tau}(f)$ to the repetition rate noise $S_{\delta f_{\text{rep}}}(f)$ via

$$(2\pi f)^2 \cdot S_{\Delta\tau}(f) = \frac{1}{f_{\text{rep}}^2} \cdot S_{\delta f_{\text{rep}}}(f). \qquad (4.20)$$

For an offset-free frequency comb, f_{ceo} is fixed at zero. In the ETM, the fix point for the repetition rate noise is at the frequency origin $\nu = 0$. Therefore, the optical frequency noise at $\nu = \nu_c$ scales quadratically with respect to ν_c [119]. In other words,

$$\begin{aligned} S_{\delta\nu_c}(f) &= \frac{\nu_c^2}{f_{\text{rep}}^2} \cdot S_{\delta f_{\text{rep}}}(f) = \frac{\nu_c^2}{f_{\text{rep}}^2} \cdot f_{\text{rep}}^2 \cdot (2\pi f)^2 \cdot S_{\Delta\tau}(f) \\ &= \nu_c^2 \cdot (4\pi^2 f^2) \cdot S_{\Delta\tau}(f). \end{aligned} \qquad (4.21)$$

Equation 4.21 shows that for an offset-free frequency comb, $1/f^2$ timing jitter noise translates to a white optical frequency noise. The level of the frequency noise scales quadratically with respect to the optical frequency ν_c. If $1/f^2$ timing jitter noise equals to $S_{\Delta\tau}(f) = \gamma \cdot f^{-2}$, the resulting white frequency noise is

$$S_{\delta\nu_c}(f) = 4\pi^2 \cdot \nu_c^2 \cdot \gamma. \qquad (4.22)$$

It then leads to a Lorentzian line shape with a FWHM line-width of $4\pi^3 \cdot \nu_c^2 \cdot \gamma$, indicating the frequency comb under $1/f^2$ timing jitter noise has a line-width that scales quadratically with respect to the optical frequency ν_c.

To calculate the $1/f^2$ coefficient γ from the timing jitter noise PSD, we use an expression of

$$\gamma = \frac{\sigma_{\Delta\tau}^2}{2 \cdot t_{\text{ob}} - 2 \cdot t_{\text{rep}}}. \qquad (4.23)$$

Note in the analytical expression that describes the relationship between the timing jitter variance and the timing jitter PSD (Eq. 4.9), the lower limit of the integral is at $1/t_{\text{ob}}$. In the numerical calculation, the noise spectrum is sampled in such a way that the element in the numerical array covers the spectrum on both sides around the point, i.e., the point at $f = 1$ kHz covers the noise spectrum from $f = 500$ Hz to $f = 1500$ Hz. Therefore, the expression for calculating γ needs to be modified to add a multiplier of 2 for the observation time t_{ob} in the denominator.

We calculate the analytical PSD from this expression and compare it with PSD derived from M-C simulations. The red dashed lines in Fig. 4.14(a) are jitter PSD calculated by $S_{\Delta\tau}(f) = \gamma/f^2$ and the solid lines are the averaged timing jitter PSD from M-C simulations. The timing jitter PSD calculated by γ/f^2 fits well with PSD from M-C simulations.

The line-width of the frequency comb can be then calculated by $4\pi^3 \cdot \nu_c^2 \cdot \gamma$. We compare this analytical FWHM with the results from M-C simulations. Figure 4.14(b) plots the comb line-width versus increased timing jitter noise. We also add few more M-C simulations that $\sigma_{\Delta\tau}$ is extended up to 30 fs.

The results show that the analytical FWHM agrees with M-C FWHM until $\sigma_{\Delta\tau}$ exceeds 20 fs. In M-C simulations, when $\sigma_{\Delta\tau}$ is large, the comb line calculated

(a) Analytical and M-C PSD

(b) Analytical and M-C FWHM
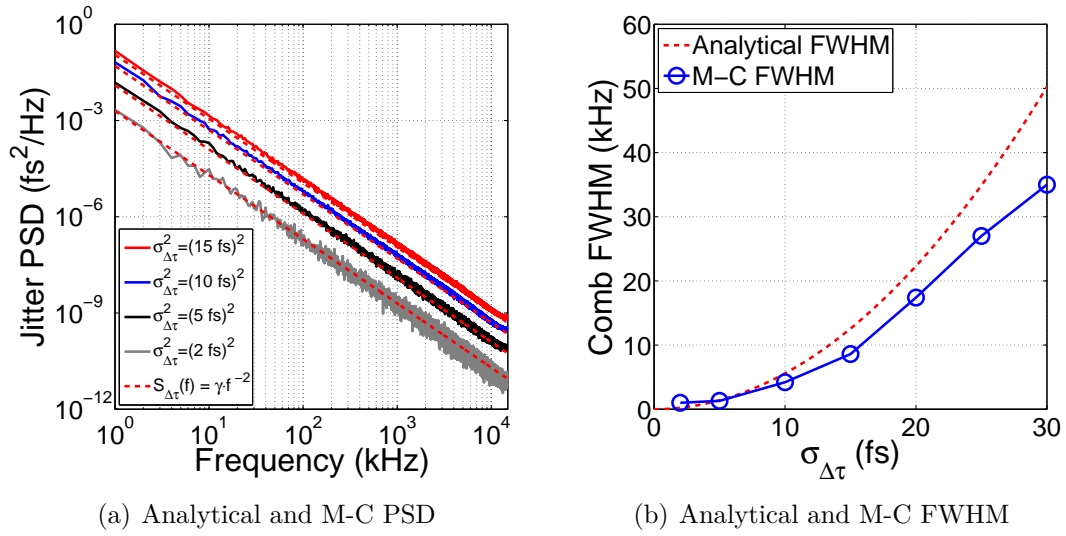
Figure 4.14: Comb line-width from analytical model and Monte-Carlo simulations.

$1/f^2$ timing jitter noise is fit by an analytical expression of $S_{\Delta\tau}(f) = \gamma \cdot f^{-2}$. The resulting coefficient γ is used to derive the comb line-width. (a) Jitter PSD from analytical expression $S_{\Delta\tau}(f) = \gamma \cdot f^{-2}$ and M-C simulations. (b) Comb line-width from analytical model and M-C results.
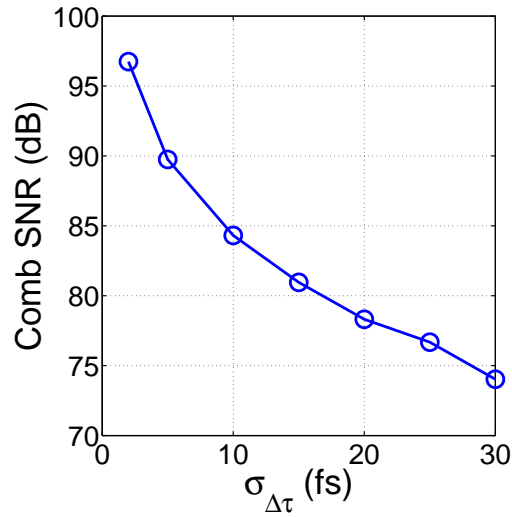

Figure 4.15: SNR of frequency comb with $1/f^2$ timing jitter noise.

An increased $1/f^2$ timing jitter noise does not lead to a significant reduced SNR.

via M-C simulations has large spectral intensity fluctuation at the center of the comb. The resulting comb spectrum can be considered as a Lorentzian line shape plus an intensity fluctuation over the spectrum. Consequently, the line-width is underestimated in M-C simulations. On the other hand, the analytical model for white frequency noise $S_{\delta\nu}(f) = h_0$ assumes an infinite observation time. In the M-C simulations, we always use 1-ms observation time. If we derive the optical frequency noise PSD $S_{\delta\nu}(f)$ via the timing jitter noise $S_{\Delta\tau}(f)$, the noise in the analytical model has a much broader bandwidth such that the resulting optical frequency noise PSD overestimates the noise, leading to an overestimated comb line-width from the analytical derivation.

When the offset-free frequency comb is dominated by $1/f^2$ timing jitter noise, the resulting comb has a much higher SNR compared with comb dominated by white timing jitter noise. Figure 4.15 plots the SNR of the comb under $1/f^2$ timing jitter noise. The variance of the timing jitter $\sigma_{\Delta\tau}^2$ is further extended up to $(30 \text{ fs})^2$. The excessive amount of $1/f^2$ noise does not lead to a significant reduction on the comb SNR. When $\sigma_{\Delta\tau} = 30$ fs, SNR is still more than 70-dB. The contribution of $1/f^2$ timing jitter noise is mainly on broadening the comb line-width rather than reducing the comb SNR.

4.4.3 Hybrid timing jitter noise with f_{knee} at 3-MHz

In reality, the timing jitter noise of an offset-free pulse train is a combination of $1/f^2$ noise and white noise. $S_{\Delta\tau}(f)$ is dominated by $1/f^2$ noise at low Fourier frequencies due to the noise from the source laser system and it is dominated by white noise at high Fourier frequencies due to the additional timing jitter noise introduced during wavelength shifting process [56]. We calculate the comb line under the influence of different hybrid timing jitter noise. We show that an effective suppression of low-frequency noise can lead to a narrower comb line-width and an increased comb SNR.

To simulate hybrid timing jitter noise, we use the computational algorithm as suggested by [121]. In [121], the knee frequency f_{knee}, which defines the frequency where the timing jitter noise transits from $1/f^2$ to white, is firstly set at 3 MHz. We choose the timing jitter noise with a variance of $(2 \text{ fs})^2$, $(5 \text{ fs})^2$, $(10 \text{ fs})^2$, and $(15 \text{ fs})^2$, and calculate the averaged comb spectra by implementing 200 M-C realizations. Figure 4.16 plots the averaged comb spectra in log scale (Fig. 4.16(a)), the zoomed-in comb spectra in linear scale (Fig. 4.16(b)), and the corresponding jitter PSD and ITJ for the simulated comb (Fig. 4.16(c)). The knee frequency is indicated by a vertical dashed line in the figure. We can see the simulated timing jitter PSD becomes white noise at the frequency beyond 3 MHz.

The results show the comb with hybrid timing jitter noise has a similar line shape as the comb with $1/f^2$ timing jitter noise, which is mainly due to the fact that the knee frequency (3 MHz) is close to the Nyquist frequency (15 MHz). Figure 4.16(c) shows that ITJ is at the level of 0.1-fs when the noise PSD integrates from 15-MHz to 3-MHz. Therefore, the majority of the ITJ is contributed by $1/f^2$ timing jitter noise at lower frequencies, which leads to a Lorentzian-like comb line

(a) Comb spectra (multiple realizations)

(b) Zoomed-in comb spectra (linear scale)
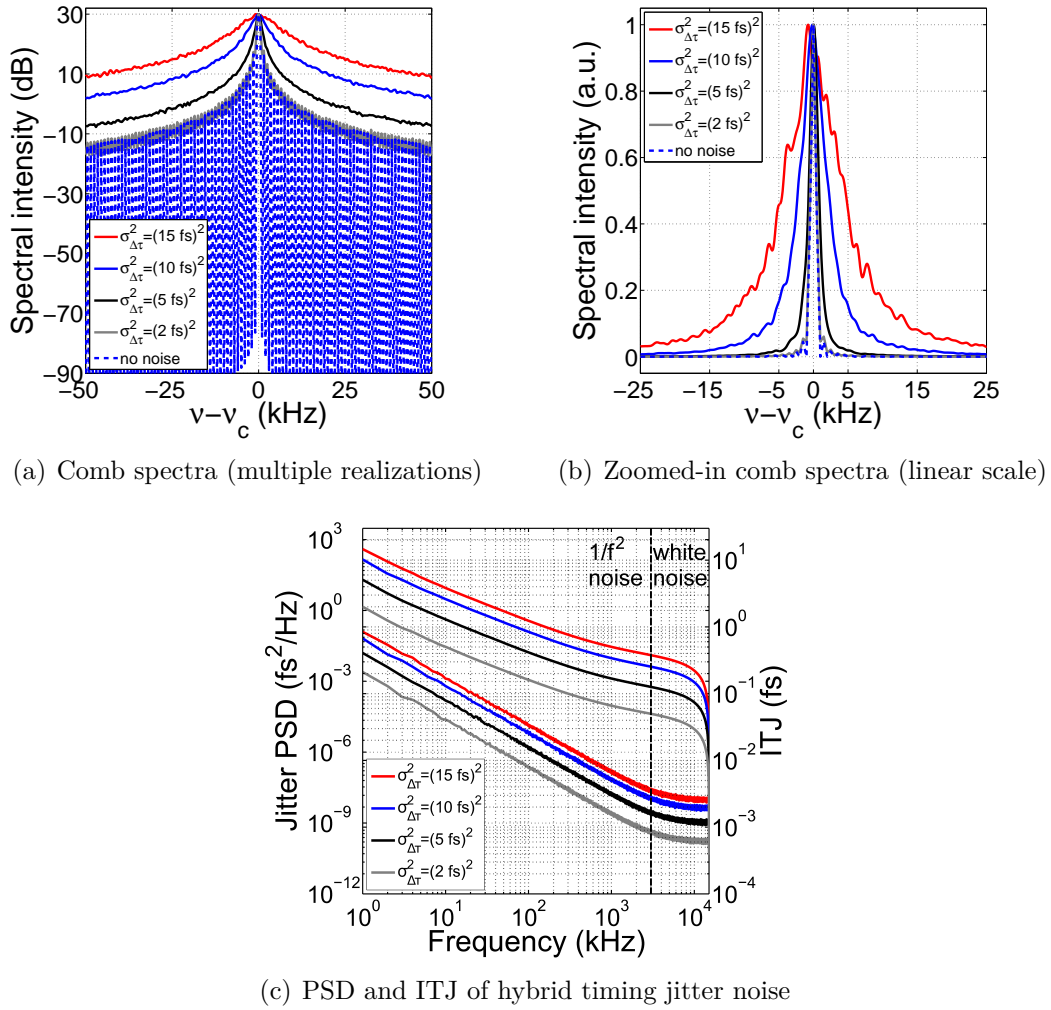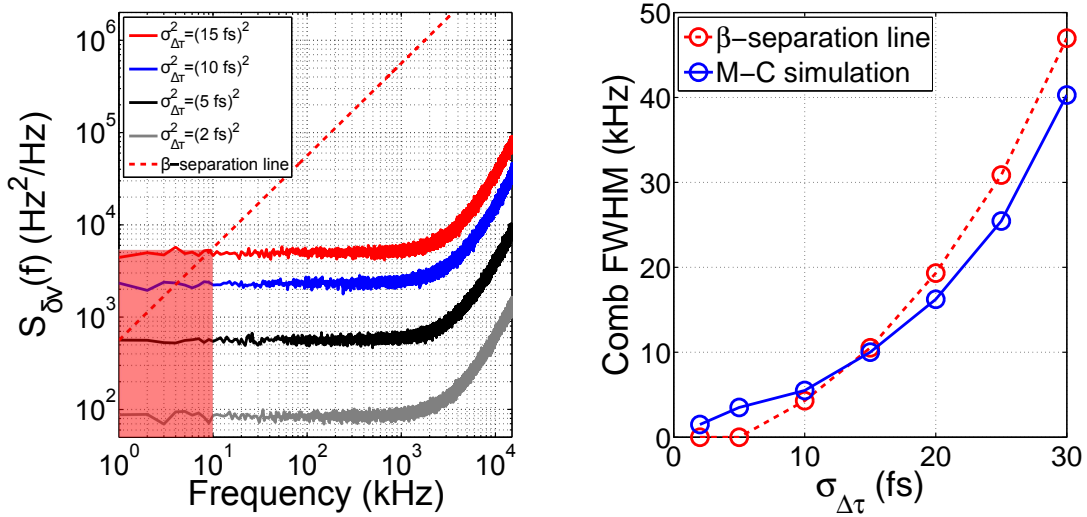

(c) PSD and ITJ of hybrid timing jitter noise

Figure 4.16: Frequency comb with hybrid timing jitter noise ($f_{\text{knee}} = 3$ MHz).

The optical spectrum at $\nu = \nu_c$ is calculated with hybrid timing jitter noise. The timing jitter noise is dominated by $1/f^2$ noise below 3 MHz and it is dominated by white noise after 3 MHz. (a) Comb spectra of multiple realizations. (b) Zoomed-in comb spectra in linear scale. (c) Power spectral density (PSD) and integrated timing jitter (ITJ). The knee frequency f_{knee} is indicated by a vertical dashed line.

---

shape. The FWHM of the comb is 1.0 kHz $((2 \text{ fs})^2)$, 1.5 kHz $((5 \text{ fs})^2)$, 3.5 kHz $((10 \text{ fs})^2)$, and 9.0 kHz $((15 \text{ fs})^2)$, respectively. Similar as the previous analysis, given the timing jitter below 2-fs, the comb line-width is caused by the limited observation time rather than the noise.

We know that the optical frequency noise $S_{\delta\nu}(f)$ can be derived from the timing jitter noise $S_{\Delta\tau}(f)$ via Eq. 4.21. For the hybrid timing jitter, the optical frequency noise is white noise before the knee frequency and then becomes proportional to frequency square beyond the knee frequency. Figure 4.17(a) plots the optical

(a) Frequency noise and β-separation line   (b) Line-width by β-separation line and M-C

Figure 4.17: Comb line-width for hybrid timing jitter noise ($f_{\text{knee}} = 3$ MHz).

Using the β-separation line method, the comb line-width can be calculated directly by the optical frequency noise PSD. (a) Optical frequency noise PSD and the β-separation line. The red shade indicates the noise of the comb with $\sigma_{\Delta\tau} = 15$ fs. (b) Comb line-width calculated by β-separation line and directly measured from M-C simulations.

frequency noise $S_{\delta\nu}(f)$ derived from the hybrid timing jitter noise. To calculate the FWHM line-width from the optical frequency noise, we use the β-separation line method [122], which has been used in analyzing continuous-wave lasers. In brief, a line defined by an empirical expression is imposed on the optical frequency noise spectra via

$$\beta\text{-line} = \frac{8\ln(2)}{\pi^2} \cdot f, \tag{4.24}$$

separateing the optical frequency noise PSD into two parts: PSD above the β-separation line produces slow frequency modulation and therefore determines the comb line-width; PSD under the β-separation line produces faster frequency modulation and affects the comb wings or the background. We plot the β-separation line in a red dashed line together with the optical frequency noise in Fig. 4.17(a). For example, the β-separation line (red dashed line) intercepts with the red PSD curve ($\sigma_{\Delta\tau} = 15$ fs) at around $f = 10$ kHz. The PSD above the β-separation line (indicated by the red shade in Fig. 4.17(a)) contributes to the comb line-width. FWHM line-width can be approximated by*

$$\text{FWHM} = (4\ln(2)A)^{1/2}, \tag{4.25}$$

---

*We use a modified expression to accommodate the results from M-C simulations.
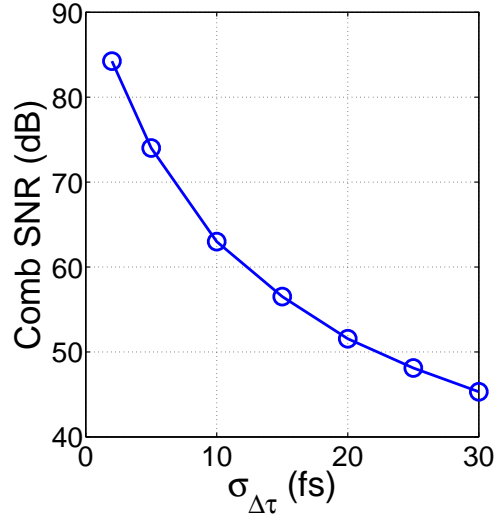
Figure 4.18: Comb SNR for hybrid timing jitter noise ($f_{\text{knee}} = 3$ MHz).

where A is the area of the optical frequency noise PSD that is above β-separation line (the area of the red shade shown in Fig. 4.17(a)).

Using the β-separation line method, the FWHM line-width can be calculated geometrically by measuring the optical frequency noise spectrum. In other words, the measurement of timing jitter noise spectrum provides sufficient information to determine the comb line-width of an offset-free frequency comb. We calculate the comb line-width using both the β-separation line method and direct measuring the comb spectrum from M-C simulations. The results are shown in Fig. 4.17(b). Few more sets of M-C simulations are added to extend $\sigma_{\Delta\tau}$ up to 30 fs. The results from β-separation line method (red circles) show good agreement with M-C results (blue circles) with an error of <15%. It is noteworthy that due to the limited "observation" time of 1-ms in the numerical calculations, β-separation line method fails to predict the comb line-width for $\sigma_{\Delta\tau}$ below 5-fs. If longer observation time is applied, the noise spectrum at lower frequencies is more accurate and provides more information to the β-separation line method.

Meanwhile we plot in Fig.4.18 the SNR of the comb under hybrid timing jitter noise. If the timing jitter noise is pure $1/f^2$ noise, SNR drops from >95-dB to <75-dB when $\sigma_{\Delta\tau}$ increases from 2-fs to 30-fs. If the timing jitter noise is hybrid noise with a knee frequency at 3-MHz, SNR drops from 85-dB to 45-dB when $\sigma_{\Delta\tau}$ increases from 2-fs to 30-fs, suggesting white timing jitter noise at high Fourier frequencies has more pronounced effect on reducing the comb SNR, compared with $1/f^2$ timing jitter noise.

4.4.4 Hybrid timing jitter noise with different f_{knee}

To further study the effect of timing jitter noise at different Fourier frequencies, we simulate hybrid timing jitter noise with an ITJ fixed at 10-fs. The knee frequency

(a) Hybrid timing jitter with different f_{knee}

(b) Comb spectra (linear scale)

(c) Optical frequency noise PSD and β-line

(d) Comb line-width and SNR
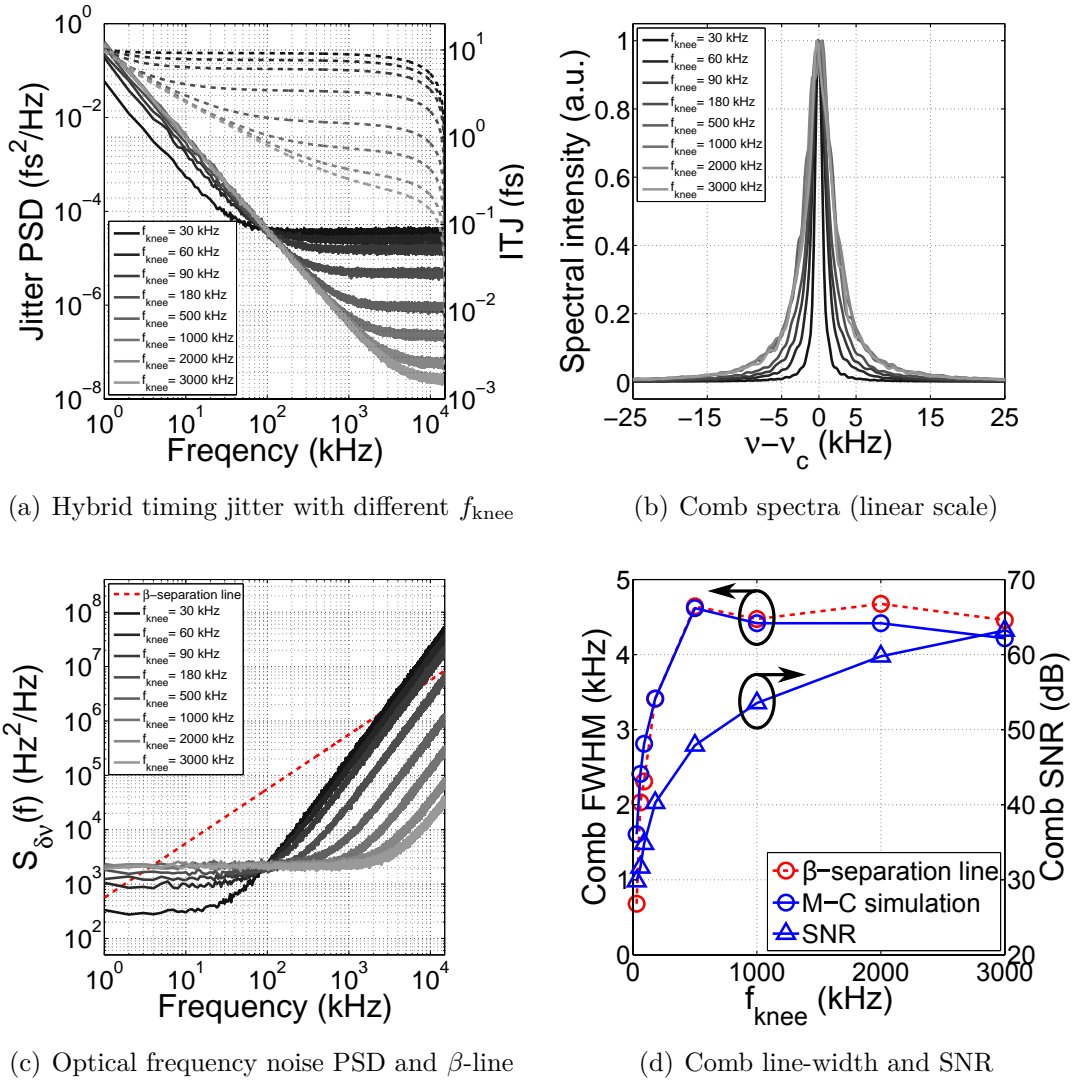
Figure 4.19: Hybrid timing jitter noise with a fixed ITJ and different f_{knee}.

The frequency comb is examined under hybrid timing jitter noise with different f_{knee}. For all cases, ITJ is 10-fs. f_{knee} varies from 30-kHz to 3000-kHz. (a) Timing jitter PSD and ITJ. (b) Comb spectra in linear scale. (c) Optical frequency noise PSD and β-separation line. (d) Comb line-width and SNR versus f_{knee}.

f_{knee} now varies from 30-kHz to 3-MHz. Since the observation time is always 1-ms and the repetition rate is fixed at 30-MHz, the change of f_{knee} changes both the level of $1/f^2$ noise at low frequencies and the level of white noise at high frequencies. The simulated jitter noise PSD and ITJ is plotted in Fig. 4.19(a). Figure 4.19(b) plots the normalized comb spectra in linear scale.

Although ITJ is 10-fs for all cases, the resulting comb spectra have different line-width. Apparently, when the majority of the timing jitter noise is at low

frequencies (f_{knee} is higher and $1/f^2$ noise is dominating), the resulting comb has a broader comb line-width. Conversely, when timing jitter noise is mostly white noise (f_{knee} is lower and white noise is dominating), the comb has a narrower line-width. We plot the optical frequency noise derived from the timing jitter noise in Fig. 4.19(c). β-separation line is also plotted in a red dashed line in the same figure. The area that is above the β-separation line becomes higher for an increased f_{knee}, also suggesting an increased comb line-width. When f_{knee} is more than 500-kHz, the cross-point between the optical frequency noise PSD and the β-separation line is at around 4-kHz, indicating the frequency comb with f_{knee} of >500-kHz has the same comb line-width.

We plot the comb line-width in Fig. 4.19(d) (to the left axis) using both β-separation line method (red circles) and direct measurement from M-C simulations (blue circles). The result agrees with the results derived from the β-separation line method that the comb line-width stays the same when f_{knee} exceeds 500-kHz. For f_{knee} between 30-kHz and 500-kHz, the comb line-width increases abruptly from 1-kHz to 4.5-kHz. Therefore, an efficient control of the timing jitter noise at low frequencies (<100-kHz) is crucial for achieving frequency comb with narrow comb line-width.

We also plot the comb SNR in the same figure (to the right axis), showing that the comb has higher SNR with increased f_{knee}. Figure 4.19(c) shows that the optical frequency noise for larger f_{knee} is significantly lower at high frequencies (>100 kHz). A reduced high-frequency timing jitter noise, therefore, leads to a higher SNR. As mentioned, timing jitter noise at high frequencies is mainly caused by source laser's RIN during the wavelength shifting process [56]. Due to the lack of effective means to control high frequency noises, higher SNR demands minimizing the noise transfer during the wavelength shifting process, which will be discussed later in Chapter 2.

In the experiment, low-frequency $1/f^2$ timing jitter noise can be optimized by controlling the mode-locked regime of the master laser [115]. To simulate the reduction of low-frequency timing jitter, we simulate the hybrid timing jitter noise with a fixed white noise level at high frequencies and a varying $1/f^2$ noise. The resulting noise spectrum has an reducing f_{knee} together with a reducing ITJ. When f_{knee} decreases from 400-kHz to 50-kHz, ITJ drops from 35-fs to 7.6-fs. The simulated timing jitter noise spectrum and ITJ are plotted in Fig. 4.20(a). The resulting comb spectra are plotted in Fig. 4.20(b) in linear scale.

The comb spectra show clearly that suppressing $1/f^2$ noise under 400-kHz results in comb with narrower line-width. The comb line has a FWHM of $\sim$60-kHz when f_{knee} is 400-kHz and it reduces to <5-kHz when f_{knee} is under 100-kHz. Figure 4.20(c) plots the optical frequency noise derived from the timing jitter noise. β-separation line is also plotted in the same figure. When low-frequency timing jitter noise is reduced, the interception point between the β-separation line and the optical frequency noise spectrum also shifts to lower frequency, indicating a narrower comb line-width. Figure 4.20(d) plots (to the left axis) the FWHM comb line-width calculated by β-separation line method and direct measurement from M-C simulations. When f_{knee} is decreasing, comb line-width drops from $\sim$50-kHz

(a) Hybrid timing jitter with different f_knee

(b) Comb spectra (linear scale)

(c) Optical frequency noise PSD and β-line

(d) Comb line-width and SNR
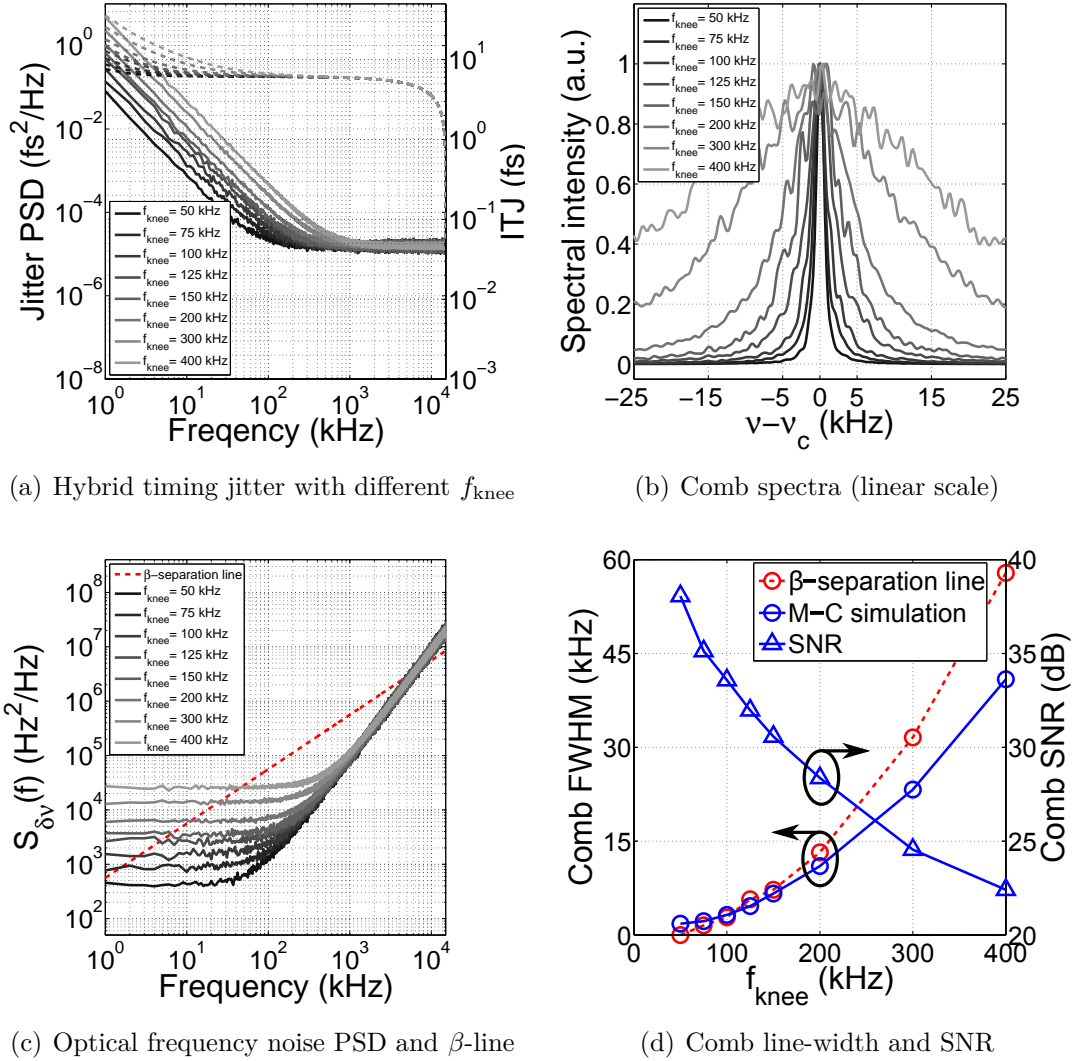
Figure 4.20: Hybrid timing jitter noise with reducing $1/f^2$ noise.

The frequency comb is examined under hybrid timing jitter noise with different f_knee and same level white noise. f_knee is set at 50, 75, 100, 125, 150, 200, 300, and 400-kHz. (a) Timing jitter PSD and ITJ. (b) Comb spectra in linear scale. (c) Optical frequency noise PSD and β-separation line. (d) Comb line-width and SNR versus f_knee.

to few kHz. Figure 4.20(d) also plots the comb SNR (to the right axis) versus f_{knee}. The reduction of low-frequency timing jitter noise also leads to an increment of the comb SNR. Comb SNR increases from ~22-dB to ~38-dB.

In conclusion, timing jitter noise at different Fourier frequencies affects the comb characteristic differently: low-frequency (<500-kHz) timing jitter noise has a significant impact on determining the line-width. It also changes the comb SNR marignally; high-frequency (>500-kHz) timing jitter noise affects the comb SNR while it has minimal influence on changing the comb line-width. By using the β-separation line method, the comb line-width of an offset-free frequency comb can be well estimated from the noise spectrum of its timing jitter noise. Meanwhile, we show that an effective reduction of low-frequency (<400-kHz) can lead to a comb line with narrower comb line-width and higher SNR. A reduction of ITJ from 35-fs to 7.6-fs leads to a narrowing of comb line-width from 40-kHz to <2-kHz and an increment of comb SNR by ~15-dB.

4.5 Summary of the chapter

In conclusion, we investigate the noise transfer during DFG process by manually imposing a relative timing jitter (RTJ) noise onto the signal pulses and studying the outcomes. Two sets of DFG with their pump wavelength fixed at 1.03-μm (1-μm driven DFG) and 2-μm (2-μm driven DFG) are compared. We show that 2-μm driven DFG has ~5 times less RTJ-RTJ noise transfer compared with 1-μm driven DFG thanks its reduced pump-signal and pump-idler group velocity mismatch (GVM). Meanwhile, 2-μm driven DFG introduces marginally higher relative intensity noise (RIN) to the output idler pulses due to its high parametric gain. When 1-μm driven DFG is operated in different regimes, the noise transfer is different: DFG in the OPA regime has the highest RTJ-RIN noise transfer due to the strengthened parametric interaction between pump/signal pulses. Meanwhile, DFG in the OPA regimes has the lowest RTJ-RTJ noise transfer due to the reduced net idler pulse propagation; DFG in the saturation regime has the highest RTJ-RTJ transfer and the lowest RTJ-RIN transfer thanks to the strong gating effect of the pump pulses; DFG in the linear regime transfers the noise in between OPA regime and saturation regime.

We also perform Monte-Carlo simulations in order to study how the timing-jitter noise of an offset-free frequency comb affects the comb characteristics. We show that low-frequency (<500-kHz) timing jitter noise determines the comb line-width and marginally changes the signal-to-noise ratio (SNR) of the comb line; high-frequency (>500-kHz) timing jitter noise affects the comb SNR while it has minimal effect in changing the comb line-width. By using the β-separation line method, the comb line-width of an offset-free frequency comb laser can be well estimated by measuring the timing jitter noise spectrum. A reduction of $1/f^2$ timing jitter noise can narrow the comb line-width from 40-kHz to 2-kHz and increase the comb SNR by 15-dB.

Chapter 5

1-GHz passively offset-free laser source

5.1 Introduction and motivation

Ultrafast lasers with multi-gigahertz (GHz) repetition rate are required in many applications, for example, arbitrary optical wave synthesis [127], astronomical frequency metrology [11], and biological imaging [128]. Increasing the spacing of the comb tooth (equivalent to increasing the repetition rate f_{rep} of the laser) can permit access to and manipulate of each individual comb line, enabling applications such as arbitrary optical wave synthesis. At same average power, increasing the comb spacing leads to higher optical power per comb line, which improves the signal-to-noise ratio (SNR) in spectroscopic measurements. In other applications such as bio-imaging, using lasers with high repetition rate and low pulse energy can effectively avoid the photo-induced damage caused by high pulse energy inside biological samples. Increasing the repetition rate to GHz also improves the SNR in detection, reduces the data acquisition time, and increases the frame-rate [128].

To construct multi-GHz frequency comb, both the repetition-rate (f_{rep}) and the carrier-envelope offset frequency (f_{ceo}) need to be stabilized. The stabilization of f_{ceo} is particularly challenging. Normally, the pulse energy of a GHz repetition rate laser is at few nanojoules level [129] while the detection of f_{ceo} using self-referenced methods requires certain pulse energy for supercontinuum generation (SCG), and, therefore, the resulting multi-GHz frequency comb has limited available power. Moreover, the feeding-back loop for controlling f_{ceo} has a locking bandwidth up to tens of kilohertz [130], leaving f_{ceo} of the laser free-running between the locking frequency and the Nyquist frequency.

Apart from using conventional $1f$-$2f$ interferometer for detecting and stabilizing f_{ceo}, another route is to generate a passively offset-free frequency comb using difference frequency generation (DFG) [131–133]. In such scheme, the output of a GHz laser is firstly spectral broadened using fiber-optic method so that two spectral components with same f_{ceo} but different center frequency are generated. Then, these two spectral lobes are frequency mixed in a nonlinear $\chi^{(2)}$ crystal to generate
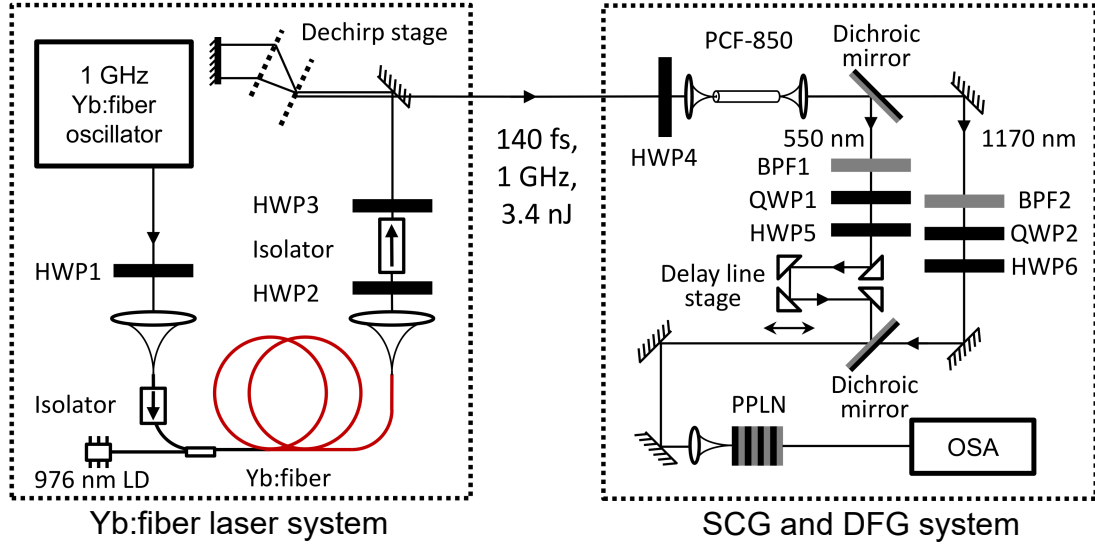
Figure 5.1: Schematic of the 1-GHz offset-free laser source.

HWP: half-wave-plate; BPF: band-pass filter; QWP: quarter-wave-plate; OSA: optical spectrum analyzer. SCG: supercontinuum generation. DFG: difference frequency generation.

the offset-free idler pulses. The generated idler pulse train has its carrier-envelope phase offset (CEP) automatically fixed at zero. The straight-forward architecture of passively offset-free frequency comb can significantly simplify the experimental setup for building a frequency comb laser.

In this chapter, we demonstrate a passively offset-free laser source with a center wavelength at 1030-nm and a repetition rate of 1-GHz. The source is driven by an 1-GHz Yb:fiber laser system. The output of the laser system is firstly spectral broadened inside a short piece of photonic crystal fiber (PCF). The generated supercontinuum spectrum consists of a dispersive-wave (DW) lobe centered at 550-nm and a Raman-soliton (RS) lobe centred at 1170-nm. The frequency mixing between DW and RS generates an output idler centered at 1030-nm. The generated idler pulses can be amplified in Yb:fiber amplifiers in further experiments. After stabilizing f_{rep} of the master laser system, the 1-GHz passively offset-free frequency comb, centered at 1030-nm, can promise many applications.

5.2 Experimental setup and results

Figure 5.1 shows the experimental setup for constructing the 1-GHz passively offset-free Yb:fiber laser source. The setup includes two parts: Yb:fiber laser system and SCG-DFG system. The Yb:fiber laser provides the high-power, 1-GHz pulse train that seeds the subsequent SCG and DFG experiments. It is driven by an 1-GHz Yb:fiber oscillator, Yb:fiber amplifier and pulse compressor.
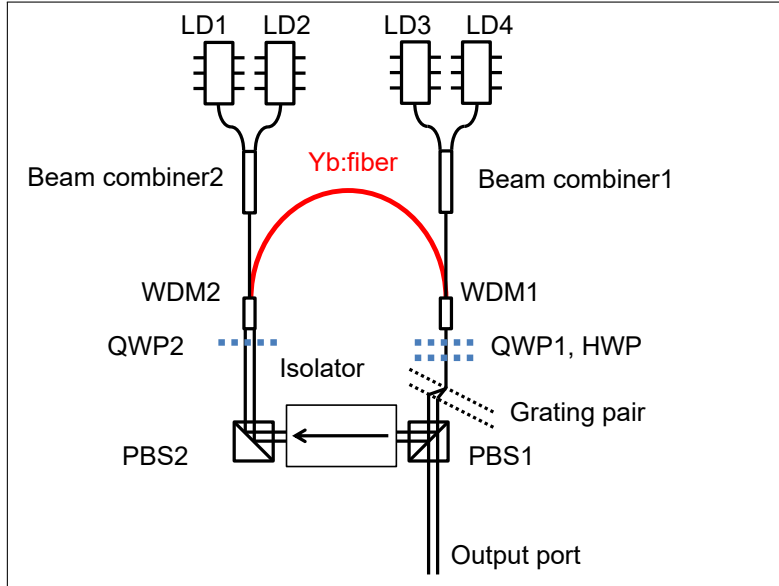
Figure 5.2: Schematic of the 1-GHz Yb:fiber oscillator.

LD: laser diode; Yb:fiber: ytterbium gain fiber (CorActvie SCF-YB550-4/125-19); WDM: wavelength division multiplier; QWP: quarter-wave-plate; HWP: half-wave-plate; PBS: polarization beam splitter.

1-GHz Yb:fiber laser system

The schematic of the 1-GHz Yb:fiber oscillator is plotted in Fig. 5.2. The cavity is operated in the stretched-pulse regime so that the output pulse train has a minimized timing jitter noise. The mode-locked operation is initiated by nonlinear polarization evolution (NPE) inside Yb:fiber. The oscillator includes 130-mm-long highly-doped fused silica fiber with a core absorption of 550-dB/m at 915-nm(CorActvie SCF-YB550-4/125-19) and a free-space length of 100-mm, setting the repetition rate at 1-GHz. The specification of the ytterbium gain fiber can be found in Appendix A. The oscillator is pumped by four laser diodes (LD) with an average pump power of 2-W. The pump is coupled into cavity by two wavelength division multipliers (WDM). The WDMs also serve as the fiber/free-space collimators. The cavity have free-space polarization control (one HWP, two QWP and two PBS), a transmission grating pair for dispersion control (grating density: 1000 lines/mm), and a free-space isolator. Inside the cavity, Yb:fiber provides a group delay dispersion (GDD) of 3,000 fs^2 and the grating pair provides a negative GDD of -8,000 fs^2. The net intra-cavity GDD is -5,000 fs^2. When the polarization controls are properly adjusted, the oscillator is mode-locked with an average output power of 360-mW. The output spectrum is plotted in Fig. 5.3. It is centered at 1034-nm with a 3-dB spectral bandwidth of 14-nm, corresponding to a 112-fs transform-limited (TL) pulse.

The cavity output is directly coupled into a passive fiber using fiber collimator
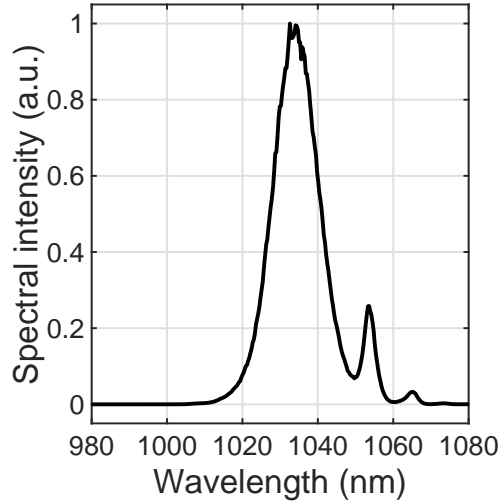
Figure 5.3: Output spectrum of the 1-GHz Yb:fiber oscillator.
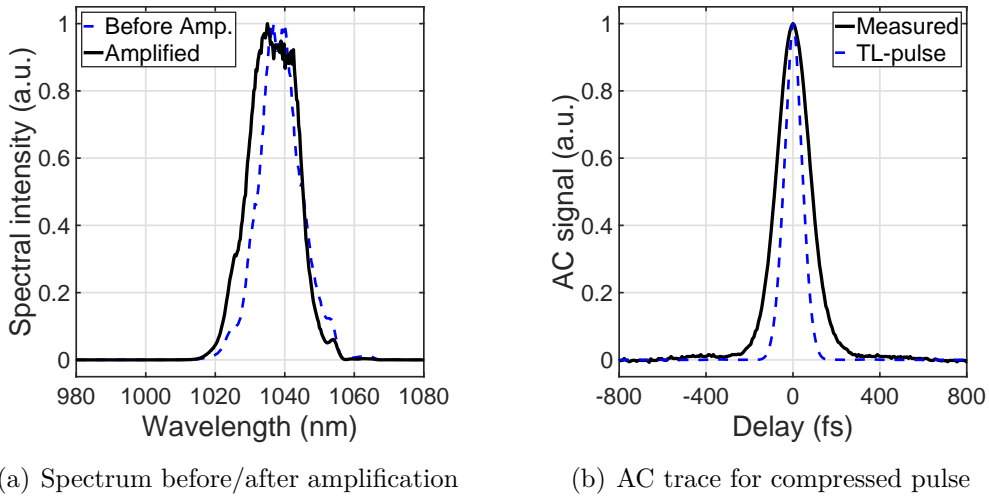
(a) Spectrum before/after amplification

(b) AC trace for compressed pulse

Figure 5.4: Characterization of the 1-GHz master laser.

(a) Optical spectrum of 1-GHz master laser system with/without pulse amplification. (b) Autocorrelation trace of the measure pulse and its TL form.

and the 1-GHz pulse train is amplified in a 1.2-m-long polarization-maintaining (PM) Liekki12/125 Yb:fiber. The specification of the Liekki fiber can be found in Appendix A. After amplification, the laser output has an average power of 4.2-W. It is then compressed by a pair of diffraction gratings with a compression efficiency of 80%. The compressed pulse has a pulse energy of 3.4-nJ, corresponding to an average power of 3.4-W. Figure 5.4(a) shows the measured optical spectrum when the amplification is turned on/off. The autocorrelation (AC) trace of the

(a) Supercontinuum spectrum

(b) Dispersive wave spectrum

(c) Raman soliton spectrum

(d) Offset-free idler spectrum
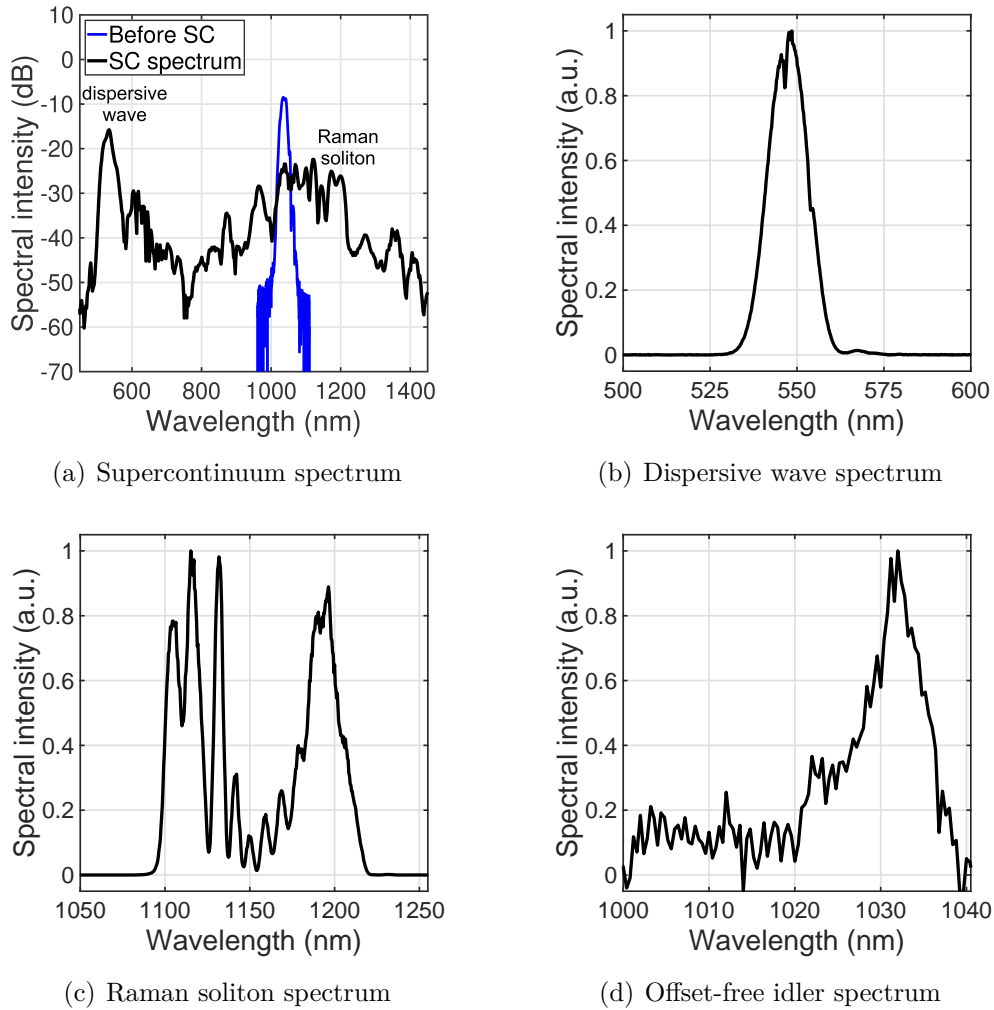
Figure 5.5: Spectrum of supercontinuum and DFG.

(a) Supercontinuum spectrum generated from a 10-cm-long PCF-850. (b) Filtered dispersive wave spectrum. (c) Filtered Raman soliton spectrum. (d) Generated 1030-nm offset-free idler spectrum.

compressed pulse after amplification is plotted in Fig. 5.4(b), together with the AC trace of the TL pulse. The compressed pulse has a FWHM pulse duration of ∼140-fs, reaching >75% the peak intensity of the TL pulse.

Supercontinuum generation and DFG

The 1-GHz, 3.4-nJ, 1034-nm, 140-fs pulse train then enters the SCG-DFG stage. It is firstly coupled into a 10-cm-long PCF-850 with a coupling efficiency of ∼40% for spectral broadening. After PCF, the pulse generates a supercontinuum (SC) with a DW centered at ∼545-nm and a RS centered at ∼1170-nm. The optical

spectrum before and after SCG is shown in Fig. 5.5(a).

The generated SC passes a dichroic mirror to split DW and RS. Both DW and RS pulses pass a QWP, a HWP, a band-pass filter, and re-combine in a 1-mm-long periodically-poled lithium niobate (PPLN) crystal. PPLN has a longitudinal period of 7.7-μm to meet the quasi-phase matching (QPM) condition for frequency mixing 545-nm and 1170-nm pulses. The filtered spectra of DW and RS are plotted in Fig. 5.5(b)and 5.5(c). After properly adjusting the relative time delay between DW and RS, they generate an output idler centered at 1030-nm. The output idler spectrum is plotted in Fig. 5.5(d). The generated idler spectrum has a center wavelength of 1030-nm and a 3-dB bandwidth of 10-nm. The generated offset-free idler has an average power of few μW. If the output idler is coupled into a single-mode, Yb:fiber amplifier, the average power can be amplified to mW-level. After stabilizing the repetition rate of the master laser system, such passively offset-free Yb:fiber laser frequency comb can be an enabling tool in spectroscopic applications.

5.3 Summary of the chapter

To conclude, we demonstrate a 1-GHz passively offset-free Yb:fiber laser source at 1.03-μm using an alternative DFG schematic. The laser source is based upon a 1-GHz Yb:fiber laser as the master laser system. The master laser output (3.4-W, 1-GHz, 3.4-nJ, 140-fs) is firstly launched into a short piece of PCF to generate a supercontinuum (SC) spectrum which includes a dispersive wave (DW) spectral lobe at 550-nm and a Raman soliton (RS) lobe at 1170-nm. The DFG between DW and RS inside 2-mm-long PPLN generates an offset-free pulse train with a center wavelength of 1030-nm. Currently, the pulse train has a limited average power of few μW due to un-optimized spectral broadening process in PCF-850. We are continuing to improve the efficiency of spectral broadening and planning to amplify the offset-free idler pulses from μW average power to mW average power using Yb:fiber amplifiers. If the experimental parameters for SCG and DFG are modified, offset-free pulses centered at other near-infrared (NIR) wavelength (1.55-μm and 2-μm) can be also accessed using similar configuration.

Chapter 6

Conclusion and outlook

Self-phase-modulation (SPM) effect inside optical fibers has enabled a straightforward implementation for wavelength-shifting the center wavelength of near-infrared (NIR) pulses to a longer center wavelength. The wavelength-shifted pulses can be used as signal pulses for seeding a DFG setup together with NIR pump pulses to generate the offset-free mid-IR idler pulses. After stabilizing the repetition rate of the master laser system, the generated mid-IR idler pulse train, located in the molecular "fingerprint" wavelength region (5–20 μm), forms a mid-IR frequency comb with well-defined optical frequencies, which has become an enabling tool in molecular spectroscopic applications.

Currently, DFG-based mid-IR frequency combs especially at long-wave mid-IR wavelength ($>$10-μm) suffer from low available power of few-mW. The power shortage can be attributed to several reasons: (1) Signal pulses generated by conventional nonlinear fiber-optic methods have a limited pulse energy of sub-nJ level; (2) Multiple photon absorption (MPA), together with other thermal related issues, prevent the use of high input power for seeding a DFG process inside non-oxide crystals. At high repetition rate (HRR), the total input pulse energy is limited under $\sim$200-nJ; (3) Un-optimized DFG configuration with large pump-signal and pump-idler group velocity mismatch (GVM) results in an inefficient generation of mid-IR idler pulses. The generated idler pulses also have large temporal chirp due to the same reason. Besides having limited available power, an un-optimized nonlinear fiber-optic wavelength-shifting process and DFG process can translate the relative intensity noise (RIN) of the pump pulses to $>$10-fs timing jitter noise of the generated mid-IR idler pulses, which significantly deteriorates the performance of the resulting mid-IR frequency combs.

In this thesis, we investigate several issues which are related with the construction of DFG-based, high-power, low-noise mid-IR frequency combs:

(1) We first study two nonlinear fiber-optic methods for generating the wavelength-shifted signal pulses: soliton self-frequency shift (SSFS) and self-phase modulation enabled spectral selection (SESS). We discover that SESS is a better candidate for providing wavelength-tunable signal pulses with a pulse energy of $>$50-nJ and a minimal relative timing jitter (RTJ).

(2) We then study the power scalability of DFG process in order to elucidate an efficient approach for generating high-power mid-IR idlers. We show that, at a HRR of >10-MHz that is required for frequency combs, the generated mid-IR idler scales linearly with respect to the power product of the input pump pulse and the input signal pulse. Therefore, increasing the signal power is as efficient as increasing the pump power for power scaling the idler. To improve the efficiency of the DFG process, we compared two sets of DFG processes with different pump wavelength, 1.03-μm and 2-μm. We show that 2-μm driven DFG can achieve a quantum efficiency of 75%, 3 times higher compared with 1-μm driven DFG under the same launching conditions. Using optimal inputs, 2-μm driven DFG can generate 10-μm mid-IR idler pulses with >44-nJ pulse energy and >300-kW peak power. At a repetition rate of 50-MHz, it corresponds to an available output power of >2.2-W.

(3) Besides generating high-power mid-IR idler, idler pulses with minimal optical noises, especially a minimized timing jitter noise, are favorable for constructing high-performance mid-IR frequency combs. We study the noise transfer during the nonlinear fiber-optic wavelength-shifting processes (SSFS and SESS) and during the DFG process. Compared with SSFS, SESS introduces ~20 times less RTJ noise from the input RIN. Meanwhile, 2-μm driven DFG has less noise transfer for the generated idler pulses thanks to its reduced GVM. We also identify the relationship between the timing jitter noise of an offset-free frequency comb with its comb characteristics. The comb line-width can be well estimated by using the β-separation line method to geometrically measure the timing jitter noise spectrum.

(4) We demonstrate a passively offset-free laser source at a repetition rate of 1-GHz. The laser source uses an alternative DFG schematic based upon a 1-GHz Yb:fiber laser system. The output of master laser system, centered at 1030-nm, is firstly launched into a short piece of PCF to generate two spectral components centered at 550-nm and 1170-nm. The DFG process seeded by these two spectra generates offset-free pulses centered at 1030-nm. After further repetition-rate stabilization and pulse amplification, the resulting 1-GHz passively offset-free frequency comb can be used for frequency synthesis and arbitrary optical wave generation in the NIR range.

Several issues deserve further investigations:

(1) In the simulation of SSFS, SESS and DFG, we use an ideal chirp-less sech^2 pulse as the input pulse. For a more precise modeling, the input pulse should be replaced by the experimental data with an inclusion of proper temporal chirp. The temporal chirp of the input pulse can be also optimized in order to minimize the noise transfer during the SSFS/SESS process.

(2) In our DFG calculation, the time-dependent coupled wave equations only model the 1-D case of the optical parametric processes. Effects such as linear loss, MPA loss, and diffraction loss are neglected in our modeling. To fully characterize a DFG process, the equations should be converted to 3-D coupled

wave equations with all these missing terms included.

(3) In the calculation of the noise transfer during the SSFS/SESS process, the input RIN is introduced by changing the pulse energy of the excitation pulse. The pulse profile is varied uniformly in order to emulate the presence of the input RIN. In reality, different noise sources, for example, pump current noise and amplified spontaneous emission noise, change the pulse profile differently, depending on the actual gain medium and the actual gain dynamics. For a more precise modeling of the input RIN, the inclusion of these noise sources needs to be addressed individually.

(4) In the investigation of the timing jitter noise and the comb characteristics, the simulated offset-free pulse train does not possess any intensity noise or phase noise. To better characterize the frequency comb, these noise terms should be included. In fact, timing jitter noise, intensity noise, and phase noise of a DFG-based frequency comb have strong correlation in high Fourier frequencies. A more systematic study on their correlation may provide better insights in building high-performance DFG-based frequency combs.

Nevertheless, our numerical simulations still have good agreement with the experimental data, for example, predicting the growing trend of the mid-IR idler with respect to the input pump/signal. Our calculation of the RIN-RTJ noise transfer based on a simplified RIN model also matches with the experimental results from the measurements in our laboratory. Our calculation, therefore, offers a good guideline for designing DFG systems to generate high-power, low-noise mid-IR frequency combs.

The key for generating high-power, low-noise mid-IR frequency combs is to use SESS for generating the wavelength-shifted signal pulses. Using SESS techniques, the signal pulse can have tens-of-nJ or even hundreds-of-nJ pulse energy. SESS also introduces minimal relative timing jitter of <0.5-fs to the signal pulses. Meanwhile, the DFG process can be optimized by shifting the center wavelength of the pump/signal pulses from 1.03-μm range to 2-μm range. 2-μm driven DFG has the advantage of having intrinsically less MPA, less pump-signal/pump-idler GVM, and a broader phase matching bandwidth, all of which facilitate the generation of ultrafast, high-power, mid-IR idler pulses with a high peak intensity. Based on our calculation, HRR mid-IR frequency combs with a watt-level average power using such optimized DFG system is experimentally viable by employing high-power Tm:fiber or Ho:fiber laser systems. The generated mid-IR idler pulses, centered at 9.87-μm, can have a pulse energy of >44-nJ and a peak power of >300-kW, corresponding to an average power of >2.2-W at 50-MHz repetition rate. We believe that such a source will open new avenues for novel scientific applications.

Bibliography

[1] Theodor W. Hänsch. Nobel Lecture: Passion for precision. *Reviews of Modern Physics*, 78(4):1297, 2006.

[2] John L. Hall. Nobel Lecture: Defining and measuring optical frequencies. *Reviews of Modern Physics*, 78(4):1279, 2006.

[3] Th. Udem, Ronald Holzwarth, and Theodor W. Hänsch. Optical frequency metrology. *Nature*, 416(6877):233, 2002.

[4] Steven T. Cundiff and Jun Ye. Colloquium: Femtosecond optical frequency combs. *Reviews of Modern Physics*, 75(1):325, 2003.

[5] Scott A. Diddams. The evolving optical frequency comb. *J. Opt. Soc. Am. B*, 27(11):B51–B62, 2010.

[6] David J. Jones, Scott A. Diddams, Jinendra K. Ranka, Andrew Stentz, Robert S. Windeler, John L. Hall, and Steven T. Cundiff. Carrier-envelope phase control of femtosecond mode-locked lasers and direct optical frequency synthesis. *Science*, 288(5466):635–639, 2000.

[7] Th. Udem, J. Reichert, R. Holzwarth, and Theodor W. Hänsch. Absolute optical frequency measurement of the Cesium D_1 line with a mode-locked laser. *Physical Review Letters*, 82(18):3568, 1999.

[8] Leo Hollberg, Chris W. Oates, E. Anne Curtis, Eugene N. Ivanov, Scott A. Diddams, Thomas Udem, Hugh Gettys Robinson, James C. Bergquist, Robert J. Rafac, Wayne M. Itano, et al. Optical frequency standards and measurements. *IEEE Journal of Quantum Electronics*, 37(12):1502–1513, 2001.

[9] S. A. Diddams, J. C. Bergquist, S. R. Jefferts, and C. W. Oates. Standards of time and frequency at the outset of the 21st century. *Science*, 306(5700):1318–1324, 2004.

[10] Christophe Daussy, Mickael Guinet, Anne Amy-Klein, Khelifa Djerroud, Yves Hermier, Stephan Briaudeau, Ch J Bordé, and Christian Chardonnet. Direct determination of the Boltzmann constant by an optical method. *Physical Review Letters*, 98(25):250801, 2007.

[11] S. P. Stark, T. Steinmetz, R. A. Probst, H. Hundertmark, T. Wilken, T. W. Hänsch, Th. Udem, P. St. J. Russell, and R. Holzwarth. 14 GHz visible supercontinuum generation: calibration sources for astronomical spectrographs. *Optics Express*, 19(17):15690–15695, Aug 2011.

[12] J. Reichert, M. Niering, R. Holzwarth, M. Weitz, Th. Udem, and T.W. Hänsch. Phase coherent vacuum-ultraviolet to radio frequency comparison with a mode-locked laser. *Physical Review Letters*, 84(15):3232, 2000.

[13] S. A. Diddams, Th. Udem, J. C. Bergquist, E. A. Curtis, R. E. Drullinger, L. Hollberg, W. M. Itano, W. D. Lee, C. W. Oates, K. R. Vogel, and D. J. Wineland. An optical clock based on a single trapped ^{199}Hg$^+$ ion. *Science*, 293(5531):825–828, 2001.

[14] Jean-Daniel Deschênes, Laura C. Sinclair, Fabrizio R. Giorgetta, William C Swann, Esther Baumann, Hugo Bergeron, Michael Cermak, Ian Coddington, and Nathan R. Newbury. Synchronization of distant optical clocks at the femtosecond level. *Physical Review X*, 6(2):021016, 2016.

[15] Michael J. Thorpe, Darren D. Hudson, Kevin D. Moll, Jacob Lasri, and Jun Ye. Cavity-ringdown molecular spectroscopy based on an optical frequency comb at 1.45-1.65 μm. *Optics Letters*, 32(3):307–309, 2007.

[16] Albert Schliesser, Nathalie Picqué, and Theodor W Hänsch. Mid-infrared frequency combs. *Nature Photonics*, 6(7):440, 2012.

[17] H. Pires, M. Baudisch, D. Sanchez, M. Hemmer, and J. Biegert. Ultrashort pulse generation in the mid-IR. *Progress in Quantum Electronics*, 43:1 – 30, 2015.

[18] Fritz Keilmann, Christoph Gohle, and Ronald Holzwarth. Time-domain mid-infrared frequency-comb spectrometer. *Optics Letters*, 29(13):1542–1544, Jul 2004.

[19] Albert Schliesser, Markus Brehm, Fritz Keilmann, and Daniel W. van der Weide. Frequency-comb infrared spectrometer for rapid, remote chemical sensing. *Optics Express*, 13(22):9029–9038, Oct 2005.

[20] Ulrike Willer, Mohammad Saraji, Alireza Khorsandi, Peter Geiser, and Wolfgang Schade. Near- and mid-infrared laser monitoring of industrial processes, environment and security applications. *Optics and Lasers in Engineering*, 44(7):699 – 710, 2006. Optical Diagnostics and Monitoring: Advanced monitoring techniques and coherent sources.

[21] Steven T. Cundiff and Andrew M. Weiner. Optical arbitrary waveform generation. *Nature Photonics*, 4(11):760, 2010.

[22] Nathaniel M. Fried and Keith E. Murray. High-power thulium fiber laser ablation of urinary tissues at 1.94 μm. *Journal of Endourology*, 19(1):25–31, 2005. PMID: 15735378.

[23] P. Agostini and L.F. DiMauro. Atoms in high intensity mid-infrared pulses. *Contemporary Physics*, 49(3):179–197, 2008.

[24] Jannick Weisshaupt, Vincent Juvé, Marcel Holtz, ShinAn Ku, Michael Woerner, Thomas Elsaesser, Skirmantas Ališauskas, Audrius Pugžlys, and Andrius Baltuška. High-brightness table-top hard X-ray source driven by sub-100-femtosecond mid-infrared pulses. *Nature Photonics*, 8(12):927, 2014.

[25] Tenio Popmintchev, Ming-Chang Chen, Dimitar Popmintchev, Paul Arpin, Susannah Brown, Skirmantas Ališauskas, Giedrius Andriukaitis, Tadas Balčiunas, Oliver D. Mücke, Audrius Pugzlys, Andrius Baltuška, Bonggu Shim, Samuel E. Schrauth, Alexander Gaeta, Carlos Hernández-García, Luis Plaja, Andreas Becker, Agnieszka Jaron-Becker, Margaret M. Murnane, and Henry C. Kapteyn. Bright coherent ultrahigh harmonics in the keV X-ray regime from mid-infrared femtosecond lasers. *Science*, 336(6086):1287–1291, 2012.

[26] Kyung-Han Hong, Chien-Jen Lai, Jonathas P. Siqueira, Peter Krogen, Jeffrey Moses, Chun-Lin Chang, Gregory J. Stein, Luis E. Zapata, and Franz X. Kärtner. Multi-mJ, kHz, 2.1 μm optical parametric chirped-pulse amplifier and high-flux soft x-ray high-harmonic generation. *Optics Letters*, 39(11):3145–3148, Jun 2014.

[27] Houkun Liang, Peter Krogen, Zhou Wang, Hyunwook Park, Tobias Kroh, Kevin Zawilski, Peter Schunemann, Jeffrey Moses, Louis F. DiMauro, Franz X. Kärtner, and Kyung-Han Hong. High-energy mid-infrared subcycle pulse synthesis from a parametric amplifier. *Nature Communications*, 8(1):141, 2017.

[28] L. E. Myers and W. R. Bosenberg. Periodically poled lithium niobate and quasi-phase-matched optical parametric oscillators. *IEEE Journal of Quantum Electronics*, 33(10):1663–1672, Oct 1997.

[29] Nick Leindecker, Alireza Marandi, Robert L. Byer, and Konstantin L. Vodopyanov. Broadband degenerate OPO for mid-infrared frequency comb generation. *Optics Express*, 19(7):6296–6302, 2011.

[30] Alireza Marandi, Nick C. Leindecker, Vladimir Pervak, Robert L. Byer, and Konstantin L. Vodopyanov. Coherence properties of a broadband femtosecond mid-IR optical parametric oscillator operating at degeneracy. *Optics Express*, 20(7):7255–7262, Mar 2012.

[31] N. Hendaoui, A. Peremans, P.G. Schunemann, K.T. Zawilski, and V. Petrov. Synchronously pumped OPO for picosecond pulse generation in the mid-infrared near 6.45 μm using AgGaS$_2$ and CdSiP$_2$: a comparative study. *Laser Physics*, 23(8):085401, 2013.

[32] Fritz Keilmann and Sergiu Amarie. Mid-infrared frequency comb spanning an octave based on an Er fiber laser and difference-frequency generation. *Journal of Infrared, Millimeter, and Terahertz Waves*, 33(5):479–484, 2012.

[33] Axel Ruehl, Alessio Gambetta, Ingmar Hartl, Martin E. Fermann, Kjeld S. E. Eikema, and Marco Marangoni. Widely-tunable mid-infrared frequency comb source based on difference frequency generation. *Optics Letters*, 37(12):2232–2234, Jun 2012.

[34] C. R. Phillips, J. Jiang, C. Mohr, A. C. Lin, C. Langrock, M. Snure, D. Bliss, M. Zhu, I. Hartl, J. S. Harris, M. E. Fermann, and M. M. Fejer. Widely tunable midinfrared difference frequency generation in orientation-patterned GaAs pumped with a femtosecond Tm-fiber system. *Optics Letters*, 37(14):2928–2930, Jul 2012.

[35] Alessio Gambetta, Nicola Coluccelli, Marco Cassinerio, Davide Gatti, Paolo Laporta, Gianluca Galzerano, and Marco Marangoni. Milliwatt-level frequency combs in the 8–14 μm range via difference frequency generation from an Er:fiber oscillator. *Optics Letters*, 38(7):1155–1157, Apr 2013.

[36] Gengji Zhou, Qian Cao, Franz X. Kärtner, and Guoqing Chang. Energy scalable, offset-free ultrafast mid-infrared source harnessing self-phase-modulation-enabled spectral selection. *Optics Letters*, 43(12):2953–2956, Jun 2018.

[37] Andrius Baltuška, Takao Fuji, and Takayoshi Kobayashi. Controlling the carrier-envelope phase of ultrashort light pulses with optical parametric amplifiers. *Physics Review Letters*, 88:133901, Mar 2002.

[38] Jarosław Sotor, Tadeusz Martynkien, Peter G. Schunemann, Paweł Mergo, Lucile Rutkowski, and Grzegorz Soboń. All-fiber mid-infrared source tunable from 6 to 9 μm based on difference frequency generation in OP-GaP crystal. *Optics Express*, 26(9):11756–11763, Apr 2018.

[39] Jungwon Kim and Youjian Song. Ultralow-noise mode-locked fiber lasers and frequency combs: principles, status, and applications. *Advances in Optics and Photonics*, 8(3):465–540, 2016.

[40] Govind P. Agrawal. *Nonlinear Fiber Optics*. Springer Berlin Heidelberg, 2000.

[41] J. P. Gordon and H. A. Haus. Random walk of coherently amplified solitons in optical fiber transmission. *Optics Letters*, 11(10):665–667, Oct 1986.

[42] F. M. Mitschke and L. F. Mollenauer. Discovery of the soliton self-frequency shift. *Optics Letters*, 11(10):659–661, Oct 1986.

[43] J. Santhanam and Govind P. Agrawal. Raman-induced spectral shifts in optical fibers: general theory based on the moment method. *Optics Communications*, 222(1):413 – 420, 2003.

[44] John M. Dudley, Goëry Genty, and Stéphane Coen. Supercontinuum generation in photonic crystal fiber. *Reviews of Modern Physics*, 78:1135–1184, 2006.

[45] S. Ramachandran, J. M. Fini, M. Mermelstein, J. W. Nicholson, S. Ghalmi, and M. F. Yan. Ultra-large effective-area, higher-order mode fibers: a new strategy for high-power lasers. *Laser & Photonics Reviews*, 2(6):429–448.

[46] James van Howe, Jennifer H. Lee, Shian Zhou, Frank Wise, Chris Xu, Siddharth Ramachandran, Samir Ghalmi, and Man F. Yan. Demonstration of soliton self-frequency shift below 1300 nm in higher-order mode, solid silica-based fiber. *Optics Letters*, 32(4):340–342, Feb 2007.

[47] S. Ramachandran, J. W. Nicholson, S. Ghalmi, M. F. Yan, P. Wisk, E. Monberg, and F. V. Dimarcello. Light propagation with ultralarge modal areas in optical fibers. *Optics Letters*, 31(12):1797–1799, Jun 2006.

[48] Y. Kodama and K. Nozaki. Soliton interaction in optical fibers. *Optics Letters*, 12(12):1038–1040, Dec 1987.

[49] P. K. A. Wai, C. R. Menyuk, Y. C. Lee, and H. H. Chen. Nonlinear pulse propagation in the neighborhood of the zero-dispersion wavelength of monomode optical fibers. *Optics Letters*, 11(7):464–466, Jul 1986.

[50] Nail Akhmediev and Magnus Karlsson. Cherenkov radiation emitted by solitons in optical fibers. *Physical Review A*, 51:2602–2607, Mar 1995.

[51] Wei Liu, Chen Li, Zhigang Zhang, Franz X. Kärtner, and Guoqing Chang. Self-phase modulation enabled, wavelength-tunable ultrafast fiber laser sources: an energy scalable approach. *Optics Express*, 24(14):15328–15340, Jul 2016.

[52] J. C. Knight, T. A. Birks, R. F. Cregan, P. S. J. Russell, and P. D. de Sandro. Large mode area photonic crystal fibre. *Electronics Letters*, 34(13):1347–1348, June 1998.

[53] N. G. R. Broderick, H. L. Offerhaus, D. J. Richardson, R. A. Sammut, J. Caplen, and L. Dong. Large mode area fibers for high power applications. *Optical Fiber Technology*, 5(2):185 – 196, 1999.

133

[54] Wei Liu, Shih-Hsuan Chia, Hsiang-Yu Chung, Rüdiger Greinert, Franz X. Kärtner, and Guoqing Chang. Energetic ultrafast fiber laser sources tunable in 1030–1215 nm for deep tissue multi-photon microscopy. *Optics Express*, 25(6):6822–6831, Mar 2017.

[55] H. Chung, W. Liu, Q. Cao, R. Greinert, Franz X. Kärtner, and G. Chang. Tunable, ultrafast fiber-laser between 1.15 and 1.35 μm for harmonic generation microscopy in human skin. *IEEE Journal of Selected Topics in Quantum Electronics*, 25(1):1–8, Jan 2019.

[56] Gengji Zhou, Ming Xin, Franz X. Kaertner, and Guoqing Chang. Timing jitter of Raman solitons. *Optics Letters*, 40(21):5105–5108, Nov 2015.

[57] Yi Hua, Gengji Zhou, Wei Liu, Franz X. Kärtner, and Guoqing Chang. Tightly synchronized two-color femtosecond source based on low-noise SPM-enabled spectral selection. In *Conference on Lasers and Electro-Optics*, page JTh2A.162. Optical Society of America, 2018.

[58] Ioachim Pupeza, D. Sánchez, Jinwei Zhang, Nicolai Lilienfein, Marcus Seidel, Nicholas Karpowicz, T. Paasch-Colberg, Irina Znakovskaya, M. Pescher, W. Schweinberger, V. Pervak, E. Fill, O. Pronin, Z. Wei, F. Krausz, A. Apolonski, and J. Biegert. High-power sub-two-cycle mid-infrared pulses at 100 MHz repetition rate. *Nature Photonics*, 9(11):721, 2015.

[59] J. A. Armstrong, N. Bloembergen, J. Ducuing, and P. S. Pershan. Interactions between light waves in a nonlinear dielectric. *Physical Review*, 127:1918–1939, Sep 1962.

[60] Robert W. Boyd. *Nonlinear Optics, Third Edition*. Academic Press, Inc., Orlando, FL, USA, 3rd edition, 2008.

[61] P.E. Powers. *Fundamentals of Nonlinear Optics*. Taylor & Francis, 2011.

[62] Robin Hegenbarth, Andy Steinmann, Sergey Sarkisov, and Harald Giessen. Milliwatt-level mid-infrared (10.5–16.5 μm) difference frequency generation with a femtosecond dual-signal-wavelength optical parametric oscillator. *Optics Letters*, 37(17):3513–3515, Sep 2012.

[63] Jinwei Zhang, Ka Fai Mak, Nathalie Nagl, Marcus Seidel, Dominik Bauer, Dirk Sutter, Vladimir Pervak, Ferenc Krausz, and Oleg Pronin. Multi-mW, few-cycle mid-infrared continuum spanning from 500 to 2250 cm^{-1}. *Light: Science & Applications*, 7(2):17180, 2018.

[64] Christian Gaida, Martin Gebhardt, Tobias Heuermann, Fabian Stutzki, Cesar Jauregui, Jose Antonio-Lopez, Axel Schülzgen, Rodrigo Amezcua-Correa, Andreas Tünnermann, Ioachim Pupeza, and Jens Limpert. Watt-scale super-octave mid-infrared intrapulse difference frequency generation. *Light: Science & Applications*, 7(1):94, 2018.

[65] T. P. Butler, D. Gerz, C. Hofer, J. Xu, C. Gaida, T. Heuermann, M. Gebhardt, L. Vamos, W. Schweinberger, J. A. Gessner, T. Siefke, M. Heusinger, U. Zeitner, A. Apolonski, N. Karpowicz, J. Limpert, F. Krausz, and I. Pupeza. Watt-scale 50-MHz source of single-cycle waveform-stable pulses in the molecular fingerprint region. *Optics Letters*, 44(7):1730–1733, Apr 2019.

[66] Sergey Vasilyev, Igor S. Moskalev, Viktor O. Smolski, Jeremy M. Peppers, Mike Mirov, Andrey V. Muraviev, Kevin Zawilski, Peter G. Schunemann, Sergey B. Mirov, Konstantin L. Vodopyanov, and Valentin P. Gapontsev. Super-octave longwave mid-infrared coherent transients produced by optical rectification of few-cycle 2.5-μm pulses. *Optica*, 6(1):111–114, Jan 2019.

[67] Qing Wang, Jinwei Zhang, Alexander Kessel, Nathalie Nagl, Vladimir Pervak, Oleg Pronin, and Ka Fai Mak. Broadband mid-infrared coverage (2–17 μm) with few-cycle pulses via cascaded parametric processes. *Optics Letters*, 44(10):2566–2569, May 2019.

[68] D. Sánchez, M. Hemmer, M. Baudisch, K. Zawilski, P. Schunemann, H. Hoogland, R. Holzwarth, and J. Biegert. Broadband mid-ir frequency comb with $CdSiP_2$ and $AgGaS_2$ from an Er,Tm:Ho fiber laser. *Optics Letters*, 39(24):6883–6886, Dec 2014.

[69] Kazi Sarwar Abedin, Sajjad Haidar, Yuji Konno, Choichi Takyu, and Hiromasa Ito. Difference frequency generation of 5–18 μm in a $AgGaSe_2$ crystal. *Applied Optics*, 37(9):1642–1646, Mar 1998.

[70] Marcus Beutler, Ingo Rimke, Edlef Büttner, Paolo Farinello, Antonio Agnesi, Valeriy Badikov, Dmitrii Badikov, and Valentin Petrov. Difference-frequency generation of ultrashort pulses in the mid-IR using Yb-fiber pump systems and $AgGaSe_2$. *Optics Express*, 23(3):2730–2736, Feb 2015.

[71] Tobias Steinle, Florian Mörz, Andy Steinmann, and Harald Giessen. Ultrastable high average power femtosecond laser system tunable from 1.33 to 20 μm. *Optics Letters*, 41(21):4863–4866, Nov 2016.

[72] D. Sanchez, M. Hemmer, M. Baudisch, S. L. Cousin, K. Zawilski, P. Schunemann, O. Chalus, C. Simon-Boisson, and J. Biegert. 7 μm, ultrafast, sub-millijoule-level mid-infrared optical parametric chirped pulse amplifier pumped at 2 μm. *Optica*, 3(2):147–150, Feb 2016.

[73] Kun Liu, Houkun Liang, Lifeng Wang, Shizhen Qu, Tino Lang, Hao Li, Qi Jie Wang, and Ying Zhang. Multimicrojoule gase-based midinfrared optical parametric amplifier with an ultrabroad idler spectrum covering 4.2 μm. *Optics Letters*, 44(4):1003–1006, Feb 2019.

[74] Hsiang-Yu Chung, Wei Liu, Qian Cao, Liwei Song, Franz X Kärtner, and Guoqing Chang. Megawatt peak power tunable femtosecond source based on

self-phase modulation enabled spectral selection. *Optics Express*, 26(3):3684–3695, 2018.

[75] N. Haverkamp, H. Hundertmark, C. Fallnich, and H.R. Telle. Frequency stabilization of mode-locked Erbium fiber lasers using pump power control. *Applied Physics B*, 78(3):321–324, Feb 2004.

[76] M. D. Swallows, M. J. Martin, M. Bishof, C. Benko, Y. Lin, S. Blatt, A. M. Rey, and J. Ye. Operating a ^{87}Sr optical lattice clock with high precision and at high density. *IEEE Transactions on Ultrasonics, Ferroelectrics, and Frequency Control*, 59(3):416–425, March 2012.

[77] Ian Coddington, Nathan Newbury, and William Swann. Dual-comb spectroscopy. *Optica*, 3(4):414–426, Apr 2016.

[78] Gabriel Ycas, Fabrizio R. Giorgetta, Esther Baumann, Ian Coddington, Daniel Herman, Scott A. Diddams, and Nathan R. Newbury. High-coherence mid-infrared dual-comb spectroscopy spanning 2.6 to 5.2 μm. *Nature Photonics*, 12(4):202, 2018.

[79] Henry Timmers, Abijith Kowligy, Alex Lind, Flavio C. Cruz, Nima Nader, Myles Silfies, Gabriel Ycas, Thomas K. Allison, Peter G. Schunemann, Scott B. Papp, et al. Molecular fingerprinting with bright, broadband infrared frequency combs. *Optica*, 5(6):727–732, 2018.

[80] Birgitta Bernhardt, Akira Ozawa, Patrick Jacquet, Marion Jacquey, Yohei Kobayashi, Thomas Udem, Ronald Holzwarth, Guy Guelachvili, Theodor W. Hänsch, and Nathalie Picqué. Cavity-enhanced dual-comb spectroscopy. *Nature Photonics*, 4(1):55, 2010.

[81] A. Foltynowicz, P. Masłowski, A. J. Fleisher, B. J. Bjork, and J. Ye. Cavity-enhanced optical frequency comb spectroscopy in the mid-infrared application to trace detection of hydrogen peroxide. *Applied Physics B*, 110(2):163–175, Feb 2013.

[82] Rupert Huber, A. Brodschelm, F. Tauser, and A. Leitenstorfer. Generation and field-resolved detection of femtosecond electromagnetic pulses tunable up to 41 THz. *Applied Physics Letters*, 76(22):3191–3193, 2000.

[83] N. R. Newbury and B. R. Washburn. Theory of the frequency comb output from a femtosecond fiber laser. *IEEE Journal of Quantum Electronics*, 41(11):1388–1402, Nov 2005.

[84] D. von der Linde. Characterization of the noise in continuously operating mode-locked lasers. *Applied Physics B*, 39(4):201–217, Apr 1986.

[85] Jens Rauschenberger, Tara M. Fortier, David J. Jones, Jun Ye, and Steven T. Cundiff. Control of the frequency comb from a mode-locked Erbium-doped fiber laser. *Optics Express*, 10(24):1404–1410, Dec 2002.

[86] Brian R. Washburn, Scott A. Diddams, Nathan R. Newbury, Jeffrey W. Nicholson, Man F. Yan, and Carsten G. Jørgensen. Phase-locked, erbium-fiber-laser-based frequency comb in the near infrared. *Optics Letters*, 29(3):250–252, Feb 2004.

[87] T. R. Schibli, K. Minoshima, F.-L. Hong, H. Inaba, A. Onae, H. Matsumoto, I. Hartl, and M. E. Fermann. Frequency metrology with a turnkey all-fiber system. *Optics Letters*, 29(21):2467–2469, Nov 2004.

[88] B. R. Washburn, R. W. Fox, N. R. Newbury, J. W. Nicholson, K. Feder, P. S. Westbrook, and C. G. Jørgensen. Fiber-laser-based frequency comb with a tunable repetition rate. *Optics Express*, 12(20):4999–5004, Oct 2004.

[89] Travis C. Briles, Dylan C. Yost, Arman Cingöz, Jun Ye, and Thomas R. Schibli. Simple piezoelectric-actuated mirror with 180 kHz servo bandwidth. *Optics Express*, 18(10):9739–9746, May 2010.

[90] Laura C. Sinclair, J.-D. Deschênes, L. Sonderhouse, William C. Swann, Isaac H. Khader, Esther Baumann, Nathan R. Newbury, and I. Coddington. Invited article: A compact optically coherent fiber frequency comb. *Review of Scientific Instruments*, 86(8):081301, 2015.

[91] Darren D. Hudson, Kevin W. Holman, R. Jason Jones, Steven T. Cundiff, Jun Ye, and David J. Jones. Mode-locked fiber laser frequency-controlled with an intracavity electro-optic modulator. *Optics Letters*, 30(21):2948–2950, Nov 2005.

[92] Esther Baumann, Fabrizio R Giorgetta, Jeffrey W Nicholson, William C Swann, Ian Coddington, and Nathan R Newbury. High-performance, vibration-immune, fiber-laser frequency comb. *Optics Letters*, 34(5):638–640, 2009.

[93] C. Benko, A. Ruehl, M. J. Martin, K. S. E. Eikema, M. E. Fermann, I. Hartl, and J. Ye. Full phase stabilization of a Yb:fiber femtosecond frequency comb via high-bandwidth transducers. *Optics Letters*, 37(12):2196–2198, 2012.

[94] N. Kuse, J. Jiang, C.-C. Lee, T. R. Schibli, and M. E. Fermann. All polarization-maintaining Er fiber-based optical frequency combs with nonlinear amplifying loop mirror. *Optics Express*, 24(3):3095–3102, Feb 2016.

[95] H. R. Telle, G. Steinmeyer, A. E. Dunlop, J. Stenger, D. H. Sutter, and U. Keller. Carrier-envelope offset phase control: A novel concept for absolute optical frequency measurement and ultrashort pulse generation. *Applied Physics B*, 69(4):327–332, Oct 1999.

[96] Holger Hundertmark, Dieter Wandt, Carsten Fallnich, Nils Haverkamp, and Harald R. Telle. Phase-locked carrier-envelope-offset frequency at 1560 nm. *Optics Express*, 12(5):770–775, Mar 2004.

[97] A. Poppe, R. Holzwarth, A. Apolonski, G. Tempea, Ch. Spielmann, T. W. Hänsch, and F. Krausz. Few-cycle optical waveform synthesis. *Applied Physics B*, 72(3):373–376, Feb 2001.

[98] C.-C. Lee, C. Mohr, J. Bethge, S. Suzuki, M. E. Fermann, I. Hartl, and T. R. Schibli. Frequency comb stabilization with bandwidth beyond the limit of gain lifetime by an intracavity graphene electro-optic modulator. *Optics Letters*, 37(15):3084–3086, Aug 2012.

[99] Martin Hoffmann, Stéphane Schilt, and Thomas Südmeyer. CEO stabilization of a femtosecond laser using a SESAM as fast opto-optical modulator. *Optics Express*, 21(24):30054–30064, Dec 2013.

[100] Sebastian Koke, Christian Grebing, Harald Frei, Alexandria Anderson, Andreas Assion, and Günter Steinmeyer. Direct frequency comb synthesis with arbitrary offset and shot-noise-limited phase noise. *Nature Photonics*, 4(7):462, 2010.

[101] B. Borchers, S. Koke, A. Husakou, J. Herrmann, and G. Steinmeyer. Carrier-envelope phase stabilization with sub-10 as residual timing jitter. *Optics Letters*, 36(21):4146–4148, Nov 2011.

[102] Fabian Lücking, Andreas Assion, Alexander Apolonski, Ferenc Krausz, and Günter Steinmeyer. Long-term carrier-envelope-phase-stable few-cycle pulses by use of the feed-forward method. *Optics Letters*, 37(11):2076–2078, Jun 2012.

[103] Herman A Haus and Antonio Mecozzi. Noise of mode-locked lasers. *IEEE Journal of Quantum Electronics*, 29(3):983–996, 1993.

[104] R Paschotta. Noise of mode-locked lasers (Part I): numerical model. *Applied Physics B*, 79(2):153–162, 2004.

[105] R Paschotta. Noise of mode-locked lasers (Part II): timing jitter and other fluctuations. *Applied Physics B*, 79(2):163–173, 2004.

[106] Nathan R Newbury and William C Swann. Low-noise fiber-laser frequency combs. *J. Opt. Soc. Am. B*, 24(8):1756–1770, 2007.

[107] H. A. Haus and Y. Lai. Quantum theory of soliton squeezing: a linearized approach. *J. Opt. Soc. Am. B*, 7(3):386–392, Mar 1990.

[108] S. Namiki and H. A. Haus. Noise of the stretched pulse fiber laser. I. Theory. *IEEE Journal of Quantum Electronics*, 33(5):649–659, May 1997.

[109] Youjian Song, Chur Kim, Kwangyun Jung, Hyoji Kim, and Jungwon Kim. Timing jitter optimization of mode-locked Yb-fiber lasers toward the attosecond regime. *Optics Express*, 19(15):14518–14525, Jul 2011.

[110] Chur Kim, Sangho Bae, Khanh Kieu, and Jungwon Kim. Sub-femtosecond timing jitter, all-fiber, CNT-mode-locked Er-laser at telecom wavelength. *Optics Express*, 21(22):26533–26541, Nov 2013.

[111] John Zweck and Curtis R. Menyuk. Computation of the timing jitter, phase jitter, and linewidth of a similariton laser. *J. Opt. Soc. Am. B*, 35(5):1200–1210, May 2018.

[112] Leaf A. Jiang, Matthew E. Grein, Erich P. Ippen, Cameron McNeilage, Jesse Searls, and Hiroyuki Yokoyama. Quantum-limited noise performance of a mode-locked laser diode. *Optics Letters*, 27(1):49–51, Jan 2002.

[113] Chunmei Ouyang, Ping Shum, Honghai Wang, Jia Haur Wong, Kan Wu, Songnian Fu, Ruoming Li, E. J. R. Kelleher, A. I. Chernov, and E. D. Obraztsova. Observation of timing jitter reduction induced by spectral filtering in a fiber laser mode locked with a carbon nanotube-based saturable absorber. *Optics Letters*, 35(14):2320–2322, Jul 2010.

[114] Peng Qin, Youjian Song, Hyoji Kim, Junho Shin, Dohyeon Kwon, Minglie Hu, Chingyue Wang, and Jungwon Kim. Reduction of timing jitter and intensity noise in normal-dispersion passively mode-locked fiber lasers by narrow band-pass filtering. *Optics Express*, 22(23):28276–28283, Nov 2014.

[115] Youjian Song, Kwangyun Jung, and Jungwon Kim. Impact of pulse dynamics on timing jitter in mode-locked fiber lasers. *Optics Letters*, 36(10):1761–1763, May 2011.

[116] K. Tamura, H. A. Haus, and E. P. Ippen. Self-starting additive pulse mode-locked erbium fibre ring laser. *Electronics Letters*, 28(24):2226–2228, 1992.

[117] H. R. Telle, B. Lipphardt, and J. Stenger. Kerr-lens, mode-locked lasers as transfer oscillators for optical frequency measurements. *Applied Physics B*, 74(1):1–6, Jan 2002.

[118] T. R. Schibli, J. Kim, O. Kuzucu, J. T. Gopinath, S. N. Tandon, G. S. Petrich, L. A. Kolodziejski, J. G. Fujimoto, E. P. Ippen, and F. X. Kaertner. Attosecond active synchronization of passively mode-locked lasers by balanced cross correlation. *Optics Letters*, 28(11):947–949, Jun 2003.

[119] Thomas Puppe, Alexander Sell, Russell Kliese, Nazanin Hoghooghi, Armin Zach, and Wilhelm Kaenders. Characterization of a DFG comb showing quadratic scaling of the phase noise with frequency. *Optics Letters*, 41(8):1877–1880, Apr 2016.

[120] Franz X Kärtner. *Few-cycle laser pulse generation and its applications*, volume 95. Springer Science & Business Media, 2004.

[121] Stéphane Plaszczynski. Generating long streams of $1/f^\alpha$ noise. *Fluctuation and Noise Letters*, 7(01):R1–R13, 2007.

[122] Gianni Di Domenico, Stéphane Schilt, and Pierre Thomann. Simple approach to the relation between laser frequency noise and laser line shape. *Applied Optics*, 49(25):4801–4807, Sep 2010.

[123] A. L. Schawlow and C. H. Townes. Infrared and optical masers. *Physical Review*, 112:1940–1949, Dec 1958.

[124] C. Henry. Theory of the linewidth of semiconductor lasers. *IEEE Journal of Quantum Electronics*, 18(2):259–264, February 1982.

[125] D. S. Elliott, Rajarshi Roy, and S. J. Smith. Extracavity laser band-shape and bandwidth modification. *Physical Review A*, 26:12–18, Jul 1982.

[126] Erik Benkler, Harald R. Telle, Armin Zach, and Florian Tauser. Circumvention of noise contributions in fiber laser based frequency combs. *Optics Express*, 13(15):5662–5668, Jul 2005.

[127] Tolga Yilmaz, Christopher M. DePriest, Terry Turpin, Joseph H. Abeles, and P. J. Delfyett. Toward a photonic arbitrary waveform generator using a modelocked external cavity semiconductor laser. *IEEE Photonics Technology Letters*, 14(11):1608–1610, 2002.

[128] Na Ji, Jeffrey C. Magee, and Eric Betzig. High-speed, low-photodamage nonlinear imaging using passive pulse splitters. *Nature Methods*, 5(2):197, 2008.

[129] Chen Li, Yuxuan Ma, Xiang Gao, Fuzeng Niu, Tongxiao Jiang, Aimin Wang, and Zhigang Zhang. 1 GHz repetition rate femtosecond Yb:fiber laser for direct generation of carrier-envelope offset frequency. *Applied Optics*, 54(28):8350–8353, Oct 2015.

[130] Bo Xu, Hideaki Yasui, Yoshiaki Nakajima, Yuxuan Ma, Zhigang Zhang, and Kaoru Minoshima. Fully stabilized 750-MHz Yb: fiber frequency comb. *Optics Express*, 25(10):11910–11918, May 2017.

[131] Marcus Zimmermann, Christoph Gohle, Ronald Holzwarth, Thomas Udem, and Theodor W. Hänsch. Optical clockwork with an offset-free difference-frequency comb: accuracy of sum-and difference-frequency generation. *Optics Letters*, 29(3):310–312, 2004.

[132] Takuma Nakamura, Isao Ito, and Yohei Kobayashi. Offset-free broadband Yb: fiber optical frequency comb for optical clocks. *Optics Express*, 23(15):19376–19381, 2015.

[133] David Fehrenbacher, Philipp Sulzer, Andreas Liehl, Thomas Kälberer, Claudius Riek, Denis V. Seletskiy, and Alfred Leitenstorfer. Free-running performance and full control of a passively phase-stable Er: fiber frequency comb. *Optica*, 2(10):917–923, 2015.

Appendix A

Fiber specifications

PCF type	ZDW (nm)	MFD (μm)	MFA (μm^2)	γ (W^{-1}km^{-1})
PCF-850	850	1.9	2.84	55.8
PCF-945	945	2.8	6.16	25.7
PCF-975	975	3.3	8.55	17.9

Table A.1: Specification for PCF-850/945/975

ZDW: zero dispersion wavelength; MFD: mode field diameter; MFA: mode field area; γ: nonlinear coefficient (see Equation 2.2).

LMA type	ZDW (nm)	MFD (μm)	MFA (μm^2)	γ (W^{-1}km^{-1})
LMA-8	1170	7.5	45.4	3.5
LMA-10	1195	8.6	58.1	2.7
LMA-15	1240	12.6	124.7	1.3

Table A.2: Specification for LMA-8/10/15.

CRYSTAL FIBRE

Typical measured near field profile (log scale)

Optical properties

• Zero dispersion wavelength (λ_0)			850±5 nm
• Dispersion slope at λ_0			0.48 ps·nm^{-2}·km^{-1}
• Attenuation	λ_0	<	10 dB/km
	1550 nm	<	6 dB/km
	1380 nm	<	40 dB/km
	1000 nm	<	10 dB/km
	600 nm	<	17 dB/km
• Mode field diameter[1] at λ_0			1.9±0.1 µm
• Numerical aperture[2] at λ_0			0.38
• Effective nonlinear area[3]			4.0 µm^2
• Nonlinear coefficient[4] at λ_0			47 W^{-1}·km^{-1}

Physical properties

• Core diameter (average)	2.8±0.1µm
• Pitch (distance between cladding holes)	2.7 µm
• Air Filling Fraction in the holey region	>88%
• Width of struts holding the core	160 nm
• Diameter of holey region	28 µm
• Diameter of outer silica cladding (OD)	136 µm
• Coating diameter (single layer acrylate)	220 µm
• Available length	up to 1 km

To contact Crystal Fibre A/S, please visit our website www.crystal-fibre.com or send an email message to contact@crystal-fibre.com

CRYSTAL FIBRE

Figure A.1: Specification of PCF-850 (Part I).

Figure A.2: Specification of PCF-850 (Part II).

Nonlinear Photonic Crystal Fibers for 1060 nm Pumping

CRYSTAL FIBRE

Description
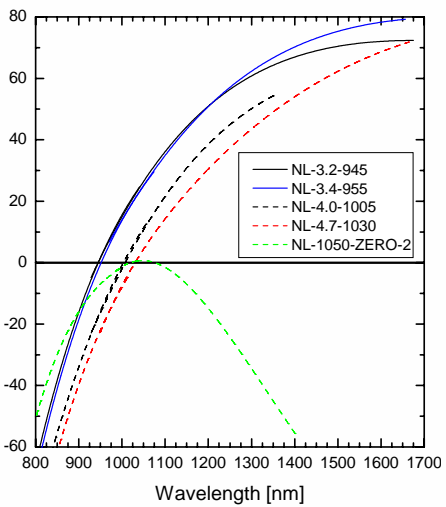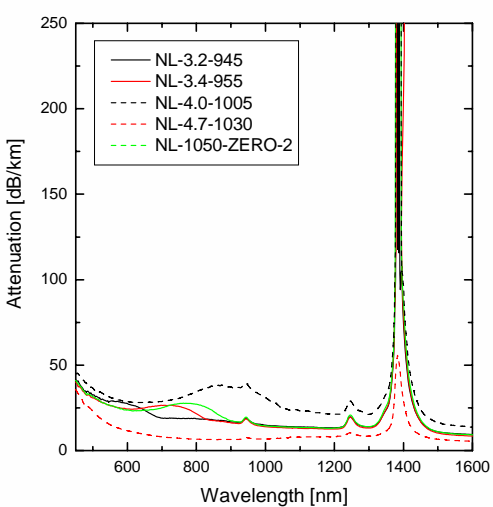
Photonic crystal fibers use a microstructured cladding region with air holes to guide light in a pure silica core, giving rise to novel functionalities. These nonlinear photonic crystal fibers combine a very small effective mode field area and zero dispersion to allow efficient supercontinuum generation with 1060 nm pump sources. The fibers are available with hermetically sealed ends and FC/PC connectors or could be spliced to standard single mode fiber or large mode area PCF on a custom order basis.

Fiber Properties

Item Name	C,S	Core Diameter [μm]	Cladding Diameter [μm]	Estimated ZDW [nm]	Attenuation @ 1060 nm [dB/km]	SM cut-off Wavelength [nm]	Mode Field Diameter [μm]	NA @ 1060 nm [5 %]	γ @ 1060 nm [Wkm^{-1}]
NL-3.2-945	C	3.2	137	945	‹20	730	2.8	0.29	23
NL-3.4-955	C	3.4	145	955	‹20	775	2.9	0.28	22
NL-4.0-1005	C	4.0	173	1005	‹35	1015	3.4	0.24	16
NL-4.7-1030	C,S	4.7	124	1030	‹15	1024	3.8	0.21	12
SC-5.0-1040	C,S	4.8	125	1040	‹2	1000	4.0	0.2	11
NL-1050-NEG-1	C,S	2.3	127	None	‹30	300	2.2	0.37	37
NL-1050-ZERO-2	C,S	2.3	127	1050	‹30	300	2.2	0.37	37
NL-5.0-1065	C,S	5.0	121	1065	‹20	1000	4.2	0.2	11

ZDW: Zero Dispersion Wavelength
C: Available with hermetically sealed ends and Connectors
S: Available with Splicing to standard fiber. All fibers can be provided with standard fiber pigtails on a custom order basis.

Dispersion and attenuation

Please also refer to individual datasheets for SC-5.0-1040, NL-1050-NEG-1, NL-1050-ZERO-2 and NL-5.0-1065

Crystal Fibre A/S – ☎ US toll-free: 877-810-2800 – ☎ International: +45 4348 2800 – contact@crystal-fibre.com – www.crystal-fibre.com

NL-1060 List Rev 1.2 July 2006

Figure A.3: Specification of PCF-945.

Crystal Fibre ● *aero*LASE ● Koheras ● SuperK

SC-3.7-975

Nonlinear fiber for supercontinuum generation

Single Mode | Highly Nonlinear

- **Single mode**
- **Pure silica**
- **Dispersion optimized for 1 µm wavelength pumping**

This single-mode nonlinear photonic crystal fiber combines a high nonlinear coefficient with zero dispersion around 975 nm to allow efficient nonlinear interactions using 1060 nm range lasers.

The fiber is designed for high power ps pumped supercontinuum generation. Due to the optimized dispersion profile, a length of only 10-15 m of this fiber is sufficient to generate octave spanning spectra when pumped with high power ps sources.

The fiber is available spliced to standard single mode fiber or endlessly single mode fiber, and is also available with hermetically sealed ends and FC/PC connectors.

Applications
Broadband continuum generation for:
- Spectroscopy
- Microscopy
- Metrology
- Optical coherence tomography, OCT
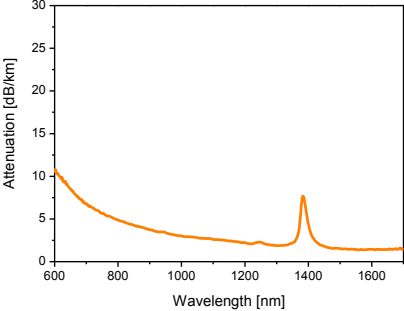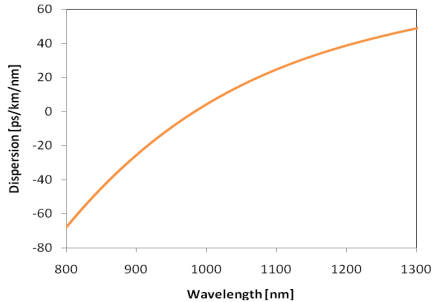
Physical properties	
Material	Pure silica
Cladding diameter	125 ± 10 µm
Coating diameter	245 ± 10 µm
Coating material	HT Acrylate
Core diameter	3.7 ± 0.3 µm

Optical properties	
Zero dispersion wavelength	975± 15 nm
Cut-off wavelength	‹ 1000 nm
Nonlinear coefficient @ 1060 nm	~18 (W·km)$^{-1}$
Attenuation @ 1060nm	‹ 5 dB/km
Attenuation @ 1550 nm	‹ 3 dB/km
Attenuation @ 600 nm	‹ 15 dB/km
Mode Field Diameter	3.3 ± 0.3 µm
NA @ 1060 nm	0.25 ± 0.05

Typical measured spectral attenuation

Typical measured dispersion

SC-3.7-975-131008

Figure A.4: Specification of PCF-975.

NKT Photonics
the power of light

Crystal Fibre ● *aero*LASE ● Koheras ● SuperK

Single Mode

Large Mode-area

LMA-8
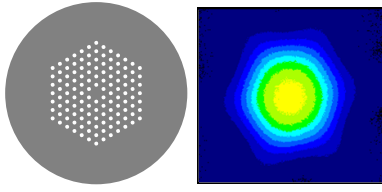
Single-Mode 8 μm Core Fiber

- Low fiber loss from 400 nm to 1700 nm
- Single-mode at all wavelengths
- Radiation hard pure silica fiber
- Wavelength independent MFD

This single-mode photonic crystal fiber is optimized to exhibit low loss across the widest possible wavelength region from 400 nm to above 1700 nm while keeping an almost constant mode field diameter.

The fiber is endlessly single-mode with no higher order mode cut-off and delivers pristine mode quality at all wavelengths.
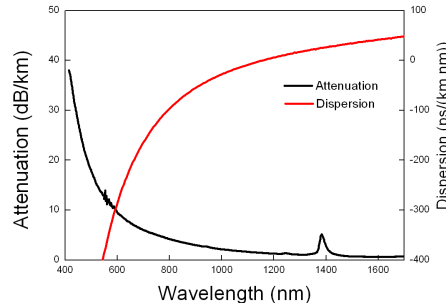
The fiber has a standard 125 μm outer diameter and is compatible with all common fiber tools.
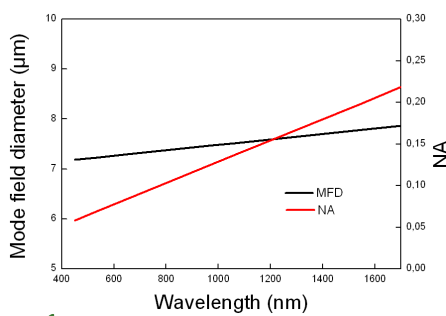
Applications
- Single-mode delivery and pigtailing
- RGB transmission
- Mode filtering
- Short pulse delivery

Optical properties	
Single mode cut-off wavelength*	None
Attenuation @ 532 nm**	‹ 20 dB/km
Attenuation @ 632 nm	‹ 10 dB/km
Attenuation @ 1064 nm	‹ 5 dB/km
Mode field diameter @ 532 nm $(1/e^2)$	7.2 ± 1.0 μm
Mode field diameter @ 1064 nm $(1/e^2)$	7.5 ± 1.0 μm
NA @ 1064 nm (5%)	0.14 ± 0.02

Physical properties	
Core diameter	8.6 ± 0.5 μm
Outer cladding diameter, OD	125 ± 2 μm
Coating diameter	245 ± 10 μm
Core and cladding material	Pure silica
Coating material, single layer	Acrylate
Coating-Cladding concent. error	‹ 10 μm
Proof test level	0.5 %

Standard interfacing options	
FC/PC connector	0.0 ± 0.5 deg angle
FC/APC connector	8.0 ± 0.5 deg angle
Collapse and cleave	0.0 ± 0.5 deg angle

All interfaces are provided with a 150 ± 25 μm sealing length of the PCF structure.

Please contact us for other custom interfacing options.

* TIA-455-80-C standard   ** 16 cm bend diameter

Typical spectral attenuation and dispersion

Typical MFD and dispersion

RoHS
2002/95/EC

LMA-8, v. 1-120611

Figure A.5: Specification of LMA-8.

NKT Photonics
the power of light

Crystal Fibre ● *aero*LASE ● Koheras ● SuperK

Single Mode

Large Mode-area
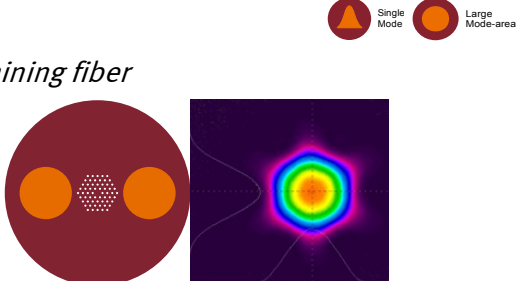
LMA-PM-10
Single-mode 10 µm polarization-maintaining fiber

- **Low loss fiber from 500 to 1700 nm**
- **Single mode at all wavelengths**
- **Polarization Maintaining**
- **Radiation hard pure silica fiber**
- **Wavelength independent MFD**

This polarization-maintaining single-mode fiber is optimized to exhibit low loss from 500 nm to 1700 nm while keeping an almost constant mode field diameter.

The fiber is endlessly single-mode (i.e. it has no higher order mode cut-off) and delivers excellent mode quality at all wavelengths.

This product is also available in a non polarization-maintaining version as the LMA-10
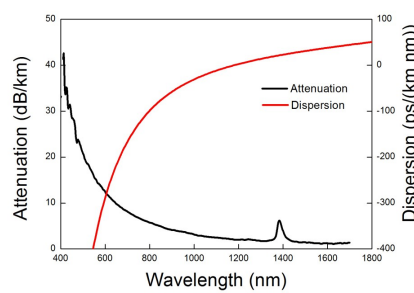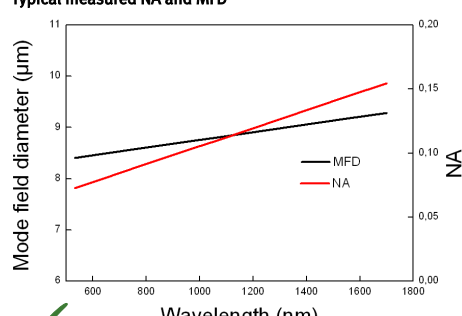
Applications
- Single-mode PM short wavelength delivery
- Multi-wavelength transmission
- Mode filtering
- Single-mode PM pigtailing
- Short pulse delivery

Typical spectral attenuation and dispersion

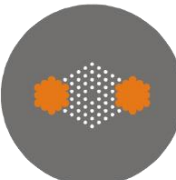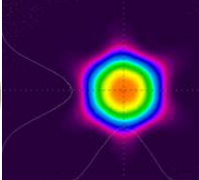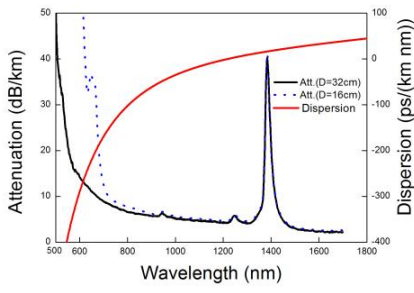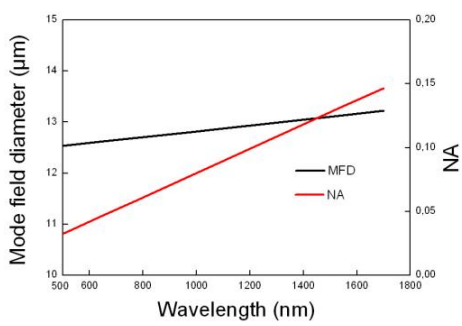| Optical properties	
Single mode cut-off wavelength*	None
Attenuation @ 532 nm**	‹ 25 dB/km
Attenuation @ 632 nm	‹ 15 dB/km
Attenuation @ 1064 nm	‹ 5 dB/km
Mode field diameter @ 532 nm (1/e²)	8.4 ± 1.0 µm
Mode field diameter @ 1064 nm (1/e²)	8.6 ± 1.0 µm
NA @ 1064 nm (5%)	0.12 ± 0.02
Birefringence Δn @ 1064 nm	$1.4 \cdot 10^{-4}$
Polarization Extinction Ratio***	› 18 dB
Physical properties	
Core diameter	10.0 ± 0.5 µm
Outer cladding diameter, OD	230 ± 5 µm
Coating diameter	350 ± 10 µm
Core and cladding material	Pure silica
Coating material, single layer	Acrylate
Coating-Cladding concent. error	‹ 10 µm
Proof test level	0.33 %
Standard interfacing options	
FC/PC PM connector	0.0 ± 0.5 deg angle
FC/APC PMconnector	8.0 ± 0.5 deg angle
SMA 905	0.0 or 5.0 ± 0.5 deg angle
Collapse and cleave	0.0 ± 0.5 deg angle

All interfaces are provided with a 75 ± 25 µm sealing length of the PCF structure. PM connectors are keyd to the slow axis. Please contact us for other custom interfacing options.

* TIA-455-80-C standard
** 16 cm bend diameter

*** AKA PXtalk on a 2 m sample

Typical measured NA and MFD

RoHS 2002/95/EC

LMA-PM-10-v1-130417

Figure A.6: Specification of LMA-10.

Figure A.7: Specification of LMA-15.

STANDARD MODELS

Ytterbium (YB) Doped Single Clad Fibers						
Model	Core Diameter (µm)	Clad Diameter (µm)	MFD @ 1060nm (µm)	Core NA	Core Absorption @ 915nm (dB/m)	Birefringence	Note
YB 103	N/A	125 ± 1	3.5 ± 1.0	0.26 ± 0.02	> 9	N/A	
SCF-YB40-4/125-16	4.0 ± 1.0	125 ± 1	N/A	0.16 ± 0.02	40 ± 10	N/A	
YB 115	N/A	125 ± 1	4.0 ± 1.0	0.22 ± 0.02	50 ± 10	N/A	Photosensitive (high Ge content)
YB 118	N/A	125 ± 1	4.0 ± 1.0	0.22 ± 0.02	> 75	N/A	Photosensitive (high Ge content)
YB 501	N/A	125 ± 1	6.0 ± 1.0	0.14 ± 0.02	> 125	N/A	Matched to HI 1060, Confined[1] Matched PM Version: YB 501-PM
YB 401	N/A	125 ± 1	6.0 ± 1.0	0.14 ± 0.02	140 ± 25	N/A	Matched to HI 1060, Photodarkening-resistant Matched Non-PM Version: YB 401-PM
YB 198	N/A	125 ± 1	4.0 ± 1.0	0.22 ± 0.02	> 250	N/A	
YB 214	N/A	125 ± 1	6.0 ± 1.0	0.14 ± 0.02	> 300	N/A	
YB 402	N/A	125 ± 1	7.0 ± 1.0	0.12 ± 0.02	250 ± 50	N/A	Photodarkening-resistant
YB 125	N/A	125 ± 1	5.0 ± 1.0	0.18 ± 0.02	> 350	N/A	
YB 404	N/A	125 ± 1	5.0 ± 1.0	0.16 ± 0.02	475 ± 100	N/A	Photodarkening-resistant
SCF-YB550-4/125-19	4.0 ± 1.0	125 ± 1	N/A	0.19 ± 0.02	550 ± 100	N/A	
YB 406	N/A	125 ± 1	5.0 ± 1.0	0.16 ± 0.02	600 ± 100	N/A	Photodarkening-resistant
YB 100-PM	N/A	125 ± 2	5.0 ± 1.0	0.16 ± 0.02	> 8	≥ 2.0E-04	PM
YB 200-PM	N/A	125 ± 2	5.0 ± 1.0	0.16 ± 0.02	> 12	≥ 2.0E-04	PM
YB 401-PM	N/A	125 ± 2	6.0 ± 1.0	0.14 ± 0.02	140 ± 25	> 2.0E-04	Photodarkening-resistant, Matched Non-PM Version: Yb 401
YB 501-PM	N/A	125 ± 2	6.0 ± 1.0	0.14 ± 0.02	140 ± 25	> 2.0E-04	Confined[1] Matched Non-PM Version: Yb 164

Note 1: A confined optical fiber refers to an active fiber where only a fraction of the core is doped. This is typically done to improve fiber efficiency.
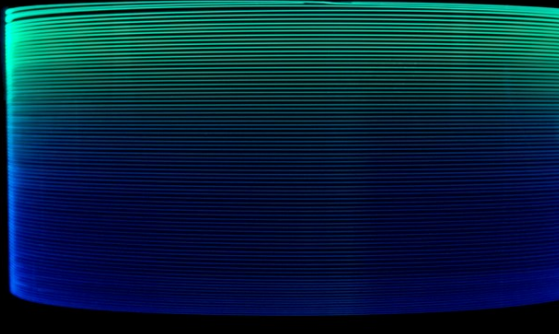
Figure A.8: Specification of SCF-YB550-4/125-19.

LIEKKI®

Yb1200-12/125 – Large Mode Area Ytterbium Doped Fiber

LIEKKI® Yb1200-12/125 fibers are very highly doped large mode area fibers for medium power fiber laser and amplifier applications, where high beam quality and compact design are essential.

LIEKKI® Yb1200-12/125 fibers are available as double-clad (Yb1200-12/125DC) and double-clad polarization maintaining (Yb1200-12/125DC-PM) fibers.

Features

- Industry leading fiber deposition process — Direct Nanoparticle Deposition
- *real*NA — most accurate fiber core NA to enable superior predictability of fiber performance and minimal splice loss
- Large, low-NA core for low nonlinearity and high beam quality applications
- Combining high pump absorption with low photodarkening loss
- Acrylate coating enables fiber applications in extreme environmental conditions: Proven to operate up to 120˚C and in extreme humidity.
- Matching passive fibers available with optimized design for minimal splice loss

Applications

- Medium power amplifiers and lasers
- Pulsed and CW applications
- IR source for frequency doubling
- Industrial, medical and scientific applications

Typical Fiber Specifications

Fiber Optical	Units	LIEKKI® Yb1200-12/125DC	LIEKKI® Yb1200-12/125DC-PM
Peak Cladding Absorption at 976 nm (nominal)	dB/m	(11.1)	(11.1)
Cladding Absorption at 920 nm	dB/m	2.6 ± 0.4	2.6 ± 0.4
Mode Field Diameter [1] (nominal)	μm	(11.9)	(11.9)
Core Numerical Aperture (*real*NA)		0.080 ± 0.005	0.080 ± 0.005
Cladding Numerical Aperture, ≥		0.48	0.48
Core background loss at 1200 nm, ≤	dB/km	25	25
Birefringence, ≥	1E-04	-	1.6
Geometrical and mechanical			
Core Diameter	μm	12.5 ± 1.0	12.5 ± 1.0
Core Concentricity Error, ≤	μm	1.0	1.0
Cladding Diameter (flat-to-flat)	μm	125 ± 2	125 ± 2
Cladding Geometry		Octagonal	Round, PANDA
Coating Diameter		245 ± 15	245 ± 15
Coating Material		Dual coated low index acrylate	Dual coated low index acrylate
Proof Test, ≥	kpsi	100	100

[1] Far-field Mode Field Diameter at 1060nm

+358 19 357391 • fibers@nlight.net • www.nlight.net

*n*LIGHT

Figure A.9: Specification of LIEKKI Yb1200-12/125.